Lithotripter Shock Wave induced RNA-based Gene Therapy



Sandra Nwokeoha

Pembroke College

University of Oxford

Supervised by
Professor Robert Carlisle and Professor Robin Cleveland

A thesis submitted to the Department of Engineering Science for the degree of

Doctor of Philosophy

Hilary 2017

Declaration

I hereby declare that this thesis is entirely the product of my own research and work. Any contribution made to the research by others with whom I have worked at the University of Oxford, is explicitly acknowledged in the text.

Sandra Nwokeoha

March 2017

This thesis is dedicated to
the heroes that make up my family and my community.

On Christ, the solid rock, I stand –
all other ground is shifting sand
-Edward Mote

Abstract

Gene therapy is the process of introducing genes to augment or minimise the expression of absent or defective genes, respectively. Non-viral gene delivery systems for the treatment of genetic diseases, have evolved into highly appreciable nucleic acid based therapies due to considerably less risk of host immunogenicity and induction of inflammatory responses. However, they are challenged by limited delivery. Thus, more efficient strategies are continually being sought. Lithotripter shock waves (LSW) are powerful acoustic waves that are an attractive choice of delivery system, as they offer a non-invasive, targeted and safe approach. Furthermore, the delivery of messenger ribonucleic acid (mRNA) possesses several advantages over commonly delivered plasmid deoxyribonucleic acids (pDNA), because it does not require opening of the nuclear envelope, thereby reducing the level of cell injury necessary for transfection.

This work presents the first investigation on the efficacy of LSW mediated mRNA delivery, based on optimised SW parameters that balance the desired enhanced permeability of cell membranes against undesired cytotoxicity, and maintain the structural and biological stability of the RNA. A transfectability measure that defines the ability of SWs to permeabilise a cell whilst keeping it alive was established for dissimilar cell types, as a function of the acoustic pressure and number of SWs. Statistically significant RNA uptake was recorded in a tissue mimicking system, and using RNA analogs at various concentrations, the SW induced bio-distribution was characterised. In addition to LSW induced gene augmentation using mRNA, it was shown that LSWs could be used to effect gene inhibition through the delivery of siRNA.

Kinetic experiments were carried out to measure mRNA uptake during shock wave exposure and indicated that rate of delivery was highest at the start of the SW dose and decreased during treatment. The results also suggested that the enhancement of cell permeability was significantly transient, and that mRNA was highly susceptible to degradation in its naked state. Furthermore, mRNA-based gene expression was shown to be predictive but quantal.

The *in vitro* tissue model was improved from a gel-based system, to one that incorporated multi-cellular spheroids which capture aspects of 3-D tumours. Static overpressure was applied during SW exposure in order to suppress cavitation effects and isolate effects that could be attributed to shear due to cell-to-cell coupling. The results showed that mild overpressure improved RNA uptake the most, but that at higher overpressure, the level of increase in RNA uptake relative to controls, was dependent on

the type of RNA nucleotide being delivered. This suggested that a complex interaction between LSW cavitation and direct stress dominates delivery.

A final report was on the significant improvement of gene delivery when mRNA was encapsulated within a lipid nanoparticle vector, and SW exposure was assisted by cavitation agents. Also, by exposure to another acoustic stimulus – focused ultrasound (US), direct comparisons were made between SWs and US on the efficiency of delivery and tissue penetration. In conclusion, this thesis has shown that by choosing parameters appropriately, shock waves can be a promising strategy for the delivery of genes to cells.

Acknowledgements

I wish to record my appreciation to a list of individuals that have made this research possible and enjoyable. Without a shadow of doubt, I am indebted to my supervisors Prof Robert Carlisle and Prof Robin Cleveland, who equally and effectively trained me and guided my research thoughts and undertakings. Their expertise has been inspirational, and I am enormously grateful for their proposal of this project and for charging me with its development.

I am particularly thankful to the workshop technicians Jim Fisk and David Salisbury for bringing to reality my many designs, and for their helpful technical suggestions. I have thoroughly enjoyed going to the workshop for the jokes, chats and friendly advice they always had to give.

I am so thankful to Dr Jamie Collin for making my first year of study incomprehensibly smooth. Without his willingness to assist me as I familiarised myself with equipment and experimental concepts, I certainly would not have made timely progress. I would also like to take this opportunity to thank the microscopy core leader in the Department of Oncology – Graham Brown, for all the purposeful discussions we've had over all-things imaging; to Egon Jacobus for the exchange of ideas that we've had over the course of our DPhils, and to Dr Fiona Yi Lee from DPAG (Oxford) for access and training on the Bioanalyzer.

Appreciation is also due to those who made parts of this thesis possible: to Mr Ben Turney and Ms Mandy Spencer of the Oxford Stone Group at the Churchill Hospital (Oxford), for providing access to the clinical lithotripter during the first 15 months of my research. Also, to Prof Constantin Coussios, and collaborators at AstraZeneca (UK) for enabling the advancement of my research into Chapter 6; and to Dr Shamit Shrivastava for partnering in this work.

Due to the nature of my project, and my curiosity to try different things, majority of my research time was spent in the biological labs, often till the late hours of the night. Despite the long hours and lack of time for any dinner, those times were times that I will forever cherish because of the practical assistance rendered to me by Dr Arthur Dyer and Dr Janet Lei, and their friendships.

In the BUBBL laboratory I would like to thank absolutely everyone for contributing to a welcoming, happy and engaging atmosphere where I could freely ask a question and be pointed in the right direction. A special thank you goes to the friends that I closely walked this journey with: Visa Suomi, Dongli Li, Steve Bian, Yinka Oduwole,

George Qian and Andre Hallack for being intentionally supportive and for all the fun times in and out of the department.

Finally I would like to thank my faith fellowship at St Aldates Church for truly giving me another home, for the blessing of lifelong friendships, and the unplanned mentorships. In the wider community, a dear friend to me Ms Lorna Box, deserves a mention for her hospitality in my last year of study, for the making of countless & delicious hot chocolates as I wrote this thesis and for being a perfect listener and honest interpreter. Most importantly, I owe more than words can express to my father for his unfailing moral counsel, my mother and siblings for rooting for me every step of the way, and especially to my sister Uche Nwokeoha for her ever-present lending hands and comfort.

The most credit is given to the Centre for Doctoral Training in Healthcare Innovation, RCUK (Digital Economy Programme grant number EP/G036861/1) for funding me throughout my DPhil and for the provision of extra allowances.

Peer-Reviewed Journal Papers

- Nwokeoha, S., Carlisle, R., & Cleveland, R. O. (2016). The Application of Clinical Lithotripter Shock Waves to RNA Nucleotide Delivery to Cells. Ultrasound in medicine & biology, 42(10), 2478-2492.

Conference Presentations

- S. Nwokeoha, R. Carlisle, R. Cleveland. "RNA-Based Gene Delivery Using Clinical Lithotripter Shock Waves". *The 16th International Symposium on Therapeutic Ultrasound, Tel-Aviv, Israel, 14–16 March 2016.*
- S. Nwokeoha, R. Carlisle, R. Cleveland. "Lithotripter Shock Waves for RNA Delivery to Cells". *The 13th Meeting of the Therapy Ultrasound Group (THUGS), Cardiff, Wales, 10th December 2015.*

Conference Posters

- S. Nwokeoha, R. Carlisle, R. Cleveland. "Toward delivery of mRNA to cells with lithotripter shock waves". *ESGCT and NVGCT Collaborative Congress, the Hague, Netherlands, 23–26 October 2014.*

Contents

List of Figures **xiii**

List of Abbreviations **xxi**

Contributions **xxiii**

1 Introduction **1**
1.1 Motivation . . . 2
1.1.1 A clinical perspective . . . 5
1.2 Overview of Gene based Therapies . . . 5
1.3 Nucleic Acids . . . 7
1.3.1 Deoxyribonucleic acids (DNA) . . . 7
1.3.2 Ribonucleic acids (RNA) . . . 9
1.3.3 Antisense oligonucleotides (ASO, AON) . . . 12
1.3.4 Aptamers . . . 13
1.4 Non-physical methods of cell membrane permeation . . . 13
1.4.1 Calcium phosphate precipitates (CPP) . . . 14
1.4.2 Lipoplexes & Polyplexes . . . 14
1.4.3 Viral vectors . . . 15
1.5 Physical methods of cell membrane permeation . . . 16
1.5.1 Electroporation (EP) . . . 16
1.5.2 Magnetofection . . . 17
1.5.3 Microinjection . . . 17
1.5.4 Sonoporation . . . 18
1.5.5 Laser irradiation . . . 18
1.5.6 Gene gun (biolistic delivery) . . . 19
1.6 Overview of thesis . . . 19

2 Acoustic Principles in Shock Wave induced Gene Delivery **21**
2.1 Shock waves . . . 22
2.1.1 Shock formation & non-linear propagation . . . 23
2.1.2 Lithotripter sources . . . 24
2.1.3 Safety of therapeutic shock waves . . . 25

2.2 Acoustic Cavitation . . . 27
2.2.1 Cavitation defined . . . 27
2.2.2 Shock wave cavitation . . . 28
2.2.3 Cavitation detection . . . 29
2.2.4 Nucleation of cavitation . . . 30
2.3 Direct Mechanical Stresses . . . 32
2.3.1 Current knowledge in shear stress-induced bioeffects . . . 32
2.3.2 Methods of cavitation suppression for separation of shear stress-induced bioeffects . . . 34
2.4 Acoustics-mediated gene transfer . . . 35
2.4.1 State of the art in acoustics-assisted gene delivery . . . 35
2.4.2 Current limitations to shock wave-induced gene therapy . . . 36

3 Optimisation of Clinical Shock Waves and Mediation of RNA Delivery to Cells 40
3.1 Opening Remarks . . . 41
3.2 Materials and Methods . . . 42
3.2.1 Cell lines & cell culture . . . 42
3.2.2 Shock wave generation & set-up . . . 42
3.2.3 Exposure cell containment . . . 43
3.2.4 Shock wave field characterisation . . . 45
3.2.5 Sample Preparation & Treatments . . . 45
3.2.6 mRNA & siRNA stability . . . 46
3.2.7 Cell Survival & Viability Assay . . . 46
3.2.8 Cell Permeabilisation analysis . . . 47
3.2.9 FITC-dextran delivery and dissemination . . . 47
3.2.10 Transfection procedure . . . 48
3.3 Results . . . 49
3.3.1 Cell density modulates post-shock wave cell viability . . . 49
3.3.2 Influence of shock wave parameters on CT26 cell viability and permeabilisation . . . 51
3.3.3 Optimisation of shock wave parameters . . . 54
3.3.4 Shock wave pressure . . . 58
3.3.5 Permeabilisation and viability of HK-2 & MCF-7/GFP cells . . . 60
3.3.6 RNA stability . . . 60
3.3.7 Shock wave-mediated transport of 250-kDa FITC-dextran and dissemination in agarose is a function of macromolecule availability 63
3.3.8 GFP mRNA transfection . . . 67
3.3.9 GFP siRNA transfection . . . 68
3.4 Discussion . . . 71
3.5 Closing Remarks . . . 75

4 Delivery Kinetics and Predictability of Shock Wave induced Transfection 76
4.1 Opening Remarks . . . 77
4.2 Preliminary study on shock wave device equivalence . . . 78
4.2.1 Set-up of shock wave sources . . . 78
4.2.2 Determination of the critical shock wave compressional features . 79
4.2.3 Optimal shock waves for Storz Minilith . . . 82
4.3 Materials & Methods . . . 83
4.3.1 Design of experiment . . . 83
4.3.2 Configuration and preparation of samples . . . 84
4.3.3 Initial mRNA measurements . . . 85
4.3.4 RNA quantification & calibration . . . 86
4.3.4.1 Ribogreen . . . 86
4.3.4.2 In vitro translation (RRL) . . . 86
4.3.4.3 Reverse transcriptase real-time quantitative polymerase chain reaction (RT-qPCR) . . . 88
4.3.5 GFP quantification & calibration . . . 88
4.3.5.1 Bicinchoninic acid (BCA) method . . . 88
4.3.6 Flow cytometry . . . 89
4.4 Results . . . 90
4.4.1 Shock wave mediated kinetics of mRNA uptake by mass and number of positive cells . . . 90
4.4.2 Shock wave mediated kinetics of GFP translation by mass and number of positive cells . . . 95
4.5 Discussion . . . 99
4.6 Closing Remarks . . . 102

5 The Contribution of Shock Wave induced Shear Stress on Multicellular Spheroids 103
5.1 Opening Remarks . . . 104
5.2 Materials & Methods . . . 105
5.2.1 Spheroid culture & characterisation . . . 105
5.2.2 Configuration and preparation of samples . . . 106
5.2.3 Overpressure experiment . . . 107
5.2.4 Cavitation detection experiment . . . 108
5.2.5 Quantification of mRNA delivery to MCTSs and single cells . . . 110
5.2.6 Quantification of siRNA delivery to MCTSs . . . 111
5.3 Results . . . 111
5.3.1 Cavitation activity . . . 111
5.3.2 mRNA delivery: single cells versus spheroids . . . 116

5.3.3 siRNA delivery: the effect of overpressure on MCTSs 120
5.4 Discussion 125
5.5 Closing Remarks 127

6 Exploitation of a Lipid Nanoparticle and Cavitation Nuclei for Enhanced Transfection 128
6.1 Opening Remarks 129
6.2 Materials & Methods 130
6.2.1 Cell lines & culture 130
6.2.2 Gel-based cell viability assay 130
6.2.3 Lipoplexes 131
6.2.4 Configuration and preparation of samples for transfection 132
6.2.5 Ultrasound set-up & beam profile 134
6.2.6 Shock wave & Ultrasound exposure parameters 136
6.2.7 Lipid nanoparticle and cavitation agent stability 136
6.2.8 Control tests with Lipofectamine 137
6.2.9 GFP expression quantification 137
6.3 Results 138
6.3.1 Shock wave parameter optimisation & selection of Ultrasound exposure parameters 138
6.3.2 Post exposure stabilities 144
6.3.3 Evaluation of the LNP compared to Lipofectamine positive control 148
6.3.4 Shock wave & Ultrasound mediated LNP delivery in suspended cells 149
6.3.5 Shock wave & Ultrasound mediated LNP delivery in embedded cells 153
6.4 Discussion 156
6.5 Closing Remarks 159

7 Summary & Future Work 160
7.1 Summary 161
7.2 Future work 164

Appendices

A Appendix 167
A.1 siRNA delivery controls 168
A.2 Stock mRNA quantitation 168
A.3 The RT-qPCR reaction cycling programme 169
A.4 PCDs bracket design and assembly 169
A.5 Shock wave PRF effect on B16-F10(AP3) cells 170
A.6 Dynamic light scattering measurements of NCs, for phantom gels prepared in purified (Milli-Q) water 171

List of Figures

1.1 Potential clinical practice and congruence in the treatment of nephrolithiasis (NL), by concurrent extracorporeal shock wave lithotripsy (ESWL) and shock wave induced anti-nephrolithiasis gene therapy. 6
1.2 Comparison of enhanced green fluorescent protein (eGFP) expression from either eGFP mRNA or eGFP DNA in *in vitro* transfections of K562 haematopoietic cells. MFI is the mean fluorescence intensity. Image taken from [63] (Ponsaerts et al., 2003). 10
1.3 The gene silencing mechanism of siRNA. Image taken from[70] (Hall, 2004). 11

2.1 a) Pressure waveform of a typical electrohydraulic lithotripter shock wave at its focus, comprising a strong compressive shock front and rarefaction tail; b) the corresponding Fourier Transform. Image taken from [20] (Cleveland & McAteer, 2007). 22
2.2 Three types of shock wave generation and the respective typical pressure waveforms; a) electrohydraulic, b) piezoelectric, c) electromagnetic. Images taken from [151, 155](Thiel et al., 2000; Coleman & Saunders, 1989) . . . 25
2.3 Characterisation of the SonoVue microbubbles. Images taken from [190, 191](Cheung et al., 2009 & Quaia, 2006). 31
2.4 Characterisation of the Nanocup particles. Image taken from [193] (Kwan et al., 2015). 32
2.5 Probability of cavitation bio-effects based on a cell (denoted by the star) proximity to a cavitating bubble. Image taken from [219] (Guzman et al., 2003). 37

3.1 (a) Shock wave permeabilisation equipment and set-up. Shock waves were generated through a 43 L water tank, fitted above the shock wave source. Cell samples were supported by a sample holder, and maintained at 37 °C with a thermostatic heater. The flow degasser reduced O_2 content to 1 – 3 mg/L; (b) custom-made 'TMM-MODU' phantom for RNA transfection. The dimensions of the agarose + cells containment were 10 × 5 × 40 mm (L × W × H). 44

3.2 Effect of CT26 cell concentration on the cell viabilities (using the MTS assay) relative to the negative control at (a) immediately, and (b) 24 hours after exposure. Data consists of at least three same-day replicates per treatment, for three independently conducted experiments (i.e. n=9). The markers represent the means and the error bars represent the standard errors. Both statistics are expressed as percentages. 50
3.3 Influence of shock wave exposure on cell viability. CT26 cells were assayed at 1 or 24 hours after exposure using the MTS assay. The influence of number of shock waves, energy and pulse repetition frequency was investigated. Data points represent the mean values of triplicates per treatment, for at least three independently conducted experiments (i.e. n=9). Error bars are the standard errors. 51
3.4 The effect of shock wave pulse repetition frequency on the absorbance of the MTS formazan product which is proportional to the cell viability. Data consists of three triplicates per treatment, for three independently conducted experiments (n=9). 52
3.5 Light micrographs of CT26 cells, 1 hour after shock wave exposure: (a) sham, (b) treated with 3 E, 250 shocks at 1 Hz, (c) 6 E, 250 shocks at 1 Hz, (d) 3 E, 500 shocks at 1 Hz. Scale bar corresponds to 56 μm. 53
3.6 Flow cytometric measurements of CT26 cell permeabilisation and viability. Representative density-plots for three treatments: sham (top), 3 E, 125 pulses, 2 Hz (middle), 9 E, 500 pulses, 2 Hz (bottom). 55
3.7 CT26 cell permeabilisation combined with results of 24-hours viability. Data points represent the means of three same-day replicates, for at least three separate day experiments (i.e. n=9). Error bars are the standard errors. 56
3.8 Transfectability of CT26 cells as a function of the number of shock pulses (0 – 1000) and energy level (3 – 9) at 2 Hz. Transfectability is defined as the percentage of live permeabilised cells. Three independently conducted experiments at 1000 pulses, with three-same day replicates at each tested energy level were included. 57
3.9 (a) Representative shock waveform at energy level 4.5 when measured at the focal point in degassed water and inside the polypropylene (PP) vial; (b) Measurements of peak positive pressure at energy level 4.5, in the direction perpendicular to the shock wave propagation path (X-Y) and along the path (Z); n = 5. Error bars are the standard deviations (range: 0.07 - 0.86 MPa). The focal zone is marked by the dashed line representing the pressure being 6 dB less than the maximum peak positive pressure. 59

3.10 Influence of shock wave exposure on HK-2 and MCF-7/GFP cell permeabilisation (bars) and 24-hour-after cell viability (lines). Data points represent the mean values of three same-day replicates per treatment, for three separate day experiments (i.e. n=9). Error bars are the standard deviations. 61

3.11 Results of stability for (A) mRNA and B) siRNA post shock wave exposure or sham (control) treatment. Structural stability data depicts (A-1) representative mRNA electrophoretic profiles and (B) agarose gel electrophoresis for siRNA analysis (based on n=3). (A-2) mRNA biological activity data consists of one sample per treatment, for three independently conducted experiments (n=3); error bars represent the standard deviations. 62

3.12 Representative disseminations of 250-kDa FITC-dextran in the custom-made 1% agarose tissue phantoms, along the direction of shock wave propagation (i.e. from - 20 to 20 mm) after shock wave or sham treatment. The areas in-between the dash-dot lines represent the channel width. The black arrow indicates the direction of shock wave propagation. 64

3.13 FITC fluorescence-based analysis of FITC-dextran delivery to sham (blue histograms) and optimal shock wave (SW) treated (red histograms) cells, at three different dextran concentrations: (a) 5 μg, (b) 30 μg (c) 180 μg. The green histograms represent the negative control sample (non-labelled and untreated) in order to resolve the background fluorescence. Gated values correspond to the percentage of cells with fluorescence intensity above that of the background. (d) Summary of the results based on n = 3. 66

3.14 Results of eGFP mRNA delivery to CT26 cells for shock wave and sham treated samples. a) Data is expressed as the means of intensities of six replicates per treatment across two independently conducted experiments. The error bars are the standard deviations. Significance was tested using the two-tailed unpaired parametric t-test where * = p <0.05 (p = 0.04). b) Representative images of GFP expression at 48 hours after sham or shock wave treatment. Images were converted to binary by thresholding. 67

3.15 Results of anti-eGFP siRNA delivery to MCF-7/GFP cells. a) GFP intensities of shock wave treated (+ SW) and non-treated (- SW) samples consisting of three replicates per treatment for one independently conducted experiment. Error bars are the standard deviations. b) Representative spatial fluorescence intensities across the tissue phantom region of interest for SW and sham siRNA treatments. 70

4.1 Investigation of critical shock waveform characteristics by comparing the CT26 *transfectability* of piezoelectric (PE-ESWT) and electromagnetic (EM-Litho) shock wave sources. (a) Characterisation summary of the shock waveforms' positive phase characteristics; (b) matching the peak compressional pressure, (c) matching the derived positive pulse-intensity integral (with positive temporal integration limits as indicated by the red-labelled portions of the waveforms); (d) Respective results of transfectability at n = 9. Error bars are the standard deviations. The asterisk denotes statistical significance at the $p < 0.05$ level. 81

4.2 Comparison between the previously employed clinical lithotripter (EM-Litho) and the henceforth employed ESWT lithotripter (EM-Minilith), based on matched-PII shock waveforms as recorded *inside the cell containment (PP vial), in water.* 82

4.3 Outline of the analysis time course (not drawn to scale) for the three investigations indicated by the curly brackets, alongside the measurement methodologies for each investigation. Samples at each interval during SW exposure were subjected to continually degassing and heated water. Samples at each interval after SW exposure were incubated up to the interval time point. 84

4.4 Design of the 'TMM-MINI' phantom and format of the cells, RNA and agarose. A clamping plate and mylar sheet on each face of the illustrated phantom body sealed off the phantom. A second channel, 3 mm above the working channel and perpendicular to it, was used for injection of the agarose. Both channels were leak-proofed using barbed Luer fittings. The centre of the channel was aligned to the SW focus. 85

4.5 Calibrations and linear range determination for eGFP mRNA quantitation through (a) Ribogreeen, (b) Rabbit Reticulocyte Lysate in vitro translation and (c) RT-qPCR. All three standard curves are representative of at least two separate day experiments (each at n=3). Error bars are the standard deviations. 87

4.6 BCA standard curve using recombinant GFP and curve fit. Error bars are the standard deviations based on n=3. 89

4.7 Representative mRNA amplification plots of the experimental RT-qPCR reaction for samples at the analysed time points of 1 and 5 minutes of SW exposure, and 60 and 240 (4 hours) minutes after SW exposure. 90

4.8 A three-method quantification of eGFP mRNA transfer into cells, as a function of shock wave treatment duration and up to 4-hours afterwards. Data points are the mean values of triplicates and are representative of two independently conducted experiments (each at n=3). 91

4.9 Kinetics of Cy5 labelled eGFP mRNA uptake by number of cells. Representative flow cytometric measurements of Cy5 positive cells, in sham samples (a), and through the course of shock wave treatment: (b) 1 minute - (f) 5 minutes. 93
4.10 Quantification of the GFP positive population at (a) 48 hours and (b) 40 hours post, by diagonal gating of the FL1 (GFP) and FL2 channels. Sample description is shown on the top left corners. The subset population is in percentage form. 96
4.11 Kinetics of eGFP expression post shock wave exposure by flow cytometric measurements of eGFP positive cells, in comparison to sham exposure. GFP expression was probed within a 6-120 hour period after exposure, in three separate day experiments (each at n=3). The error bars are the standard deviations. 97
4.12 Kinetics of eGFP expression post shock wave or sham exposure by protein quantitation, using the BCA method. GFP synthesis relative to *non-shocked negative controls* for sham, or *shocked negative controls* for shock wave. Data represents n=3; error bars are the standard deviations. 98

5.1 Viability and size characterisation of cultured spheroids with various initial cell seeding densities. a) Phase contrast microscopy of the spheroids at 48 hours after culture. The scale bar represents 250 μm; b) mean diameter of spheroids with standard deviations and live cell count by spheroid dissociation and Trypan Blue exclusion test (n=3); c) fit (dashed line) of initial cell seeding count versus spheroid size [$y = -1.55e^{-7}x^2 + 0.022x + 325.4$]; d) percentage increase of the spheroids' live cell population indicating an increased proportion of necrotic cells with increasing initial cell seeding density. 106
5.2 Schematic of the overpressure experiment as well as the cavitation detection set-up. The inset photograph demonstrates the modified TMM-MINI phantom. The custom-made phantom holder had hollowed out faces to enable direct SW transmission and access to the phantom's openings. PCD = passive cavitation detector. 107
5.3 The sensitive field of the dual PCDs. The white rectangles demarcate the TMM boundaries. 109
5.4 Example of a dual PCD signal (with the PCD 2 trace inverted for comparison) showing coincident emissions which are characteristic of cavitation in lithotripsy. 112
5.5 Examples of the measured cavitation bubble collapse times for the first 100 shocks, within the experimental TMMs for five different conditions. The subscript numbers indicate the triplicate sample number. 114

5.6 Representative cavitation bubble collapse times for the first 100 shocks within the **degassed** TMMs (note that the subscript numbers merely indicate the triplicate sample number). 116
5.7 (a) internalised mass of eGFP mRNA as quantified by RT-qPCR, after the various treatments at n = 3, in both cell formats (single cells and MCTSs); * represent $p < 0.05$ determined by Bonferroni multiple comparison tests. (b) Two-way ANOVA statistical analysis; n.s. represents no statistical significance at the $p < 0.05$ level. 118
5.8 Examples of SiGLO Red uptake and cell viability (through Calcein Blue AM) in the spheroids, after treatment to (a) optimal shock waves (denoted by 'Opt SWs'), in addition to (b) 350 kPa overpressure or (c) 700 kPa overpressure; (d) sham treatment and (e) no treatment to SiGLO Red nor shock waves. 123
5.9 (a) Results of fluorescence intensities in the spheroids after the various treatments. Data consists of three replicate samples for one independently conducted experiment. Note that each sample consists of a set of spheroids and therefore each sample was an average itself. Error bars are the standard deviations. (b & c) statistical significance analyses for siGLO and Calcein fluorescence, using the one-way ANOVA with Bonferroni multiple comparisons tests; n.s. denotes no significance at the $p < 0.05$ (95% confidence interval) level. 124

6.1 Schematic of the cell configurations within the TMM-MINI phantom, devised for the transfections; with (a) cells in suspension and (b) cells embedded in agarose; where the lipoplexed mRNA is denoted by *LNP*, and *CA* is the cavitation agent. 133
6.2 (a) The ultrasound set-up for the delivery experiments. (b) & (c) Characterisation of the ultrasound beam profiles inside a water-filled TMM-MINI. To enable hydrophone entry the TMM-MINI was assembled without the distal Mylar sheet. (d) Pressure calibration curve. 135
6.3 A representative plate read-out image of lactate dehydrogenase (LDH) release, from CT26 cells exposed to selected US and SW conditions, 18 hours after exposure. PC = positive control. The colour intensity increased with LDH release increase. 139
6.4 US induced cell cytotoxicity measured by LDH release from the agarose-based tissue mimicking material for (a) B16-F10(AP3) & (b) CT26, at nominated conditions, in the absence or presence of SonoVue. Peak rarefactional pressures of 1.0, 1.5 and 3.0 MPa were applied, while the exposure durations were: 7.5 ms, 30 seconds and 2 minutes. Results are based on n=3 and the error bars are the standard deviations. 140

6.5 Maps of B16F10(AP3) cell viability and permeabilisation in medium, after shock wave treatment at 2 Hz PRF. Data consists of three independently conducted experiments (n=9). 142
6.6 Shock wave induced transfectability of B16-F10 cells, as a function of shock wave energy and number. 143
6.7 Percent cytotoxicity through LDH release from the TMMs comprising (a) B16-F10(AP3) or (b) CT26 cells; at exposure conditions suitable for cavitation agent-assisted US and SW treatment. N=3; error bars are the standard deviations. 145
6.8 Representative dynamic light scattering measurements of LNP/NC size distributions based on n=3, after sham, shock wave or ultrasound treatment at respective optimised conditions for CT26, (a) fresh samples, (b) LNP samples, (c) LNP and NC samples, and (d) NC samples. The small peaks at 5560 nm are disregarded as micro-sized contaminants from the non-sterile Zetasizer cells. 146
6.9 Stability results of SonoVue (SV) by optical particle size measurements (using the AccuSizer) post sham, US and SW treatments at their respective optimal conditions for CT26. Data is representative of n=3. 148
6.10 Comparison of *in vitro* lipid-based transfections on CT26 cells, between the LNP by AZ and various amounts of LF (Lipofectamine 2000). In all cases 500 ng of eGFP mRNA (Trilink Biotechnologies) was lipoplexed. Data represents n=3 for one independently conducted experiment. The error bars are the standard deviations. 149
6.11 Quantification of GFP positivity in the cells in suspension exposure configuration; (a) representative flow cytometric measurements of GFP positive cells by FL1-FL2 diagonal gating, for SW conditions and (b) for US conditions. (c) results based on n=3 for one independently conducted experiment. The two-way ANOVA with Bonferroni multiple comparisons tests, revealed statistical significance at $p < 0.05$ (*) and $p < 0.001$ (***) relative to the corresponding sham controls. 153
6.12 Selected confocal z-stack micrographs of the highest observed GFP expressions in the displayed treatment groups: (a) LNP only (or sham), (b) LNP with shock wave exposure, (c) LNP with ultrasound exposure in the presence of Nanocups, and (d) LNP with shock wave exposure in the presence of Nanocups. 155
6.13 Corresponding profiles for the NC-containing samples, of fluorescence intensity along the thickness of the TMM, up to 0.695 mm above the upper edge of the channel. 156

A.1 Supplementary controls using non-GFP MCF-7 cells to determine background fluorescence, based on n = 3. Error bars are the standard deviations. 168

A.2 A representative absorption spectrum of a 100 μg/ml mRNA stock for a kinetics independently conducted experiment. 168
A.3 PCD bracket (or holder) CAD design. 169
A.4 PCDs and bracket assembly. 170
A.5 No statistical significance (n.s.) across PRF groups was found in both the viability and permeabilisation of B16-F10(AP3) cells, using the one-way Analysis of Variance (ANOVA) test at the $p<0.05$ level. Data represents $n = 3$, and the error bars are the standard deviations. 170
A.6 Representative DLS size measurement of the water-based gel Nanocups sham. 171

List of Abbreviations

SW . . . . . Shock wave

ESWL . . . . . Extracorporeal shock wave lithotripsy

SWL . . . . . Shock wave lithotripsy

LSW . . . . . Lithotripter shock waves

E . . . . . Lithotripter Energy Level

ESWT . . . . . Extracorporeal shock wave therapy

HIFU . . . . . High intensity focused ultrasound

US . . . . . Ultrasound

RNA . . . . . Ribonucleic acid

DNA . . . . . Deoxyribonucleic acid

mRNA . . . . Messenger ribonucleic acid

siRNA . . . . . Small interfering ribonucleic acid

GFP . . . . . Green fluorescent protein

eGFP . . . . . Enhanced green fluorescent protein

PRF . . . . . Pulse repetition frequency

PRFP . . . . . Peak rarefactional pressure

FITC . . . . . Fluorescein isothiocyanate

TMM . . . . . Tissue mimicking material

PI . . . . . Propidium iodide

FI . . . . . Fluorescence intensity

PCD . . . . . Passive cavitation detect(ion/or)

LNP . . . . . Lipid nanoparticle

CA . . . . . Cavitation agent

SV . . . . . SonoVue

NC . . . . . Nanocups

wrt . . . . . with respect to

AZ . . . . . AstraZeneca

LF . . . . . Lipofectamine

Contributions

Fig 5.3 . . . . . PCD field characterisation performed by Prof. Cleveland

Fig 6.8 . . . . . Dynamic light scattering measurements conducted by Dr Shrivastava

1 Introduction

Contents

1.1 Motivation 2
1.1.1 A clinical perspective 5
1.2 Overview of Gene based Therapies 5
1.3 Nucleic Acids 7
1.3.1 Deoxyribonucleic acids (DNA) 7
1.3.2 Ribonucleic acids (RNA) 9
1.3.3 Antisense oligonucleotides (ASO, AON) 12
1.3.4 Aptamers 13
1.4 Non-physical methods of cell membrane permeation 13
1.4.1 Calcium phosphate precipitates (CPP) 14
1.4.2 Lipoplexes & Polyplexes 14
1.4.3 Viral vectors 15
1.5 Physical methods of cell membrane permeation 16
1.5.1 Electroporation (EP) 16
1.5.2 Magnetofection 17
1.5.3 Microinjection 17
1.5.4 Sonoporation 18
1.5.5 Laser irradiation 18
1.5.6 Gene gun (biolistic delivery) 19
1.6 Overview of thesis 19

1.1 Motivation

Cancer embodies a disease that poses a major worldwide public health problem. Since the 1970s, combination chemotherapies and adjuvant therapies [1] have pointed toward the exploitation of synergy to build upon the efficacy of single agent treatments. However, challenges in drug resistance have not been erased by the administration of drug combinations, as a result of mechanisms such as the innate or acquired expression of cell membrane transporters (which expel drugs from within the cytoplasm), with overlapping resistance profiles [2].

The broader scope of therapeutic genes compared to drugs, and the corrective (rather than palliative) power they exert, render genes ideal for use in the clinic. For example, cancer gene therapy offers the ability to suppress the expression of transporters such as P-glycoprotein (P-gp), which confer multidrug resistance, as well as promote the expression of proteins involved in immunity-induced cytotoxicity, such as interleukin-12 [3]. Consequently, co-delivery strategies of genes and drugs have gained traction [4].

Nevertheless, the gene delivery process has its own hurdles, partially alleviated by the use of vectors but challenged in other aspects. For instance, viral vectors, the potential of which has been demonstrated by their dominance in current gene therapy clinical trials [5], suffer from notable immune response mediated challenges. Studies have shown the inactivation of oncolytic viruses by blood components and the reticuloendothelial system, leading to rapid clearance of these therapeutics [6]. Moreover, non-viral gene therapy approaches have to date failed to show sufficient activity.

The application of therapeutic shock waves for gene therapy display less significant physiological drawbacks. Its drawbacks (which pertain to all physical methods of intracellular molecular transport) comprise the inability of naked genetic material to resist degradation through extracellular serum endonuclease and macrophage uptake in the bloodstream [5]; and the relatively low efficacy of delivery even in the absence of extracellular barriers (as is the case *in vitro*). The first limitation described above has been a major focus in nanomedicine, whereby protective gene encapsulations with effective release strategy triggered by a physical stimulus are being extensively formulated [7, 8]. However, the latter limitation is a result of insufficient consideration or experimental

investigation of the impact of such barriers. Hence, the development of strategies which address this challenge both in transgene expression and clinical translation value, forms the first objective of this work. A furtherance of efforts to optimise conditions related to the employed strategies, also holds promise in promoting enhanced gene delivery.

Current measures of delivery efficiency are rendered difficult to compare and evaluate between studies because of the existing gray area between the *internalised* nucleic acid dose and the level of transgene produced. Resolving this unknown will inform nucleic acid dosimetry for ultrasound- and shock wave-assisted gene delivery and enable prediction of the functional outcome. Furthermore, a key aspect of faltering clinical trials has been the loss of transgene expression over time [5] arising from poorly understood delivery kinetics, which are particularly under-represented in shock wave (SW) mediated cellular uptake studies, but also more broadly in ultrasound (US) [9–11]. In [9] and [11] the kinetics of plasmid DNA internalisation and reporter gene expression through ultrasound, were characterised with reference to a standard liposomal transfection reagent, but did not capture the uptake kinetics *during* US treatment. Therefore, the kinetics of internalised DNA after US treatment only reflected the rates of DNA degradation (whether intrinsic or instigated by US), cell proliferation and endocytosis. Presently, there is a need to understand what the acoustically-induced transfection profile is and the associated kinetic parameters, which will ultimately impact treatment regimens.

In view of the underlying mechanisms through which ultrasound modalities effect cellular delivery of therapeutic agents, a body of literature (reviewed in [12]) has identified two fundamental mechanisms, namely, acoustic cavitation and acoustic radiation force. Cavitation is a highly localised activity wherein micron-sized gas bodies interact with a sound field [13], by undergoing nucleation, extensive growth and finally collapse. The latter event may significantly concentrate energy onto a very small surrounding area, resulting in some degree of mechanical alteration of cells in the vicinity of the collapse [14, 15]. Cavitation is widely deemed responsible for enhanced cell membrane permeability, a process known as sonoporation, and therefore the intracellular transport of therapeutics [16, 17]. Indeed, ultrasound contrast agents or microbubbles (MBs) have served as cavitation nuclei *in vivo* and provided a strong correlation with improved transfection

[18]. Moreover, there are numerous 'pathways' to cellular structural effects by way of bubbles subjected to low frequency US conditions, comprising: erosion through pressure emissions from bubble collapse and rebound; the growth and action of intra-cellular bubbles; and finally by means of streaming effects produced by the excited bubbles [14].

Further, there are reports that have shown delivery enhancement through non-cavitational mechanisms. For example, Frenkel et al. [19] demonstrated tissue plasminogen activator (tPA) (in combination with HIFU) mediated thrombolysis, which they attributed to non-uniform displacements induced by HIFU radiation force in a blood clot model. Such displacements generate shear stresses and in turn, strains that can alter tissue permeability [12]. In shock wave lithotripsy, the typically low intensities of shock waves may not induce significant radiation forces. However, their exertion of direct shear stresses has formed a noteworthy mechanism for kidney and gall stone comminution [20]. Such a mechanism could potentially play a role in the genetic treatment of solid tumours.

Another area concerning this research work is the comparability of lithotripter shock waves to focused ultrasound for gene delivery, where the latter has received relatively more attention in the literature, probably because of its established use in treating non-musculoskeletal tissue. Furthermore, the enhancement of SW- [21] or US- [22] mediated delivery of encapsulated DNA has been demonstrated. Accurate comparisons of transfection efficiencies between the competing acoustic modalities, demand that experimental protocols (i.e. set-up, ambient conditions as well as the configuration and handling of cells) are kept the same. To date, by having performed experiments in parallel, only one study (Huber et al., 1999 [23]) qualifies for such analysis. However the study, which employed the commonly delivered plasmid DNA, was limited by *in vitro* experimental strategies that insufficiently recreated the cell's native 3-D environment, and evaluated transfection by SW or US alone. In light of a prospective adoption of SW or US-assisted gene therapy in the clinic, tolerance toward the physiological environment makes the application of protective vectors indispensable for hindering premature degradation of the genetic agent during *in vivo* circulation. Thus, beside an understanding of how sound waves interact with naked nucleotides, insight into how lithotripter shock waves and focused ultrasound interact with such vectors (that

may be lipid or polymer based) and perform in RNA delivery, relative to each other, presents an important gap in the knowledge.

1.1.1 A clinical perspective

A 2009 analysis stated that "renal stone disease (clinically referred to as *nephrolithiasis*) affects 3-5% of the population" [24]. Recently, an increasing incidence in pediatric nephrolithiasis has emerged [25]. The 52% 10-year recurrence rate [26], when considering the increasingly affected child population, indicates that in their lifetimes they may experience a series of incidences. Hypercalciuric nephrolithiasis is evident in a subgroup of patients representing over 35% of stone-forming patients, and is caused by a mutation to single genes involved in regulating calcium reabsorption in the renal tubules, giving rise to monogenic forms of the disorder [24].

Currently lithotripsy is the front-line treatment for renal stones, compared to ureteroscopy and percutaneous nephrostolithotomy. Despite the high success rate observed in lithotripsy, there have been cases of remnant stone fragments that may furnish nuclei for successive stone developments, leading to higher recurrence rates relative to its counterparts [27]. Therefore, while lithotripsy addresses existing renal stones, recurrence could be concurrently targeted by augmentation of expression of the deficient ion transporter or channel genes, in renal cells. Examples include the *CLCN5* chloride channel in Dent's disease or the *CASR* calcium-sensing receptor in the Bartter syndrome type V. Another proposed application is in the treatment of *cystinuria*, whereby a gene (SLC3A1) involved in cystine reabsorption is mutated, leading to the formation of renal stones [28]. The amenability of acoustic waves to gene transfer in rat kidney has been demonstrated, using continuous wave ultrasound [29]. Figure 1.1 depicts the unique advantage of employing shock waves in anti-nephrolithiasis gene therapy.

1.2 Overview of Gene based Therapies

The concept of gene therapy was first tested in a 1940s experiment, in which exogenous nucleic acids were used to transfer genes into pneumococci bacteria [30], and approximately 20 years later into mammalian cells [31]. Subsequent advances in gene technology –

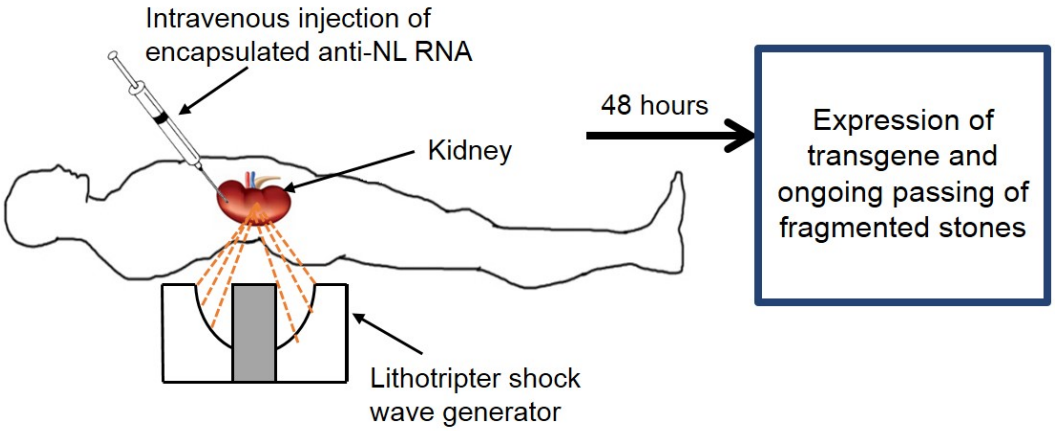


Figure 1.1: Potential clinical practice and congruence in the treatment of nephrolithiasis (NL), by concurrent extracorporeal shock wave lithotripsy (ESWL) and shock wave induced anti-nephrolithiasis gene therapy.

sparked by the development of recombinant DNA and cloning techniques – have rendered gene-based therapy one of the most promising approaches in modern medicine.

Accordingly, genetic disease can be cured by employing any of three different strategies: 1) *gene augmentation* by way of incorporating a functional copy of the defective gene into the affected cells, to reinstate expression of the missing protein [32, 33]; 2) *gene inhibition* whereby genetic material with gene-specific repressive function is introduced to inhibit expression of the faulty protein [34, 35]; and 3) *gene repair* in which a predefined break in the defected genetic sequence is produced using artificial endonucleases. The break is then resealed with the desired exogenous template via the DNA metabolic process of homologous recombination, in order to correct – by editing or disrupting – the mutated site [36, 37].

An impressive range of diseases has been addressed using gene therapy, including: single gene disorders such as severe combined immunodeficiency (SCID) (X-linked [38] and ADA-deficient [39]), haemophilia [40] and hereditary blindness [41]. Further applications have been in multigenic and multifactorial diseases like cancer, by targeting either the tumour cell or the immune system, in both solid and haematological malignancies [42]; infectious diseases such as HIV [43]; and neuromuscular disorders [44].

The ethics surrounding the practice of gene therapy has long been cleared for somatic cells of affected tissue, and is now widely accepted to be morally comparable to aspirin

usage. In contrast, cell targets such as the reproductive (germ line) cells are ethically more controversial, and face a greater challenge in achieving regulatory clearance. This is because of their proximity to gene pool alteration and genetic enhancement of the human species; in spite of their potential in preventing inheritable disorders being passed down to offspring [45, 46].

1.3 Nucleic Acids

Genetic information is encoded in DNA molecules, and disseminated to new cells by DNA replication prior to cell division. Structurally, nucleic acids are heteropolymers composed of monomers known as nucleotides, where the latter consists of a sugar, a phosphate group and a nitrogenous base [45]. Conversion of a DNA gene sequence into a protein product, requires a process of transcription whereby an RNA transcript is produced, followed by translation of this RNA into a protein (a polymer comprised of appropriately sequenced amino acids). The level, timing and duration of protein expression is therefore regulated by control of DNA and RNA, such that therapeutic intervention can aim to target these structures and processes in a range of ways. The choice of genetic agent is described as follows.

1.3.1 Deoxyribonucleic acids (DNA)

DNA structure consists of two antiparallel polynucleotide chains, helically wound around each other. In the transverse view, the deoxyribose sugar-phosphate groups make up the backbones of the DNA molecule; the nitrogenous bases protrude from the inner sides of the helix and hydrogen bond with opposing bases to give specific and complementary base pairing. The strategy used to deliver therapeutic DNA cargo has implications on the level and rate of transgene expression, because DNA requires access into the nucleus and therefore must traverse the cell cytoplasm and the nuclear membrane in order to be transcribed. Attainment of nuclear entry is restricted by the relatively large size/distended structure of exogenously delivered DNA. However, the power (due to amplification) and selectivity of the approach are notable advantages [47–49].

Improving therapeutic DNA expression has been tackled from the perspectives of enhanced stability and gene targeting, for which plasmid DNA (pDNA) and DNAzymes have been employed respectively. However, avoiding compartmentalisation into endosomes or lysosomes and consequently DNA inactivation or degradation, marks another huge obstacle [49, 50]. Plasmids are in essence circular DNA molecules, mostly derived from the extra chromosomal space of bacteria [45]. They are designed to contain promoter and enhancer sequences for gene expression regulation, as well as sites for processing of the resultant pre-mRNA transcript [49]. Effective plasmids comprise an origin of replication, thereby reproducing the behaviour of endogenous DNA prior to mitosis; and include a selectable marker usually based on pDNA intrinsic genes that confer antibiotic resistance, for the selection of transformed cells [51]. However, these features are primarily used for enabling their large scale production in bacteria before they are used in humans.

DNAzymes are described as synthetic catalysts capable of gene-specific chemical transformations [50]. They are single antisense (non-coding) DNA strands that target sequence-specific RNA/DNA and by cleaving them or ligating their fragments, cause some degree of gene inhibition (often used endogenously against viral RNA) [52] or gene sequence mending (that may be applicable to pre-mRNA exon processing) [53] respectively [54, 55]. Moreover, DNAzyme's double ability has been shown in [54] to be programmable such that upon specific substrate conditions, either activity (catalytic or gene transforming) can be de-/activated.

Another form of DNA molecule that has received considerable attention in the literature has been triplex DNA – emerging from antigene oligonucleotides whose triplex-forming mechanism of action inhibits specific mRNA transcription thereby providing gene suppression function [56]. An expanded range of sequences can be targeted, by a DNA oligonucleotide binding to a homopurine (adenine and guanine bases) region of duplex DNA [57, 58].

Finally, although amongst all gene therapy clinical trials to date naked/plasmid DNA has been the third leading gene vector utilised, almost all of these trials relied upon direct delivery into shallow tissues such as muscle [59]. It follows that questions would be raised on the challenge of DNA delivery to and into the nucleus of cells deep within tissue.

1.3.2 Ribonucleic acids (RNA)

Human RNA-based therapy can be classified into three categories: 1) uses RNA involved in the central dogma; 2) uses a type of RNA originating from double-stranded RNA (dsRNA) that targets homologous messenger RNA (mRNA); 3) uses naturally occurring catalytic RNA.

The first mentioned therapeutic RNA class constitutes mRNA. This single-stranded molecule acts as the carrier of genetic information from DNA in the nucleus, to the ribosomes in the cytoplasm. mRNA is produced by transcription of the antisense (non-coding) strand of DNA whereby RNA polymerase, helps unwind the region of DNA double helix that contains a given gene, and as it travels along the antisense strand reads the code and synthesises the pre-mRNA transcript. As a result, the mRNA will have the same sequence as the coding (complementary) strand of DNA, but with the thymine bases replaced by uracil [45, 47]. This intra-nuclear event is followed by splicing of the pre-mRNA transcript in which sequence sections, known as introns, are excised from it. The remaining sequences (or exons) are joined together into a single mRNA strand that represent the final coding sequence for a particular protein [60]. Further modifications based on the addition of a 'cap' at a terminus and a 'tail' of adenine residues (or poly(A) tail) at the other, render the final mature mRNA ready for transport outside of the nucleus and consequently translation [45].

In its three dimensional structure, mRNA is likely to display self-folded regions that create double helices (or stems) partially distending along the molecule. This is possible in regions that have complementary or nearly complementary sequences when folded [47]. However, the generally single-stranded nature of mRNA bestows chemical instability and as such *in vivo* delivery of therapeutic RNA is subject to degradation by extracellular RNAses [61].

It is possible to exert control at different levels of gene expression. Levels such as protein processing, recruit transfer RNA (tRNA) which is placed as another potential RNA molecule for use in targeted cancer therapy [62]. Delivering exogenous mRNA applies genetic commands at translational level, for synthesis of the protein it encodes, without the initial requirement of transcription or nuclear delivery of DNA [60, 61]. Consequently

mRNA can provide more efficient and faster exogeneous gene expression than DNA, as demonstrated in both electroporation-based [63](Figure 1.2) and liposomal-based [64] delivery studies. However the long-term duration of expression is expected to be shorter.

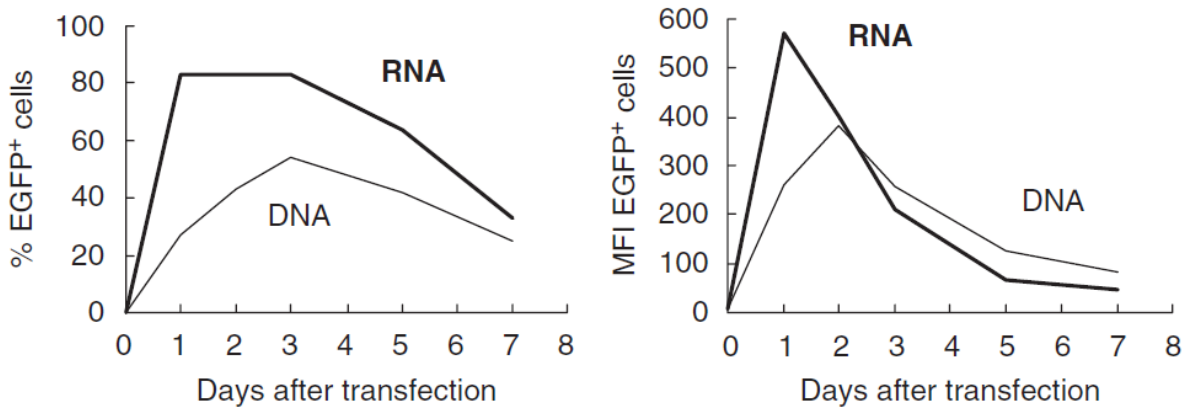


Figure 1.2: Comparison of enhanced green fluorescent protein (eGFP) expression from either eGFP mRNA or eGFP DNA in *in vitro* transfections of K562 haematopoietic cells. MFI is the mean fluorescence intensity. Image taken from [63] (Ponsaerts et al., 2003).

The second listed class of RNA has reference to a gene inhibitory intervention, known as RNA interference (RNAi). The process entails the introduction into cells of namely: small interfering RNA (siRNA), microRNA (miRNA), or short hairpin RNA (shRNA) having an antisense (excluding miRNA which is single-stranded) strand sequence that is complementary to the target mRNA [65].

SiRNA duplexes are usually synthesised to be no more than 30 nucleotides long to avoid a toxic interferon response, as observed with longer molecules [66]. Moreover, having a two-nucleotide overhang at the opposing 3' termini (wherein the last sugar group contains the 3' carbon, attached to a hydroxyl group [45]) has been reported as the optimal overhang length for RNAi mediation, because it allows for the most recognition by the RNAi-attributed enzymes [67, 68]. In fact these characteristics are in-line with the physical structure of naturally derived siRNA via the Dicer enzyme [69]. A further feature of selection or design of an siRNA sequence is the presence of multiple mismatches to all other homologous sites of other mRNAs, to circumvent off-target binding; and an A+U rich region at the antisense 5' end for potency [70, 71]. The mechanism of action for siRNA is depicted in Figure 1.3. Briefly, following cytoplasmic access, siRNA

is loaded onto large protein assemblies or RNA-induced silencing complexes (RISC) and the sense strand is removed by the nuclease activity of a RISC enzyme. A core RISC protein called Argonaute, guides the hybridisation of the antisense siRNA strand with the complementary target mRNA. An associated enzyme (Ago-2) then slices up the mRNA and is released from the RISC [65, 70, 72].

The alternative shRNA therapeutic consists of a 25-29 nucleotides stem and a loop of 4-23 nucleotides [68]. RNAi mediation through shRNA is usually based on the delivery of a vector (e.g. plasmids) encoding shRNA, that upon transcription is converted into siRNA in the cytoplasm by the action of Dicer enzymes and interacting proteins. At this point, the same cleavage-dependent mechanism of mRNA degradation by siRNA is carried out [73, 74]. ShRNA boosts the loading process onto RISC by ten times more than siRNA, and can therefore afford to use lower concentrations. However the limiting factor lies in the inefficiency of nuclear entry [75].

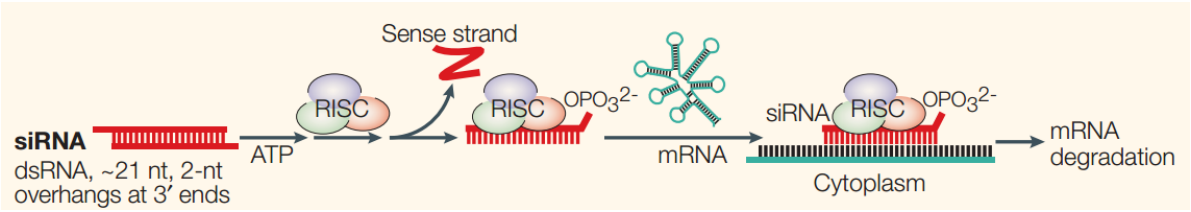


Figure 1.3: The gene silencing mechanism of siRNA. Image taken from[70] (Hall, 2004).

Finally, miRNAs – endogenously derived molecules that similarly to siRNA and shRNA have some gene expression repression function – have been synthesised for therapy to mimic the activity of endogenous anti-cancer miRNAs such as mir-34 (known to be transcribed by the p53 tumour suppressor gene) [76]. These, 20-24 nucleotide long antisense strands, follow a similar mechanism of action to siRNA (i.e. involving RISC); however, due to miRNA's partial base complementarity to target mRNA, degradation of mRNA is induced by translational repression and excision of its poly(A)tails [68, 72]. In addition, because miRNAs have incomplete sequence matching with their target, they possess the ability to affect hundreds of mRNAs and thus multiple genes, which can be a mixed blessing [77]. Such gene regulating power may be especially useful in tissue-specific diseases using tissue-specific miRNAs. However, due to the complexity of

diseases such as cancer, where a myriad of mutations can be present within one tumour [78], knocking down a family of genes may not ultimately impact on therapy.

The last listed class of therapeutic RNA refers to the ribozymes or catalytically active RNA molecules. Ribozymes consist of flanking sequences with respect to a core, that base pair with the target mRNA thus providing specificity; whereas in the catalytic core binding and subsequently cleaving of the target mRNA occurs. The ribozyme then dissociates from the degraded RNA and recycles itself [79, 80]. The relative unpopularity of ribozymes as a selected transgene therapeutic is the result of several factors: 1) reported toxicological issues [81]; 2) comparative studies between hammerhead ribozymes and siRNA revealed ribozymes to be less effective [82] although usually accompanied by minimal to no off-target effects [83]; 3) shorter duration of gene silencing compared to siRNA [82]. However they have appeared to be a common choice for HIV gene therapy [83–86]. It follows that synthesising ribozymes is open to relatively greater degrees and types of structural modifications (to enhance half-life and efficacy) without compromising its activity [87].

1.3.3 Antisense oligonucleotides (ASO, AON)

ASOs are short single-stranded DNA molecules of typically 18-21 nucleotides that exhibit gene inhibition function through complementary base-pairing with a target mRNA [68]. They differ from the above described modes of action in that they entail multiple mechanisms, as follows:- 1) translational arrest, 2) RNase-H activation, and 3) triplex formation [49, 56]. The fate of mode depends on the ASO chemical modifications and sequence [49]. Translational arrest is achieved by steric blocking of the ribosome entry site to circumvent protein synthesis initiation or peptide elongation. However, promotion of this mechanism requires delivery of stoichiometric amounts as well as the selection of strongly binding ASOs [88]. Moreover, high levels of gene repression have been reported via the RNase-H activation mode, using locked nucleic acid (LNA) ASOs (i.e. ASO analogues that possess a chemical substitution designed to increase binding affinity toward complementary RNA) [89, 90]. In this mode of action, the ASO forms a duplex with the target mRNA which consequently triggers the recruitment of RNase-H leading to mRNA degradation [49]. The triplex formation mode, which is

achieved by nuclear entry and ASO combining with DNA helix, has been exploited for gene regulation applications at the transcriptional level [91].

Emerging ASOs that regulate certain endogenous miRNA have elucidated the extensive applicability of ASOs [88, 92]. Lastly, comparative studies demonstrated significantly lower amounts and duration of protein expression inhibition using standard ASO, versus siRNA [93], while competitive efficiencies relative to siRNA were reported for LNA ASO [89].

1.3.4 Aptamers

Aptamers offer a distinct alternative to antibodies. Characterised as *in vitro*-selected single-stranded DNA or RNA molecules of 15-60 nucleotides, aptamers have high binding affinity and high specificity for target proteins [92, 94]. This interaction with proteins that participate in disease promotion leads to their inhibition and thus repression of the corresponding gene [49]. The major advantage of aptamers over antibodies is that they elicit little to no immunogenicity [95]. However, in gene therapy, these molecules have mostly only served in conjugates with siRNA, ribozymes and miRNA, as delivery vehicles or in ligand recognition-based gene regulation (by inducing a conformational change) [92]. The leading application has been in the treatment of ocular diseases such as age-related macular degeneration through anti-VEGF aptamers [50, 95].

1.4 Non-physical methods of cell membrane permeation

The call for more effective nucleic acid delivery systems or vehicles is ubiquitous in the transfection literature. Beside efficacy, other equally important attributes the system should have are safety, target locus specificity, scalability and clinical practicality in order to hold promise in human gene therapy. In this light, below is a review of the gene transfer methods developed and tested to date.

1.4.1 Calcium phosphate precipitates (CPP)

CPPs are chemical vehicles designed to protect (to some extent) the genetic material they carry from nuclease activity [96]. Methodically, a co-precipitation of calcium phosphate with typically pDNA is performed to form CPP nanoparticles with the DNA adsorbed on to the precipitates [97, 98]. However, since the preparation reaction is driven by super-saturation of calcium and phosphate, there is limited control of the size and structure distribution of the resultant precipitates [99], rendering unreproducible transfection efficiencies that strongly depend on the methodology. CPPs mechanism of action exploits the cell's natural mechanism of endocytosis whereby intracellular vesicles engulf the exogenous material and upon fusion with lysosomes release their content into the cytoplasm [96]. While they provide excellent biocompatibility and biodegradability [100] they have not been applied beyond *in vitro*. In fact, transfection must be carried out shortly after precipitation to maintain CPPs' activity [96], challenging any prospects for a CPP-based therapeutic.

1.4.2 Lipoplexes & Polyplexes

These commonly employed nucleic acid carriers are better suited for protecting and facilitating cellular uptake than CPPs because by configuration, the cationic lipid (in lipoplexes) or polymer (in polyplexes) condenses the anionic genetic cargo through electrostatic attraction (as opposed to CPP complexation with nucleic acid wherein the latter is found on the outside surface of the precipitate). When the lipid or polymer amine (N) to nucleotide phosphate (P) ratio reaches equivalence, a process of hydrophobic collapse is triggered, water is expelled and results in a condensed particle. This collapse has been shown to reduce the hydrodynamic diameter of plasmid DNA up to 1 million fold. Notably, the addition of excess amine then creates a net positive surface charge allowing electrostatic repulsion between particles and interaction with the negatively charged cell membranes, enabling cell entry [68, 101, 102]. However, cationic lipids or polymers have been reported to provoke cell shrinkage, reduce cell division and cause vacuolisation of the cytoplasm due to their cationic strength and charge ratio to the nucleic acid [103, 104]. This drawback has been alleviated *in vitro* by the addition

of neutral lipids such as DOPE [105], DOPC [106] and cholesterol [107], providing lower cytotoxicity. Moreover, increased membrane bilayer destabilisation and therefore membrane fluidity have been associated to such 'helper' lipids [108]. Nonetheless, these formulations suffer from instability in serum which disturbs the electrostatic interaction between nucleic acid and cationic lipid or polymer, making them inappropriate for *in vivo* use [109]. Consequently the good-to-high transfection efficiencies observed *in vitro* [110] are significantly attenuated *in vivo*, although shielding from proteins by PEGylation of polyplexes has been demonstrated [111].

The major mechanism of complex internalisation is by endocytosis while only 2% of cells undergo transfection via complex fusion with the cellular membrane [112]. It follows that proper nucleic acid condensation is necessary and polyplexes offer the advantage of efficiently achieving this, producing complexes of smaller sizes compared to lipoplexes [110]. Finally, ease of scaling-up as well as lower immunogenicity [109] renders these vectors attractive choices especially in combination with targeting (physical) delivery systems [21]. Examples of commercial complex-forming agents include Lipofectamine^{TM} and jetPEI^{TM} (lipid and polymer based respectively), which although effective *in vitro* have yet to demonstrate *in vivo* utility. This is largely because the high net surface charge required for good condensation leads to a large amount of non-specific interaction with cells of the blood and vascular system. Cationic dendrimers, usually comprised of amino groups branching out from a central core, have also been widely applied to administer nucleic acids to tumours (forming dendriplexes). While the addition of branches consistently improves transfection it also yields increased cytotoxicity. Despite this, dendrimer's cytotoxicity has been found to be significantly lower than that of PEI [113].

1.4.3 Viral vectors

As obligate pathogens, viruses have evolved highly efficient mechanisms for the delivery and replication of their genomes. Viruses can function as therapeutic gene delivery vectors if their DNA or RNA encoding structural, replication and pathogenicity sequences are replaced with a therapeutic gene, whilst maintaining their ability to infect cells [45]. A huge range of viral vectors exist (integrating, non-integrating, RNA, DNA, enveloped, non-enveloped, lytic, non-lytic) providing gene therapists with a virus to meet

each particular disease requirement. Prime examples include 1) the treatment of SCID using a retrovirus which achieves stable integration and long-term expression [38], 2) the treatment of haemophilia using an adeno-associated virus which achieves low but physiologically relevant levels of transgene over extended periods [114] and 3) the use of 'oncolytic' Herpes virus encoding GM-CSF to rapidly provide high transgene levels and a cell-kill effect in the treatment of cancer [115]. Notably, although consistently high transfection efficiencies (reported range of 45% – 95%) and disease cures have only been accomplished with viral vectors thus far [49], they are ultimately set back by inflammatory activity upon delivery and the potential for random integration into the host genome and host antiviral immune response against infected cells [116]. Despite such issues, adenovirus and retrovirus vectors have led the way in recent clinical trials [59]. The need for vigilance regarding the safety of viral vectors is emphasised by the past death of patient Jesse Gelsinger [117] and the low risk of insertion into the germ line [118].

1.5 Physical methods of cell membrane permeation

1.5.1 Electroporation (EP)

Electroporation refers to the physical process of transiently permeabilising the cell membrane by exposure to short high-voltage pulses with electric field strengths in the order of 200 V/cm, allowing the uptake of nucleic acids. These molecules are then maintained within the cell by the natural process of membrane resealing which has been shown to occur over the minute range following EP [119, 120]. The exact mechanism by which cells are permeabilised has yet to be defined, but there is basic understanding of potential difference-induced instability of the membrane bilayer and subsequent alteration into aqueous pores [121]. The procedure requires a pulse generator, delivery cable and electrodes which apply the electric field onto the desired tissue. Thus, for obvious reasons, deep tissue targets result in the invasive use of needle or catheter electrodes [122], explaining why the focus of the work on electroporation has been in the treatment of surface tissue diseases such as melanoma and muscular disorders [123, 124]. Safe amplitudes of current and voltage restrict the size and distance between electrodes, thereby limiting the volume of tissue that can be treated at once [125]. Reported transfection

efficiencies range between 100- to 1000-fold increase in gene expression relative to standard pDNA injection [120], conferring relatively excellent transfection reliability through EP. Moreover, target locus specificity is promoted as the placement of electrodes delineates the target area [119]. Still, a number of studies reveal EP-induced immunogenic effects [126, 127]. EP also poses risks of electrical injury and tissue infection due to the required surgical intervention, and is associated with considerable pain and cell death [125].

1.5.2 Magnetofection

Magnetofection is the method of using an external magnetic field in association with magnetic nanoparticles complexed with the genetic material, to pull the latter across the plasma membrane and into the cell [128]. This method is disadvantaged by low transfection efficiencies and reliance on transfection reagents (such as liposomes) or viral vectors in order to attain detectable levels of transgene expression [122]. Compared to other methods though, improved gene kinetics have been reported and thus rapid transfection of cells [129]. In addition, unlike other synthetically derived particles such as lipoplexes and polyplexes, the application of magnetic nanoparticles *in vivo* has not been found to be toxic [130]. Since magnetofection merely represents a transfection-assistive mechanism and requires magnet blocks to be fixed locally to the diseased tissue [131], this method turns out to be amongst the most complex. Other applications have been sought with due success, such as *in vivo* magnetic resonance imaging for the detection of tumours using paramagnetic iron oxide nanoparticles [132].

1.5.3 Microinjection

This rudimentary method entails direct nucleic acid injection into the cytoplasm or nucleus of cells. The required instrumentation consists of a fine needle, a micro manipulator and a micro injector to affect a target cell on a cell-to-cell basis [122], ensuring up to 100% transfection efficiencies [133]. The key advantage with nuclear microinjection lies in the evasion of intracellular trafficking. However, the labour involved to inject cells one by one [122] makes this technique relevant only to *in vitro* conditions. It is noted that microfluidic systems have been developed to stream cells through a beam for high-throughput injection [134].

1.5.4 Sonoporation

Sonoporation is the process by which cells exposed to ultrasound become transiently permeabilised, facilitating transport of desired molecules into the cells [135]. The mechanism of action has not yet been determined but hypotheses include the stretching of the cell membrane intrinsic porosity or the creation of new pores. In [136] the resultant pores were characterised for size to be in the order of 100 nm, with membrane resealing occurring approximately 5 seconds after sonication. Sonoporation has been extensively associated with inertial cavitation phenomena. In this type of cavitation, the bubble dynamics are characterised by rapid timescales over which gas bubbles will grow very large during the tensile phase of the sound wave [14]. The subsequent compressional phase of the sound wave or even just the ambient pressure, transforms the high potential energy stored within the expanded bubbles, into high energy density collapsing bubbles. The collapses are violent enough to produce the high pressures and temperatures necessary to cause structural insult to cells [137].

While sonoporation is often compared to EP, sonoporation is generally preferred as it can be focused non-invasively on deep tissues and operates with high safety; even though the transfection efficiencies are generally lower than those reported for EP, viral vectors and lipoplexes [135]. Nonetheless, there are sonoporation reports revealing gene expression up to two orders of magnitude higher than injecting pDNA alone [138], or three times higher gene inhibition by delivering antigene ASO through shock waves, compared to EP [139].

1.5.5 Laser irradiation

Cell exposure to laser light has been shown to increase cellular activity including proliferation and gene upregulation [140], alongside evidence emerging on its use/effectiveness in gene transfer [122]. Successful transfection has been shown intradermally in [141], where a 532-nm Nd:YAG laser was used to irradiate rat skin that had been exposed to plasmid DNA encoding firefly luciferase. Using an energy density of 1.9 J/cm^2 and 4 pulses, the authors reported two orders of magnitude higher luciferase activity compared to DNA injection alone. Further noteworthy transfection efficiencies have

been demonstrated using argon laser (8-fold increase compared to controls *in vitro*) [142], and an Er:YAG laser (12-fold increase relative to non-irradiated rat skin) [143]. The proposed mechanism of gene uptake is optic cavitation [137]. Lasers are thought to induce cell membrane changes either by directional absorption that results in thermal expansion and sound production, or by cavitation at high enough energies, through boiling of the tissue. However, because tissue scatters and absorbs light, penetration has not been observed beyond the stratum corneum of the skin [144, 145]. Also, the high expense of high-power lasers and the technical complexity involved impinge on the translatability of laser gene therapy [122]. Finally, a recent application has been in laser-induced gene release from nanoparticle vectors without increasing the local temperature, thereby promoting gene and cell survival upon irradiation [146].

1.5.6 Gene gun (biolistic delivery)

The gene gun essentially launches DNA-coated microscopic particles known as micro-projectiles through the skin and into a target area, with an acceleration produced by a helium discharge or high-voltage electric spark. The employed particles have usually been tungsten or gold [45, 122]. This direct method of propelling nucleic acid into target cells has its limitations: 1) pain to the patient; 2) cannot be extended to the delivery of RNA since it is a labile molecule and thus highly susceptible to degradation in a projectile system; 3) limited to skin target procedures such as DNA immunisation [147]; 4) too many parameters contribute to the efficacy of transfection including particle features and concentration, and degree of DNA coat which may be difficult to control or systematise [122]. However, an important advantage over standard DNA injections is that the gene gun requires significantly less DNA to achieve equal transfection levels [148]. Finally, it should be mentioned that interest in this delivery mode appears to have disappeared in the last ten years.

1.6 Overview of thesis

In this chapter, the competing counterparts of the strategies implemented in this thesis have been discussed.

Chapter 2 reviews in detail the proposed application of lithotripter shock waves for gene delivery, by describing its modes of action and evaluating the relevant state-of-the-art literature.

Chapter 3 employs a clinical lithotripter to optimise shock wave parameters with respect to a trade-off that exists between high cell viability and high cell permeabilisation, for three different cell types. At the optimal shock wave condition for one cell line, an *in vitro* tissue phantom system is developed for the delivery of enhanced green fluorescent protein (eGFP) mRNA and siRNA.

Chapter 4 evolves the understanding of shock wave mediated RNA transfection by quantifying the kinetics of RNA internalisation and GFP expression in the forms of number of RNA copies, number of positive cells, and mass quantities of transferred RNA and translated protein.

Chapter 5 identifies the mechanisms of shock wave induced RNA delivery in a 3-D tumour model compared to a single cells format, through the detection and suppression of cavitation.

Chapter 6 assesses the enhancement of mRNA delivery by lithotripter shock waves or focused ultrasound, through the exploitation of cavitation nuclei and a proprietary lipid nanoparticle formulation.

In summary, the key aims of this thesis are to:

1. assess the conceptual advantage of exploiting RNA for gene transfer by clinical lithotripter shock wave mediation, providing a pathway to translation.

2. characterise the shock wave induced mRNA delivery profile and bridge the gap between the effective RNA dose and the level (both by number of cells and mass) of transgene produced.

3. determine the contribution of shock wave induced shear stress on RNA transfer in tumour spheroids.

4. assess the potential of lipid-mRNA assemblies in acoustically-induced gene delivery, in which lithotripter shock waves are compared to focused ultrasound.

2

Acoustic Principles in Shock Wave induced Gene Delivery

Contents

2.1 Shock waves 22
2.1.1 Shock formation & non-linear propagation 23
2.1.2 Lithotripter sources 24
2.1.3 Safety of therapeutic shock waves 25
2.2 Acoustic Cavitation 27
2.2.1 Cavitation defined 27
2.2.2 Shock wave cavitation 28
2.2.3 Cavitation detection 29
2.2.4 Nucleation of cavitation 30
2.3 Direct Mechanical Stresses 32
2.3.1 Current knowledge in shear stress-induced bioeffects 32
2.3.2 Methods of cavitation suppression for separation of shear stress-induced bioeffects 34
2.4 Acoustics-mediated gene transfer 35
2.4.1 State of the art in acoustics-assisted gene delivery 35
2.4.2 Current limitations to shock wave-induced gene therapy . . . 36

2.1 Shock waves

A shock wave is a type of acoustic wave that may be defined as a high amplitude localised pressure pulse. A shock represents a narrow zone where a near discontinuity (compared to the duration of the waveform) in pressure, particle velocity, density and entropy occurs between a non-disturbed and disturbed medium. They emanate from waves generated by sources, or by an initial disturbance, moving with a speed greater than the ambient sound speed. The distinctive feature of a nonlinear wave is that the discontinuity is necessarily large, and the interaction with one another breaks down the principle of superposition, in contrast with linear waves. Thus, shock waves are conspicuously nonlinear [149, 150].

Figure 2.1 shows a shock wave generated by a lithotripter – a clinical device used to fragment kidney stones. It consists of a short rise time of less than 10 ns, a high peak positive (compressional) pressure of up to 120 MPa (45 MPa in the case of 2.1), followed by a negative phase approximately 1 μs later. The negative (rarefactional) pressure amplitudes are approximately up to -10 MPa and the pulse width is about just 5 μs. In its amplitude spectrum, the energy distribution of the shock encompasses a broad frequency range of up to 20 MHz, although most of the shock energy is between 100 kHz and 1 MHz [20, 151].

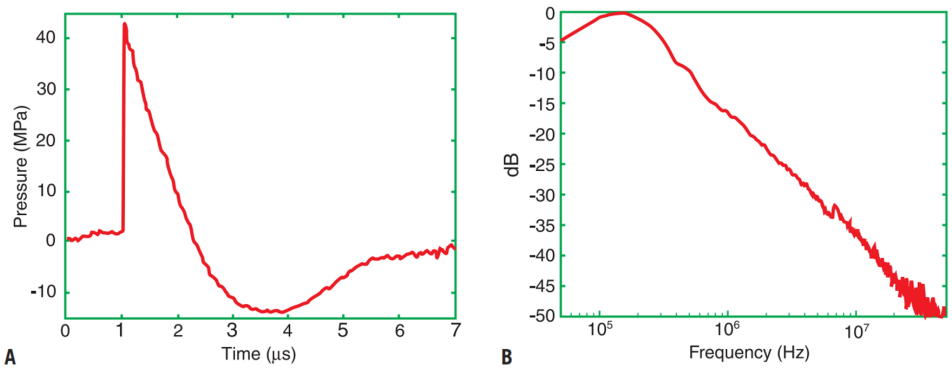


Figure 2.1: a) Pressure waveform of a typical electrohydraulic lithotripter shock wave at its focus, comprising a strong compressive shock front and rarefaction tail; b) the corresponding Fourier Transform. Image taken from [20] (Cleveland & McAteer, 2007).

Shock waves in medicine have had an established role not only in urology (through clinical lithotripsy) but also in orthopaedics, through specialist treatment of muscu-

loskeletal indications such as plantar fasciitis [152]. They have also been of beneficial use for pain therapy in equine and small animals [151, 152].

2.1.1 Shock formation & non-linear propagation

For any acoustic wave the local phase speed varies depending on the local pressure. For a progressive wave the phase speed is given with respect to position x on the waveform; and also depends on the acoustic 'wind' due to convection as ascribed by the continuity equation. The phase speed is described as:

$$c_{ph} = c_0 + \left(1 + \frac{B}{2A}\right) \frac{p}{\rho_0 c_0} \tag{2.1}$$

where c_0 is the speed of sound, p is the local pressure, ρ_0 is the ambient density and the term $(1 + \frac{B}{2A})$ represents the coefficient of nonlinearity (β). The coefficient of nonlinearity is a material property in which the local particle velocity is greater in the compressive region of the wave (peaks travel faster) and lower in the tensile region (troughs travel slower). Only the compressive wave velocity exceeds c_0 and is thus 'supersonic' [153].

For a nonlinear wave, the shortest distance $\bar{x}$ to the point of shock formation is:

$$\bar{x} = \frac{\rho_0 c_0^3}{\beta \cdot max(\frac{dp}{dt})} \tag{2.2}$$

where *max(dp/dt)* is the maximum of the time derivative of pressure. Essentially, the propagated distance must be greater than $\bar{x}$ for the waveform to distort and produce a shock. However, relatively short lengths are necessary with spherically converging or focused waves (which typify biomedical ultrasound and lithotripsy) because at their reasonably high pressures, the shock formation distance is small compared to the path length [20]. For example, typical values for a shock wave in biomedical applications are $dp = 10$ MPa and $dt = 0.1$ μs, while β can be taken to be 5.0 for normal soft tissue [20], resulting in a shock formation distance of 6.8 mm, which is smaller than most propagation distances.

2.1.2 Lithotripter sources

The method of shock wave generation for biomedical applications takes one of three forms: electrohydraulic, piezoelectric and electromagnetic.

Electrohydraulic (EH) sources – the first kind of lithotripters to be developed – consist of a spark plug and a water filled ellipsoidal metal reflector. High voltage from a capacitor is applied to the spark plug to generate an electrical spark across the spark gap, leading to the discharge of a shock wave due to surrounding water vaporisation [151, 154]. The shock is a spherically diverging wave at the point of initiation, but is converged as it bounces off of the ellipsoidal reflector [155]. The axial diameter of the EH focal zone is typically larger than those created by its counterparts because of the lengthening effect from potential misalignment of the spark plug. The acoustic output in EH lithotripters is largely affected by the variability in the exact location of the shock wave discharge across the spark gap, as well as by the presence of a weaker pulse preceding the focused pulse, that directly propagates from the spark plug to the target. Furthermore, the eventual wear of the plug's electrode may also reduce the shock wave amplitude [20].

Piezoelectric (PE) sources employ over a thousand piezoelectric crystals lining the inner face of a spherical dish surrounded in water. Upon application of a high voltage, the crystals contract and expand giving rise to an acoustic wave which will focus due to the spherical arrangement of the elements. The pulse finally develops into a shock as it nonlinearly propagates to the focal point. PE lithotripters produce very reproducible acoustic outputs as the crystals are stable [20, 151].

Thirdly, electromagnetic (EM) sources operate by exciting an electromagnetic coil held close to a metal membrane, in water. The excitation is caused by an electrical discharge that consequently induces a high current in the conductive membrane. Subject to the strong electromagnetic forces from the coil, the membrane manifests an acceleration away from the coil, producing a pressure pulse [151]. Depending on the geometry of the membrane, focusing the pulse is achieved by either an acoustic lens or a parabolic reflector. Similarly to PE sources, shocks are created by nonlinear distortion along the propagation path to the focus [20]. A summary of these methods is illustrated in Figure 2.2 (*left side*).

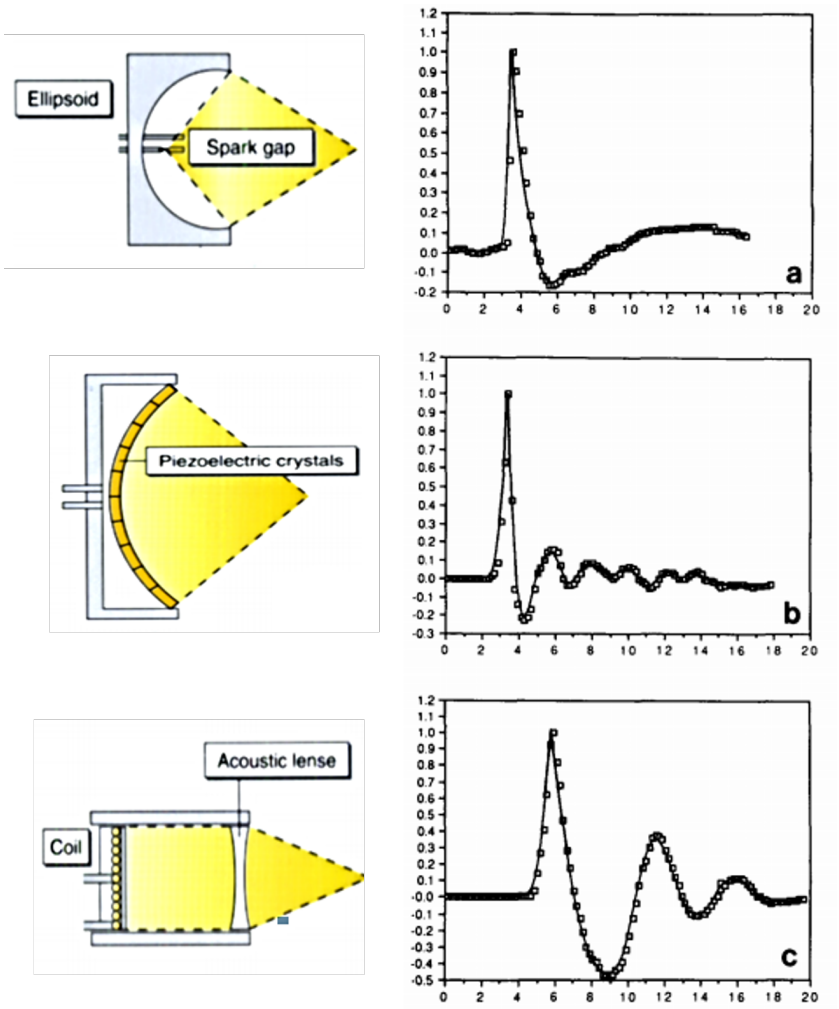


Figure 2.2: Three types of shock wave generation and the respective typical pressure waveforms; a) electrohydraulic, b) piezoelectric, c) electromagnetic. Images taken from [151, 155](Thiel et al., 2000; Coleman & Saunders, 1989)

.

Coleman & Saunders [155] characterised all three types of lithotripters, revealing some similarities in their basic waveforms as shown in Figure 2.2 (*right side*). Besides the leading positive spike followed by the negative pressure undershoot of a typical shock waveform, PE and EM waveforms both advance into tails of positive pressure oscillations. However, due to the 'ringing' of the PE crystals, the PE waveform tail exhibits many more of these oscillations. Conversely, the EH coda is relatively smooth.

2.1.3 Safety of therapeutic shock waves

In the context of ESWL for cancer gene therapy, the damage to surrounding healthy tissue should be minimal. An implication on treatment safety is the potential risk of metastasis,

arising from the well-understood ultrasound-mediated increase in extravasation and macromolecule dissemination through tissue. Nevertheless, animal studies have shown that the rate of metastasis is unaffected by treating tumours with shock waves alone [156, 157]. In addition, the ability of a cell propelled out of a tumour to engender metastasis is highly dependent on the aggressiveness of the cancer, as well as the likelihood that the shock wave has not lysed it.

Furthermore, according to pre-FDA approval studies, lithotripsy produced adverse effects in only 1% of cases [158]. Several animal studies have consistently found hemorrhage in the kidney to be the main side effect, with collateral hemorrhage found in the intenstine [159] and lungs [160], at peak compressional pressures of 48 or 80 MPa (in water) and 200 or 1000 shock waves, respectively; which were well below the 2000 to 4000 shocks typically used in clinical SWL. Consistent with the above animal studies, hematuria has been found to occur in patients following lithotripsy [161]. However, with their incidence statistic of nearly 100% [161], the level of severity required for a side effect to be taken as adverse appears to be unresolved. It should be noted that Kishimoto et al.[162] found increased levels of free haemoglobin in the blood specimens of patients post-ESWL, which returned to normal after day 4; indicating that haemolysis is a transient effect.

The mechanisms of action through which ultrasound is able to modify tissue, have been broadly categorised into thermal and non-thermal effects. The neglegible $\leq 1\,^{\circ}\mathrm{C}$ temperature rise during lithotripter shock wave administration at up to 3000 pulses [163], has long established that the biological effects harnessed in lithotripsy are non-thermal. On the contrary, other treatment methods such as High Intensity Focused Ultrasound (HIFU) rely on considerable heat deposition to ablate malignant tissue.

To preclude the potential risks of tissue damage during diagnostic ultrasonic treatment, safety indices have been developed to inform the operating personnel in real-time, on the output display. These indices may be applied to therapy only for reference purposes, since the motivation is to *alter* tissue. Of relevance to lithotripter shock waves, the Mechanical Index (MI) may be considered to be an estimator of the likelihood of non-thermal effects (where cavitation is the most probable) [164] and is defined as:

$$MI = \frac{p_{r.3}(z_{sp})}{\sqrt{f_c}} \tag{2.3}$$

where, $p_{r.3}$ is the peak rarefactional pressure in MPa derated by 0.3 dB/cm-MHz at each point along the beam axis, z_{sp}, where the pulse intensity integral ($PII_{.3}$) is highest; and f_c is the centre frequency in MHz of the transducer. The maximum permissible MI value in diagnostic practice is 1.9 for soft tissue [165]. In SWL, the MI far exceeds this value; for example a lithotripter f_c of 0.25 MHz and a $p_{r.3}$ of 8 MPa, yields an MI of 16. Further safety limits are based on ultrasound intensities. As the US beam is non-uniform both spatially and temporally, various forms of intensities can be calculated. Given that cell damage increases with increasing applied pressure amplitude, the peak pressure delivered to any part of the tissue is more telling than the average pressure over the area of interest. Thus, spatial peak intensities have been used to describe clinical acoustic output. Coleman & Saunders [155] surveyed commercial electrohydraulic, pieozoelectric and electromagnetic lithotripters, and found similar spatial-peak temporal-average intensities ($I_{SPTA} = \frac{p^2}{2\rho c}DC$) of around 50 mW/cm^2; while the spatial-peak pulse-average intensities ($I_{SPPA} = \frac{p^2}{2\rho c}$) ranged from 6.6 $\times$ 10^3 to 1.24 $\times$ 10^5 W/cm^2. By contrast with the I_{SPTA} and I_{SPPA} upper limits of 720 mW/cm^2 and 190 W/cm^2 respectively [165], typical lithotripters output very low I_{SPTA} that are comparable to diagnostic ultrasound machines, whereas the I_{SPPA} (which exceed the diagnostic limit by 1 to 3 orders of magnitude) are necessarily high to generate mechanical effects.

2.2 Acoustic Cavitation

2.2.1 Cavitation defined

Cavitation is the production of cavities in a fluid due to a pressure drop rupturing the fluid. In acoustic cavitation the presence of compression and rarefaction in the sound wave, results in oscillations of the cavities. As noted in Chapter 1 (section 1.5.4) acoustic cavitation is implicated in sonoporation, but also in a variety of other bio-effects including sonothrombolysis [166], chemical degradation [167], sonoluminescence [168] and sonophoresis [169].

In therapeutic ultrasound, two distinctions are usually made based on the motion of bubbles involved in the cavitation activity. These are *stable cavitation* (SC) and *inertial cavitation* (IC). In the former category, the response of a gas and vapour-filled bubble

to an acoustic stimulus, is to non-linearly oscillate about an equilibrium size, for long periods of the applied sound pressure [137]. Contrarily, in inertial cavitation a bubble is expanded by a negative phase so rapidly, that its subsequent dynamics and collapse are dominated by the inertia of the surrounding fluid rather than the sound wave. Such differences in bubble motion are imparted by the amplitude of the peak negative pressure and the compressibility of the gas phase [170], promoting IC with increase. However, in therapeutic shock waves, these distinctions are irrelevant because apart from the typically high amplitudes which instigate IC, the pulses do not have a continuous-wave profile and are generally too short to promote stable cavitation.

2.2.2 Shock wave cavitation

Lithotripter shock waves produce transient (inertial) cavitation. The associated rapid changes in bubble size and energetic implosion, have been shown to produce two distinct acoustic emissions [171], which is consistent with theoretical predictions by Church [172]. The amplitude of the secondary emission (associated to the main bubble collapse), and the time interval between the two emissions (also known as the characteristic or collapse time, t_c) have been utilised as indicators of the cavitation strength [171, 173]. Choi et al.[174] numerically assessed the bubble dynamics in lithotripsy fields and conclusively defined the second acoustic emission amplitude and t_c to be significantly high compared to that emitted from diagnostic-level fields; and that the relationship between t_c and peak rarefactional pressures (PRFP) greater than 2 MPa, is close to linear. This latter characteristic of SW cavitation, was confirmed by Huber et al.[175] whereby the time to main bubble collapse (t_c) was shown to strongly correlate with the lithotripter output setting.

An early study [176] characterised the effects of lithotripter shock wave cavitation both *in vitro* and *in vivo* by exposure to a water-flowing plastic tube and aortic blood in dogs respectively. It was found that contrary to the *in vitro* study, the aortic blood did not experience cavitation. However, such conclusions were derived from quantification using a resonant bubble detector (RBD) which confined transient cavitation to the activity of only resonant bubbles. Improved methods of shock wave cavitation detection are described in section 2.2.3. Improved detection systems though, demonstrated reduced

cavitation in tissue mimicking gelatine compared to water as suggested by the lower double emission amplitudes detected in the gelatine [173]. Using similar methods, Coleman et al.[177] provided some evidence of cavitation in human tissue at the focus of the lithotripter, through an acoustic receiver placed on the patient's skin. However, only four patients were recruited for the study, and there was no significant increase in the *mean* t_c with increasing lithotripter output setting.

Significant amounts of transient cavitation in underwater thin aluminium foils and metal plates were readily observed by Coleman et al.[178], through the formation of deep surface depressions or pits, when exposed near the focus of lithotripter shock waves. Such effects were attributed to liquid jet impacts, as a result of collapsing bubbles at a boundary, and the consequential inward motion of fluid (which had been clearly demonstrated by Crum, 1982 ([179])).

Furthermore, Dalecki et al.[180] showed that lithotripter shock waves focused in the centre of mice abdomen at positive pressures as low as 2 MPa, instigated intestinal and pulmonary hemorrhage in 31% and 56% of the animals respectively, supporting the idea that inertial cavitation may take place *in vivo*. Interestingly, Zhong et al.[181] determined the bubble collapse times in various sized vessel phantoms which were surrounded by castor oil in order to suppress the detection of cavitation outside of the vessels. They found that t_c was highest in free water and decreased with decreasing vessel diameter, elucidating the significant influence of spatial constraint on bubble growth, thus weakening cavitation.

2.2.3 Cavitation detection

A number of detection techniques have been developed for SWL cavitation. The most widely applied technique in the literature has been passive cavitation detection (PCD), having the advantage of not contributing to the delivered acoustic energy, while being able to be performed non-invasively. PCD entails one or multiple transducers in receive mode that listen to scattered sound or acoustic emissions from the cavitating bubble cloud. Coleman et al.[171] were the first to employ a 1 MHz hydrophone as the passive detector, with its beam focus aligned to that of an electrohydraulic lithotripter field, to detect the double emission signature of a single shock wave discharge. This cavitation-attributed

double signature was verified by artificially attenuating the shock wave by more than -50 dB using a thick polystyrene sheet, which only produced an electrical spike corresponding to the time of SW discharge. Using a photomultiplier tube to detect light, there was agreement between the double signatures of light and sound emissions, yielding strong evidence for cavitation-induced sonoluminescence. Zhong et al.[182] supplemented the above study by demonstrating the feasibility of such detection *in vivo*.

Single element focused PCDs provide limited spatial resolution. Consequently, Cleveland et al.[183] developed a dual PCD transducer system for SWL cavitation, that improved upon the shortfalls of a single element set-up, by localising cavitation events to a roughly spherical volume of 5 mm in diameter. This is significant because the tissue area of interest may otherwise remain untreated. For detection at higher spatial resolution, an array of PCD transducers together with beamforming have enabled the mapping of spatio-temporal cavitation activity from HIFU exposure [184].

Additionally, insight on *in vivo* SWL cavitation activity has been demonstrated through recording of the returning echo in B-mode imaging by Bailey et al.[185] in pig kidney. Echogenicity increased as the number of deployed shock waves increased from 150 to 350 for fluid-filled kidney space, and from 1000 for kidney tissue space; thus producing bright areas of high echo amplitudes on the B-mode images. Hence, echogenicity has been interpreted as a visual marker of inertial cavitation. However, it has been argued that some tissues are naturally hyperechogenic which has limited its use [15].

Optical means have also been involved in cavitation detection through high-speed photography at rates of 20,000 [182], 40,500 [183] and up to 1 million [186] frames/s, in order to capture the dynamics of the bubble clouds. Also, Jochle et al.[187] developed a laser-based system that quantified the laser scatter signals from the surface of bubbles. Nonetheless, optical techniques are limited to *in vitro* investigations, and even then are only suitable for applications with optical access.

2.2.4 Nucleation of cavitation

Cavitation is a stochastic process as bubble formation occurs at randomly distributed nucleation sites and at different times [188]. In order to exploit cavitation for therapy it is useful to be able to control the occurrence and amount of cavitation, which

can be achieved in a number of ways. Pre-existing gas bubbles can be stabilised at a size sufficiently small not to be removed by buoyancy, yet sufficiently large to respond to an applied negative pressure. Solid entities present in or around the liquid such as crevices, motes and impurities will create gas pockets which expand under negative pressure [189]. It follows that artificial cavitation nuclei would be developed to exert a controlling power on the degree of bio-effect desired. Purely at the *in vitro* experimental level, many investigations have incorporated talc, an immunogenic hydrophobic particle that provides a multitude of crevices for trapping gas bubbles. For clinical use, micro-bubbles – inert gas-filled particles shelled by a biocompatible lipid, polymer or protein – have been intravenously administered to improve ultrasonography. Several micro-bubble formulations (or ultrasound contrast agents (UCA)) have been approved primarily for echocardiography. Amongst these, SonoVue bubbles (Figure 2.3) are commonly utilised sulphur hexafluoride-filled micro-bubbles encapsulated in phospholipid shells. As per its clinical diagnostic use, SonoVue offers good passage into

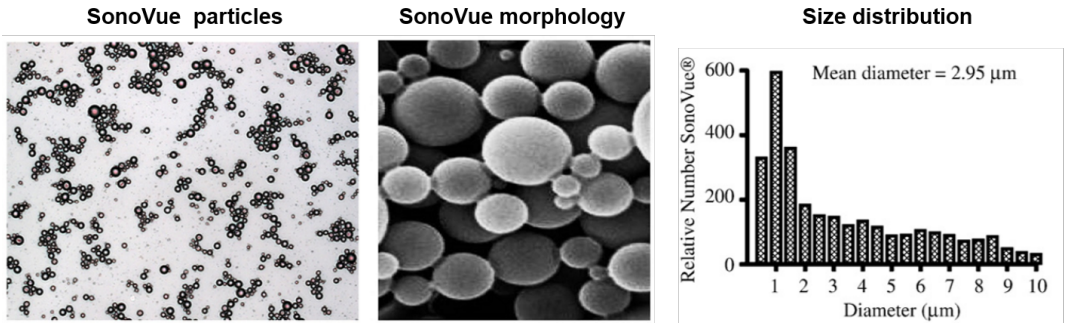


Figure 2.3: Characterisation of the SonoVue microbubbles. Images taken from [190, 191](Cheung et al., 2009 & Quaia, 2006).

the capillary bed due to its small mean diameter of 2.95 μm, and improved stability in blood compared to air-filled microbubbles [191]. Nevertheless, despite UCA's ability to lower the cavitation threshold (thus, minimising potential tissue damage to the patient), effective application to therapeutic ultrasound is hindered by low UCA fragmentation thresholds of approximately 0.15 MPa at > 4 acoustic cycles, as found by Chen et al.[192]. To overcome this drawback, Kwan et al.[193] developed polymeric nanoparticles (Figure 2.4), with a cup geometry suitable for the entrapment (and thereby stabilisation) of nano-bubbles, which were also sensitive enough to release the nano-bubbles upon

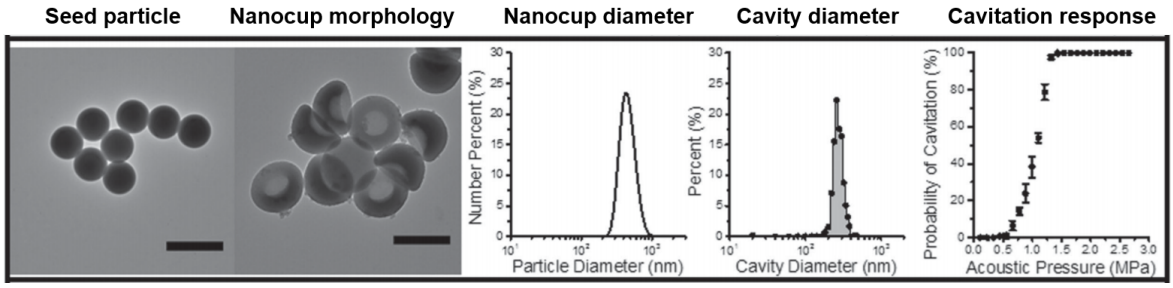


Figure 2.4: Characterisation of the Nanocup particles. Image taken from [193] (Kwan et al., 2015).

ultrasound exposure. They reported a sustained cavitation activity of up to two minutes at therapeutically relevant US pressures.

2.3 Direct Mechanical Stresses

Although cavitation is considered to be the dominant mechanism in sonoporation, acoustic waves are stress waves and thus inherently induce direct stress on cells. The nonlinear effects of shock wave propagation (as discussed in section 2.1.1) as well as the scattering effect on shock wave focusing due to the heterogeneity and anisotropy of tissue [20], alter the details of the direct stress. Here, studies that investigate shock wave generated direct stresses are reviewed.

2.3.1 Current knowledge in shear stress-induced bioeffects

In solids or compact structures such as gallstones, Sass et al. [194] speculated that crack formation is a result of direct mechanical stress through SWL, because they demonstrated that the collapsing bubbles within the cracks did not initiate disintegration but were responsible for advancing them. Interestingly, Xi & Zhong, [195] found the crack-initiating direct stress to stem from the reflected part of the incident shock wave – a tensile wave. This can be expected as stones are brittle materials, which are weak in tension. Moreover, they reported the refracted part of the wave (which generates transverse (shear) waves within the solid) plays a role in extending the cracks. But such dynamics are likely to be very different in soft solids (e.g. tumours) because the impedance mismatch between tissue and water is much lower than that of water to stone; hence reflections are typically less severe in soft solids. In addition, a study on shock wave treated multicellular

spheroids which mimic tumours, attributed much of the observed cell damage to the shearing forces originating from cavitational and non-cavitational sources [196].

In the context of lithotripter shock waves, two theories have been proposed on the effected disruption of cells and soft tissue:-

1) A dose of shock waves exerts cyclic loading on cells which is characteristic of failure due to fatigue. Howard & Sturtevant, [197] performed insonations on thin nitrocellulose membranes in non-cavitating (degassed castor oil) and cavitating (distilled water) media, as well as in the presence of heterogeneities such as animal tissue phantoms and glass spheres. They found that the membranes failed not only in cavitating medium, but also in the heterogeneous non-cavitating case. Furthermore, they found that the damage was progressive with increasing number of shock waves, and developed an analytical model inferring SWL induced strain rates as high as 60,000 s^{-1}. Subsequently, Lokhandwalla & Sturtevant [198] numerically derived the inertial force produced by a SW-induced flow field, and found that the resulting strains were sufficiently large to induce cell membrane pores, but unlikely to cause cell lysis.

Additionally, Freund et al.[199] postulated that repetitive acoustic straining would lead to tissue damage by cumulative shear. Using a computational model, they determined a $\sim$15% shear strain at 1000 shocks which they deemed sufficient to cause mechanical damage, due to some contributing small-scale strains arising from the viscoelastic stress-relaxation behaviour of tissue.

2) Acoustic microstreaming of the liquid surrounding a non-cavitational oscillating source can subject nearby cells to shear stresses. Such sources have been: stably oscillating bubbles and transversely vibrating wires [200]. It is noted that shear stresses are alternatively formed by high velocity streams arising from the collapse of a cavitating bubble. However, it is emphasised that this mechanism is only possible in fluid based systems such as in the vasculature and renal collecting system, but not in tissue where spatial constraints exist. Also, to sustain microstreaming, high SW pulse repetition frequencies would be necessary.

2.3.2 Methods of cavitation suppression for separation of shear stress-induced bioeffects

To better determine the effect of non-cavitational stresses, a number of studies have implemented techniques that in principle minimise the negative pressure at the focus, either by excess supply of positive pressure (overpressure), or by suppressing the shock wave tensile wave (through lithotripter reflector geometry), or by tensile component transmission reduction (through a mechanical device called the acoustic diode); which would otherwise all be conducive to inertial cavitation.

Using red blood cells (RBC) to quantify the reduction of haemoglobin release (or cell lysis) due to the mitigation or suppression of cavitation, Stonehill et al.[201] and Williams et al.[202] implemented chambers that were overpressurised by compressed nitrogen gas. Cells were in suspension and contained in vials that were held within the chambers. Delius et al.[203] devised a simple syringe-pressurising system connected to a cell-containing pipette, which was based on compression of the fluid in the syringe by its plunger. In all three studies, a significant decline in RBC lysis was noted when SWs were emitted in the presence of very low (100 kPa) or very high ($>$ 12,200 kPa) overpressure compared to without overpressure; but did not decrease to a level below controls, suggesting the involvement of a non-cavitational mechanism in the net disruption of cells. Moreover, to achieve overpressure, compression of air has also been reported [204], whereby a 50 kPa elevation in ambient pressure significantly decreased the growth and number of cavitation bubbles observed.

As hypothesised by Cleveland et al.[205], the effect of overpressure on suspended cells is a result of bubble dissolution into the solution, explaining why less of an effect has been shown in solids. Thus, suppression of cavitation was deemed to be more difficult to attain in tissue. Evan et al.[206] conducted an *in vivo* study on pig kidneys exposed to lithotripter shock waves modified by a pressure release reflector which reversed the order of the compressive and tensile phases in the waveform, leading to limited bubble growth. Unlike exposure to SWs from a rigid reflector, no kidney lesion was found with application of the pressure release reflector, revealing the feasibility and effectiveness of such method in the minimisation of cavitation-induced tissue injury. Also modifying

or inserting reflectors, Zhou & Zhong, [207] and Lokhandwalla et al.[198] respectively, were able to modulate the observed bio-effects by precluding cavitation.

Finally, in a different approach, Zhu et al.[208] constructed an acoustic diode consisting of two acoustically transparent membranes held in parallel, with controlled surface contact. The passage of the shock wave, was then only altered during its tensile phase, as the tensile pressure pulled the membranes apart, thus increasing the impedance mismatch. The end result was undetected rupture of a small vessel phantom with exposure to 100 SWs, compared to an average of 31 SWs required to rupture the phantoms not treated to the acoustic diode.

2.4 Acoustics-mediated gene transfer

2.4.1 State of the art in acoustics-assisted gene delivery

Three different acoustic modalities have been applied to facilitate gene augmentation:- high-intensity focused ultrasound [18], lithotripter shock waves [209] and low-intensity ultrasound [210]. It should be noted that all three modalities have been primarily utilised elsewhere: thermal ablation of solid tumours, extracorporeal pulverisation of kidney and gall bladder stones, and echography, respectively. Although diagnostic US systems (like those used in echography) have been used for the mediation of gene transfer [211], they typically utilise high centre frequencies which limit the depth of tissue that can be safely penetrated.

In comparing the three modalities, shock waves contrast HIFU as they preclude significant temperature rise, resulting in negligible thermal effects (*recall* section 2.1.3). This is generally not the case for HIFU [23], which may therefore jeopardise cell survival and nucleic acid integrity. On the other hand, the acoustic energies required for transfection are not reached with low-intensity US (i.e. in the mW/cm^2 range). Average intensities of around 0.5 – 2 W/cm^2 have had the highest reported transfection levels from this US mode, which lie between values for diagnostic and therapeutic ultrasound, but the vast majority have either included microbubble contrast agents or liposomes [212–214].

Efforts to boost acoustics-mediated transfection – where at best ∼40% has been reported for T84 cells (against several other cell lines) using low-intensity US [215] –

include tandem shock wave generation [216], combination therapies [217, 218], and the optimisation of acoustic and experimental parameters [215, 219].

The idea supporting tandem shock waves, is that by controlling the time delay (in the range of 10-900 μs [220]) between two successive shock waves, the second pulse can be set to arrive shortly before the start of bubble collapse caused by the first pulse; thereby increasing the collapse energy and in turn the bio-effects. Loske et al.[216] found that transfer of DNA into fungal cells was significantly enhanced at a delay of 300 μs.

As for combination therapies, a host of literature has substantiated enhanced gene delivery. For example, Stride et al.[217] combined ultrasound with magnetic field exposure to transfect cells with naked pLuc DNA in the presence of magnetic microbubbles, which resulted in approximately 2.5 times greater transfection than the compounded transfection from individual (e.g. US only) exposures. Another study demonstrated delivery of siRNA by liposomal bubbles and ultrasound [218], wherein the formulated liposomes entrapped a gas commonly used in UCAs (perfluoropropane) and then proceeded to form complexes with the siRNA.

Moreover, through variable degrees of optimisation across studies that employed US, there appears to be unanimity in the acoustic regime that favours gene delivery the most; consisting of $\leq$1 MHz centre frequency, a median intensity of 2 W/cm^2, and 20-30% duty cycle, while the duration of exposure varies [11, 215]. Equivalence in LSW has not yet been determined. Additional parameters such as the relative cell and UCA concentrations have also been previously optimised [219].

Finally, in a separate endeavour to improve the acoustics-assisted delivery of therapeutics, Guzman et al.[219] determined the length scales over which a bubble may affect or kill a cell, as depicted in Figure 2.5. By deriving the length magnitudes as a function of cell density, they found that cells within the 'killing radius' (R_K) of a bubble were irreversibly damaged, while those within the 'blast radius' (R_B) had a probability of being permeabilised.

2.4.2 Current limitations to shock wave-induced gene therapy

At present, low transfection efficiencies have been reported when using shock waves, which have been evidenced both *in vitro* and *in vivo*, as summarised in Table 2.1.

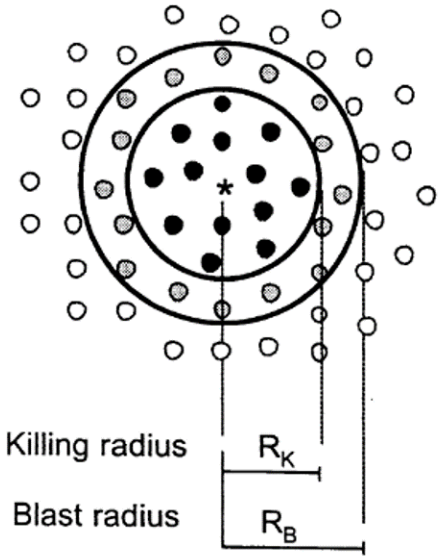


Figure 2.5: Probability of cavitation bio-effects based on a cell (denoted by the star) proximity to a cavitating bubble. Image taken from [219] (Guzman et al., 2003).

Moreover, any given biological outcome is invariably influenced by its experimental configuration. These reasons render the relatively small field of shock wave induced gene delivery difficult to motivate or define in terms of its efficacy. For instance, Lauer *et al.* [221] observed poor permeabilisation levels of between 0.1-0.5% which was found to be independent of the cell concentration utilised. Huber *et al.* [23] optimised the acoustic parameters and determined a 3-fold enhancement of gene reporter expression. Miller *et al.* [222] deemed the injection of 10% air into mice tumours necessary for meaningful transfection levels, as it instigated additional cavitation nuclei. On the other hand, Bao *et al.* [209] showed that at a satisfactory cell viability (i.e. $\geq$50%), the 200-shock wave treated cells produced a 50-fold increase in reporter gene expression per million of cells, relative to non-treated controls.

Another limiting factor is the frequently reported collateral cytotoxicity, despite attempts to minimise the acoustic energy. Gene therapy necessitates that the target cell is kept alive in order for therapeutic protein transcription and translation to occur. Consequently, maximal treatment is gained with minimal cell kill and maximal cell transformation. As outlined in Table 2.1, the numbers of positive (or transformed) cells were extracted at $\geq$50% cell survival data points. Murata et al. [225] reported

Year	Author	Cell Line	Nucleic Acid	*In*	Shock wave generator	∼No. of positive cells/10^6 cells (at ≥50% cell viability)
1997	Lauer et al.[221]	HeLa	pDNA	vitro	Experimental Dornier XL1	450
1998/ 1999	Bao/Miller et al.[209, 222]	B16	pDNA	vitro	Dornier HM-3 analog	n.d.†
				vivo		20,000†
1999	Huber et al. [23]	HeLa	pDNA	vitro	Siemens Lithostar	400†
2001	Tschoep et al.[139]	HPBMC	ASO	vitro	Experimental Dornier XL1	n.d.
2002/ 2003	Miller & Song/ Song et al.[18, 223]	B16 & RENCA	pDNA	vivo	Dornier HM-3 analog	n.d.$^{\varphi}$
2004	Michel et al.[224]	COS-7	pDNA	vitro	Storz Modulith SLK	20,000†
2007	Murata et al.[225]	Rabbit chondrocytes	pDNA	vitro	Electro Medical Systems Swiss Dolorclast	All cell viabilities < 50%
	Bekeredjian et al.[226]	HEK 293	pDNA	vitro	Dornier EPOS	n.d.$^{\varphi}$
2014	Millan-Chiu et al.[21]	HEK 293	pDNA	vitro	Piezoson 100	29,000*
2015	Ha et al.[227]	HUVEC	siRNA	vitro	Dornier AR2 ESWT	n.d.
		CT26		vivo		
2016	Lopez-Marin et al.[228]	HEK 293	pDNA	vitro	Piezolith 2501	19,400
		MCF-7				8,000

Table 2.1: Survey of shock wave-mediated gene transfer studies (n.d. = not determinable; † = residual air in the exposure volume; $^{\varphi}$ = with cavitation nucleation agent; * = no difference relative to controls).

transfection only when more than 50% of cells were killed, which would not translate into clinical practice.

A pressing issue is the lack of standardisation on how transfection is reported. The most apt measure of transfection is the *number of positive cells per million exposed cells* which for the most part is not determined nor explicitly reported in studies that employ cell models fit to be characterised in this way. Although it is informative to provide results of gene expression in relation to the percentage/fold increase or decrease of the detected protein compared to non-exposed controls, *in vitro* transfections usually make use of 'reporter' genes (e.g. based on fluorescence or luminescence) and cannot be compared as they have dissimilar dynamic ranges. This measure also does not indicate

how far or close it is from transgene expression in 100% of cells. It follows that for shock wave mediated gene therapy to gain traction, conclusive results of pre-clinical transfection need to be established.

Furthermore, there are some device-based limitations. The tissue volume that can be treated at once is confined to the focal zone of the lithotripter [20]. In practice, areas that are larger than the focal volume require multiple treatments to fully treat the area, whereas areas that are smaller may experience collateral damage in the surrounding tissue. Thus, not all target sizes qualify for SWL. Even though SW generators can be moved in 3-D, sweeping a large tissue area during treatment is ultimately impractical as lithotripters are heavy equipment with large therapy heads. To resolve the aspect of a fixed focal zone length and width, modern lithotripters feature two or three settings (e.g. the Storz Modulith SLX-F2 and the PiezoLith 3000 triple focus, respectively) spanning narrow to broad focal zones.

In conclusion, despite the above limitations, there is opportunity to improve upon the low SW-mediated transfection efficiency and the quality of its reporting. The discussed propensity of LSWs to induce inertial cavitation and non-cavitational mechanisms (section 2.3) can be managed in order to minimise cytotoxicity while enhancing gene delivery. It is hoped that the insight gained from this research will stimulate the development of suitable SW-based cell therapies.

3

Optimisation of Clinical Shock Waves and Mediation of RNA Delivery to Cells

Contents

3.1 Opening Remarks 41
3.2 Materials and Methods 42
3.2.1 Cell lines & cell culture 42
3.2.2 Shock wave generation & set-up 42
3.2.3 Exposure cell containment 43
3.2.4 Shock wave field characterisation 45
3.2.5 Sample Preparation & Treatments 45
3.2.6 mRNA & siRNA stability 46
3.2.7 Cell Survival & Viability Assay 46
3.2.8 Cell Permeabilisation analysis 47
3.2.9 FITC-dextran delivery and dissemination 47
3.2.10 Transfection procedure 48
3.3 Results 49
3.3.1 Cell density modulates post-shock wave cell viability 49
3.3.2 Influence of shock wave parameters on CT26 cell viability and permeabilisation 51
3.3.3 Optimisation of shock wave parameters 54
3.3.4 Shock wave pressure 58
3.3.5 Permeabilisation and viability of HK-2 & MCF-7/GFP cells . 60
3.3.6 RNA stability 60
3.3.7 Shock wave-mediated transport of 250-kDa FITC-dextran and dissemination in agarose is a function of macromolecule availability 63
3.3.8 GFP mRNA transfection 67
3.3.9 GFP siRNA transfection 68
3.4 Discussion 71
3.5 Closing Remarks 75

3.1 Opening Remarks

Nucleic acid-based therapies provide a powerful approach to the treatment of genetic diseases, by introducing healthy replacements of mutated or absent genes via mRNA, or gene-specific inhibitory molecules via siRNA into target cells; to ultimately reinstate typical cellular function either through the expression of normal protein or the repression of defective protein. As reviewed in Chapter 1, sonoporation provides the most practical and least invasive device-based option when deep access is needed [229]. Nonetheless, the efficacy of sonoporation strongly depends on the acoustic parameters of the employed technology, because a trade-off exists between being able to maintain high cell viability and also achieve nucleotide uptake. Thus, the majority of shock wave mediated transfection studies have only qualitatively demonstrated the potential for gene delivery, because by adopting an approach based on selecting the best approximate parameter values out of a few others, these researchers failed to identify the optimal shock wave exposures.

To date [1], shock waves have not yet been exploited for mRNA-based transgene expression, and in the context of *in vitro* studies, the application of tissue mimicking materials (TMM) and techniques has been scarce. Similarly, there are few reports of shock wave induced siRNA delivery in the literature. In addition, reports detailing shock wave dose dependent bioeffects, were performed using early generation technologies (reviewed in [230]) with a considerable number of studies using machines such as the Dornier XL1 lithotripter [221, 231–233] and the Siemens Lithostar [23, 234] which are no longer available. In light of newer clinical lithotripter technologies, which provide an enabling pathway to translation, very little work has been conducted on shock wave mediated cancer treatment at the cellular level.

In this work, we present studies aimed at achieving and describing delivery of RNA to cells using a state-of-the-art clinical shock wave source. We report cell line based optimal shock wave parameters for the enhancement of RNA transfection of cancer cells.

[1] excluding the work presented in this chapter which has been published in the journal publication: Nwokeoha, S., Carlisle, R., & Cleveland, R. O. (2016). The Application of Clinical Lithotripter Shock Waves to RNA Nucleotide Delivery to Cells. Ultrasound in Medicine & Biology, 42(10), 2478-2492.

3.2 Materials and Methods

3.2.1 Cell lines & cell culture

Mouse colorectal carcinoma CT26.WT cells (ATCC, CRL-2638; American Type Culture Collection, Rockville, MD, USA), were grown in Roswell Park Memorial Institute (RPMI) 1640 medium (Sigma-Aldrich, St. Louis, MO, USA) supplemented with 10% fetal bovine serum (FBS; Thermo Fisher Scientific, Waltham, MA, USA), in a humidified atmosphere containing 5% CO_2, at 37 °C. Cells were grown to a minimum of 90% confluence and ≥95% cell viability for use in shock wave experiments. Cells were washed with Dulbecco's Phosphate-Buffered Saline (PBS) solution (Thermo Fisher Scientific), harvested by brief trypsinization, and neutralised with medium twice the volume of the trypsin-EDTA (Thermo Fisher Scientific). A cell pellet was formed by centrifugation at 300×g for 5 minutes, and re-suspended in serum-containing medium. To ensure cell density and homogeneity, the prepared cell suspension was agitated using a vortex mixer for a few seconds before counting. Total cell counting was performed using the Trypan blue (Thermo Fisher Scientific) dye exclusion method and a hemocytometer. A cell stock solution was then prepared by extracting the total number of cells required from the cell suspension and diluting with medium to the total required volume. The stock solution was spun once more before dispensing into sample units.

Two other cell lines were similarly cultured: immortalised human kidney (HK-2) cells (ATCC, CRL-2190) and human breast cancer (MCF-7) cells (AKR-211, Cell Biolabs Inc., San Diego, CA, USA). The latter stably expressed GFP. Both cell lines were treated using 10% FBS supplemented Dulbecco's modified Eagle medium (DMEM; Thermo Fisher Scientific) in lieu of RPMI 1640. These cell types were selected because of the fitting application of lithotripter shock waves to kidney cell treatment, as well as because GFP expressing cells (for the study of GFP knock-down through siRNA delivery) were commercially available with the MCF-7 cell line.

3.2.2 Shock wave generation & set-up

The shock waves were generated by the Storz Modulith SLX-F2 lithotripter (Storz Medical, Kreuzlingen, Switzerland) with the kind permission of Oxford Stone Group

(Churchill Hospital, Oxford, England). The lithotripter consisted of an electromagnetic cylinder coil with dual focal zones. The wide focus zone was applied to all experiments, with a nominal size of 9 × 50 mm (diameter × length) at peak positive pressures ranging from 5 to 90 MPa. Experiments were carried out in a water-filled tank with a low density polyethylene (LDPE) membrane for shock waves to enter, which was coupled to the shock wave transducer by a thin layer of silicone oil. Cell samples were suspended underwater (Figure 3.1a) and positioned centrally in the focus through fluoroscopic projections at 0 ° and 30 ° relative to the vertical axis.

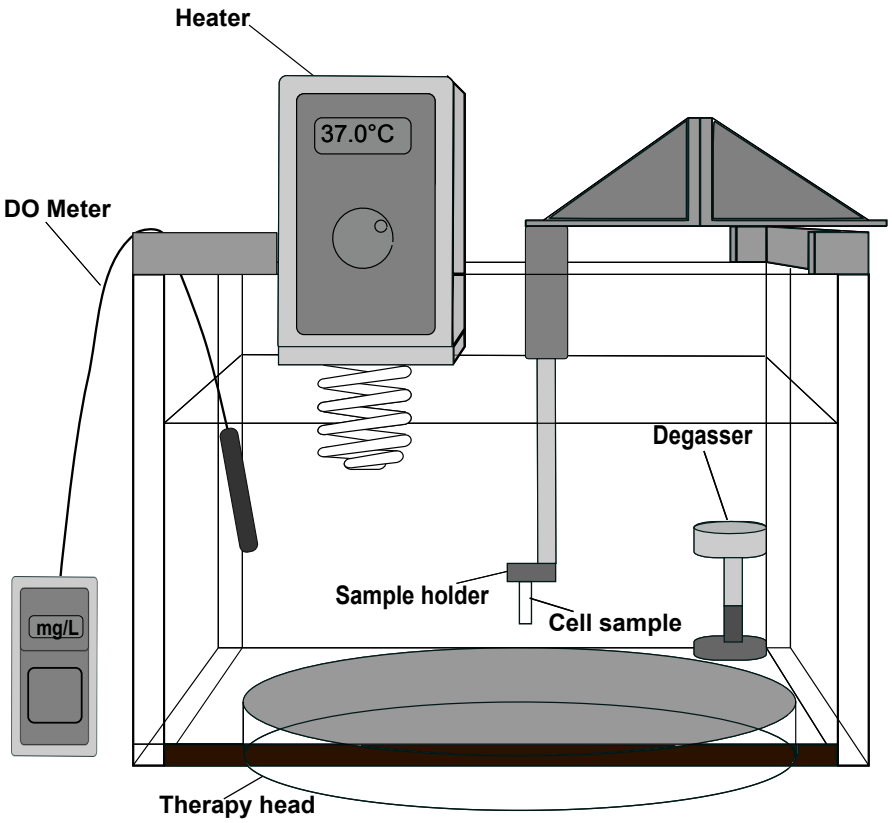
Ideal experimental conditions for cells were created by heating the tank water to 37 °C using a Grant GD100 water heater (Grant Instruments Ltd, Royston, UK). For experimental reproducibility as well as in view of a lack of cavitation nuclei in non-gas-bearing body tissues, the water was degassed using a pinhole degasser for a minimum of one hour prior to the start of SW exposure.

3.2.3 Exposure cell containment

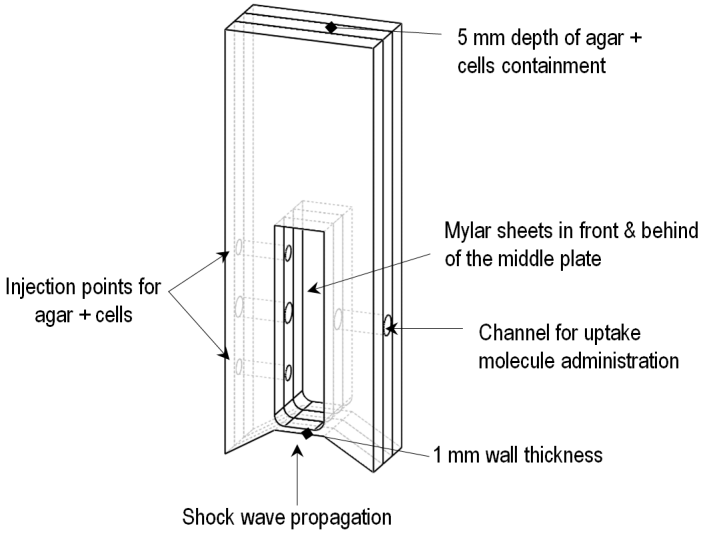
Two cell containments – a 96-well flat-bottom plate and a 2 mL (10 mm outer diameter) snap cap vial with a small conical bottom – were tested for amenability to shock wave exposure, using appropriate custom built holders.

The vials were tested both upright and upside-down (i.e. with the conical bottom pointing away from the shock wave source). In the upside-down position, cell viability was circa 10% higher than when placed upright. It was thought that the material thickness of the cap increased the acoustic attenuation in the upside-down arrangement, leading to shock wave amplitude decrease.

Cell samples in the well plate format were plated in every third well (horizontally and vertically), excluding all outermost wells. Empty wells were filled with PBS to circumvent air spaces. The well plate was then sealed off with an adhesive film. At $\leq$ 100 shocks, a measurable cytotoxicity effect was observed. However, at $\geq$ 250 shocks a chemical effect was also noted as perceived by a colour change of the cell medium during exposure. Evidence in [167] suggests that the enhanced acoustic cavitation at high number of shock waves may have induced degradation of the phenol red pigment present in the medium. This inadvertent result was exclusive to the well plate format revealing container-based



(a)



(b)

Figure 3.1: (a) Shock wave permeabilisation equipment and set-up. Shock waves were generated through a 43 L water tank, fitted above the shock wave source. Cell samples were supported by a sample holder, and maintained at 37 °C with a thermostatic heater. The flow degasser reduced O_2 content to 1 – 3 mg/L; (b) custom-made 'TMM-MODU' phantom for RNA transfection. The dimensions of the agarose + cells containment were 10 × 5 × 40 mm (L × W × H).

influences on shock wave phenomena. Thus, the snap cap vials in the upright position were thereafter employed for all suspension experiments. In the transfection experiments (*see* section 3.2.10) cells were not suspended, but were embedded within a 3-D matrix of tissue mimicking material (TMM). The tissue mimicking phantom is illustrated in Figure 3.1(b).

3.2.4 Shock wave field characterisation

To determine the pressure at the focal point, the acoustic field was measured using a Müller-Platte polyvinylidene fluoride (PVDF) needle hydrophone (Article-No.: 100-100-1, Müller Instruments, Oberursel, Germany) with a 40 ns rise time. The signals produced by the hydrophone were recorded using a digital oscilloscope (LeCroy waveRunner 44Xi, 400 MHz sampling rate; LeCroy Corporation, Santa Clara, CA, USA). The hydrophone was positioned using a manual three-axis linear stage. Measurements were taken along the lateral axes (X and Y) in the focal region area, in increments of 1 mm for up to 10 mm, and along the propagation axis (Z) in increments of 2-5 mm for up to 45 mm. Five waveforms were recorded at each location and converted to pressure using the calibration provided by the manufacturer. The procedure was repeated with the hydrophone inside a vial only at the focal point.

3.2.5 Sample Preparation & Treatments

The above mentioned polypropylene (PP) vials (T7813, Sigma-Aldrich) with a volume of 2 mL were filled with the suspended cells at a concentration of 500,000/mL without any visible residual air in the vials. Prepared vials were immediately chilled and maintained in an ice-box throughout the duration of the experiment, except during treatment. This prevented the occurrence of the temperature-dependent endocytosis process during sample and experiment preparation [235]. For every independently conducted experiment, triplicate shams were prepared alongside the treated samples which were also in triplicates per treatment. Shams captured the effect of the heated water by being placed inside the tank for the duration of the average shock wave treatment, but not being subjected to any shock wave impulses. Sample vials were treated to a combination of shock wave parameter variations: number (125, 250, 500, 1000), energy level (E):- 3, 6, and 9; and pulse repetition frequency (PRF):- 1 and 2 Hz.

3.2.6 mRNA & siRNA stability

Sterilised vials were filled with 1 μg/mL of eGFP mRNA (StemMACS, Miltenyi Biotec Ltd, Woking, UK) in serum-free RPMI 1640 medium, in the absence of cells, and exposed to shock waves. The rabbit reticulocyte lysate (RRL) cell-free gene expression system (Nuclease Treated L4960, Promega, Madison, WI, USA) was utilised to assess mRNA translation activity after shock wave treatment. The translation reaction was prepared in accordance to the supplier's protocol. Constituent volumes were adapted to the mRNA concentration as well as to permit micro-plate fluorometric reading, while maintaining relative proportions. A control mixture not containing any mRNA was also prepared to measure background due to the RRL. The reactions were incubated at 37 °C for 75 minutes. Fluorometry was then performed at 485 nm excitation and 520 nm emission using the FLUOstar Omega microplate reader (BMG Labtech GmbH, Ortenberg, Germany).

Electrophoresis-based nucleic acid structural integrity post shock waves was tested. eGFP siRNA (Silencer, Thermo Fisher Scientific) and eGFP mRNA cell-free samples were prepared at 15 and 2.5 μg/mL respectively in UltraPure DNAse/RNAse free distilled water (Thermo Fisher Scientific). For siRNA analysis, traditional 1% agarose gel electrophoresis in 1X Tris-Borate-EDTA buffer was performed. For mRNA analysis the Agilent 2100 Bioanalyzer (Agilent Technologies, Palo Alto, USA) and RNA 6000 pico kit (due to low concentrated mRNA samples) were employed. The assay was conducted following the Agilent guide for the required kit. RNaseZAP cleaning agent (R2020, Sigma-Aldrich) was applied to all equipment at the start of the procedure.

3.2.7 Cell Survival & Viability Assay

The viability of cells was tested with the MTS assay (CellTiter 96 AQ_{ueous} One Solution Cell Proliferation Assay [3-(4,5-dimethylthiazol-2-yl)-5-(3-carboxymethoxyphenyl)-2-(4-sulfophenyl)-2H-tetrazolium], Promega). After exposure, 200 μL of cell suspension from each vial was plated into a 96-well plate at two wells per vial. The procedure was repeated for a second 96-well plate. 20 μL of MTS solution was added to each well of the first well plate and incubated for 30 minutes, representing the 1-hour-after-exposure assay; the second well plate was incubated with the MTS following 24 hours of

incubation post exposure. Absorbance was read at 490 nm (1.0 second measurement time) using a Wallac 1420 Victor^2 microplate reader (Perkin Elmer, Inc., Beaconsfield, UK). Cell viability was calculated as follows:

$$\text{viability}(\%) = \frac{\text{treated } \overline{\text{x}}_{\text{absorbance}}}{\text{sham } \overline{\text{x}}_{\text{absorbance}}} \times 100 \tag{3.1}$$

Cell survival was also captured optically by looking for absence of cellular debris/fragments, to enable a low-level check of the cell viabilities, because the assay is limited by the inability to discriminate between a cytotoxic and a cytostatic (reduced growth rate) effect [236].

3.2.8 Cell Permeabilisation analysis

Membrane permeabilisation analyses were carried out using a Becton Dickinson FACSCalibur flow cytometer (BD Biosciences, Franklin Lakes, NJ, USA). 500 μL of cell suspension from each vial was transferred into tubes, maintaining cells in a chilled environment. A solution of 6 μg/mL propidium iodide (PI; Sigma-Aldrich) was prepared, which is a fluorescent nuclear stain that is not permeant to cells with intact plasma membranes, and can be detected upon its binding to cellular DNA. 100 μL of the solution was added to each tube and briefly vortexed immediately before analysis. An argon laser provided excitation at 488 nm. The software programme CellQuest Pro (BD Biosciences) was used to acquire and analyse the data. 10,000 cells per sample were recorded and sorted by gating in two ways: 1. forward scatter/side scatter in order to identify viable cells and 2. PI staining to identify molecule-internalised cells. Data acquisition was initialised with the negative control samples followed by all other samples in the absence of PI. The percentage of PI-positive cells was obtained by setting a gate in the PI fluorescence intensity frequency histogram of sham samples above which only circa 0.1% of cells fell.

3.2.9 FITC-dextran delivery and dissemination

To study the mRNA concentration (or dose) dependent effects on the shock wave induced delivery and dissemination, a eGFP mRNA analogue – FITC-dextran (FITC-D; FD250S, Sigma Aldrich) was employed, at a molecular weight of 250 kDa to simulate as closely as possible the size of the eGFP mRNA (1000 nucleotides = $\sim$ 320 kDa). Delivery into

CT26 cells was performed in cell suspension experiments and assessed by flow cytometry, whereas the dissemination study was conducted in TMM experiments and assessed by fluorometry. FITC-D was employed in order to determine the *immediate* macromolecule dispersion (through spatial green fluorescence measurements), thus distinguishing shock wave induced delivery from passive diffusion which is concentration gradient driven and time dependent. A range of FITC-D amounts were tested, consisting of the mRNA dose applied in transfection, the average *in vitro* 20 - 30 μg transferred DNA amounts reported in the literature ([222], [221]), and a proportionally scaled up dose. Thus, 5, 30 or 180 μg of FITC-D dissolved in PBS was added to the prepared cells in vials for the delivery experiment, or into the channel of the phantoms for the dissemination experiment. In the delivery experiment, after shock wave exposure cells were washed twice by centrifugation (1500 g, 5 minutes) and resuspension in PBS. The efficiency of the washing procedure was checked by fluorometric measurements read at 490 nm excitation and 520 nm emission.

3.2.10 Transfection procedure

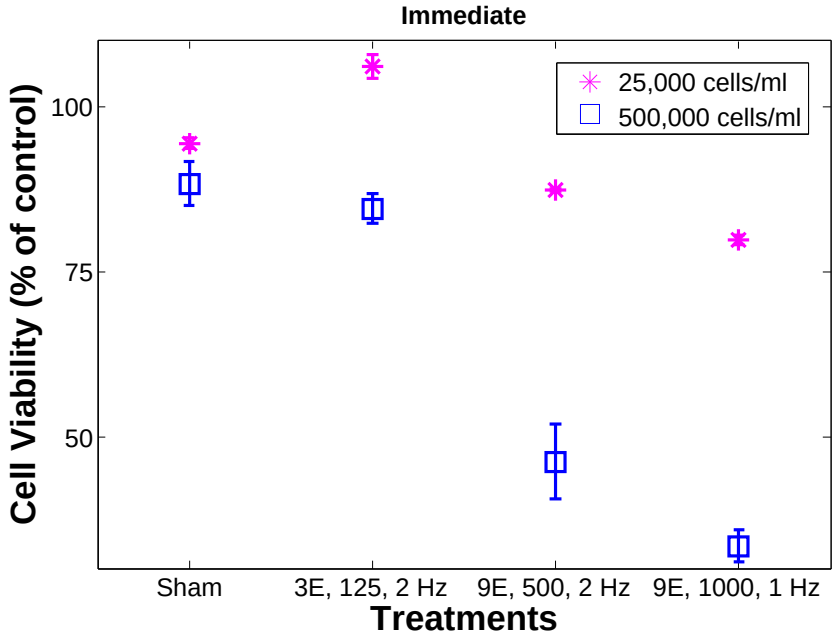
GFP production or knock-down was tested using eGFP mRNA or eGFP siRNA respectively. This reporter gene was selected due to its inherent stability allowing its accumulation and easy detection in living cells [237]. CT26 cells at a density of 2.5 million/mL were employed for mRNA transfection experiments while MCF-7/GFP cells at 1.5 million/mL were employed for siRNA transfections. Cells were immobilised in 1% agarose (UltraPure low melting point agarose, Thermo Fisher Scientific) in 2 mL custom-made tissue phantom vessels (Figure 3.1(b)), and 5 μg mRNA or 10 μg siRNA in UltraPure DNAse/RNAse-free distilled water was supplied into the channel of each phantom, prior to shock wave treatment. For the siRNA transfections, both the agarose and the cells were prepared in Opti-MEM Reduced Serum Medium (Thermo Fisher Scientific) before mixing, while for mRNA transfections, cells and agarose were prepared in RPMI 1640 Medium and PBS respectively. Transfection shams consisted of samples supplied with the nucleotide of interest but not exposed to any shock wave pulses. Afterwards, vessels were maintained at 37 °C in cell culture incubators and removed only for analyses.

Transfection levels were assayed by fluorometry using the FLUOstar Omega microplate reader. For mRNA transfection, fluorescence intensity (FI) was read at 24 and 48 hours after shock wave treatment to allow all potential cells to synthesise and express the GFP. Similarly, siRNA mediated knock-down was assayed at 24, 48 and 72 hours – a time frame defined to capture the translational arrest subsequent to target mRNA degradation. Green fluorescence from the mRNA transfections, was visualised at the respective final assay time point using the Nikon Eclipse TiE2000 inverted microscope (Nikon Corporation, Tokyo, Japan) with a 10× objective lens; microscopic views within the upper agarose region of the tissue phantom vessel were generated using NIS-Elements AR software (Nikon Corporation).

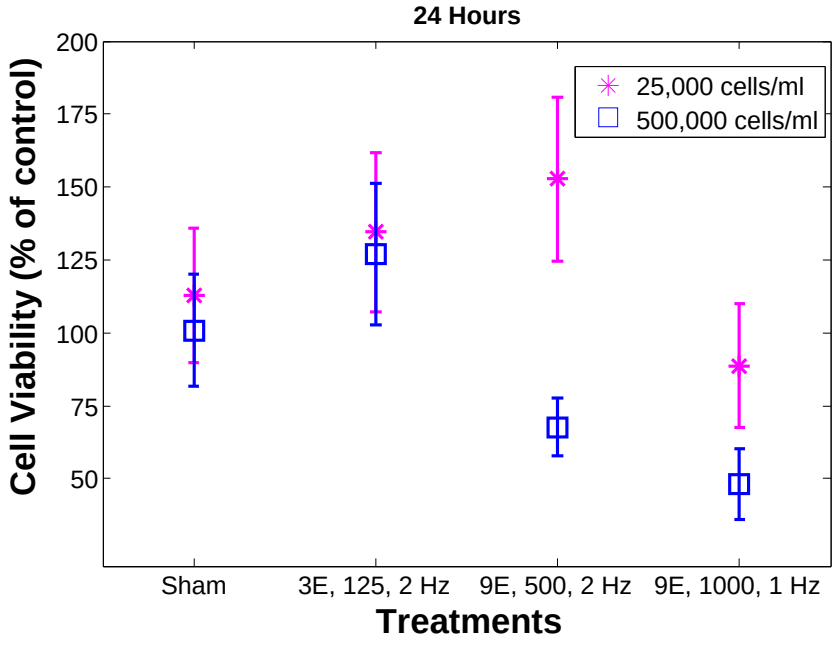
3.3 Results

3.3.1 Cell density modulates post-shock wave cell viability

Two cell concentrations varying by more than one order of magnitude were treated with shock waves. The effect of cell concentration on the viabilities is shown in Figure 3.2 for three selected treatments, immediately after shock wave exposure and 24 hours later. A marked shock wave dose dependency was revealed at the relatively high 500,000 cells/mL concentration, at both time points. Conversely, viabilities appeared to be scattered across treatments at the lower (25,000 cells/mL) concentration with no clear dose dependency. It was found that the highest cytotoxicity was produced at 9 E, 1000 shocks, 1-Hz, although viability was still reasonably high (79.8%). Applying the same treatment to the higher cell concentration reduced viability to 33%. A minimal shock wave dose consisting of low energy and low number of shock waves (3 E, 125 pulses) suggested that at the lower cell concentration, shock waves can stimulate cell proliferation leading to enhanced viability. One-way ANOVA was used to compare the viability means between treatment groups. At both cell concentrations there was a statistical difference at the $p < 0.05$ level across groups.



(a)



(b)

Figure 3.2: Effect of CT26 cell concentration on the cell viabilities (using the MTS assay) relative to the negative control at (a) immediately, and (b) 24 hours after exposure. Data consists of at least three same-day replicates per treatment, for three independently conducted experiments (i.e. n=9). The markers represent the means and the error bars represent the standard errors. Both statistics are expressed as percentages.

3.3.2 Influence of shock wave parameters on CT26 cell viability and permeabilisation

Expression of delivered transgenes is only possible where live cells exist. Cell response to shock waves is dependent on several factors including SW parameters, the physical environment of cells and the cell type. Shock waves can result in enhanced proliferation [238], or marked cytotoxicity [222, 231, 239]. Thus, shock wave-induced cytotoxicity was investigated to identify a parameter space that maximised the cell viability.

Figure 3.3 demonstrates a shock wave dose-dependent decrease in the viability of CT26 cells 1 hour after exposure. This effect was greater with increasing energy level and number of shock waves where 500 pulses at the highest attainable energy level (9 E)

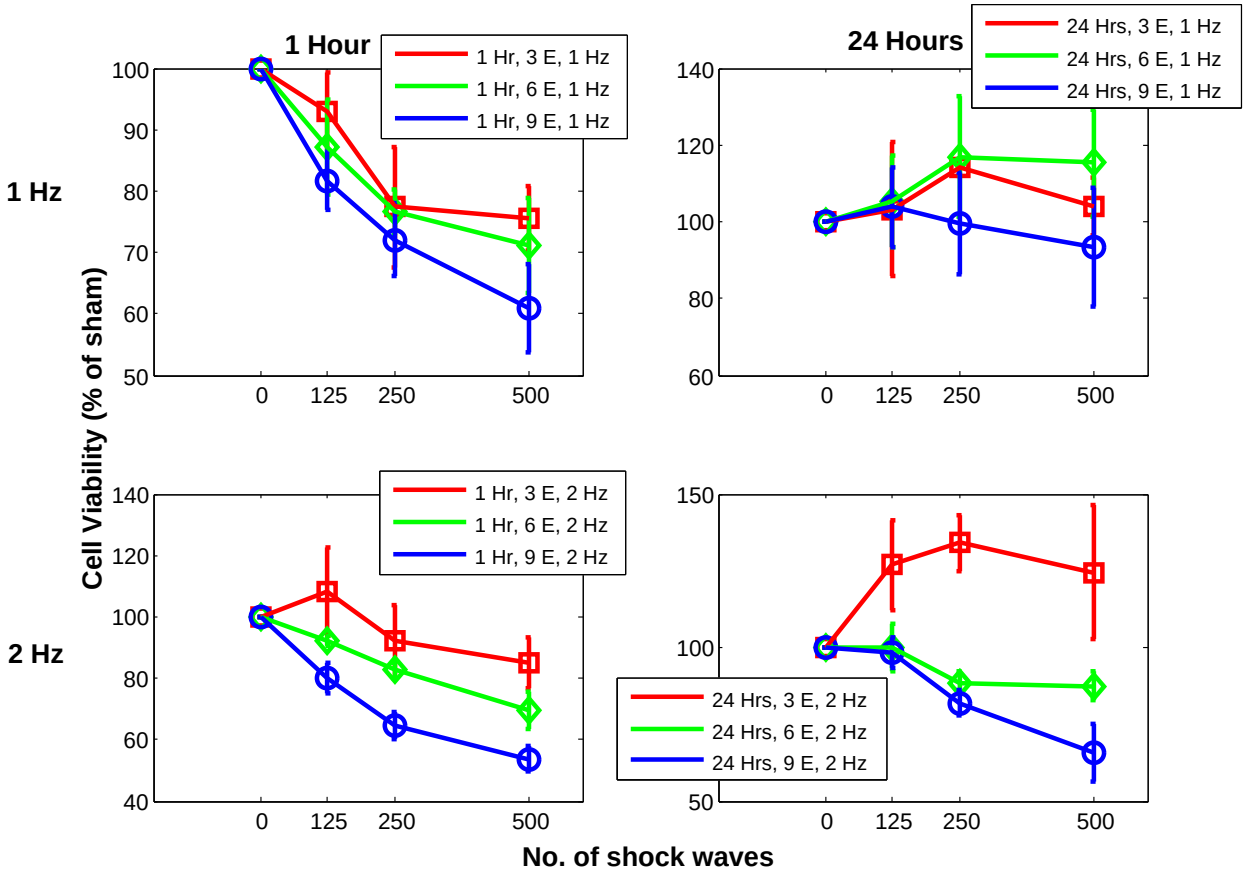


Figure 3.3: Influence of shock wave exposure on cell viability. CT26 cells were assayed at 1 or 24 hours after exposure using the MTS assay. The influence of number of shock waves, energy and pulse repetition frequency was investigated. Data points represent the mean values of triplicates per treatment, for at least three independently conducted experiments (i.e. n=9). Error bars are the standard errors.

amounted to a viability of 50–60%. Varying PRF from 1 to 2 Hz did not alter the overall

pattern of this loss of viability. At 24 hours, MTS assays were performed again and comparison to 1 hour data allowed the recovery of cells to be characterised. The 24-hour viabilities were comparably elevated in the majority of cases, indicating a population growth phase at or within 24 hours. However, the extent of growth differed between treatments as well as within treatment replicates, with some treatments (e.g. 3 E, 250 pulses, 2 Hz) suggesting metabolic activity within the samples was doubling between the 1 hour and 24 hour readings; while others (e.g. 9 E, 500, 2 Hz) showed sustained depletion of viability implying that in those conditions, shock waves instigated damage from which the cells could not recover. The shock wave stimulative effect at low energy was evidenced at both pulse repetition frequencies in the 24-hour assay; a wider range of energies displayed this effect at 1 Hz, while proliferation peaked at 2 Hz.

The influence of PRF on cell viability was also investigated, to a maximum of 4-Hz, which could only be realised for energy levels 3 and 6 (Figure 3.4) due to the capacitance of the shock wave source. For a fixed number of shock waves (250) while varying the

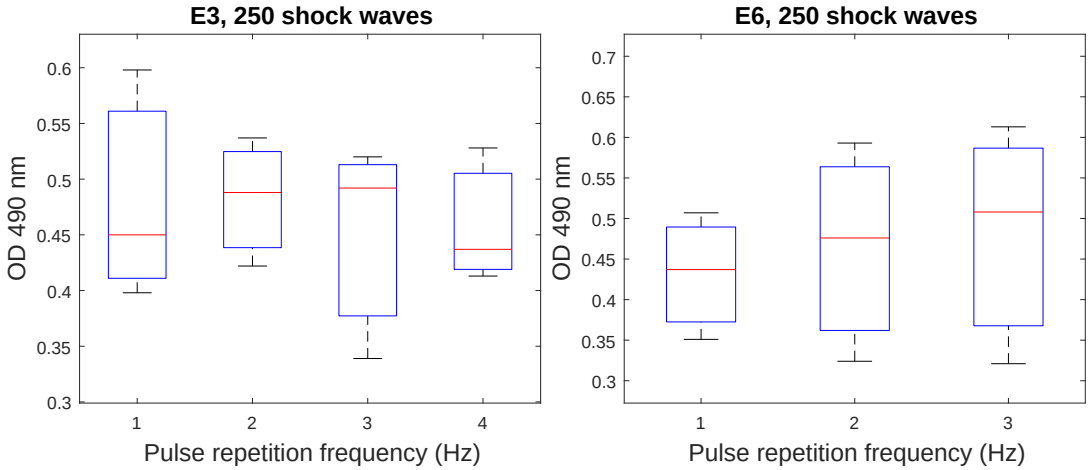


Figure 3.4: The effect of shock wave pulse repetition frequency on the absorbance of the MTS formazan product which is proportional to the cell viability. Data consists of three triplicates per treatment, for three independently conducted experiments (n=9).

PRF in increments of 1 Hz, no statistical significance was found between PRFs in both energy level sets ($p = 0.8$ and 0.49 for the 3 E and 6 E sets respectively). Thus, it was thought that for any two treatments where only the PRF was the varying parameter, any

difference in apparent viability was due to changes in cell morphology (i.e. cell injury) rather than cell destruction; due to PRF-effectuated cell accelerations and/or collisions.

Despite insignificance across PRF treatments, Figure 3.4(b) shows a pattern between 1 and 3 Hz which is suggestive of the possibility that at higher acoustic energies, there may be a pronounced trend whereby the faster the shock rate is the lower the cell kill (and therefore higher absorbance). The acquired cell viability data (Figure 3.3) revealed high statistical power ($p<0.01$) between 125, 250 and 500 pulse number sets (encompassing the various tested energy levels and PRFs) indicating that the acoustic parameter with the greatest modulating influence on cell viability was the number of SWs rather than SW energy. In fact, as shown in Figure 3.5 microscopic examination demonstrated that doubling the number of pulses produced progressively shrunken cells in addition to some cellular debris ((b) and (d)) unlike doubling the energy ((b) and (c)).

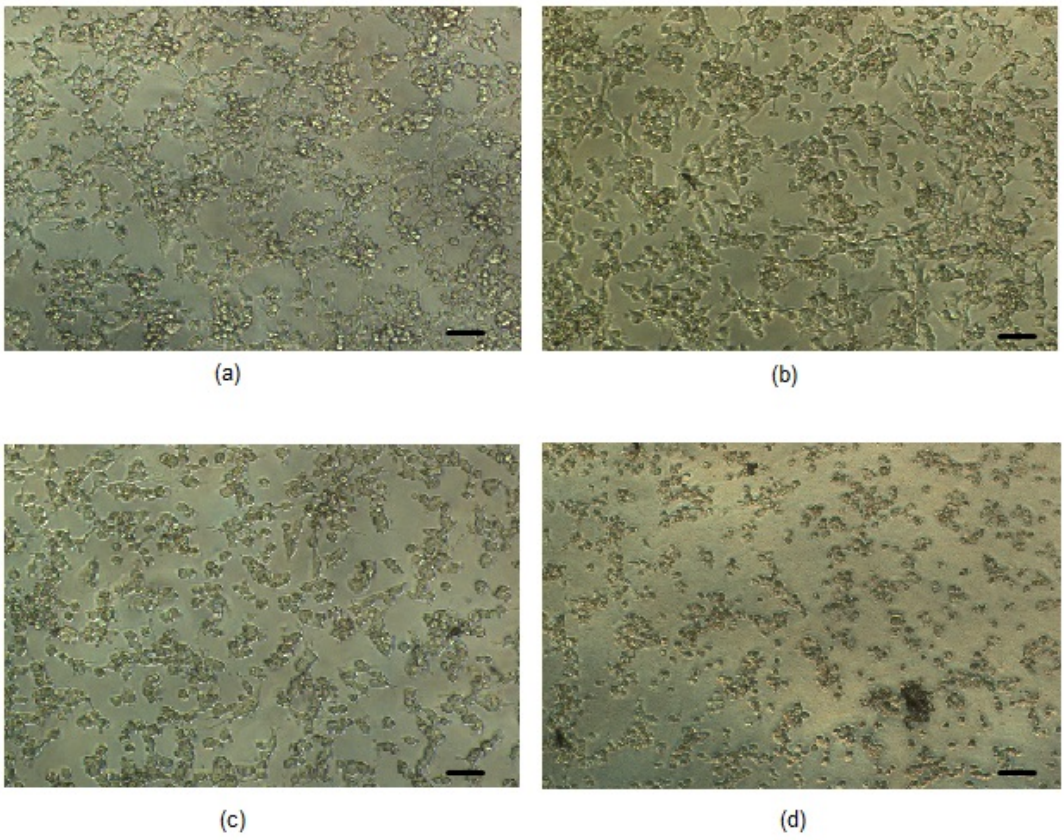


Figure 3.5: Light micrographs of CT26 cells, 1 hour after shock wave exposure: (a) sham, (b) treated with 3 E, 250 shocks at 1 Hz, (c) 6 E, 250 shocks at 1 Hz, (d) 3 E, 500 shocks at 1 Hz. Scale bar corresponds to 56 μm.

Shock wave impact on the cell viability was probed further using flow cytometry (*see* methods). Figure 3.6 shows example distributions for a sham treated population (top row), a minimally exposed population (middle row, (3 E, 125 shocks, 2 Hz)) and a maximally exposed population (last row, (9 E, 500 shocks, 2 Hz)). Based on the untreated (sham) cells, sub-populations such as fragmented cells and cellular debris were identified by side scatter (SSC), which is proportional to cell granularity. The pink polygon gate was set to enclose the normal population of intact cells. A substantial negative FSC shift in population density was noted, as the treatment intensity was increased to energy level 9, as well as reduced SSC signal. Cell permeabilisation, as characterised by cell staining with PI immediately after shock wave exposure, was quantified by the fluorescence gate separating the SSC/FL2-H plots into left and right halves as shown in Figure 3.6 (where FL2 is a channel for the detection of emission wavelengths comprising the emission peak of PI). Events in the right half represented the proportion of total PI-positive cells which is shown to increase with increasing shock wave parameter. The minimum SSC of the untreated population provided a baseline for an additional gate to separate intact from damaged cells, where the top right quadrant identifies the population of whole and permeabilised (i.e. capable of taking up the PI) cells. It is noted that less than 4% of cells were intact and PI-positive in the sham samples, suggesting that a small proportion of cells became compromised by the removal of culture conditions. The level of reversible damage (that is, transiently permeabilised cells) was determined by correlating total PI-positive cells with the cell viabilities at 24 hours (from Figure 3.3). In so doing, a parameter space defined by 9 E, 125, 2 Hz and 3 E, 500, 2 Hz was found that permitted temporal membrane permeabilisation to the PI of up to ∼15%, without any associated cell death (Figure 3.7). For almost all shock wave conditions, results demonstrated an inverse correlation between the percentage of permeabilised cells and viability.

3.3.3 Optimisation of shock wave parameters

The shock wave settings that imparted the maximum number of permeabilised (as detected by PI staining), but still viable (as detected by MTS) cells was sought. This value may be considered the 'transfectable' population. While all killed cells are permeabilised, not all permeabilised cells are killed. A 2-D interpolation of all the

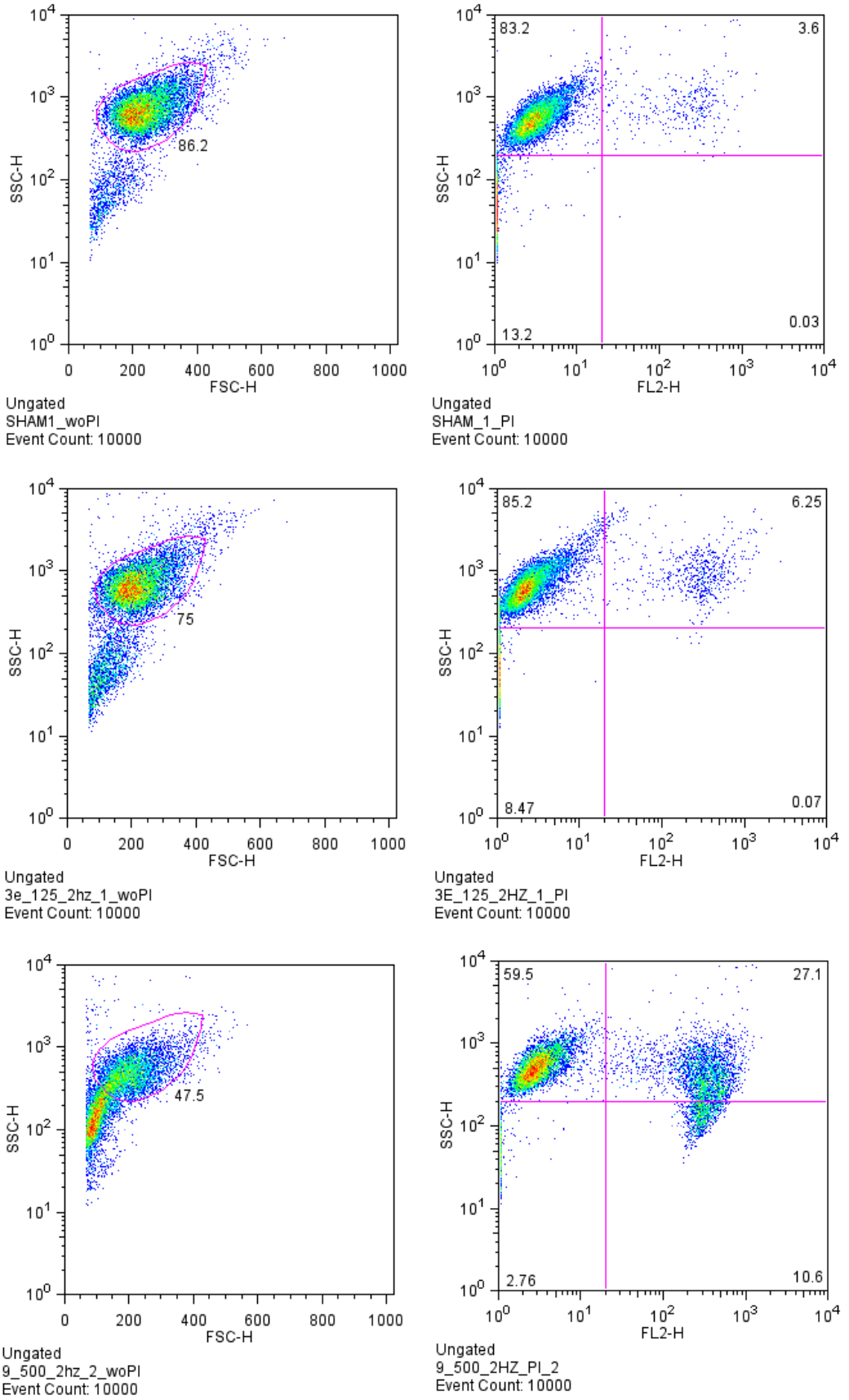


Figure 3.6: Flow cytometric measurements of CT26 cell permeabilisation and viability. Representative density-plots for three treatments: sham (top), 3 E, 125 pulses, 2 Hz (middle), 9 E, 500 pulses, 2 Hz (bottom).

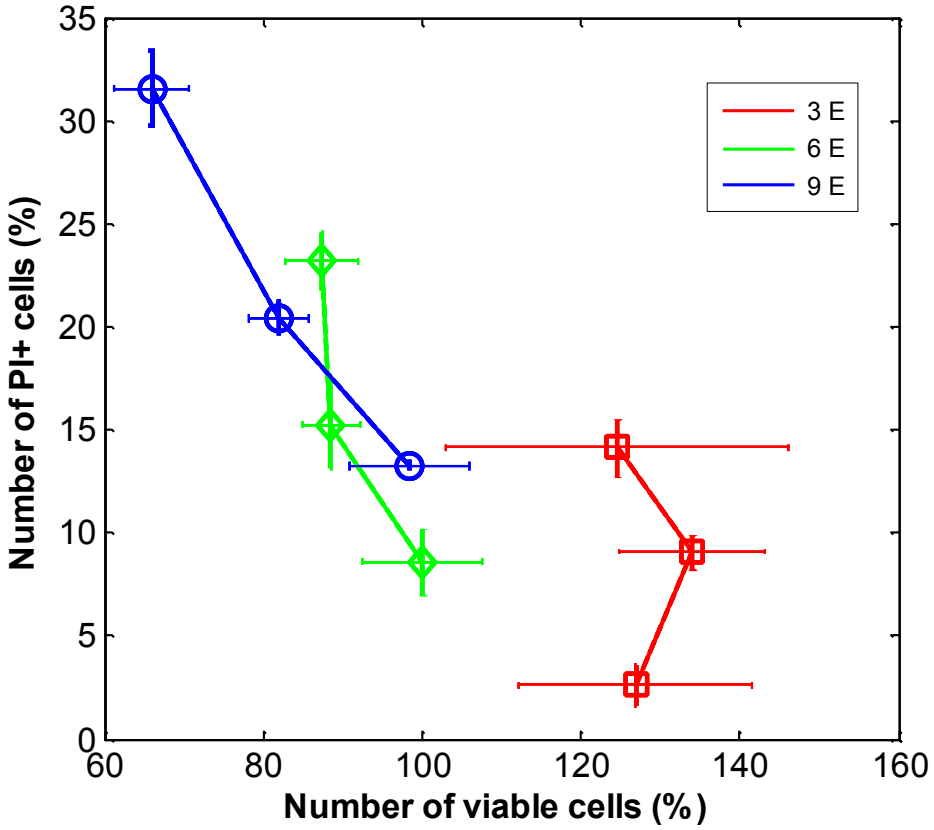


Figure 3.7: CT26 cell permeabilisation combined with results of 24-hours viability. Data points represent the means of three same-day replicates, for at least three separate day experiments (i.e. n=9). Error bars are the standard errors.

CT26 cell permeabilisation and 24-hours viability data was performed between data points, in increments that related to attainable lithotripter settings, and the proportions of permeabilised cells above the proportions of non-viable cells were derived. Figure 3.8 demonstrates the resulting contours of high and low transfection power across shock wave energies and number of pulses. The highest value was predicted to be produced by 548 shock waves, at 4.5 energy level (*see* white arrow), where 20.19% of total cells were theoretically capable of being transfected in the presence of a nucleic acid, whilst maintaining 24-hour cell survival rates at 100%. To validate this prediction, the optimum shock wave setting was experimentally tested and a reversible cell permeabilisation of 20.5 $\pm$ 2.7% was found. Karshafian et al.[240] optimised their ultrasound exposure system by deriving a similar measure that compared the desired and destructive effects

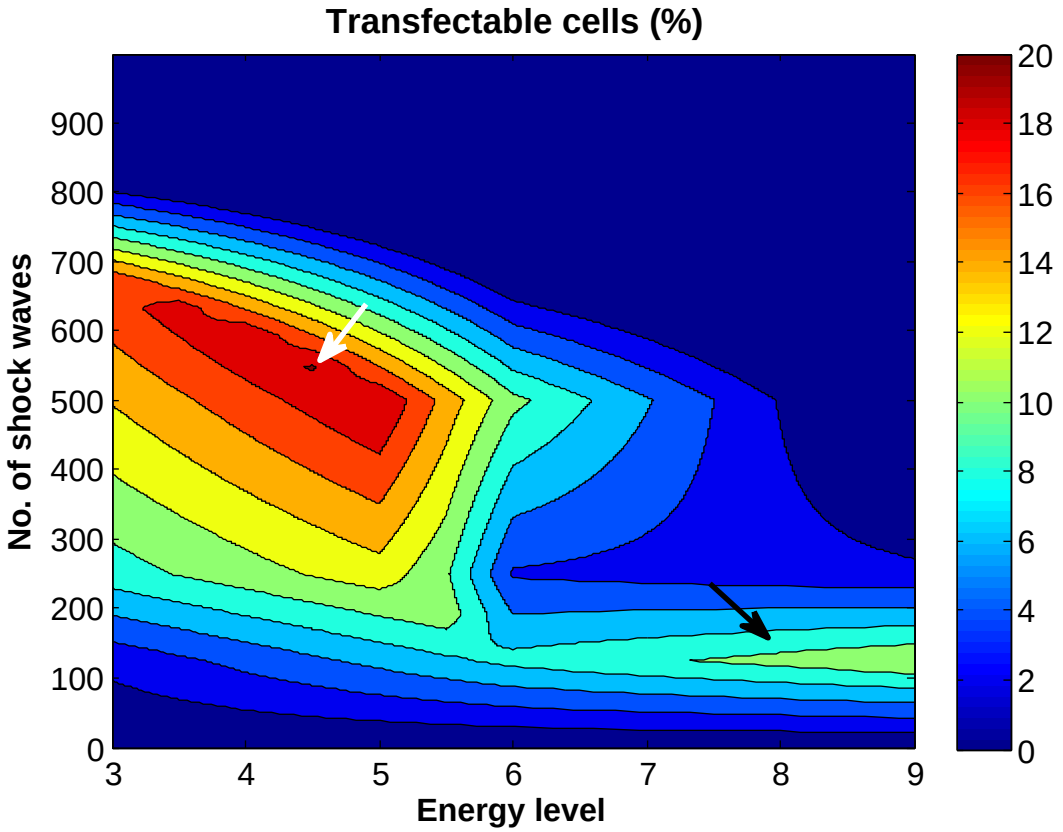


Figure 3.8: Transfectability of CT26 cells as a function of the number of shock pulses (0 – 1000) and energy level (3 – 9) at 2 Hz. Transfectability is defined as the percentage of live permeabilised cells. Three independently conducted experiments at 1000 pulses, with three-same day replicates at each tested energy level were included.

of any given shock wave condition. Notably, Figure 3.8 also shows that at the highest energies and circa 150 pulses (*see* black arrow), there is a local increase in the percentage of live permeabilised cells, suggesting that a regime consisting of a few shock waves at high peak pressures may exist where appreciable cell permeabilisation is also attained.

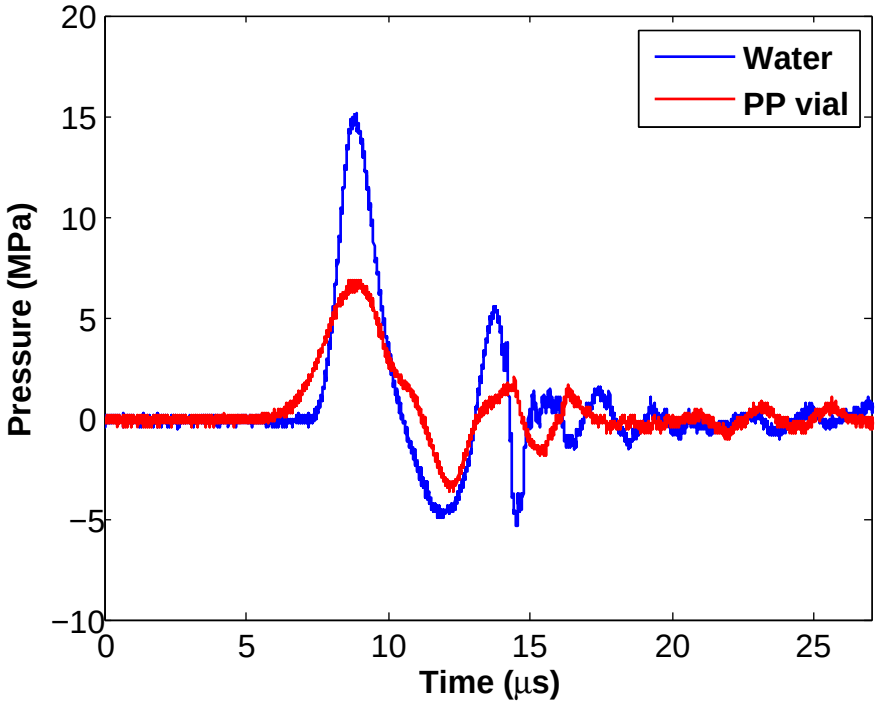
3.3.4 Shock wave pressure

Figure 3.9(a) shows pressure waveforms measured at the focus of the lithotripter at the optimal energy level for CT26 cells, in degassed water and with the needle hydrophone in the polypropylene vial. The presence of the vial decreased the peak positive pressure by 57% and increased the duration of the compressive phase from 2.57 μs to 4.63 μs, which was measured from the positive pressure that first exceeds 10% of the peak positive pressure, up to the first time the positive pressure reduces below 10% of the peak positive pressure [241]. The negative pressure did not change substantially as evidenced by a 1.3 MPa decrease when inside the vial, either as a result of the limiting hydrophone's susceptibility to damage, stemming from cavitation during the negative phase [242], or because the negative phase is more sensitive to the low frequency components of the signal and thus less affected by the vial. The presence of the vial did not appreciably change the shape of the waveform. At the focal point, the peak pressures for energy levels 3, 4.5, 6 and 9 are given in Table 3.1.

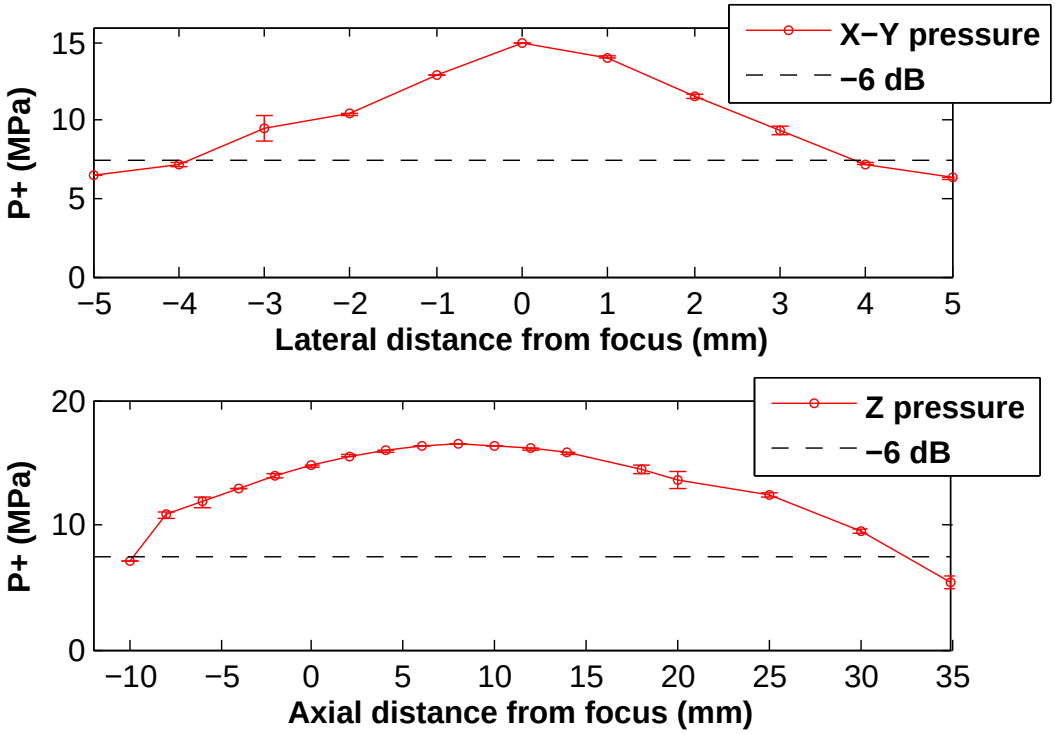
Table 3.1: Shock wave Focal Pressure

Energy Level	Peak Positive (MPa)	Peak Negative (MPa)
3 E	8.6 ± 0.3	4.7 ± 0.3
4.5 E	14.9 ± 0.2	5.0 ± 0.1
6 E	20.7 ± 0.8	6.4 ± 0.4
9 E	37.0 ± 0.5	7.2 ± 0.5

The variation in peak positive pressure in the focal zone of the lithotripter at energy level 4.5 was also measured. Figure 3.9(b) shows peak pressure in the lateral plane (X,Y) and along the propagation path (Z). The maximum error in hydrophone positioning was a standard deviation of 0.86 MPa. In the lateral direction the pressure amplitude dropped to 50% as demarcated by the -6 dB threshold line, at a radial distance of 3.9 mm, while in the axial direction the -6 dB focal zone was asymmetric about the focus, and spanned 42.4 mm. Therefore the incident pressure field was relatively uniform within the exposure vessels (vial & TMM were 9 or 10 mm wide and 40 mm long), although the vessel material is likely to have resulted in some variation.



(a)



(b)

Figure 3.9: (a) Representative shock waveform at energy level 4.5 when measured at the focal point in degassed water and inside the polypropylene (PP) vial; (b) Measurements of peak positive pressure at energy level 4.5, in the direction perpendicular to the shock wave propagation path (X-Y) and along the path (Z); n = 5. Error bars are the standard deviations (range: 0.07 - 0.86 MPa). The focal zone is marked by the dashed line representing the pressure being 6 dB less than the maximum peak positive pressure.

3.3.5 Permeabilisation and viability of HK-2 & MCF-7/GFP cells

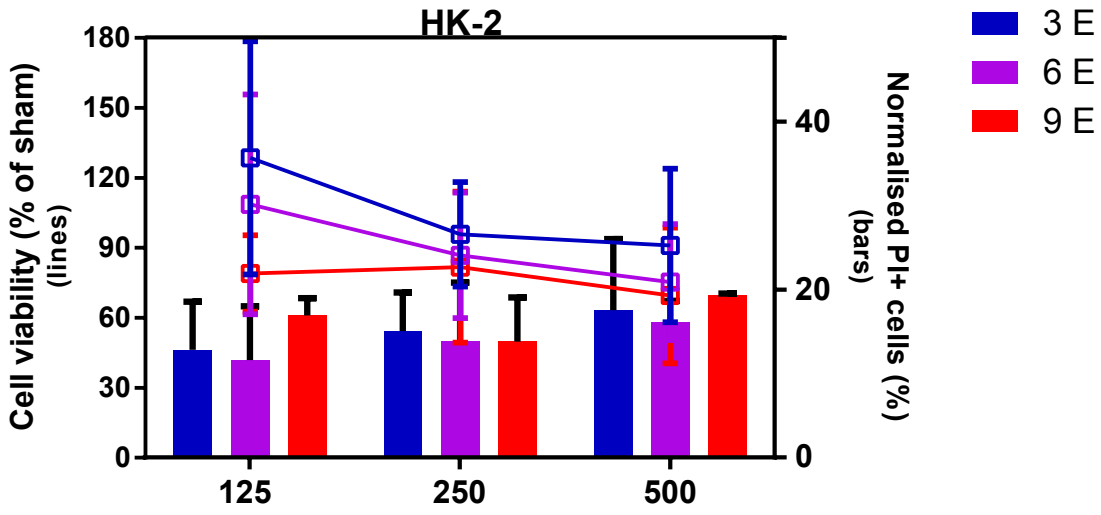
The impact of shock waves on other cell lines in suspension was investigated using HK-2 and MCF-7 cells to gauge variability across different cell types. Cell permeabilisation and viability data were processed similarly to data from CT26 cells. Appropriate settings for the flow cytometer's detectors and amplifiers were adjusted accordingly. However, for MCF-7/GFP cells, PI positivity was detected using the FL3 channel due to the GFP signal bleeding into the FL2 channel. The overlap between FL2 and FL3 detectors at 620 nm, enabled PI detection in either channel.

The cell viabilities of HK-2 cells were shock wave dose dependent, with values ranging from ∼70% to ∼129% relative to sham controls. In contrast, the permeabilisation of HK-2 cells (Figure 3.10(a)) showed little correlation with shock wave parameters. However, a measurable level of shock wave induced permeabilisation was demonstrated, highlighting the sensitivity of the cell line to ultrasound. As HK-2 cells are transformed rather than of cancer origin, this provides evidence of shock wave applicability in non-cancerous gene therapy applications.

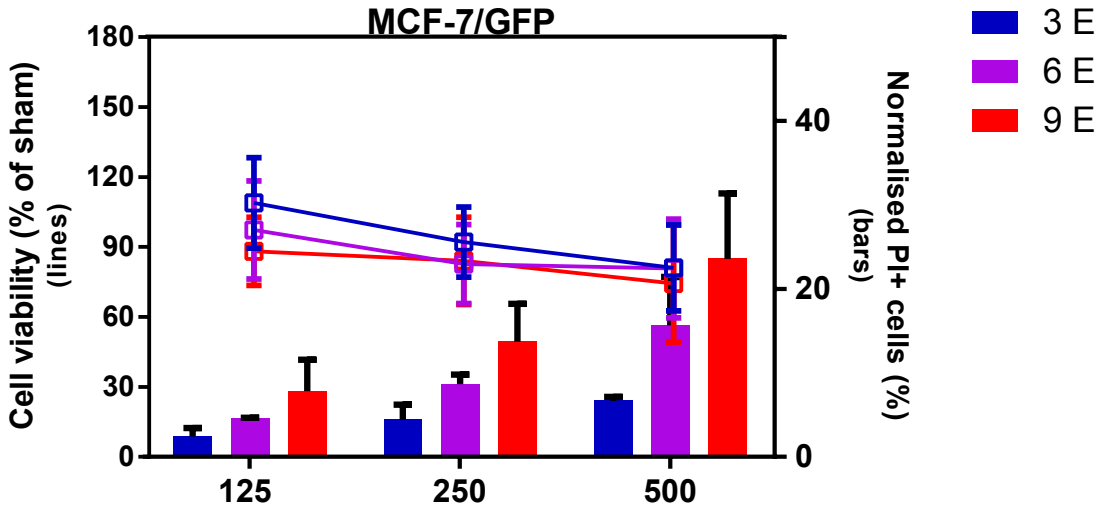
Results of MCF-7/GFP permeabilisation, shown in Figure 3.10(b), confirmed the differential effect of shock waves on cancer cells, previously observed with CT26 cells, where both shock wave energy and number of pulses were effective discriminants. However, the cell line revealed reduced amenability to efficient transfection as the highest proportion of permeabilised cells above that of killed cells was found to be only 4.1%, achieved by exposure to 134 shock waves, energy level 5.0, at 2 Hz. Although up to 23.5% of cells could be permeabilised (500 shocks, 9 E), these parameters were associated with a 25% loss in viability. This is consistent with reports that have described MCF-7 cells as 'hard-to-transfect' in the literature [243].

3.3.6 RNA stability

Having identified shock wave parameters that would allow transfection whilst maintaining cell viability, the effect of shock waves on the stability of nucleotide was tested. The structural stabilities of mRNA and siRNA were determined using the Bioanalyzer and



(a)



(b)

Figure 3.10: Influence of shock wave exposure on HK-2 and MCF-7/GFP cell permeabilisation (bars) and 24-hour-after cell viability (lines). Data points represent the mean values of three same-day replicates per treatment, for three separate day experiments (i.e. n=9). Error bars are the standard deviations.

traditional gel electrophoresis respectively. Figure 3.11(A-1) depicts representative electropherograms of sham and optimum-shock wave treated mRNA. The distinct 18S and 28S ribosomal peaks of typical RNA were present in both treatments. No shift

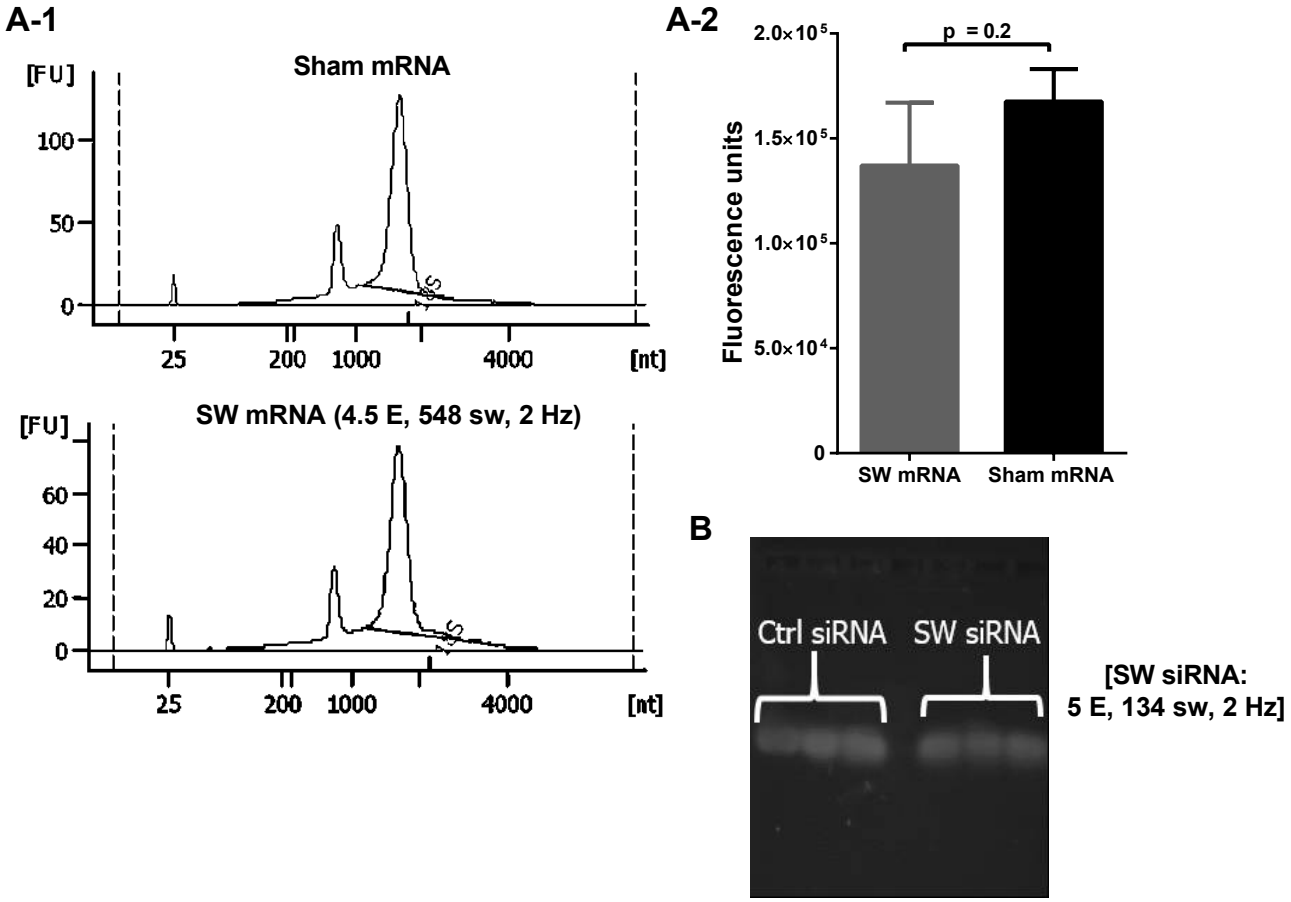


Figure 3.11: Results of stability for (A) mRNA and B) siRNA post shock wave exposure or sham (control) treatment. Structural stability data depicts (A-1) representative mRNA electrophoretic profiles and (B) agarose gel electrophoresis for siRNA analysis (based on n=3). (A-2) mRNA biological activity data consists of one sample per treatment, for three independently conducted experiments (n=3); error bars represent the standard deviations.

in nucleotide [nt] size of both peaks was observed with optimal shock wave exposure. In addition, the absence of smaller peaks between the two ribosomal peaks (typically observed in partially digested RNA) suggested that the structure-based functionality of the exposed mRNA had not been impaired. However, a 22% decrease in the 28S ribosomal peak intensity was detected with shock wave exposure (1,765 $\pm$ 183 pg/μL for the shams versus 1,363 $\pm$ 115 pg/μL for the shock wave treated, based on n=3). On the stability of siRNA, Figure 3.11(B) demonstrated that optimal shock waves for MCF-7/GFP cells did not substantially impact the structure or concentration of

siRNA, with comparably equal migration and similar fluorescence intensity of the bands with respect to the non-shocked siRNA.

Maintenance of mRNA biological stability was assayed by performing cell-free protein translations of the GFP mRNA transcript, allowing for absolute measurements of shock wave-induced damage to the activity of the mRNA as there was no cell interference during exposure. Figure 3.11(A-2) demonstrates the translational activity of sham controls and optimum-shock wave treated samples, in terms of GFP fluorescence intensities. An 18% drop in mean fluorescence intensity between sham and optimum shock wave was observed (167,570 versus 137,125 fluorescence units, respectively) which was not found to be statistically significant. Thus, results from both stability methods were in agreement on the mRNA effects impacted by shock waves. Though direct investigations on the (in)stability of mRNA in acoustic fields have not been previously presented, Forbrich et al.[244] reported ultrasound-enhanced cellular liberation of endogenous mRNA. They determined significant numbers of liberated mRNA molecules as assayed by reverse transcription and quantitative polymerase chain reaction (qPCR), thus entailing functional post-exposure mRNA. Furthermore, while ultrasound-assisted delivery of complexed mRNA has been reported [245], no comparison can be made between free and complexed mRNA.

Ultimately, the reported reduction in RNA quality due to shock waves was shown to be slight and non-significant compared to the potential of enhanced nucleotide delivery.

3.3.7 Shock wave-mediated transport of 250-kDa FITC-dextran and dissemination in agarose is a function of macromolecule availability

The application of shock waves has the added potential to improve the transfer of nucleotide from blood vessels and into target tissue. Having identified shock wave exposure conditions which were conducive to cell viability and maintenance of nucleotide structure, the impact of these conditions on mass transfer out of a model vessel and into the tissue mimicking material (TMM) was investigated. Using the custom-made tissue phantoms (*see* Figure 3.1(b)), FITC-D was loaded into the channel (0 mm), exposed to

shock waves from beneath and transfer toward the shock wave source (up to -20 mm) or away from the shock wave source (up to +20 mm) was measured.

Figure 3.12 depicts results of scaled fluorescence against distance below (-2.5 to -20 mm) and above (2.5 to 20 mm) the channel. The channel is illustratively demarcated by the dash-dot lines. At all three amounts of dextran, an elevated fluorescence signal in the upper agarose region (between +2.5 mm and +20 mm) in the presence of shock waves (red

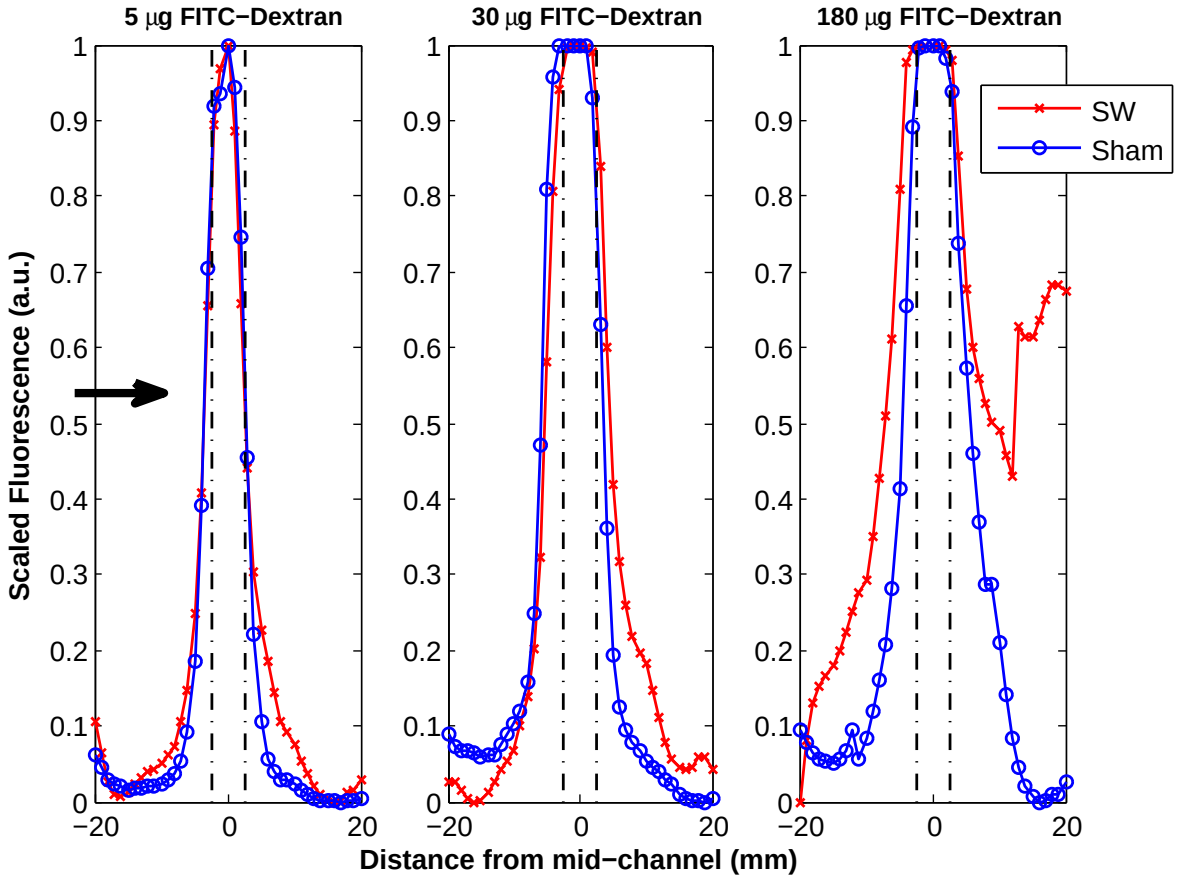
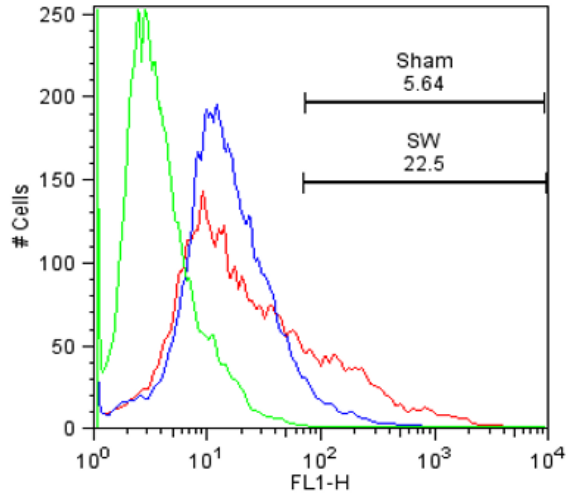


Figure 3.12: Representative disseminations of 250-kDa FITC-dextran in the custom-made 1% agarose tissue phantoms, along the direction of shock wave propagation (i.e. from - 20 to 20 mm) after shock wave or sham treatment. The areas in-between the dash-dot lines represent the channel width. The black arrow indicates the direction of shock wave propagation.

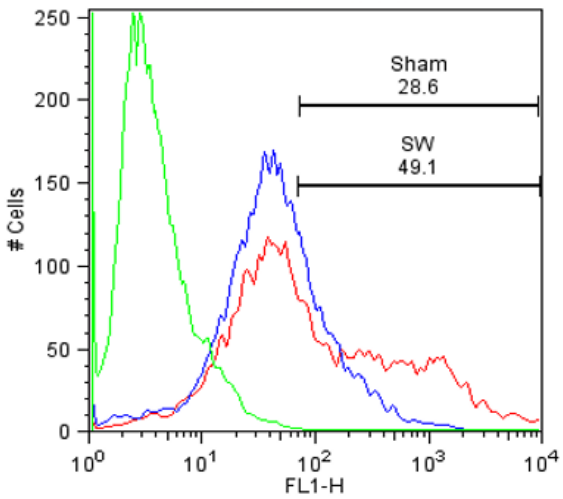
line) was demonstrated compared to the sham treated samples (blue line). At the farthest distance (20 mm), scaled fluorescence intensities were $\sim$ 6, 8 and 25 -fold higher than corresponding sham values at 5, 30 and 180 μg FITC-D respectively. Contrast between shams revealed some degree of passive dissemination into the agarose from the channel, where increasing dextran mass increased the fluorescence in the vicinity of the channel.

Dextran uptake was determined by flow cytometric fluorescence intensity (FI) measurements greater than those of the sham samples. Although washing of cells was repeatedly performed to eliminate cell membrane binding events, failure to achieve total blocking of dextran attachment to sham controls was inevitable as shown in Figure 3.13. The FI geometric mean (of the gated FITC+ cells) was determined in order to ignore bias due to the logarithmic range. Mean values corresponded to a collection of three-replicates per treatment for one independently conducted experiment. Shock wave samples were treated to the optimal shock wave dose and displayed a positive shift in their fluorescence relative to the sham treated samples implying internal dextran accumulation into the cells, as opposed to dextran attachment which is loosely bound to cells (given its extracellular placement) and thus produce reduced fluorescence intensity. After sham-correction the true proportion of shock wave mediated FITC-D+ cells was 12.5, 6.7 and 42.9 % at 5, 30 and 80 μg FITC-dextran, respectively. Thus we show, similarly to the cell density (whereby the level of cytotoxicity depended on the cell concentration), that the number of molecule uptake events was significantly dependent on molecule availability.

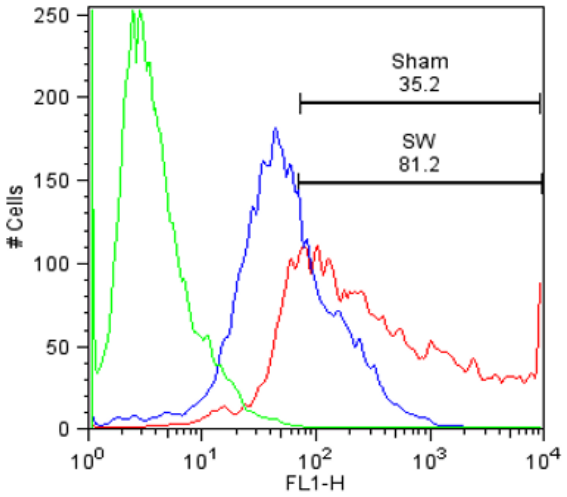
a)



b)



c)



d)

FITC-D/SW	Mean FITC+ (%)	FI Geometric Mean
5 μg/ +	20.5 ± 2.5	223 ± 27.4
5 μg/ -	8.04 ± 1.2	138 ± 0.6
30 μg/ +	42.5 ± 4.6	348 ± 35.7
30 μg/ -	35.8 ± 3.7	168 ± 5.3
180 μg/ +	78.1 ± 2.2	466 ± 13.5
180 μg/ -	35.2 ± 3.7	157 ± 5.1

Figure 3.13: FITC fluorescence-based analysis of FITC-dextran delivery to sham (blue histograms) and optimal shock wave (SW) treated (red histograms) cells, at three different dextran concentrations: (a) 5 μg, (b) 30 μg (c) 180 μg. The green histograms represent the negative control sample (non-labelled and untreated) in order to resolve the background fluorescence. Gated values correspond to the percentage of cells with fluorescence intensity above that of the background. (d) Summary of the results based on n = 3.

3.3.8 GFP mRNA transfection

Experiments were performed to investigate if cells embedded in TMM could produce transgene from nucleotide delivered through a channel compartment within the phantom. Cells were transfected with eGFP mRNA in the absence and presence of the optimal shock waves and incubated for periods of 24 and 48 hours. For fluorescence reading, the 40 x 10 x 5 mm mylar window was discretised into 1 x 1 x 5 mm volumes and fluorescence values recorded for each. Due to cell growth and/or migration, the calculated mean FIs included the channel regions as well. Figure 3.14(a) reports the levels of GFP expression

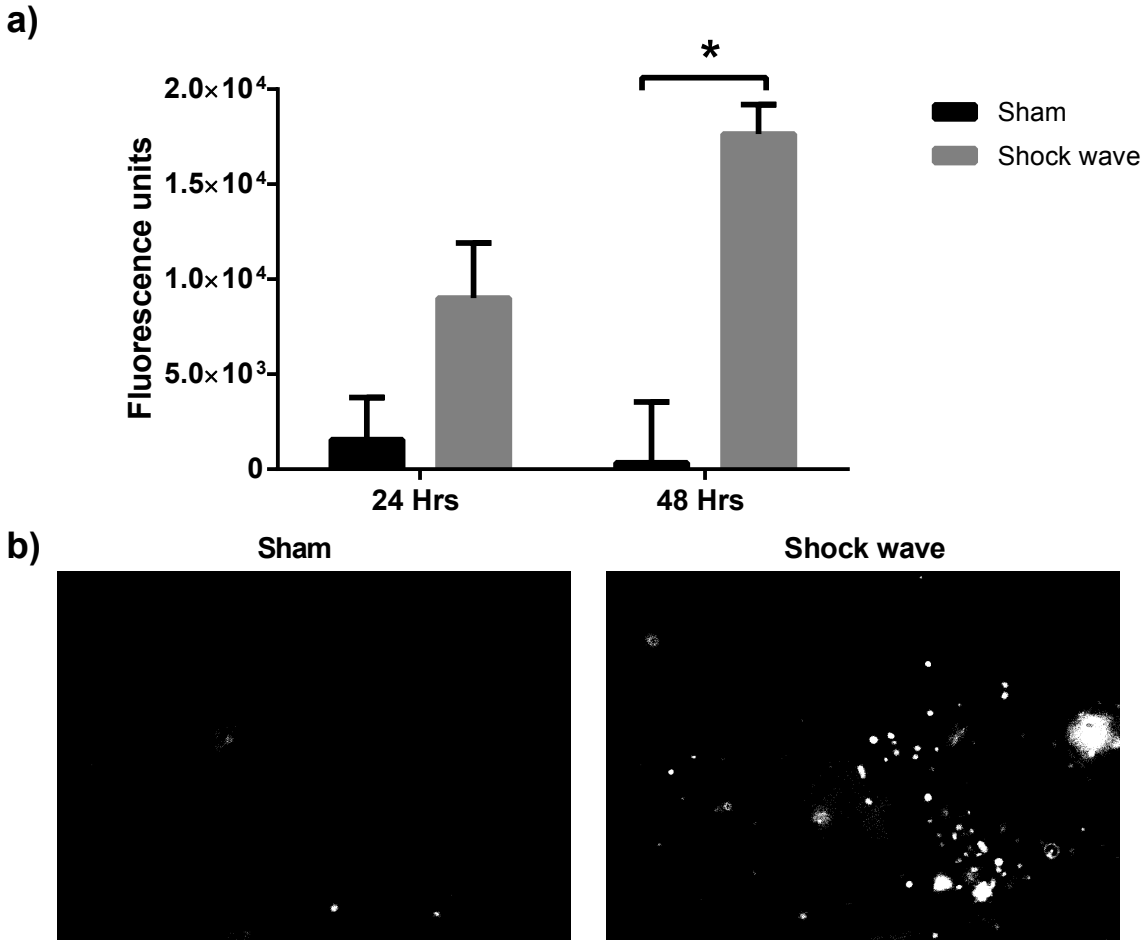


Figure 3.14: Results of eGFP mRNA delivery to CT26 cells for shock wave and sham treated samples. a) Data is expressed as the means of intensities of six replicates per treatment across two independently conducted experiments. The error bars are the standard deviations. Significance was tested using the two-tailed unpaired parametric t-test where * = $p < 0.05$ ($p = 0.04$). b) Representative images of GFP expression at 48 hours after sham or shock wave treatment. Images were converted to binary by thresholding.

at the two time points for sham and shock wave treated cells. The fluorescence of no-treatment samples comprising just cells was subtracted from the recorded GFP FIs of the shock wave and sham treated samples. For a given independently conducted experiment, the FI variance between replicates was generally higher at 24 hours than at 48 hours, which was thought to be due to time differences in the onset of protein synthesis. Low numbers of successfully transferred nucleic acids have been previously attributed to the often observed stochasticity in gene expression [246].

At 24 hours after shock wave exposure or sham treatment, the GFP FI of shock wave treated cells, compared to sham was substantially $\sim$ 6-fold higher. When cells were incubated for a further 24 hours, a $\sim$ 52-fold increase ($p < 0.05$) in FI was evident for the shock wave treated cells. FI levels could not be correlated with the number of GFP-positive cells, due to the multiplanar presence of cells in deep tissue phantom samples as well as the GFP spatial heterogeneity observed microscopically (*see* Figure 3.14(b)). The images represent 835.2 $\times$ 624 μm areas (0.6 μm/px @ 1392 $\times$ 1040), depicting intensely green fluorescent cells when exposed to the optimum shock waves. In contrast, little GFP signal could be detected microscopically in the sham samples. RNA transfection promotes transient gene expression, hence, strongly expressing cells are desirable to produce sufficient therapeutic benefit.

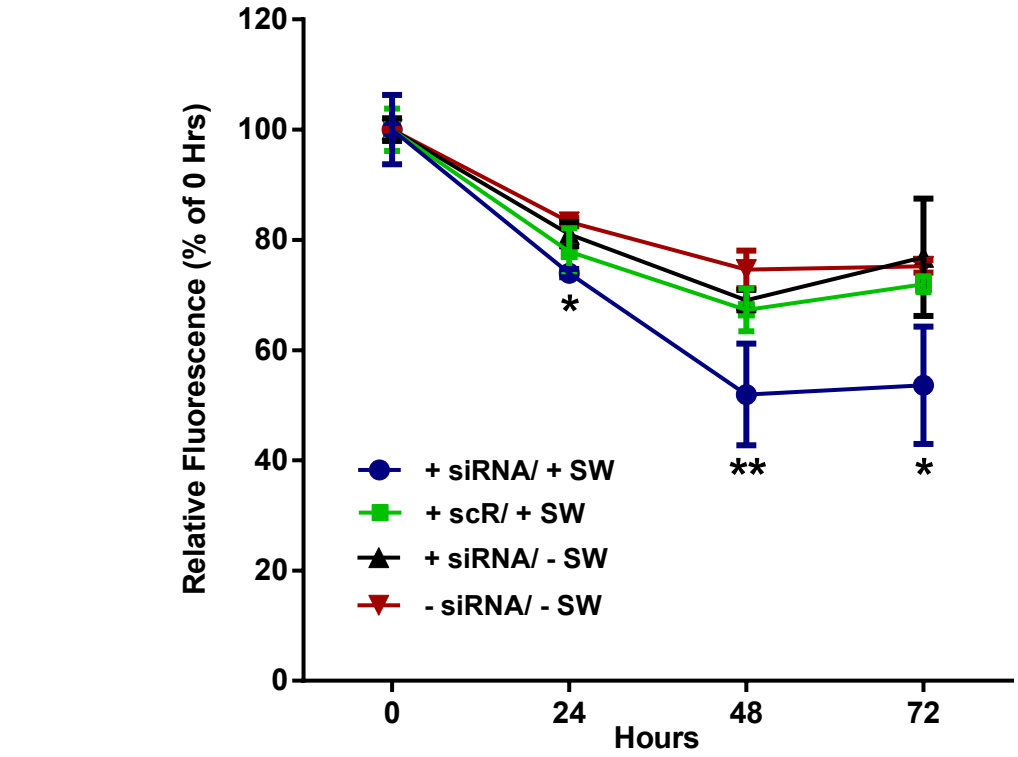
3.3.9 GFP siRNA transfection

In addition to providing production of therapeutic protein, the tissue mimicking phantom developed here was used to test if the delivery of siRNA could be achieved to provide knock-down of a GFP reporter gene. An initial assessment was performed on fluorescence quantification for four MCF-7/GFP concentrations over a 4 log range, and a linear relationship was found between FI and cell concentration indicating the ability of the quantification method to detect small changes in the number of fluorescent cells (*data not shown*).

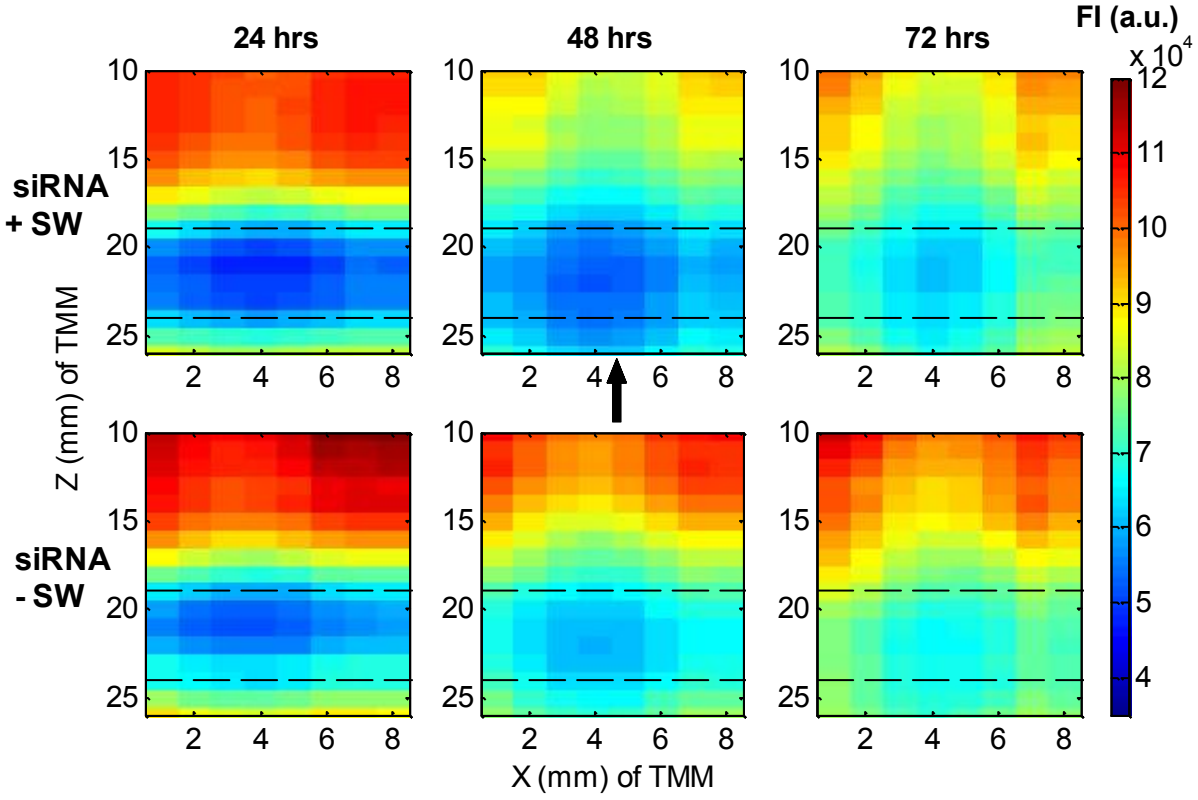
Results of shock wave mediated GFP knock-down are shown in Figure 3.15(A). For siRNA delivery, the optimal shock waves for MCF-7/GFP cells were 134 SWs, energy level 5, 2 Hz (*recall section 3.3.5*). Three forms of negative control were tested: 1) gene knock-down specificity (using scrambled siRNA (denoted by scR) whose sequence

is intentionally non-complementary to that of the mRNA encoding GFP), 2) sham treatment and 3) no treatment (absence of both GFP siRNA and shock wave exposure). An additional no-treatment control based on non-GFP MCF-7 cells was tested to distinguish between GFP and autofluorescence detection. For all samples, the region of analysis was restricted to the agarose area 5 mm above the channel, in which a differential effect between treatments was shown.

Comparisons of relative fluorescence between treatment groups using one-way ANOVA, revealed statistical significance at all three time points ($p < 0.05$). The maximum depletion of GFP signal occurred at 48 hours in cells exposed to siRNA and shock waves. This result was 17% higher than sham controls. The largest difference in GFP fluorescence ($\sim$23%) between sham and siRNA + shock waves was recorded at 72 hours. Figure 3.15(B) compares the spatial fluorescence across the TMM phantom between siRNA/+ SW and sham siRNA. The dashed lines demarcate the siRNA-incorporated channel while the black arrow represents the direction of SW propagation. GFP reduction was also observed in all three negative controls with a peak loss of $\sim$5% relative to sham, occurring in the scrambled siRNA + shock waves samples, implying a small percentage of shock wave induced cell death at 72 hours. The FI decrease over time was generally invariable between negative controls, suggesting a degree of cytotoxicity affected MCF-7 cells grown in the TMM *in vitro* system for over 24 hours. Furthermore, at 72 hours an increase in fluorescence in all groups, but particularly in the nucleotide containing treatments was observed. Two possible reasons for the slight fluorescence recovery are: 1) non-GFP MCF-7 cells revealed an upward trend in cellular fluorescence with increasing time, to a maximum of 12% relative to the initial (background) fluorescence read at zero hours (*see Appendix A1*). Such autofluorescence, which is indicative of cell necrosis and increases with decreasing metabolic activity, may have explained the upturn of fluorescence at 72 hours. 2) Cell proliferation up to 72 hours was likely to have produced the increased GFP signal due to an increase in the number of cells. In the case of the siRNA + SW treatment, the net increase in fluorescence was due to a concurrent loss of siRNA function due to its degradation (of which 72 hours defines a time well beyond its onset, considering siRNA's half-life of 24 hours [247]).



(a)



(b)

Figure 3.15: Results of anti-eGFP siRNA delivery to MCF-7/GFP cells. a) GFP intensities of shock wave treated (+ SW) and non-treated (- SW) samples consisting of three replicates per treatment for one independently conducted experiment. Error bars are the standard deviations. b) Representative spatial fluorescence intensities across the tissue phantom region of interest for SW and sham siRNA treatments.

Using the Tukey Range test, post-hoc pairwise comparisons did not prove statistical significance for scrambled siRNA or no-treatment samples, compared to sham siRNA, at any analysed time point. However, significant difference was detected between siRNA + shock waves and sham siRNA [q = 7.08 >q(crit = 6.35), q = 17.12 >q(crit = 13.67), q = 23.2 >q(crit = 19.8) at 24, 48 and 72 hours respectively] as denoted by the single asterisk in Figure 3.15(B). At 48 hours, significance was also found between the two shock waves (+ SW) groups (denoted by the double asterisk), signifying treatment specificity as well as enabling separation of the proportion of siRNA silenced GFP cells, from those collaterally silenced due to shock wave induced damage.

Finally, it should be noted that the spatial fluorescence distribution observed in the sham siRNA samples over time (3.15(B); siRNA -SW) consistently had a relatively low fluorescence region in the middle of the phantom and higher fluorescence on the sides. It was inferred that cell death would be greater in the inner embedded cells due to a greater likelihood of inadequate gas exchange.

3.4 Discussion

Externally applied acoustic stimuli offer an increasingly popular approach to tackling the challenge of gene delivery [248]. Shock wave exposure may be particularly attractive in certain situations because it is comparatively low cost, clinically available and has a safety track-record through lithotripsy. The presented studies showed that cancer cell lines exposed *in vitro* to lithotripter shock waves, using clinically available parameter settings, resulted in differential cell viability and reversible membrane permeabilisation. In the mouse colorectal carcinoma cell line, there was a progressive decrease in viability and increase in permeabilisation with increasing number of shock waves, which became more linear with increasing SW energy (Figure 3.7). The pulse repetition frequency did not have an effect on the cell viabilities, which was in accordance with an ultrasound induced gene delivery study by Rahim et al.[249]. In fact, Huber et al.[175] found that varying the SW PRF from 0.5 to 5 Hz did not affect the size or lifespan of cavitation bubbles which are typically held responsible for cellular bioeffects.

In the human breast cancer cells, comparably more irreversible permeabilisation was noted as demonstrated by the poor recovery of viability at 24 hours (Figure 3.10(b)). A study by Guck et al.[250] on the elasticity of MCF-7 cells, based on an optical stretching technique, revealed an approximate 10% increase in peak deformability compared to other malignant cells. We speculate that the lower elasticity of MCF-7 cells resulted in greater deformation when subjected to shock waves hence producing greater damage and irreversible permeabilisation. On the other hand, cell viability data of the transformed non-cancerous human kidney cells, demonstrated a sensitivity to shock waves comparable to CT26 cells. Brummer et al.[230] made a similar conclusion regarding malignant and normal cells as they found no significant difference in their median lethal dose (LD50) values. While HK-2 manifests both normal and cancerous cell characteristics, these non-malignant cells further agreed with the non-distinguishing dose effect of normal cells observed in [230] because uniquely high cell permeabilisation levels could not be established.

Shock wave parametric studies were conducted to determine the settings that maximised cell permeabilisation with no effect on the viability. The optimal number of pulses for MCF-7 cells was four times less than the number required for CT26 cells, whereas the similarity in optimal shock wave energy (5.0 E for MCF-7 versus 4.5 E for CT26) indicated the presence of an energy threshold below which reversible permeabilisation is negligible.

Sonoporation is a process of temporary benefit, as the cell membrane naturally reforms afterwards if the cell remains viable. The time taken for such repair has not been defined for most cell lines and there is little data concerning the differences between cancer cell lines and primary cells. The ability of transiently damaged cells to permit PI entry was characterised as a measure of permeabilisation. Given that PI detection is based on its intercalation with cellular DNA, PI is a late marker in the context of plasma membrane permeability, and excludes the population of cells whose nuclear membrane is intact but whose plasma membrane is compromised. It follows that our reversible plasma membrane permeabilisation result of 20.5% and 4.1% for CT26 and MCF-7 cells respectively is an underestimation of the proportion of

potentially RNA transfectable cells, as these only require perturbation of the plasma membrane. Comparable results to CT26 transfectability have been obtained using therapeutic ultrasound (centre frequencies of 1 – 5 MHz) and variable intensity levels, where 28% [251] and 32% [240] DNA transfected or transfectable cells respectively have been reported per total number of exposed cells. However, the latter was attained in the presence of ultrasound contrast agents to function as nuclei for cavitation. Our shock wave mediated transfection required no nucleation agents.

RNA degradation induced by shock waves, was another critical factor to consider in SW parameter optimisation. The existing literature regarding the effects of shock waves on nucleic acids, concerned endogenous DNA [252]. Using comet assay measurements, the study in [252] reported no strand breaks in the DNA of Chinese hamster ovary cells, for exposures up to 2000 SWs. However, the negative result on DNA integrity was accompanied by substantial cell lysis, implying that there is no correlation between cell death and endogenous DNA damage. Thus, despite evidence on some structural instability of our exogenous mRNA by 22% post shock waves, relative to shams, no additional damage to nucleic acids as per cellular DNA was expected.

Experiments were designed by considering a number of aspects that would affect shock wave propagation to the cells and gene delivery efficiency. The shock wave-induced cell streaming in fluid at low cell concentrations and subsequent reduced bioeffects inspired the development of tissue phantoms (Figure 3.1(b)) which permitted the analysis of immobilised cells without needing to rescue and process them. Firstly, cells embedded in agarose allowed shock wave forces to act directly on the cells, thus more likely reflecting the transfection levels that may be observed in tissue, than experiments using isolated cells in solution. Agarose at a final concentration of 1% wt/vol was chosen because it has been shown to mimic the mechanic and acoustic properties of tissue, and even though usually in composite it is agarose that bestows the desired elastic properties [253]. Secondly, preliminary transfection tests revealed that the cell or nucleotide concentrations were not necessarily as important as the cell-to-RNA ratio. A supporting study by Bao et al., [209] scaled up *in vitro* mRNA dose for *in vivo* use and obtained lower transfection efficiencies *in vivo* than they had *in vitro* probably because the assumed

cell-to-mRNA ratio may not have applied to both conditions. In the studies reported here, the lowest nucleotide concentrations which produced a measurable and distinguishable transfection effect between treatments, were employed. At an equivalent dose (i.e. 5 μg), RNA-like penetration in 1% agarose with optimal shock waves resulted in a maximum distance travelled of approximately 10 mm above the channel, while greater depths were attained with increasing availability of the macromolecule (Figure 3.12). However, the direct translatability of this FITC-dextran study was limited by the fact FITC-dextran can produce signal regardless of its uptake and internal processing, steps which GFP mRNA need to achieve before fluorescent signal can be obtained. In the time period required for mRNA to translate into protein, the porosity of agarose gels would have resulted in extensive diffusions of the delivered molecule. Moreover, the variability on the onset of protein synthesis across cells would have also concealed the full effect of shock waves on the transport of nucleotides.

In this work *in vitro* transfections were performed in a new tissue mimicking model, i.e. not suspended in cell culture or growth medium, and having compartmentalised RNA and cells in an effort to simulate nucleic acid administration via the bloodstream. As a result, the efficiency of gene delivery could not be assessed in a single cell fashion and thus the number of transfected cells is not given. Even so, this exposure system allowed the reporting of considerable enhancement of gene delivery and gene knock-down with optimal lithotripter shock wave treatment, compared to sham treatment. In comparison with similarly low administered nucleotide (plasmid DNA) concentrations (1 – 5 μg in 10^6 cells), Huber et al.[23] reported just 800 cells out of one million cells were successfully transfected while Murata et al.[225] showed less than a two-fold increase in luciferase expression with shock wave application, relative to the control. In this first demonstration, to our knowledge, of shock wave assisted mRNA delivery, over 50-fold increases in GFP expression were attained. Furthermore, siRNA transfection was enhanced with optimal shock wave exposure despite being challenged by the MCF-7 cell line's relatively low amenability to delivery; with a two-fold increase in knock-down relative to sham siRNA at 72 hours being demonstrated. Similarly, Ha et al.[227] transfected CT26 cells with anti-GAPDH siRNA through low energy shock wave exposure, and found a ∼three-fold

decrease in the relative GAPDH expression when compared to controls in an *in vitro* set-up comprising a shock wave probe immersed in cell suspensions. However such configuration highly contrasts *in vivo* conditions, as there is no representation of sound attenuation due to propagation through the body. In separate studies, in the presence of microbubble contrast agents and unfocused ultrasound in lieu of shock waves, Juffermans et al.[254] demonstrated approximately a four-fold decrease in GAPDH expression.

3.5 Closing Remarks

In conclusion it has been demonstrated that shock wave exposure can successfully induce RNA transfer into cells without imparting substantial cellular or nucleic acid damage, and that this may be possible in a broad range of tissue types by tuning the shock wave exposure parameters. Notably, the delivery achieved in these studies, were accomplished using a clinical electromagnetic lithotripter which provides a pathway for clinical translation. Variability in the optimum parameters is expected where different types of lithotripters (e.g. piezoelectric, electrohydraulic) are utilised, having a dissimilar focal volume and shock waveform from the one shown in this chapter.

4

Delivery Kinetics and Predictability of Shock Wave induced Transfection

Contents

4.1 Opening Remarks 77
4.2 Preliminary study on shock wave device equivalence 78
4.2.1 Set-up of shock wave sources 78
4.2.2 Determination of the critical shock wave compressional features 79
4.2.3 Optimal shock waves for Storz Minilith 82
4.3 Materials & Methods 83
4.3.1 Design of experiment 83
4.3.2 Configuration and preparation of samples 84
4.3.3 Initial mRNA measurements 85
4.3.4 RNA quantification & calibration 86
4.3.5 GFP quantification & calibration 88
4.3.6 Flow cytometry 89
4.4 Results 90
4.4.1 Shock wave mediated kinetics of mRNA uptake by mass and number of positive cells 90
4.4.2 Shock wave mediated kinetics of GFP translation by mass and number of positive cells 95
4.5 Discussion 99
4.6 Closing Remarks 102

4.1 Opening Remarks

As opposed to DNA, mRNA transfection provides a more transient effect as mRNA suffers from more rapid degradation and removal than plasmid constructs. Also, mRNA does not permanently integrate into the genome. The shorter time scales of expression and the relatively fast translation of protein in mRNA transfection, imply that insight into the kinetics of expression is crucial for detection timing. Particularly in the evaluation of newer delivery methods, it is beneficial that the reported level of expression is the peak value (at least approximately), with respect to time. Furthermore, the utility of kinetics is in the growing field of programmable RNA devices, for controlled RNAi and direct logic evaluation of the molecular environment which could be useful in making decisions about disease-related conditions [255]. Moreover, by determining the duration of expression, the course of treatments *in vivo* can be adequately scheduled.

Chapter 2 (section 2.4.2) alluded to a number of ways in which transfection efficiency can be described. Cell sample configuration often restricts the choice of descriptor. Apart from quantifying the functional outcome of the transgene, which is commonly conveyed in folds increase or decrease relative to the untreated samples, other transfection descriptors are:- 1) the number of mRNA internalised cells, 2) the total internalised mRNA dose, 3) the number of transgene expressing cells and 4) the amount of transgene (protein) produced. Thus, the work presented in this chapter aims to coordinate number (of cells) to mass (of mRNA or protein) providing a link between effective mRNA dose and proportion of gene expressing cells, due to shock wave intervention.

The uptake kinetics of mRNA during SW exposure were also sought, as a gap in the knowledge was identified on the shock wave induced gene delivery profile (as discussed in section 1.1). For instance, a number of questions remain unanswered such as: for a viable SW dose 1) does intracellular transport increase linearly? 2) is there mRNA exportation? and 3) as the number of shocks increase is there a tendency to increase either the number of transfected cells or the internalised dose per cell, or both? To address these questions, the optimal SW conditions established in Chapter 3 which instigated no cytotoxicity, were applied, in combination with an array of techniques to quantify the level of delivery.

4.2 Preliminary study on shock wave device equivalence

To detract from the possibility of device-specific effects, and ensure successful translation to other types of shock wave devices, optimal SW equivalence was determined by analysing shock waveform features that could be accurately measured and equalised between devices, to study their influence on cell transfectability. This was achieved by comparing results of transfectability for the clinical electromagnetic ESWL source employed in Chapter 3 and a piezoelectric ESWT source. Lastly, SW equivalence was sought for optimal exposure with a non-clinical ESWT device (Storz Minilith SL1), which was adopted hereafter.

4.2.1 Set-up of shock wave sources

The piezoelectric SW source was the Swiss Piezoclast (Electro Medical Systems). The device consisted of a handpiece (containing the piezoelectric elements) connected to a power unit that supplied the voltage for SW generation, and a foot pedal used to trigger the shock waves. The head of the handpiece was a gel pad that was filled with ultrasound transmission gel. From a selection of gel pad sizes, the flattest gel pad was selected in order to increase the distance between the face of the pad and the focus, enabling sufficient space for positioning of the cells at the focus.

The experimental rig was identical to that produced in Chapter 3 (Figure 3.1(a)) in order to maintain the same experimental conditions through which existing transfectability data was obtained using the clinical source, herein denoted by EM-Litho. The piezoelectric device, henceforth denoted by PE-ESWT, was mounted vertically beneath the tank, with the transducer face coupled to the LDPE membrane of the tank's bottom face, using ultrasound transmission gel.

The Storz Minilith SL1 (Storz Medical) henceforth denoted by EM-Minilith, is an electromagnetic SW source focused by a paraboloidal reflector at an aperture angle of 84°, and with a nominal focus size of 2.4 × 25 mm (D × L). Due to the limited range of rotation of the EM-Minilith therapy head, the same water tank was modified with a side LDPE window for entry of the shock waves because the source permitted horizontal alignment. The cell samples were therefore also horizontally supported for consistency,

although gravity was expected to be different as the suspended cells would have been drawn to the side of the vial, whereas in the EM-Litho and PE-ESWT experiments the cells would have been drawn to the bottom of the vial. However, such was assumed to have a negligible effect on cell transfectability due to the long focal zones of the devices.

CT26 cell samples were prepared identically to the description in Section 3.2.5. The centre of the vial was aligned to the SW focus by assuming the position where the highest voltage measured by the Müller-Platte PVDF needle hydrophone was recorded. The hydrophone was fixed to a holder which was connected to manual three-axis linear stages for three dimensional translation.

4.2.2 Determination of the critical shock wave compressional features

Firstly, the PE-ESWT device was characterised in degassed pure water by taking three focal voltage measurements per shock wave at all the available energy levels. Four features describing the compressive phase of shocks were then computed as follows [256]:

- **Peak Compressional Pressure ($\boldsymbol{P^+}$)** is the maximum positive pressure at any location in the pressure field.

- **Derived Pulse-intensity Integral ($\boldsymbol{PII}$)** is defined as "the time integral of the instantenous intensity at a particular point in a pressure pulse field over the pressure pulse waveform" [256]. The integration limits are the positive temporal (TP) duration – beginning at the positive pressure which first exceeds 10% of the P^+ and ending with the first time the positive pressure reduces below 10% of the P^+.

$$PII(r,\theta) = \frac{1}{Z}\int_{TP} p^2(r,\theta,t)dt \tag{4.1}$$

  where p is the instantaneous acoustic pressure, (r,θ) represents the spatial location where the acoustic pressure is recorded, t is time and Z is the acoustic impedance of water.

- **Rise Time ($\boldsymbol{t_R}$)** is the time taken for the acoustic pressure to increase from 10% to 90% of the peak positive pressure.

- **Compressional Pulse Duration (t_{FWHMp+})** is the time interval between the first time the positive pressure exceeds 50% of its maximum value, up to the next time the positive pressure returns to that value.

Having previously characterised the EM-Litho shock waves in water, the above features were likewise computed. By comparison, it was found that between the two devices only the peak compressional pressure and the pulse-intensity integral could be matched with at most a 10% difference, as shown in Figure 4.1(a). The matched waveforms in terms of these two properties are displayed in Figure 4.1(b & c).

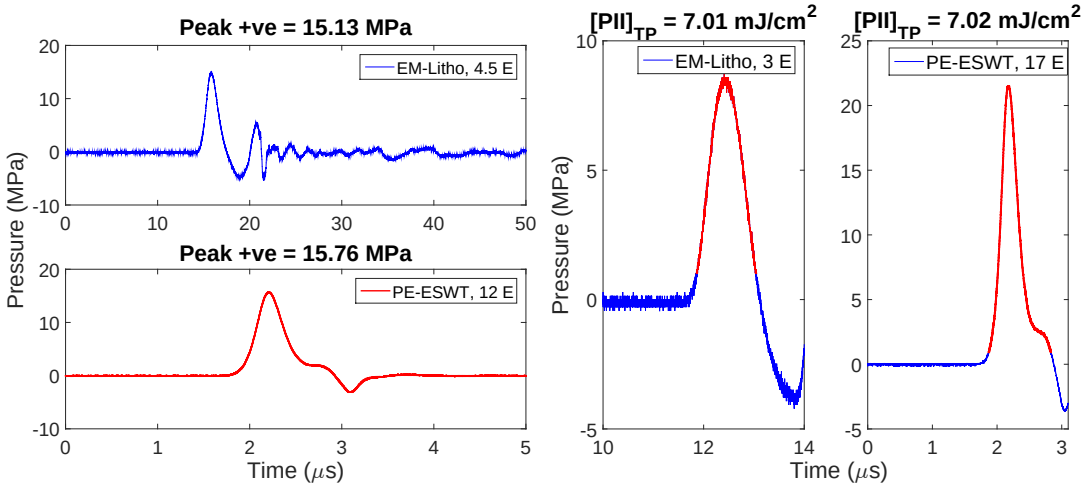
At the corresponding energy settings, experiments on the transfectability of cells were performed and assayed by MTS and PI inclusion as previously described. The results are presented in 4.1(d). Note that for the EM-Litho the *minimum* t_R, produced at the highest energy setting (level 9) was 0.57 μs, whereas for the PE-ESWT the *maximum* t_R value was 0.28 μs (at energy level 1). Further disparity was in the t_{FWHMp+} as the EM-Litho *minimum* was 0.88 and the PE-ESWT *maximum* was 0.45 μs.

Maintenance of the peak compressional pressure yielded a 12.45% difference in the amount of permeabilised live cells between devices, which was found to be statistically significant at the $p < 0.05$ level. On the other hand, when the derived pulse-intensity integral was matched, the difference in transfectability was only 2.33% which was not statistically significant, and likely to result from the smaller PE-ESWT focal zone (maximum nomimal size = 2.8 × 14.1 mm (D × L) [257]). In agreement, Kodama et al., [258] investigated the influence of shock waveform features on FITC-dextran uptake into cells, and concluded that the pressure integrated over the positive half-cycle was the driving parameter rather than the peak positive or negative pressures. Thus, these data suggested that for optimal SW exposure using another device, it would be necessary to determine the SW energy setting that generates a PII_{TP} in the region of 15.65 mJ/cm^2.

The limitations of this short study were that we could not assess the SW tensile characteristics because of the hydrophone's relatively poor tensile measurement reliability as indicated in Chapter 3. However, the potential insignificance of additionally correlating the negative phase characteristics to the transfectability of cells, may be justified by the observations made by Bailey et al.[259] whereby the spatial constraints available *in*

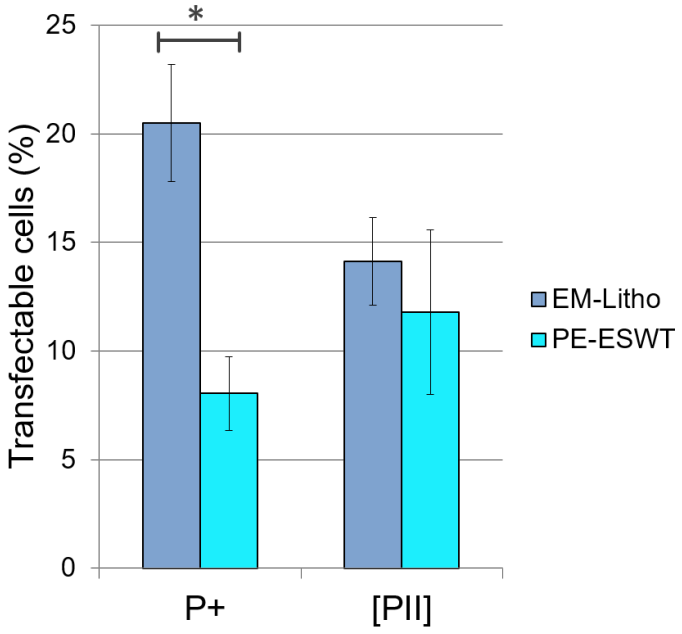
Test	SW source	Energy level	P^+ (MPa)	$[PII]_{TP}$ (mJ/cm^2)	t_R (μs)	t_{FWHMp+} (μs)
P^+ (548 sw, 2-Hz)	EM-Litho	4.5 E	15.13	15.65	0.90	1.39
	PE-ESWT	12 E	15.76	4.22	0.23	0.33
PII (500 sw, 2-Hz)	EM-Litho	3 E	8.73	7.01	1.10	1.97
	PE-ESWT	17 E	21.51	7.02	0.20	0.29

(a)



(b)

(c)



(d)

Figure 4.1: Investigation of critical shock waveform characteristics by comparing the CT26 *transfectability* of piezoelectric (PE-ESWT) and electromagnetic (EM-Litho) shock wave sources. (a) Characterisation summary of the shock waveforms' positive phase characteristics; (b) matching the peak compressional pressure, (c) matching the derived positive pulse-intensity integral (with positive temporal integration limits as indicated by the red-labelled portions of the waveforms); (d) Respective results of transfectability at n = 9. Error bars are the standard deviations. The asterisk denotes statistical significance at the $p < 0.05$ level.

vivo restrict bubble growth and thus the impact of the negative pressure; showing that in the case of fruit flies, the killing of their larvae by SW exposure to either isolated positive or negative pulses at similar peak pressures, was comparable.

4.2.3 Optimal shock waves for Storz Minilith

Shock waves at all energy levels of the EM-Minilith were characterised in the polypropylene vial described in Chapter 3, and their respective pulse-intensity integrals were calculated. Upon matching (Figure 4.2) we found the nearest PII_{TP} of the EM-Minilith to be 5.12 mJ/cm^2 relative to the EM-Litho optimum (in vial) PII_{TP} of 5.29 mJ/cm^2. To resolve the small energy density difference, the optimal number of shock waves was adjusted based on the total optimal treatment energy. Thus, the optimal EM-Minilith shock waves hereafter employed were: 3.5 E, 566 SWs, 2 Hz PRF.

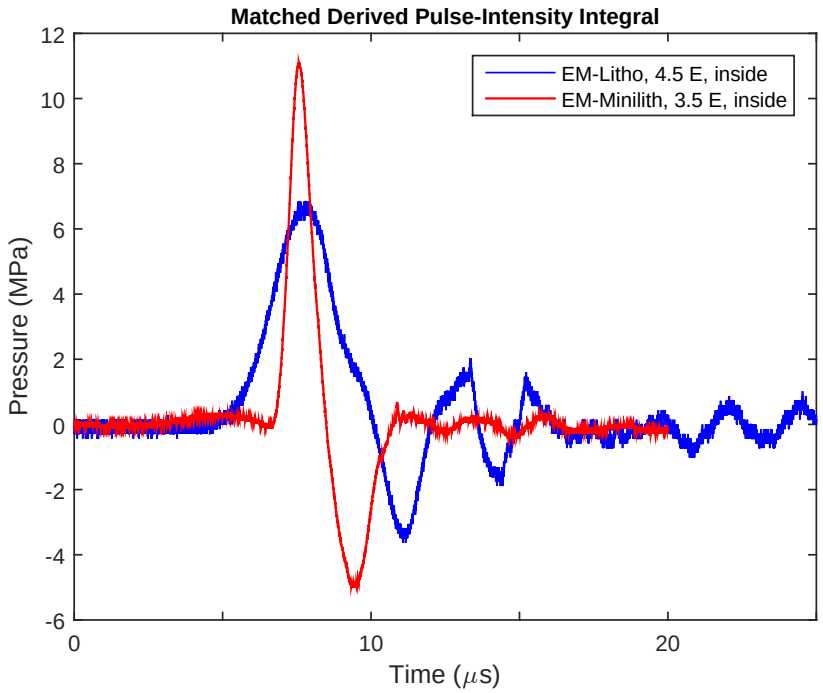


Figure 4.2: Comparison between the previously employed clinical lithotripter (EM-Litho) and the henceforth employed ESWT lithotripter (EM-Minilith), based on matched-PII shock waveforms as recorded *inside the cell containment (PP vial), in water.*

4.3 Materials & Methods

4.3.1 Design of experiment

The kinetics study was discretised into numerous analysis time points before, during and after shock wave exposure (Figure 4.3). Three separate investigations were conducted as outlined in Figure 4.3 to determine: 1) the total internalised mRNA mass, 2) the number of mRNA internalised cells and 3) the total amount of GFP produced and number of GFP expressing cells. Therefore sample sets were prepared for each investigation.

Due to the intended downstream processes for both mRNA and GFP quantitation, cell samples needed to be collected and thus *in situ* analysis was unfeasible. Continuous sample analysis (i.e. whereby an entire time course is analysed through a sample) was also unfeasible because in the mRNA investigations, removing aliquots from samples at intervals during SW exposure would have created intra-sample air spaces, as well as hindered successful cell rescue for downstream RNA extraction because of a low cell count; whereas for the GFP investigation, samples would have been subject to repeated trypsinizations to release cells at each interval. Hence, cell samples *per time point* were prepared for each independently conducted experiment. Samples consisted of 312,500 CT26 cells and 5 μg eGFP mRNA (Trilink Biotechnologies, San Diego, CA, USA) in serum-free RPMI medium, unless otherwise stated.

For the 'internalised mRNA mass' investigation, immediately after each interval (*see Figure 4.3*), the appropriate samples (in triplicates per time point) were transferred to autoclaved eppendorf tubes, microcentrifuged and washed twice with PBS. Cell pellets were then lysed with a 2-mercaptoethanol supplemented lysis buffer, and homogenised by passing the lysate through a 21 gauge needle-syringe 5-10 times. Finally, the lysates were frozen at $-80\,^{\circ}$C until further analysis (section 4.3.4).

For the GFP investigation, various time points between 6 and 120 hours after shock wave exposure were tested. The triplicate samples per 'GFP' time point were prepared in addition to sham controls per independently conducted experiment. All test samples were exposed to the optimum SW treatment, washed once, re-suspended in serum-supplemented medium, transferred into a 48-well plate and incubated up to the appropriate time point.

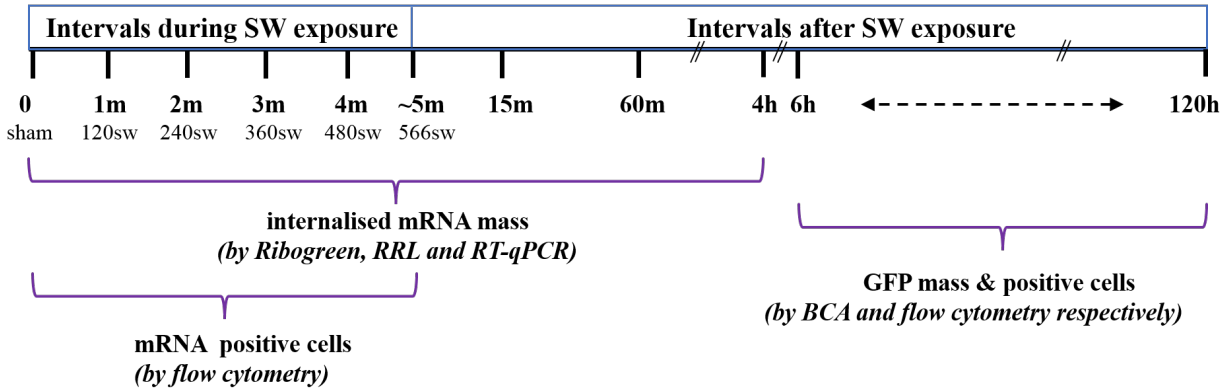


Figure 4.3: Outline of the analysis time course (not drawn to scale) for the three investigations indicated by the curly brackets, alongside the measurement methodologies for each investigation. Samples at each interval during SW exposure were subjected to continually degassing and heated water. Samples at each interval after SW exposure were incubated up to the interval time point.

Finally, for the 'mRNA positive cells' investigation a quintuplicate set of cell samples was prepared per time point, but the 5 μg eGFP mRNA was labelled with cyanine 5 (Cy5). Following SW treatment up to each respective time-point, cells were washed, re-suspended in serum-supplemented medium and assayed by flow cytometry.

For the mRNA investigations it was unnecessary to set up sham controls for each 'mRNA' time point because uptake due to endocytosis is classically immeasurably small. However, for the GFP investigation sham controls for every 'GFP' time point were necessary in order to set the baseline for GFP expression positivity and rule out false positive events. Several negative controls were included in each experiment.

4.3.2 Configuration and preparation of samples

A new TMM (Figure 4.4) was designed to have suitable dimensions with respect to: *1)* the EM-Minilith source aperture, which determines the minimum radius/width for the phantom; *2)* the focal depth (25 mm) to determine the permissible thickness; and *3)* volume minimisation in order to concentrate the cells. This resulted in a 15 × 10 mm (D × L) phantom volume (with approximate capacity of 1.8 mL). Finally, a 2 mm channel across the diameter of the TMM-MINI was incorporated by inserting a 2 mm steel rod through two collinear holes (*see Figure 4.4(right)*) before pouring in the agarose, and allowing it to set before removing the rod. The channel was used as a

blood vessel mimic and thus the cells and mRNA were administered into it, which was surrounded by 1% w/v agarose. Such configuration enabled the cells to be recovered

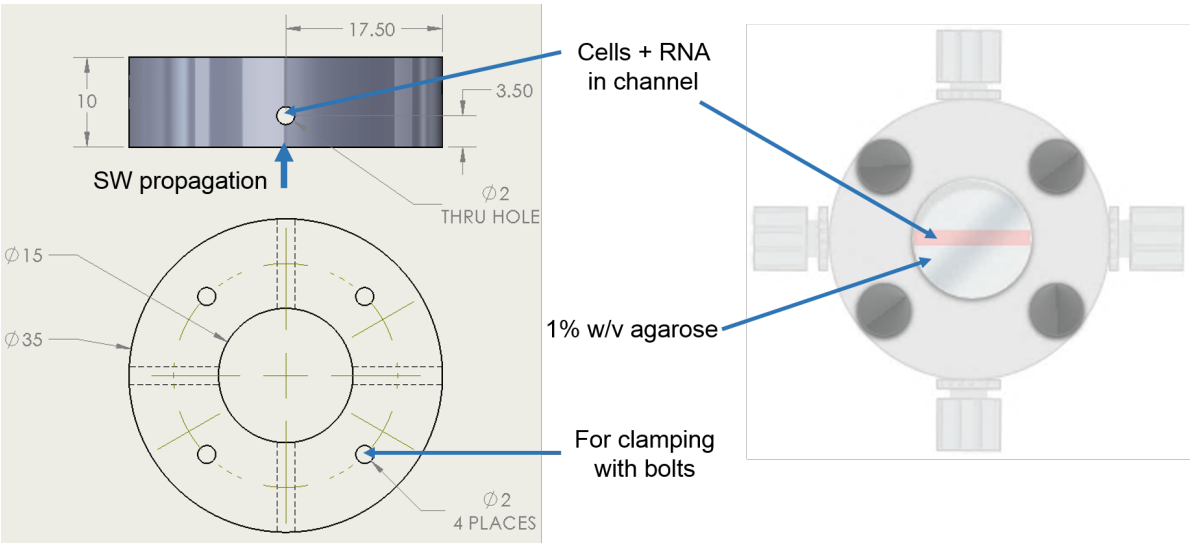


Figure 4.4: Design of the 'TMM-MINI' phantom and format of the cells, RNA and agarose. A clamping plate and mylar sheet on each face of the illustrated phantom body sealed off the phantom. A second channel, 3 mm above the working channel and perpendicular to it, was used for injection of the agarose. Both channels were leak-proofed using barbed Luer fittings. The centre of the channel was aligned to the SW focus.

after SW exposure as they were suspended in the channel, while being treated in a tissue mimicking environment. To ensure bubble-free TMMs, the phantom was stood upright and tilted during agarose injection, permitting any air to escape. A large batch of the TMM was manufactured, and prior to filling, sterilised in RNAseZap solution, rinsed with DEPC-treated water and left to dry while UV-irradiated for 1 hour.

4.3.3 Initial mRNA measurements

Concentration and quality measurements of stock eGFP mRNA for delivery, were carried out using the NanoDrop 1000 spectrophotometer (software 3.8.1). The sample absorption spectrum was read in a 0.1 cm path length, and normalised to a 1 cm path length (l). The molar extinction coefficient (ε) of RNA was taken to be 0.025 (μg/ml)cm^{-1}. Using the Beer-Lambert equation (μg/ml = $A_{260nm}/\varepsilon \times l$) the concentrations were obtained. mRNA purity was determined by the absorbance ratio A_{260}/A_{280} (*see Appendix A.2*).

4.3.4 RNA quantification & calibration

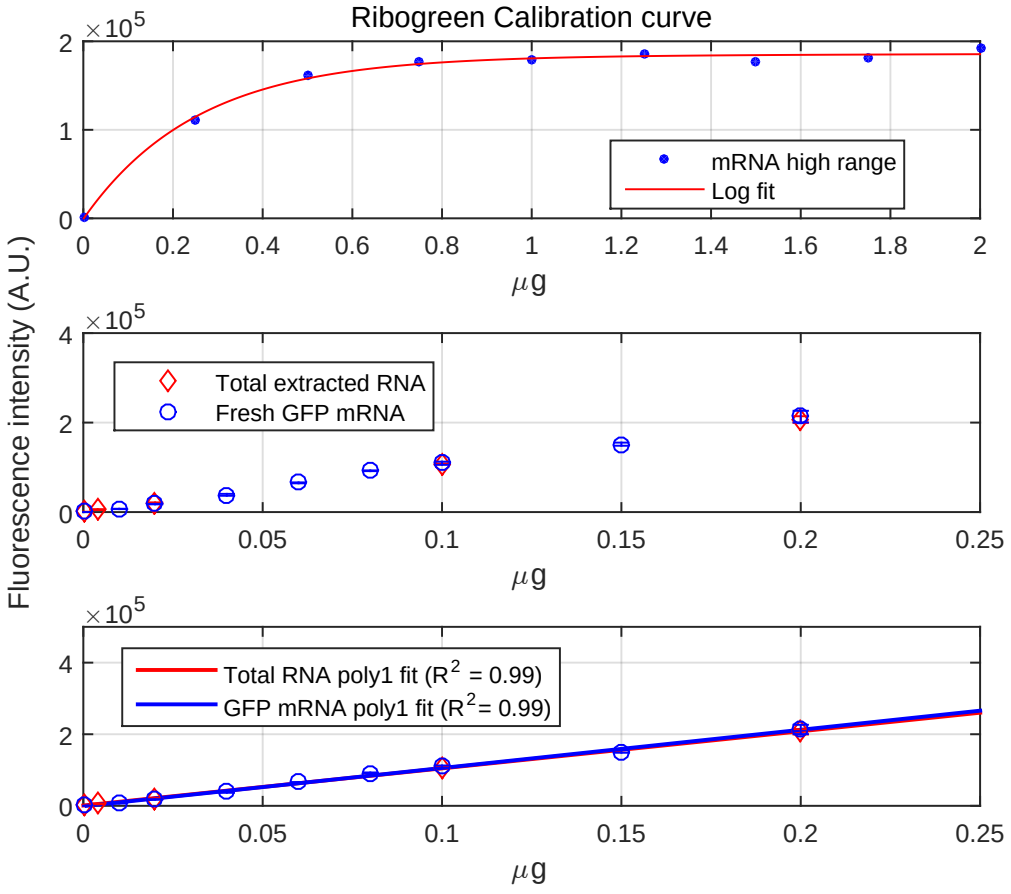
Previously frozen cell lysates were thawed at room temperature and total RNA was extracted using the PureLink RNA Mini Kit (Ambion, Thermo Fisher Scientific). The procedure was conducted following the manufacturer's instructions. Briefly, the lysates were transferred into spin columns which bound the RNA onto their membrane cartridges, and sequentially centrifuged & washed with the provided buffers. Digestion of any DNA content was achieved by on-column DNAse treatment (PureLink DNAse set, Thermo Fisher Scientific) for 15 minutes at room temperature. To confirm that the RNA yield was well below the maximum binding capacity of the spin columns, a preliminary assessment of the RNA yield mass was performed using NanoDrop. Finally, the isolated total RNA was eluted by drying the membrane at 15,000 $\times$ g for two minutes, in 100 μL RNAse-free water to ensure sufficient volume for the succeeding analyses; and was maintained on ice. The following three methods of RNA quantification were immediately performed.

4.3.4.1 Ribogreen

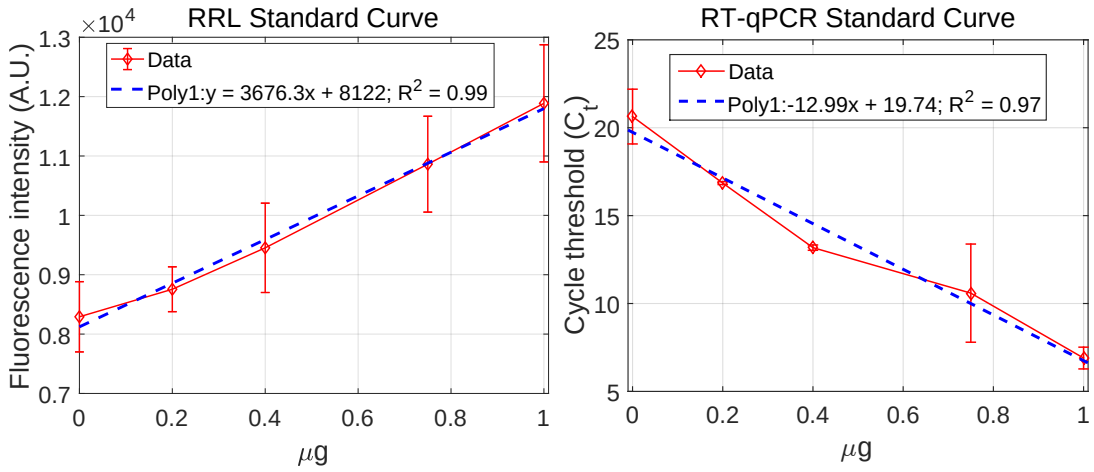
Total RNA measurements were calibrated by preparing standard curves for every independently conducted experiment. Ribogreen (Quant-iT RiboGreen RNA assay kit; Invitrogen, Thermo Fisher Scientific) assays were carried out in black 96 well plates, and sample fluorescence was read at fluorescein wavelengths (excitation: 480 nm; emission: 520 nm). As shown in Figure 4.5(a) the assay's fluorescence linear range and required sample dilution was first determined by running various concentrations of both the total RNA and the stock eGFP mRNA which served in verifying the RNA isolation process.

4.3.4.2 In vitro translation (RRL)

The RRL assay procedure was similar to that previously described. However, the assay volumes were reduced to 50 μL in half-area black well-plates to concentrate the eGFP mRNA within; which produced more detectable differences between the time-point RNA samples. Since the assay provided a direct measurement of eGFP mRNA, the fluorometer gain was fixed across experiments. For calibration, the negative control total RNA samples were spiked with known amounts of eGFP mRNA, and a line fit was plotted as shown in Figure 4.5(b).



(a)



(b) (c)

Figure 4.5: Calibrations and linear range determination for eGFP mRNA quantitation through (a) Ribogreeen, (b) Rabbit Reticulocyte Lysate in vitro translation and (c) RT-qPCR. All three standard curves are representative of at least two separate day experiments (each at n=3). Error bars are the standard deviations.

4.3.4.3 Reverse transcriptase real-time quantitative polymerase chain reaction (RT-qPCR)

GFP specific primer pairs were designed using the GFP open reading frame sequence, and selection was assisted through the open-source NCBI Primer Blast tool [260]. The design criteria consisted of an amplicon length of 90-300 base pairs with preference for mid-range, the least possible intra- and inter-primer homology, similar annealing temperatures, and approximately equal GC content. The final primer sequences were: forward– GCACCATCTTCTTCAAGGAC; reverse– GGTGTTCTGCTGGTAGTGGT. It was preferred to perform reverse transcription and PCR in one step to minimise possible inaccuracies stemming from multiple pipetting steps. Given that complementary DNA (cDNA) synthesis would be gene-specific, PCR amplicons were detected by a non-specific fluorescent probe – the SYBR Green dye. The reactions were set up using the SuperScript III Platinum SYBR Green One-Step qRT-PCR kit (Invitrogen, Thermo Fisher Scientific) in accordance with the recommended protocol. Negative controls and water blanks were prepared alongside the experimental samples. The Applied Biosystems StepOnePlus Realtime PCR System (with StepOne software v2.3) was utilised to run the RT-qPCR reactions (*see Appendix A.3 for the cycling programme*). Standard curve samples were prepared for every independently conducted experiment and consisted of negative controls spiked with known amounts of eGFP mRNA, prior to total RNA isolation (Figure 4.5(c)).

4.3.5 GFP quantification & calibration

At each 'GFP' expression time-point, assigned samples were removed from incubation, and cells were released from the well bottom by brief trypsinization. Samples were then suspended in 500 μL serum-free medium. 400 μL of the suspension was allocated to flow cytometry and the remaining 100 μL for the BCA assay.

4.3.5.1 Bicinchoninic acid (BCA) method

The amount of translated GFP was quantified through the absorbance-based BCA protein assay (Sigma Aldrich) because the alternative GFP quantification method – fluorometry – is affected by high background fluorescence which could result in no GFP detection at the earlier time points (e.g. 6-18 hours after SW exposure). Calibration

was performed using recombinant GFP (Pierce^{TM}, Thermo Fisher Scientific) as shown in Figure 4.6. One fifth of cell samples, were pelleted and lysed using a 1X lysis buffer

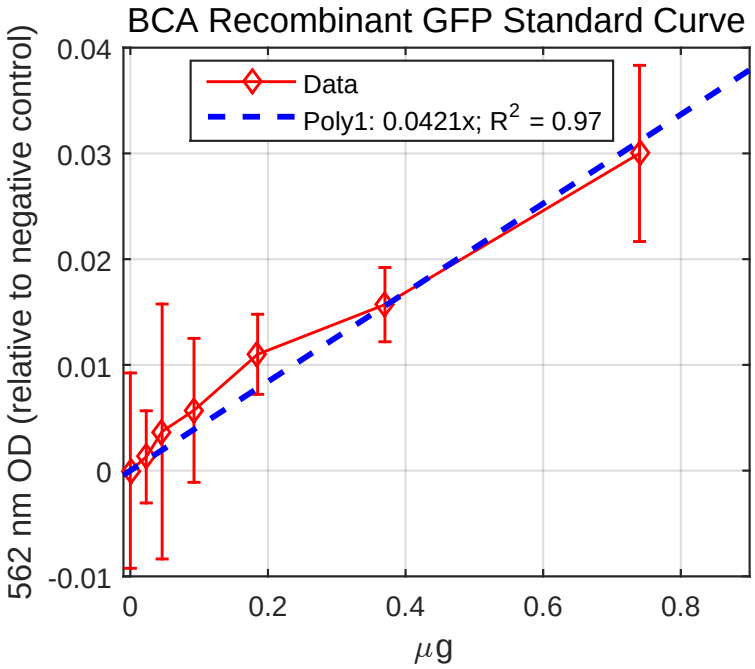


Figure 4.6: BCA standard curve using recombinant GFP and curve fit. Error bars are the standard deviations based on n=3.

(diluting Reporter 5X Lysis Buffer, Promega), following the product's protocol. On a 96 well plate, the cell lysates were then mixed with the BCA working reagent, sealed with a film, incubated for 30 minutes and the absorbance was read at 562 nm. GFP yield was calculated by reading off from the calibration curve, subtracting away the corresponding (same time point) negative control yield values, and multiplying by the dilution factor.

4.3.6 Flow cytometry

Using the Becton Dickinson FACSCalibur flow cytometer, excitation laser lines at 633/635 nm and 488 nm were employed for the detection of Cy5-labelled mRNA and GFP positivity, respectively. Detector settings were adjusted for all the fluorescence channels by running a sham sample, and were saved for subsequent data acquisition.

4.4 Results

4.4.1 Shock wave mediated kinetics of mRNA uptake by mass and number of positive cells

The sensitivity of short-period temporal events, often necessitate the use of multiple methods of detection that can validate each other. In this study, three methods of RNA mass quantification were employed. Differential masses of internalised RNA were found across the analysed time period, as shown by the RT-qPCR amplicon plots in Figure 4.7. During the early PCR cycles, because the PCR components are in excess compared to the eGFP sequence, the amount of amplified complementary DNA grows exponentially. The number of cycles it took to increase exponentially, mostly increased after shock wave treatment (as demonstrated by the 60 and 240 minutes post exposure samples in Figure 4.7), indicating that there were relatively lower amounts of the internalised eGFP mRNA compared to during treatment (e.g. 1 and 5 minutes in Figure 4.7). The

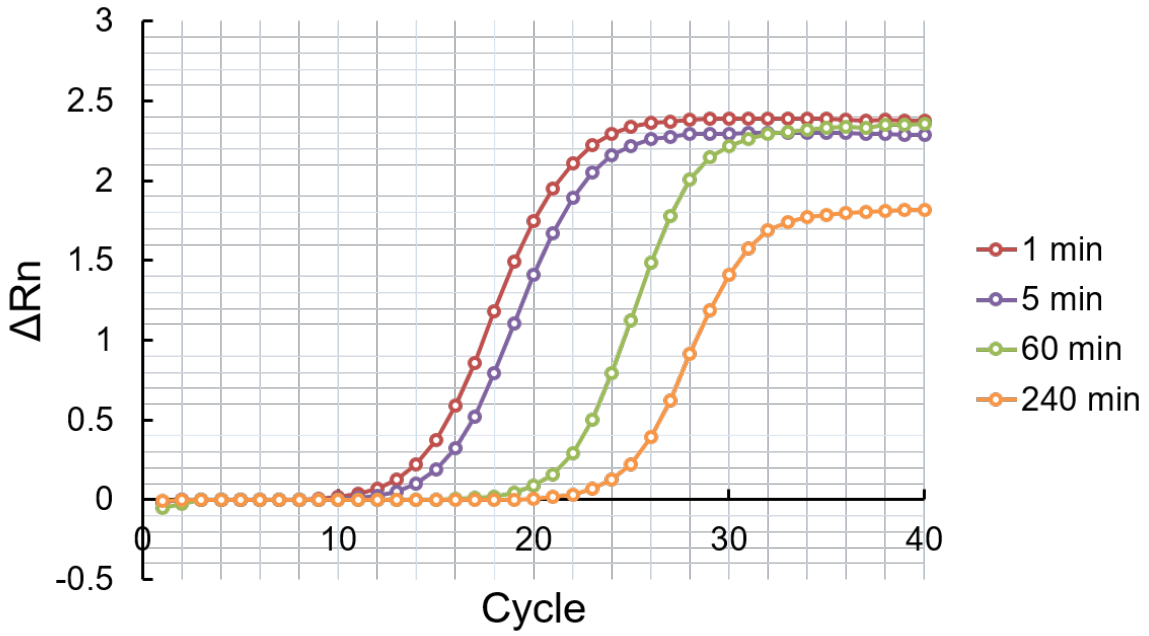


Figure 4.7: Representative mRNA amplification plots of the experimental RT-qPCR reaction for samples at the analysed time points of 1 and 5 minutes of SW exposure, and 60 and 240 (4 hours) minutes after SW exposure.

SW-induced mRNA transfer profile is shown in Figure 4.8 which is normalised with respect to shams. During SW treatment, in minute intervals, the highest influx of

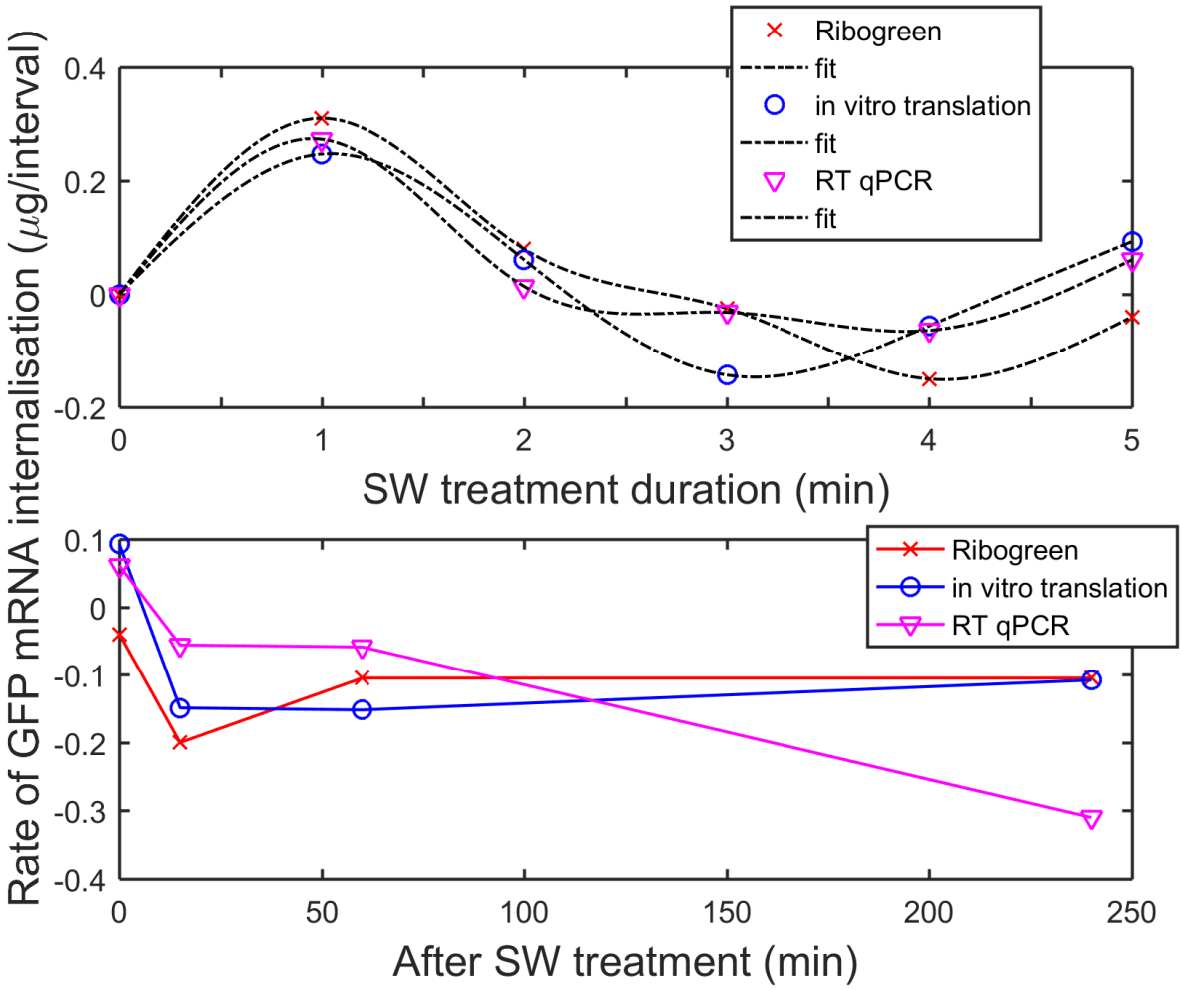


Figure 4.8: A three-method quantification of eGFP mRNA transfer into cells, as a function of shock wave treatment duration and up to 4-hours afterwards. Data points are the mean values of triplicates and are representative of two independently conducted experiments (each at n=3).

mRNA was found to occur in the first 120 shocks (i.e. 1 minute exposure). Beyond this point, the rate of transfer steeply decreased at 240 shocks, and fluctuated about the zero line up to 480 shocks, which was suspected to be due to shock wave induced mRNA degradation. At the end of treatment, with the removal of SWs at 566 shocks (circa 5 minutes) the transfer rate increased to approximately 0.1 μg/min. Thus, the average sum of internalised mRNA rates by the end of optimal SW exposure was 0.21 μg (Ribogreen: 0.175 μg; in vitro translation: 0.202 μg; RT-qPCR: 0.253 μg), corresponding to 4.2% of the administered dose.

Furthermore, the number of mRNA copies corresponding to the above effective dose was determined theoretically. Each mRNA molecule was 996 nucleotides long,

and the molecular weight per nucleotide was taken to be 321.45 g/mol. The result was an estimated total of 3.95×10^{11} mRNA copies[1] being delivered into cells, and were therefore in abundance.

After the end of shock wave treatment, the amount of internalised eGFP mRNA generally decayed, resulting in negative transfer rates. However, the good agreement between Ribogreen and in vitro translation data, suggested that only the first 'after SW' interval may be deemed as mRNA-reducing, with thereafter insignificant changes in the internalised mRNA probably because steady state was reached. The major influence on steady states is the rate of degradation. It followed that the appreciable initial drop in mRNA transfer rate after SW exposure, may not have been driven by mRNA degradation alone but possibly by some mRNA efflux as well. Houk et al.[261] modelled DNA degradation rates for different conformations, in rat plasma, revealing a half-life of 11 minutes for linear pDNA, which is the closest conformation to that of mRNA so far reported on. While mRNA's half-life is typically lower than that of DNA, half-lives in serum-free conditions (as is the case in the present study) will be to some degree higher. A study by Sharova et al.[262] found that 54 out of 19,977 genes, had an mRNA half-life of less than 1 hour.

Results of Cy5-labelled eGFP mRNA[2] uptake during shock wave exposure are shown in Figure 4.9. Background Cy5 signal was disregarded by fluorescence gating at a demarcating boundary between two forming sub-populations. The Q2 quadrants represented populations of mRNA positive cells with normal granularity (which were therefore intact and alive), whereas Q1 events corresponded to normal cells that were mRNA negative. Despite attempts to set gatings to exclude all cellular autofluorescence in the FL4 channel, there was still substantial signal from the sham sample in the Q2 quadrant which could not be excluded. As shown in Figure 4.9(a) this sham level was ∼34% and was therefore used as the zero level for mRNA uptake. The mean values of

[1]The number of mRNA copies was calculated as the number of moles × the Avogadro's constant. The number of moles = total internalised mRNA in grams/(RNA nucleotide molecular weight in g/mol × the number of nucleotides in a single eGFP mRNA molecule).

[2]the mRNA was transcribed with Cyanine 5-UTP substitution by Trilink Biotechnologies, and the fluorophore was therefore covalently attached. Note that we did not proceed to monitor GFP in this experiment because nucleotides modified in this way have been proven to interfere with the translation properties of the transcript itself.

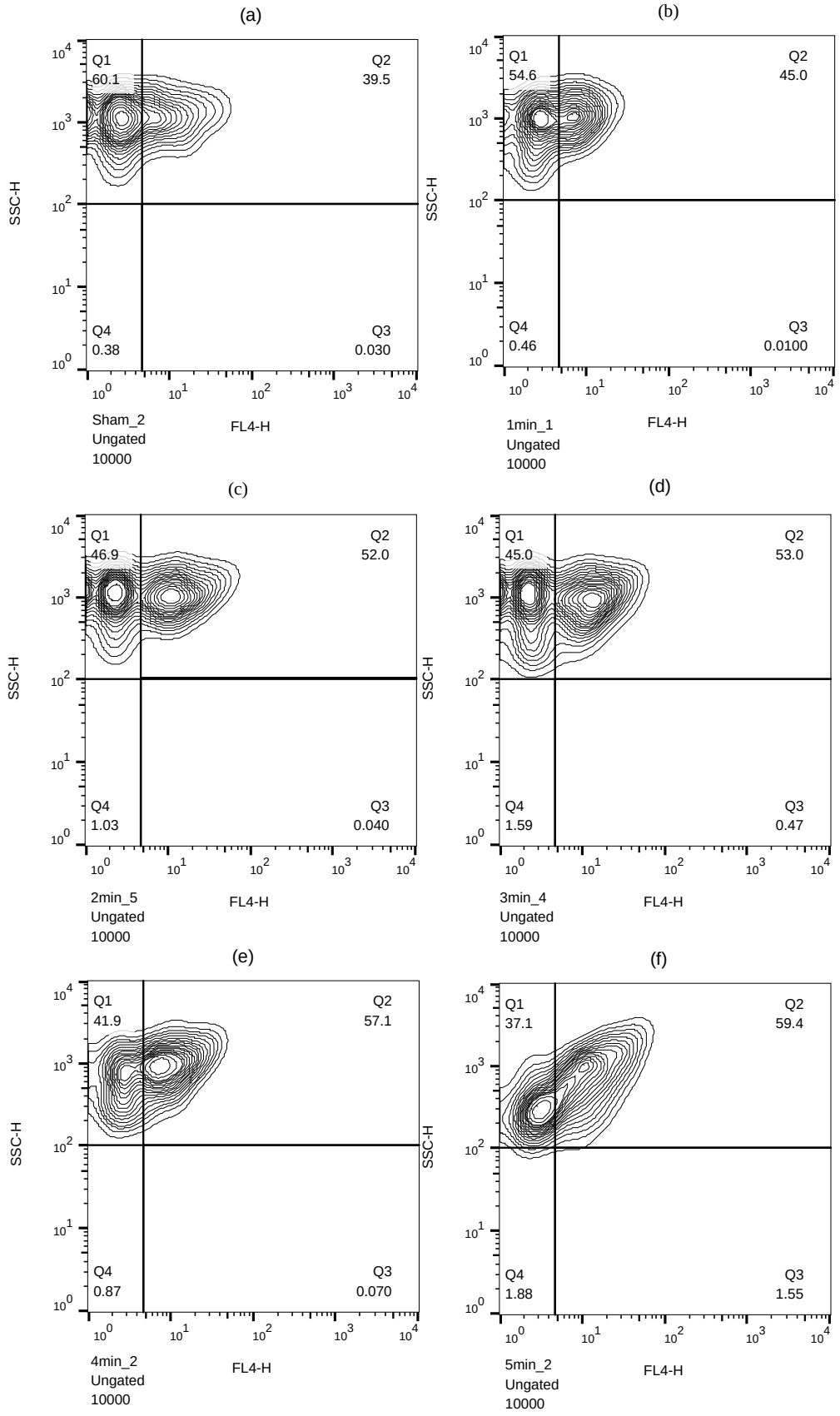


Figure 4.9: Kinetics of Cy5 labelled eGFP mRNA uptake by number of cells. Representative flow cytometric measurements of Cy5 positive cells, in sham samples (a), and through the course of shock wave treatment: (b) 1 minute - (f) 5 minutes.

Cy5+ cells are given in Table 4.1. With the application of the first 120 shocks (Figure 4.9(b)) the net amount of Cy5 eGFP mRNA internalised cells was 13.53%. Continued

Table 4.1: Results summary of Cy5 labelled eGFP mRNA uptake by cells

SW time point (min)	Mean Cy5+ cells (%)	Net Mean (%)	Rate (cells/min)	C.V.
0	34.43 ± 5.05	0	-	0.15
1	47.96 ± 8.25	13.53	13.53	0.17
2	52.12 ± 7.63	17.68	4.15	0.15
3	58.83 ± 8.80	24.39	6.71	0.15
4	59.43 ± 16.90	24.99	0.60	0.28
5	59.88 ± 11.45	25.44	0.45	0.19

Note: The zero minute time point refers to sham treatment; the Mean Cy5+ cells are reported with the standard deviations; the Net Mean is relative to the zero time point; C.V. is the coefficient of variation. Rate is the uptake of Cy5 by cells as a function of time. Data represents at least n = 4.

SW exposure, further increased the number of positive cells at a rate that progressively decreased. Similarly to the results of internalised mRNA mass, the highest uptake occurred in the first minute of SWs, with minimal amounts of transfer toward the end of the treatment. At the end of the optimal SW exposure, 25.44% of cells were transfected. Notably, the accordance of this value with the number of *transfectable* cells previously quantified through propidium iodide (PI) uptake (20.5%) in Chapter 3, demonstrated that PI uptake was indeed an effective indicator of the *transfected* cells. In fact, the ∼5% difference could be ascribed to those cells that were sufficiently permeabilised to allow plasma membrane entry (sufficient for RNA) but not nuclear entry (needed for PI). Additionally, while there was a minor downward shift in side scatter with increasing number of shock waves (Figure 4.9) which would typically indicate a deviation from the normal cell characteristics relative to the sham control, the cell viability was not altered, as previously determined in Chapter 3 at the equivalent (optimal) SW dose.

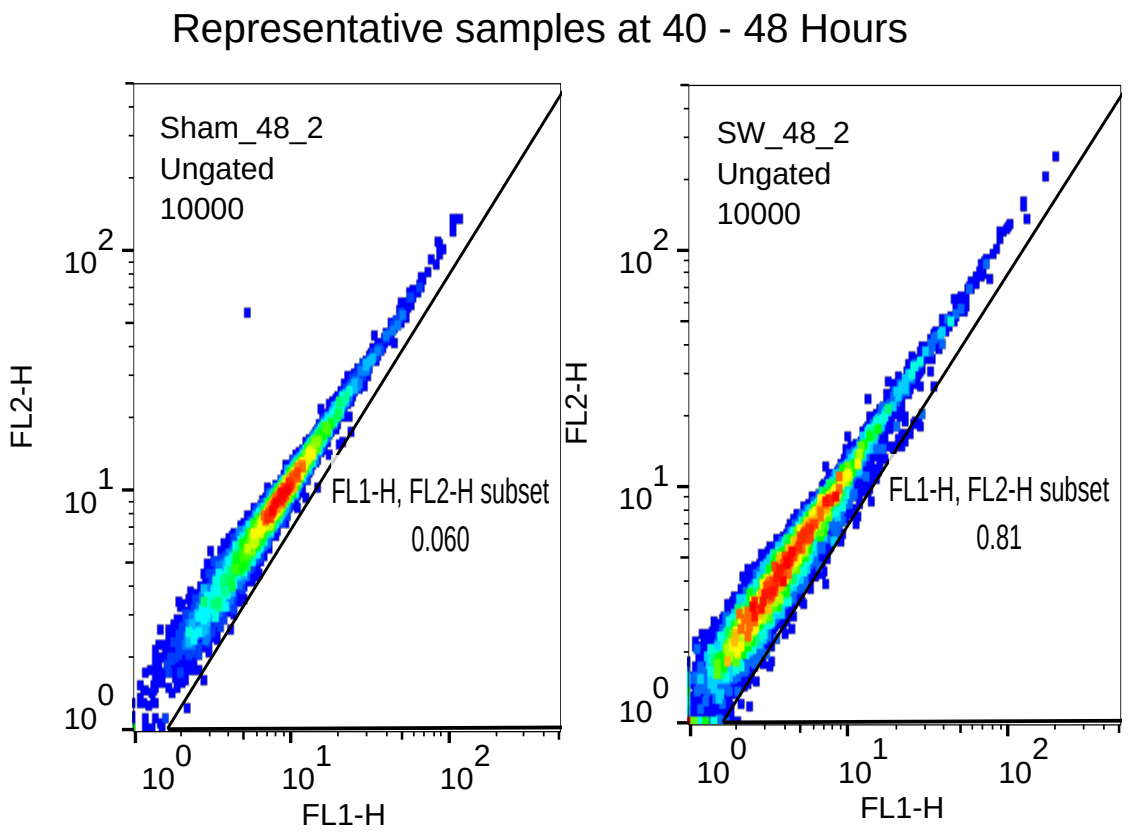
It should be emphasized that due to the nature of fluorescence activated cell sorting (FACS) the fluorophore was detected. Hence, even though the fluorophore was covalently attached to the mRNA, the latter was not specifically detected. Thus, for the internalised labelled mRNAs that later degraded either by shock waves or intracellular lysosome action, the affected cells would have continued to fluoresce because the Cy5 dye was

not as susceptible to degradation. It was on such account that the 'after SW-exposure' samples were not part of this experiment, and that the increment of positive cells at 3 and 4 minutes probably indicated cells with unstable internalised eGFP mRNA since there was zero detected mRNA transfer at those time points.

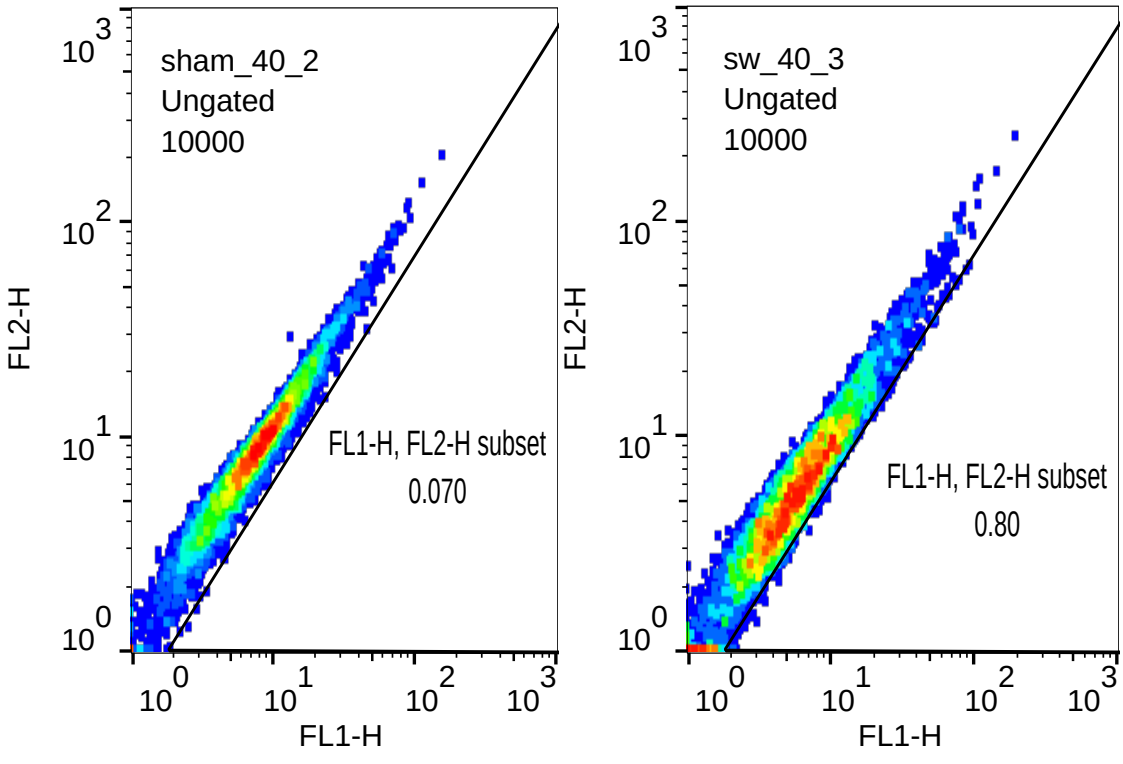
Comparing results of mRNA mass transfer (Figure 4.8 (top)) with results of cell GFP positivity (Figure 4.9) may be conducive to answering the question as to whether the internalised dose per cell changes during SW treatment. The average mass net transfers (between the three quantification methods) were 0.28, 0.05, -0.07, -0.09 and 0.04 μg at 1, 2, 3, 4 and 5 minutes of SW exposure, respectively (Figure 4.8). Using these values and the number of *new* Cy5+ cells per interval, it could be estimated that the highest average mRNA mass per cell (27 picograms) occurred at 5 minutes, while the lowest was at 3 & 4 minutes (zero transfer, as per the negative rates). The average mRNA mass per cell at 1 minute was 6.5 picograms, and at 2 minutes it was 4 picograms. Thus, the shock wave induced transfer of mRNA per cell was inconsistent over the course of the treatment.

4.4.2 Shock wave mediated kinetics of GFP translation by mass and number of positive cells

Following the transfection quantification of numbers associated to the mRNA, the next step was to relate mRNA uptake to transgene expression which was quantified by GFP expression cell positivity and yield. Figure 4.10 demonstrates representative flow cytometric measurements of maximum GFP positivity at 40-48 hours post shock wave treatment, compared to controls; which was in rough agreement with a study by Duvshani et al.[11], where the peak GFP expression was found to be at 15-48 hours following low-intensity US treatment. Diagonal gates were placed in the FL1 versus FL2 plots in order to eliminate autofluorescent events whose emissions were equal for both FL1 and FL2 channels. Consequently, events in the lower triangular areas, represented GFP positivity. These events reflected true GFP events because they were not present in any of the sham controls, and also because they occurred at a range of fluorescence intensities, which is in agreement with the varying levels of cellular gene expression in a population of transfected cells. Two days after SW treatment, the percentage of expressing cells was one order of magnitude higher than in the sham-treated cells.



(a)



(b)

Figure 4.10: Quantification of the GFP positive population at (a) 48 hours and (b) 40 hours post, by diagonal gating of the FL1 (GFP) and FL2 channels. Sample description is shown on the top left corners. The subset population is in percentage form.

Nevertheless, ≤1% were found to be GFP positive.

The three independently conducted experiments of GFP expression over time, shown in Figure 4.11, demonstrated similar kinetics and predictability of gene expression. This was consistent with predictions by Kærn et al.[263] on the low molecular-level noise in systems with high numbers of RNA or DNA, resulting in gene expression kinetics that were more or less fixed. In one of those experiments ('exp2') GFP positivity was tested

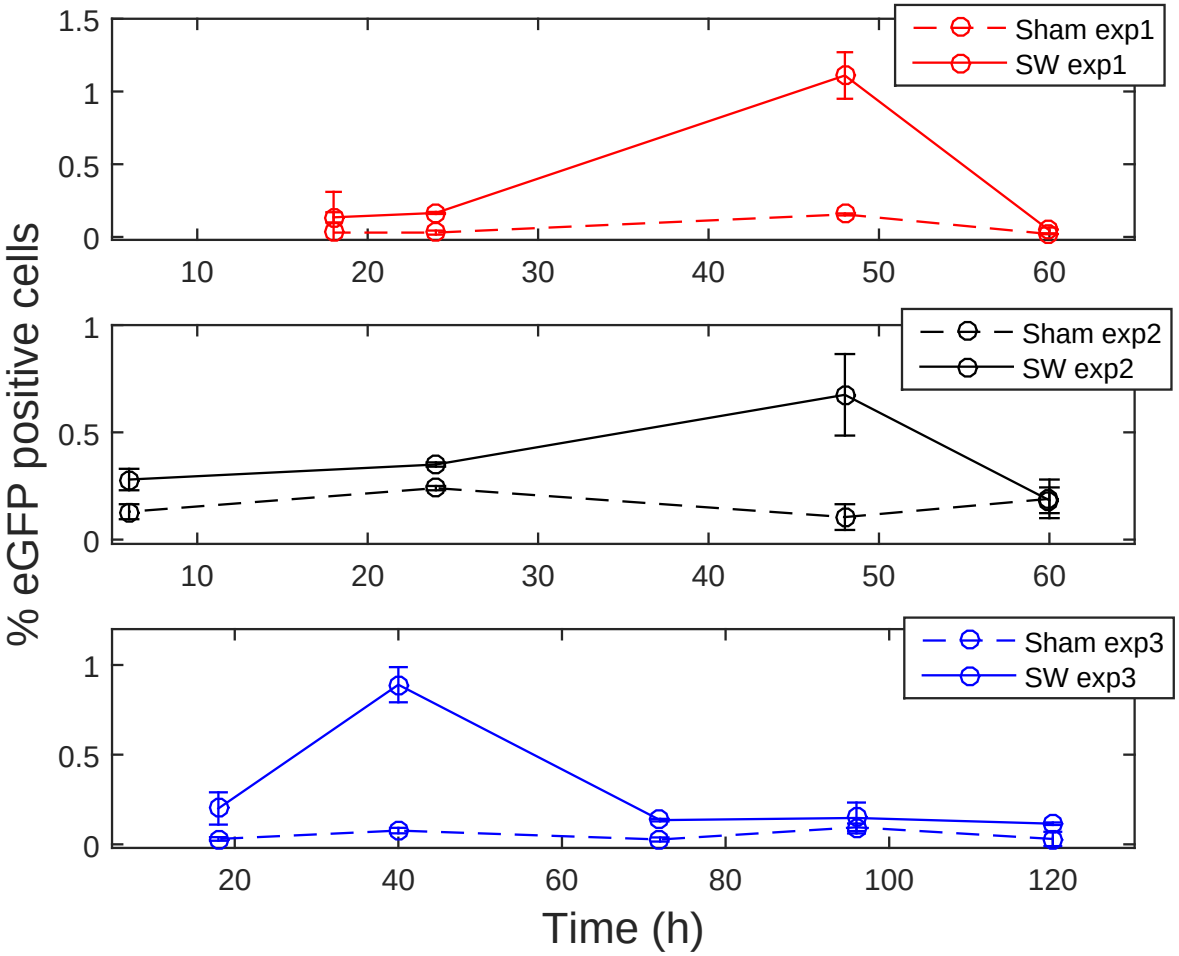


Figure 4.11: Kinetics of eGFP expression post shock wave exposure by flow cytometric measurements of eGFP positive cells, in comparison to sham exposure. GFP expression was probed within a 6-120 hour period after exposure, in three separate day experiments (each at n=3). The error bars are the standard deviations.

at time-points as early as 6 hours post SW exposure, in which a normalised 0.15% of total cells were GFP-expressing. There was continued insignificance in SW mediated GFP positivity up to ∼40 hours post. Beyond 48 hours, positivity began to decline which has been attributed to GFP's half-life of approximately 26 hours [264], as well

as by then, the significant dilution of GFP cells, given that the doubling time of CT26 cells is known to be approximately 20 hours [265] and bearing in mind that the number of sampled events during flow cytometry was unchanged. A similar decrease in GFP positivity was observed by Mehier-Humbert et al.[9].

Measurement of fluorescence positivity does not enable quantification of protein on a microgram basis. For this the BCA assay was used. Under shock wave conditions, cells will synthesise heat stress proteins (HSPs) to protect themselves from stress-induced damage by preventing protein misfolding, as well as by facilitating recovery [266]. In this way, cells would have increased their total cellular protein content. Accordingly, GFP yield was quantified by including SW treated negative controls in the analysis, in order to correct for the SW-induced increased level of protein content. Thus, only the sham samples were normalised with respect to the ordinary (non-shocked) negative controls. Figure 4.12 displays GFP yield with respect to time after SW or sham treatment.

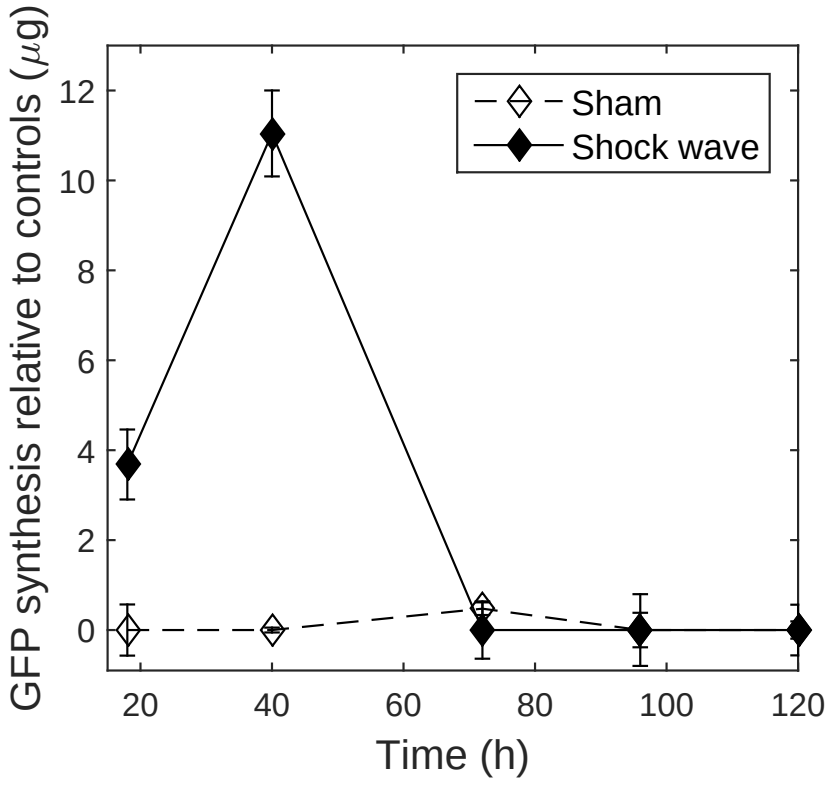


Figure 4.12: Kinetics of eGFP expression post shock wave or sham exposure by protein quantitation, using the BCA method. GFP synthesis relative to *non-shocked negative controls* for sham, or *shocked negative controls* for shock wave. Data represents n=3; error bars are the standard deviations.

With SW application, elevated GFP levels were observed at 18 and 40 hours, which by the subsequent analysis time point had declined to sham level. Further, the 11 μg of GFP synthesised by 40 hours, revealed a protein-to-mRNA mass ratio of 1:0.018 in micrograms. However, there are currently no benchmarks on transfection protein yields that are linked to effective therapeutic gain.

Finally, it should also be mentioned that GFP expression was not achieved in every independently conducted experiment, whereby one out of four experiments (*not shown*) did not yield any GFP positivity above the corresponding sham level.

4.5 Discussion

Every delivery system, inclusive of the administered nucleic acid-based therapeutic, demands an understanding of its delivery kinetics. In this work, the rates of SW-induced internalisation of mRNA and transgene production were characterised. For reliable mRNA quantification, a three-way method was carried out which was critical for making temporal comparisons at the sub-microgram scale. Micro UV-visible spectrophotometry using the NanoDrop, was another technique that could have been employed for RNA quantification. However, apart from NanoDrop's inability to carry out high-throughput measurements, the required microlitre volumes gave room to minute pipetting variability (across the large number of samples) rendering inaccurate results especially for the observed time points that were marginally different from each other. Additionally, a lengthy GFP detection period was defined in order to make observations that were neither too early or too late. Experimental bias due to the unequally spaced intervals of the after-SW exposure analyses, was minimised by maintaining a multiplication factor of 4 between the 'mRNA' samples (i.e. 15 min, 60 min, 240 min), and by selecting some different time points at which the GFP cell positivity was quantified per independently conducted experiment.

The onset of cell permeabilisation (as implied by mRNA uptake) occurred in the first interval of SW exposure, suggesting that the threshold on the number of shock waves required to permeabilise a single cell was low. Thus, increasing SW number up to a viable dose, mainly served in increasing the number of affected cells, rather than in enhancing the cell's permeability. Derieppe et al.[10] applied low intensity US to cells *in vitro* and

monitored uptake of a model drug (a flourescent dye) during exposure, revealing an onset time of 2-3 seconds after US trigger, in a 30 seconds long exposure. Thus in accord with the literature, therapeutic sound waves instigate early onsets of cell permeabilisation with respect to the applied dose. Interestingly, 80% of the total permeabilised cells in [10] manifested in the first third of the exposure. Similarly, in this study >80% of Cy5-labelled mRNA positive cells were conceived halfway through the optimal SW treatment. The presented data also attested to short temporal enhancements of cellular permeabilities because no increase in internalised mRNA numbers was detected 15 minutes after SW exposure (Figure 4.8). Recently, using US, the duration of enhanced permeability was reported to be in the order of a few hours by uptake of a model drug [267] and thereby did not necessarily apply to a permeability with pore size that enabled the entry of larger macromolecules like nucleic acids. Moreover, endocytosis upregulation by ultrasound has emerged as least probable [268], suggesting a short time scale for uptake.

One of the only studies that characterised the kinetics of positive cells at the nucleic acid internalisation level was by Mehier et al.[9] who demonstrated up to 20% of cells had internalised fluorescently stained plasmids through US exposure alone. While they did not determine the 'during' exposure kinetics, they looked at the long-term effects post exposure. However, there are limitations to using fluorescent stains for such analysis, because the DNA intercalated stain will still somewhat fluoresce whilst DNA is degrading, and also because the non-covalent binding properties of such dyes (as was the case for the YOYO-1 stain utilised by Mehier et al.[9]) hold the risk of generic binding to endogenous nucleic acids.

Further, GFP quantification by number of expressing cells revealed disparity with the number of mRNA positive cells. Even more, each RNA internalised cell may have carried almost 5 million RNA copies by the end of SW treatment (assumming equal distribution), making the above disparity more difficult to comprehend. A possible explanation was the apparent instability of naked mRNA at time scales beyond which mRNA cell positivity was studied (Figure 4.9). Another explanation was the potentially negative impact that SWs can have on cellular organelles. Brümmer et al.[230] found SWs to cause swelling of mitochondria plus cristae distortion in rat prostatic carcinoma cells. Therefore, there

may have been an effect on ribosomes and the associated tRNAs. Nonetheless, in a 10^6 cell population, up to 10,000 cells were expected to be GFP positive which was within the reported range by comparison with other investigations (*recall Table 2.1*), although the vast majority introduced air or UCAs in basic *in vitro* configurations.

A noted characteristic of mRNA-based expression was the predictability of its transient course as shown by the timing homogeneity (Figure 4.11), which has also been observed in populations of single cell transfections reported by Leonhardt et al.[269]. Moreover, the presented kinetics of GFP expression through SW induced mRNA delivery greatly differed from that of low-intensity US induced pDNA delivery reported in [9, 251]. In this study, the first time maximum expression was reached was in the region of 40 hours post exposure, compared to approximately 10 or 15 hours for the above-cited US with pDNA studies; which was contradictory to the relatively early expression onset times of mRNA versus DNA confirmed in the literature [63, 64]. It was postulated that the viable SW dose employed in this study, whereby the affected cells recovered within 24 hours (*recall Chapter 3, section 3.3.2*), may have been the reason for the delayed attainment of maximal expression.

Furthermore, a rapid decline in GFP expression was demonstrated by the 12-hours transition from peak expression to no expression (Figure 4.11), and while this was inherent to characteristics pertaining to the type of transgenic protein and target cell line themselves, the transient nature of mRNA based gene expression was clearly displayed in this study, suggesting the need for re-dosing scheduling in a SW delivery strategy. It follows that some target diseases may be less (or more) appropriate for this form of gene delivery strategy than others, because the total therapeutic vector dose that can be administered to a patient is typically dependent not only on the body surface area but also on the pathology [270]. Therefore, the need to re-dose in order to prolong gene expression in SW-induced mRNA delivery implies that it is critical for the shock waves not to induce cytotoxicity, so as not to cause accumulated tissue damage. This is consistent with the shock wave optimisation criterion that was established in Chapter 3, in which the optimum search was driven by the least cytotoxicity and highest cell permeabilisation.

Even in the case of tumour targets, although tissue damage that is confined to the target may not be deleterious, cell transformation may not reach its maximum potential.

Finally, the above findings revealed that SW-mediated naked mRNA delivery into cells required relatively low accumulation of shock wave energy (as obtained at 120 shocks) to permeabilise over half of the total amount of permeabilised cells. It also highlighted the major hurdle of mRNA degradation by intracellular nucleases. mRNA-based expression has been previously described as quantal [269] which agreed with the shape profile of GFP cell positivity.

4.6 Closing Remarks

In conclusion, it was found that translatability between two different SW devices was possible through definition of the optimal SW dose in terms of the pulse intensity integral.

Within a tissue-vessel phantom system, the delivery of RNA into cells took place at variable rates during optimal SW treatment, informing the course of shock wave impact on biological material. It is thought that for the regulation of mRNA delivery, knowledge of the effective dose in connection to the fraction of successfully treated cells, as well as the rate of delivery, are aspects of great importance in the proper planning of SW treatment. The data presented here provide valuable information towards defining these essential parameters.

5

The Contribution of Shock Wave induced Shear Stress on Multicellular Spheroids

Contents

5.1 Opening Remarks 104
5.2 Materials & Methods 105
5.2.1 Spheroid culture & characterisation 105
5.2.2 Configuration and preparation of samples 106
5.2.3 Overpressure experiment 107
5.2.4 Cavitation detection experiment 108
5.2.5 Quantification of mRNA delivery to MCTSs and single cells . 110
5.2.6 Quantification of siRNA delivery to MCTSs 111
5.3 Results 111
5.3.1 Cavitation activity 111
5.3.2 mRNA delivery: single cells versus spheroids 116
5.3.3 siRNA delivery: the effect of overpressure on MCTSs 120
5.4 Discussion 125
5.5 Closing Remarks 127

5.1 Opening Remarks

In the context of cancer gene therapy, the complexity of the tumour environment *in vivo* has led to loss or significant reduction in the efficacy of anti-cancer strategies tested *in vitro*. While gel-based cell systems provide a further layer toward tissue resemblance, they do not mimic the 3-D structure of tumours through which pathophysiological gradients are established *in vivo*. Multicellular tumour spheroid (MCTS) cultures of 200-500 μm in diameter, have addressed this issue as they have been shown to develop oxygen, nutrient and catabolite gradients; and possess a necrotic core and proliferative periphery which is true of tumours [271]. Moreover, spheroid cultures remarkably mirror the initial stage of avascular tumour growth, micrometastases and micro-regions at the farthest distance to a capillary [272].

Actually, MCTSs may also serve in better understanding the role of stresses induced by shock waves, because shearing is expected when shock waves travel through areas of cohesion and thus in tightly packed solid structures. Increased shear stress has been shown to increase the fluidity of cell membranes [273], therefore becoming more amenable to molecular transport. Compact spheroids can sustain both longitudinal (compressional) and transverse (shear) waves. Furthermore, the application of overpressure has been previously reported to suppress cavitation as reviewed in Chapter 2 (section 2.3.2), allowing the assessment of bio-effects in non-cavitational regimes. Taken altogether, in this work it was hypothesised that by separately exposing single cells and spheroids to SWs in the absence or presence of overpressure, would result in sustained RNA delivery in the spheroids, but not in the single cells.

Complete isolation of direct stress-induced bio-effects cannot be ascertained at therapeutic shock wave amplitudes, because even though sufficient excess pressure may reduce the negative pressure to below the inertial cavitation threshold, stresses may also derive from local effects due to oscillating bubbles. As such, this study considers the generated shear stresses in a broad sense, which are indirectly determined by observing changes in RNA uptake. Early speculation on the SW-induced creation of smaller membrane pores or wounds if inertial cavitation were to be absent, motivated the delivery of the relatively smaller siRNA molecule, as well as testing the delivery of mRNA.

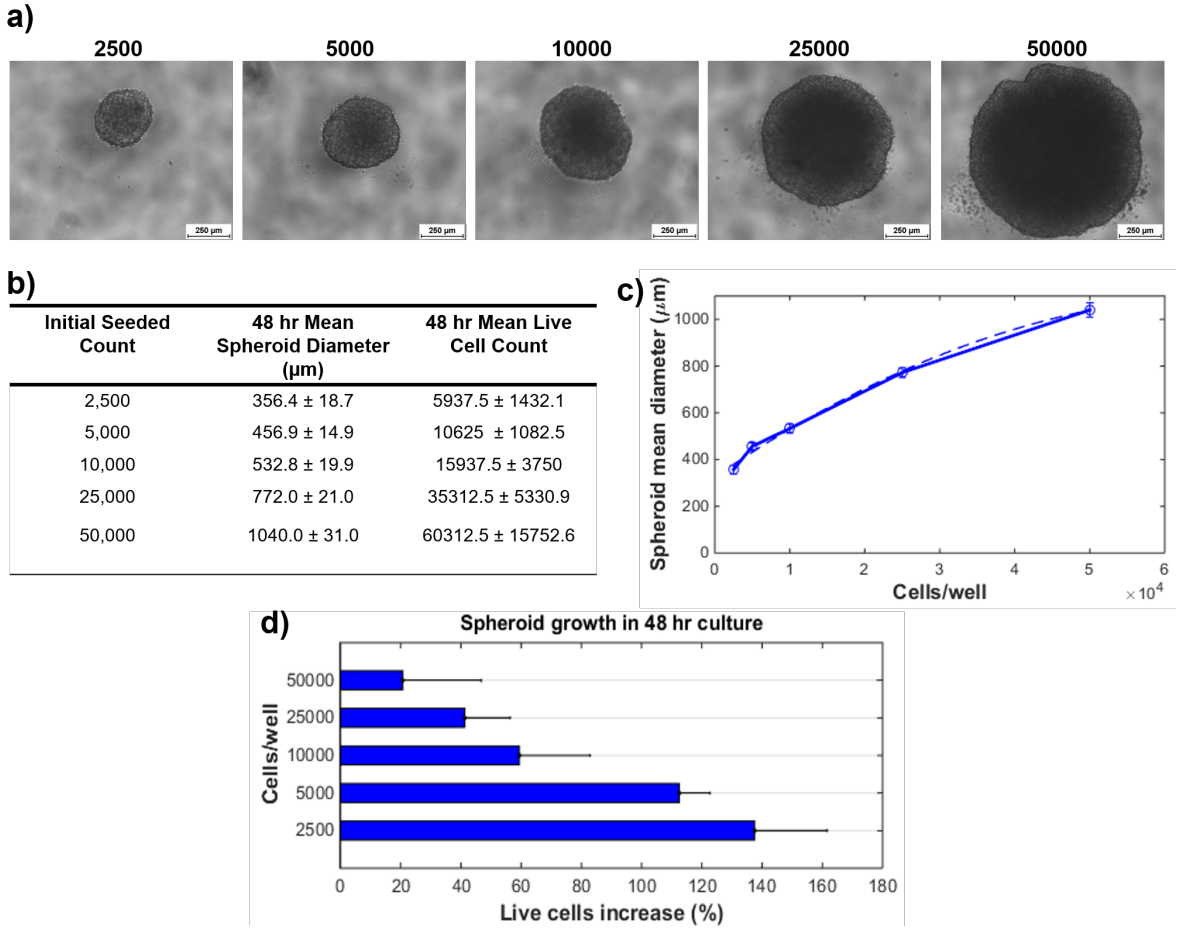
5.2 Materials & Methods

5.2.1 Spheroid culture & characterisation

Firstly, preliminary testing of three different techniques for making spheroids was carried out; namely: agarose underlying, the use of ultra-low attachment (ULA) round bottom plates, and the hanging drop method. In a two-day culture time frame, it was found that the ULA plates produced loose but highly consistent CT26 aggregates, while the hanging drop method required extended culture periods to form the spheroids. On the other hand, by 48 hours the agarose underlays produced tight spheroids with a reproducibility of $\geq$90%. Thus, the agarose underlying method was used for further experimentation.

Sterile 96-well flat bottom plates were briefly pre-heated to 37 °C, and coated with 50 μL of 1.5% agarose which had been autoclaved beforehand. For spheroid characterisation, a range of initial CT26 cell concentrations were employed ranging from 2,500 to 50,000 cells in 50 μL FCS-supplemented RPMI media, per well. Subsequently plates were incubated (humidified atmosphere containing 5% CO_2, at 37 °C) for 48 hours. It should be mentioned that the plates were not centrifuged after cell seeding because doing so resulted in less uniform spheroids. Spheroids were then imaged through phase contrast microscopy (Nikon Eclipse TiE2000) as shown in Figure 5.1(a) revealing the approximate round shape of the spheroids. Images were saved in their native file format (.nd2). The spheroid diameter was defined as the average of its horizontal and vertical width, using ImageJ. Figure 5.1(b & c) displays the mean diameters for triplicate spheroids at each cell seeding concentration.

Next, the spheroids were dissociated for counting of live cells through the Trypan Blue dye exclusion method. This was achieved by transferring the spheroids into empty wells, adding 250 μL Accumax solution (Sigma-Aldrich) and gently mixing by pipetting. The well plate was then placed on a platform rocker for 1 hour at room temperature. Halfway through rocking, spheroids were gently agitated by pipetting several times to release the cells. To ensure an exact volume in order to reliably calculate the number of cells, dissociated cells were pelleted and re-suspended. The percentage increase in the number of live cells within the 48 hours of spheroid culture is shown in Figure 5.1(d).



Initial Seeded Count	48 hr Mean Spheroid Diameter (μm)	48 hr Mean Live Cell Count
2,500	356.4 ± 18.7	5937.5 ± 1432.1
5,000	456.9 ± 14.9	10625 ± 1082.5
10,000	532.8 ± 19.9	15937.5 ± 3750
25,000	772.0 ± 21.0	35312.5 ± 5330.9
50,000	1040.0 ± 31.0	60312.5 ± 15752.6

Figure 5.1: Viability and size characterisation of cultured spheroids with various initial cell seeding densities. a) Phase contrast microscopy of the spheroids at 48 hours after culture. The scale bar represents 250 μm; b) mean diameter of spheroids with standard deviations and live cell count by spheroid dissociation and Trypan Blue exclusion test (n=3); c) fit (dashed line) of initial cell seeding count versus spheroid size [$y = -1.55e^{-7}x^2 + 0.022x + 325.4$]; d) percentage increase of the spheroids' live cell population indicating an increased proportion of necrotic cells with increasing initial cell seeding density.

5.2.2 Configuration and preparation of samples

To enable firm connection of the TMM-MINI phantom (*recall Chapter 4, Figure 4.4*) to the externally applied pressure, the TMM-MINI was modified by bonding a hollow metal adapter onto its upper hole as shown in the inset of Figure 5.2. The inner diameter of the adapter conformed with the diameter of the hole (2 mm). The cell configuration was identical to that of Figure 4.4, however, the agarose also filled the adapter in order to prevent compression within the phantom during pressurisation. For the single-cells and spheroid formats, 500,000 cells and 31 spheroids at 10,000 initial

cell count respectively, were suspended in serum-free medium, into the channel. For mRNA delivery, 5 μg of eGFP mRNA was added to the channel, whereas for siRNA, 2 μM of siGLO Red (GE Dharmacon, Lafayette, CO, USA) was used, which is a non-targeting siRNA labelled with a Cy3 analog.

5.2.3 Overpressure experiment

A diaphragm pressure pump (model 2522Z-01, Welch, IL, USA) was employed to pressurise the samples. A semi-rigid 5 mm inner diameter hose cut to the required length was intermediately connected to a valve, and securely fit on one end to a metal adapter on the pressure pump, and to the metal adapter of the phantom on the other

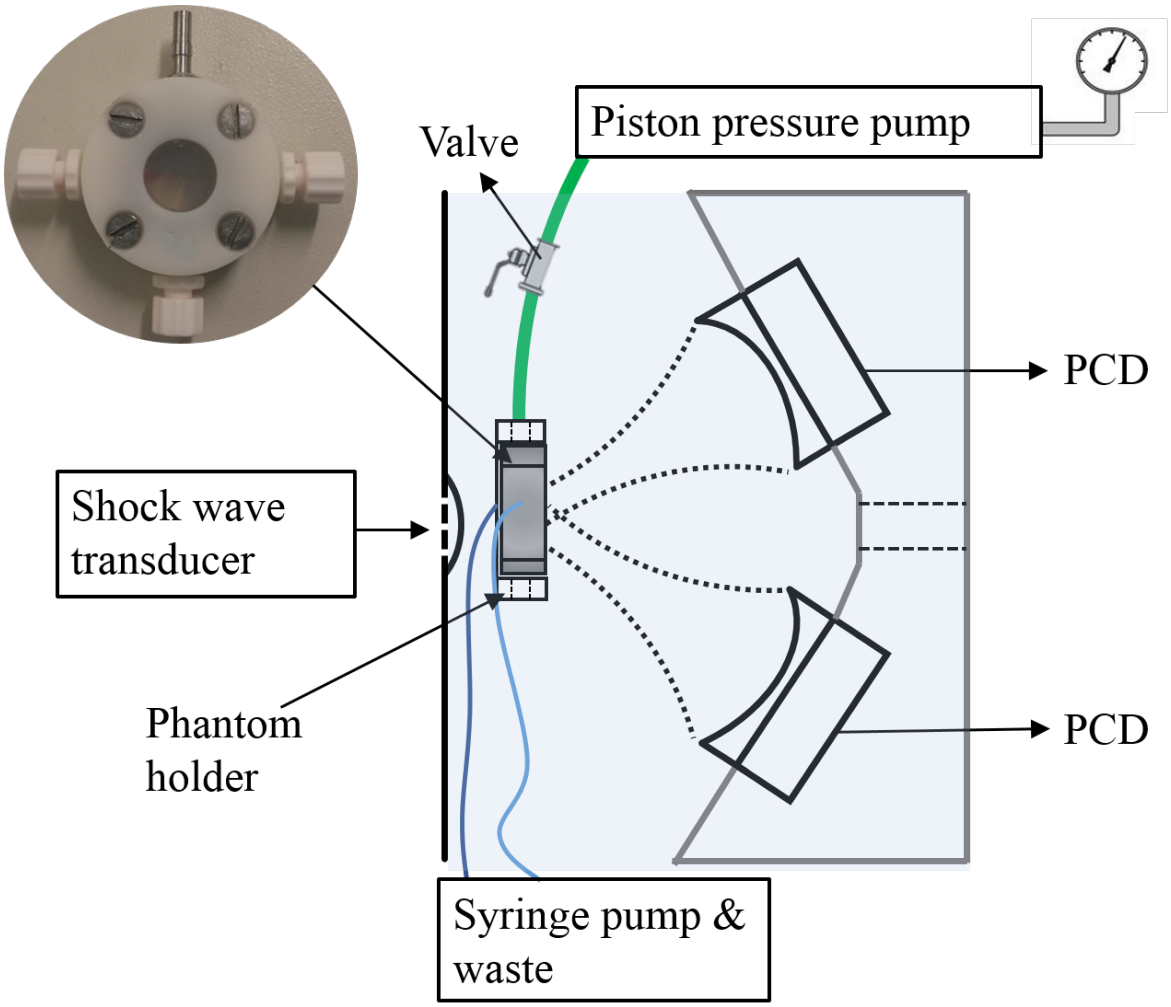


Figure 5.2: Schematic of the overpressure experiment as well as the cavitation detection set-up. The inset photograph demonstrates the modified TMM-MINI phantom. The custom-made phantom holder had hollowed out faces to enable direct SW transmission and access to the phantom's openings. PCD = passive cavitation detector.

end. Static pressure was generated by the pump and read by a gauge. The valve was partially closed or opened to obtain measured excess static pressures of 350 kPa or 700 kPa at the centre of the TMM. Figure 5.2 illustrates this arrangement with respect to the SW source. Once the pressure had been applied, optimal shock waves (3.5 E, 566 SWs, 2 Hz PRF) were delivered through the Mylar window of the TMM. Vibrations from the pump were isolated by placing it on a separate platform from that which held the water tank and phantoms. The tank water was continuously degassed and heated at 37 °C with an aquarium heater (AquaEL, Warsaw, Poland).

5.2.4 Cavitation detection experiment

Acoustic emissions were detected passively by two confocally aligned spherically focused single-element 1 MHz transducers, with a 50 mm focal length and minimum point target focus diameter of 48.26 mm (style V394-SU-F50MM-PFT, Panametrics), herein denoted as passive cavitation detectors or PCDs. Similarly to Cleveland et al. [183] and Bailey et al. [185], this PCD frequency was selected because it allowed for the detection of signals in tissue with a localisation of about 2 mm [185]. A custom-made angular bracket was designed (*see Appendix A.4*) to hold the PCDs at an inclination angle of 26.50 ° from the normal, as illustrated in Figure 5.2. The coincidence field of this dual PCD arrangement is shown in Figure 5.3, demonstrating geometric fitness with the TMM size, and having a focus bounded by the intersection region of 3 × 3 × 3 mm. The bracket was hollow in the middle to minimise shock wave reflections.

The phantom holder was connected to a 3-D translational system for alignment of the TMM target point with the focus of the SW source, using the previously described needle hydrophone. The target point corresponded to the centre of the TMM, at ∼1 mm above the channel. A custom-made connector was built to support from beneath the phantom holder and the PCDs bracket, and was designed to have the exact height and length (the latter with some extra room) required to align the PCD focuses to the TMM target point (which by now coincided with the SW focus). The length (or distance) between the two objects was fine-adjusted by operating the PCDs as sources using two ultrasonic pulser/receivers, while maintaining the hydrophone tip at the TMM target point.

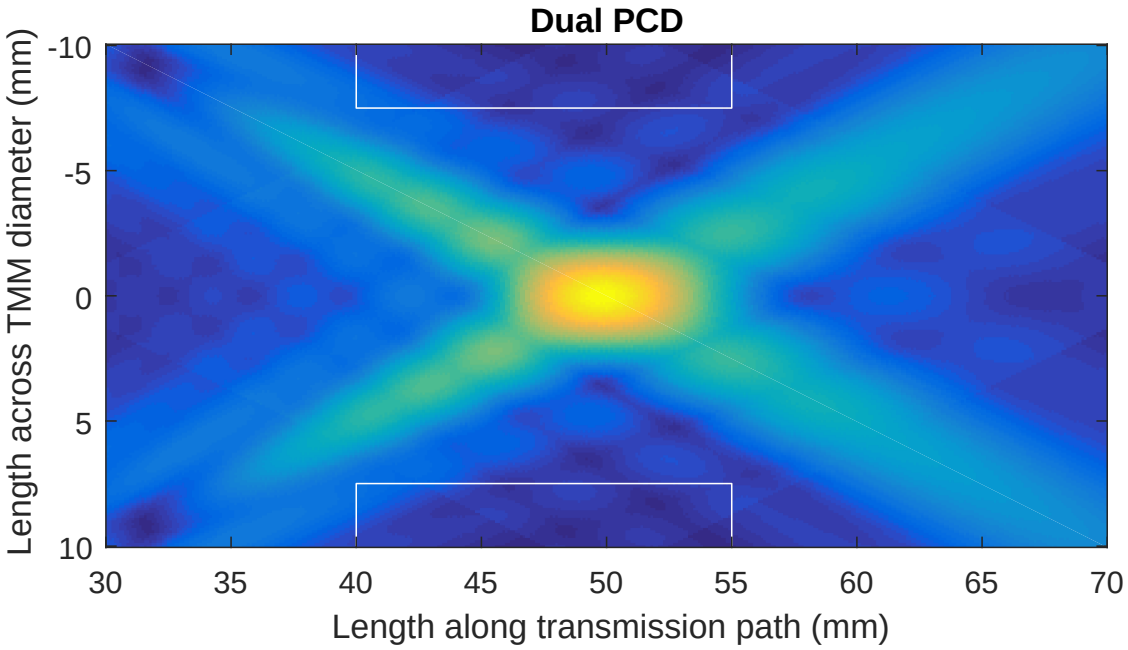


Figure 5.3: The sensitive field of the dual PCDs. The white rectangles demarcate the TMM boundaries.

A series of TMM conditions was tested comprising: non-degassed agarose gels with 1 million embedded CT26 cells, with or without 350 or 700 kPa overpressure, and with or without flow at a rate of 500 μL/min which was equivalent to half of the flow rate expected in a 2 mm blood vessel [274]. This flow rate was implemented to mimic delivery of RNA due to blood flow, but exact representation could not be accomplished at the realistic rate of 1 mL/min due to the finite amounts of RNA. The channel was filled with degassed Milli-Q water to reduce echo signals masking sample cavitation. Flow conditions were generated by a syringe pump (model AL1000-220, World Precision Instruments, Hertfordshire, UK) via a thin perfusor line with luer lock fittings (ref: 8255172, B. Braun, Sheffield, UK) for connection to the TMM channel. The flow was applied approximately one minute before applying the shock waves and/or overpressures.

The gels were not degassed because the laboratory degasser equipment was inherently unsterile. Also, given that the agarose solution and the medium (in which the cells would later be suspended in) needed to be degassed separately due to differences in the degassing temperature[1], the high temperature required to maintain the agarose in its liquid state,

[1]for the agarose a minimum of 70 °C was necessary whereas for the cell medium a maximum of 37 °C ensured that its constituents did not denature.

meant that after degassing, ample time was necessary to allow the temperature to come down to that at which it could be mixed with the cells in medium, which was thought to promote the re-introduction of gas, to some degree. Note that the mixing and stirring together of the agarose and cells solutions (in order to homogenise the TMM) may have also compounded the gas content of the samples. For these reasons, degassed TMM (under a vacuum for 1.5 hours for every 50 mL) gels were tested, without the overpressures, only to verify the effect of relatively lower gas contents on cavitation activity.

The signals from both PCDs were simultaneously recorded throughout SW delivery by sequence mode acquisition on a digital oscilloscope (LeCroy waveRunner 64Xi-A, 600 MHz, 10 GS/s, LeCroy) at a sampling rate of 25 million samples per second, and pulse trace length of 1 millisecond. The sequence to record was defined as the number of shocks such that the oscilloscope automatically terminated acquisition upon collecting the last sequence segment. Acquisition was initiated by the shock wave trigger. Finally, the voltage waveforms were saved directly onto an external drive.

5.2.5 Quantification of mRNA delivery to MCTSs and single cells

eGFP mRNA delivery was quantified by total internalised eGFP mRNA mass using RT-qPCR, rather than by GFP expression, because RT-qPCR demonstrated less variance and thus was deemed more robust for inferring the efficiency of delivery. Single cells or spheroids were rescued from the channel using a fine needle and syringe. To ensure maximal rescue, the channels and syringes were flushed with RPMI medium and collected in low bind microcentrifuge tubes (Eppendorf, LoBind tubes, Thermo Fisher Scientific) because the spheroids had the tendency to stick to plastic-ware. Samples were then microcentrifuged and the supernatant was removed without subsequent PBS washes to minimise spheroid-to-plastic interaction. Thus, for consistency, the single cells samples were similarly treated. Sample lysis and homogenisation, total RNA extraction and RT-qPCR were performed as described in Chapter 4.

5.2.6 Quantification of siRNA delivery to MCTSs

SiGLO Red delivery was assessed using an imaging cytometer (Celigo, Nexcelom Bioscience Ltd, Manchester, UK). After the SW/overpressure treatments, the spheroids were rescued from the TMM channels as detailed above, and re-suspended in PBS for staining with Calcein Blue AM at a final concentration of 10 μM. Gently, ten spheroids per TMM were transferred into a round bottom well plate at one spheroid/well, briefly spun to position the spheroids into the centre of the wells and incubated for 30 minutes. The plate was then imaged in the Celigo cytometer, by image-based auto focusing in brightfield, on any spheroid-containing well. Red (siRNA) and blue (Calcein viability marker) fluorescence acquisition was specified by exposure time and low gain for the red (100,000 μs; 100) and blue (1,500 μs; 50) channels. The cytometer's maximum exposure settings were 670 for the gain (dimensionless) and 1 second for the exposure time. The red illumination was at 531/629 nm and for the blue it was 377/477 nm. Finally, the well plate was scanned and the images were post-processed on the Celigo by specifying the expected maximum spheroid diameter, the minimum aspect ratio (to avoid the Celigo algorithm picking up any dust particles) and by intensity thresholding (to remove the background). Spheroid intensity measurements were acquired for each channel.

5.3 Results

5.3.1 Cavitation activity

The dual passive cavitation detection method adopted in this study, readily registered simultaneous acoustic signals, characteristic of cavitation events at the target site. Based on the dual PCD analysis by Cleveland et al.[183], a sliding-window cross correlation algorithm using Matlab was implemented to correlate corresponding PCD traces and identify the coincident maximum peak occurring within a specified waveform time window (which will be later explained). Prior to this, the acquired voltage data was high-pass filtered using a Butterworth filter, at a cut-off frequency of 300 kHz, 4th order; and the envelopes were then extracted from the signals using the Hilbert transform, in Matlab.

Figure 5.4 displays an example dual PCD trace for one optimal shock wave pulse. PCD 1 & 2 are plotted as if reflecting one another, for comparison, and therefore the voltage

readouts are magnitudes. In the example trace, the first spike that can be observed occurred at 65 μs, arising from nonlinear scattering of the shock wave, by impedance mismatches at the phantom interface, and any gas bubbles present. This arrival time was also accurately predicted by the total travel distance of 100 mm, comprising the SW focal length (50 mm) and the PCDs focal length (50 mm), and taking the speed of sound to be 1,500 m/s. The second peak at 265 μs, occurred consistently at this time irrespective of the energy setting and was identified as a reflection in the system, and thus not associated to cavitation. The third spike (at approximately 380 μs in the example trace), was attributed to bubble collapse emission, through which the time to collapse (t_c) from the first spike, is calculated. Therefore, the absence of this emission meant a lack of cavitation, whereas the longer the duration of t_c, the more the bubbles were driven and thus the greater the 'intensity' of their collapse. Occasionally, a fourth smaller spike appeared at about 500 μs (*not shown in the figure below*) representing re-growth of the bubble and secondary collapse.

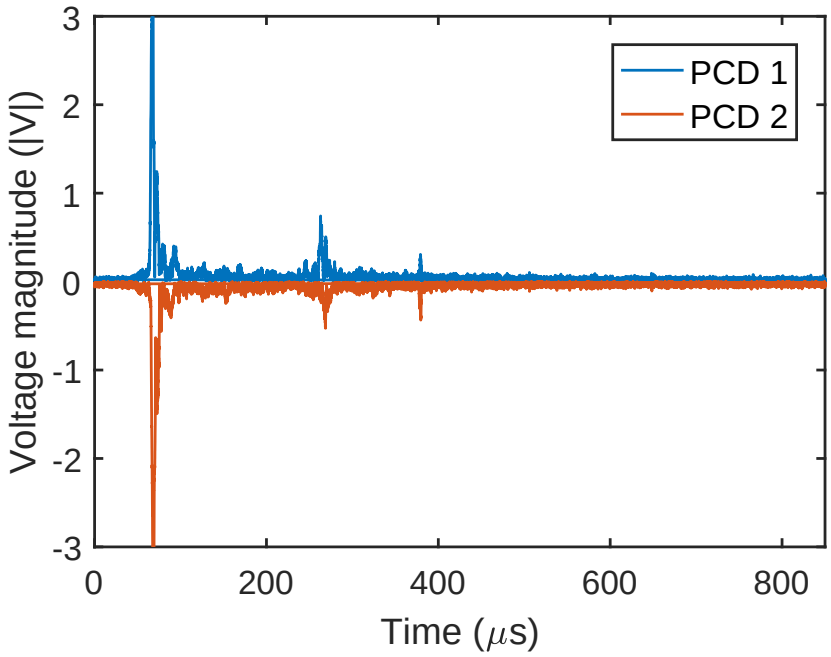


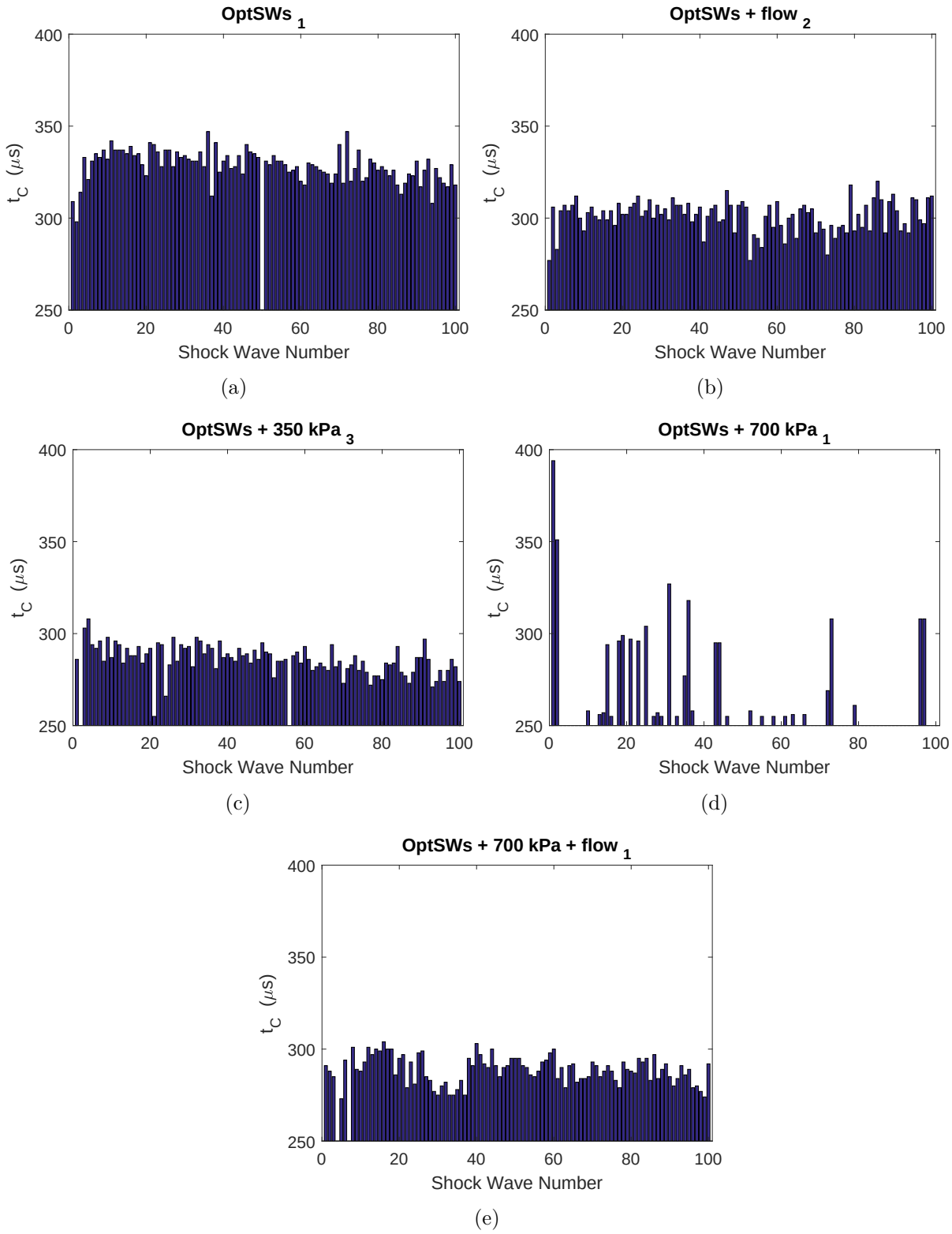
Figure 5.4: Example of a dual PCD signal (with the PCD 2 trace inverted for comparison) showing coincident emissions which are characteristic of cavitation in lithotripsy.

Going back to the windowing procedure, both PCD traces were windowed between 300 μs and 480 μs in order to detect the main bubble collapse emission, and exclude the reflected wave (at 265 μs). In instances where the third peak was not detected, the

idea that perhaps this peak was outside of the above timespan and overlapping with the reflected wave was not found to be true, because the shape of the latter was invariant. A small window length was selected for PCD 1 and was cross-correlated with PCD 2 for time shifts of 1 μs, and the peak correlation was recorded. This was repeated along the gated window. The time associated with the maximum cross-correlation was used to determine t_c. The window length was 3 μs as to prevent blurring of the variations in time; and the 1 μs time shift was used to increase the sensitivity of coincidence detection.

The collapse times for the first 100 shock waves delivered to the TMM are shown in Figure 5.5. Shock waves beyond the first 100, provided no extra information on the evolution of cavitation activity as there was minimal variation in the collapse times, indicating stabilisation of the bubble cloud. This was similar to reports by Bailey et al. [185], who noted persistent cavitation after 150 shocks. The optimal shock waves (denoted by 'OptSWs') alone, displayed the highest collapse times, and thus the most inertial cavitation among the tested groups. The addition of flow (Figure 5.5(b)) or overpressure (c & d) decreased the collapse times or number of cavitation events compared to optimal SWs alone. These findings corroborated with the following predictions:- that the flow would remove nuclei from the previous SWs, which would have increased cavitation if they had remained as they were likely to be experiencing growth; and that at the selected range of overpressure there would be significant alterations on the cavitation observed *in vitro*, supported by the study by Delius et al.[203] whereby 400 kPa overpressure was sufficient to effect substantial changes in the release of haemoglobin from red blood cells.

However, when overpressure and flow were combined (e) there was a decrease in t_c relative to flow + SWs (b), and an increase relative to 700 kPa overpressure + SWs (d). The former was the result of the modulating power of the overpressure at reducing the strength of cavitation. However, despite this relative reduction, the latter revealed that flow imparted a greater effect on the overpressure than on the SWs. In other words, these results suggested that the flow minimised the influence of the overpressure more than it minimised that of the SWs. The continuous flushing of the over-pressurised channel may have reduced the energy in the fluid which in turn reduced the static pressure experienced at the focus, thus restoring cavitation. Note that the dual PCD focal region



(a) (b) (c) (d) (e)

Figure 5.5: Examples of the measured cavitation bubble collapse times for the first 100 shocks, within the experimental TMMs for five different conditions. The subscript numbers indicate the triplicate sample number.

corresponded to a volume in the TMM comprised of part agarose and part channel, and therefore the effect of flow would have manifested here.

Interestingly in the Opt SWs + 700 kPa samples, there were a few cavitation events (<10 out of 100) with t_c similar to those observed in the optimal SWs alone, but these were likely to have resulted by contributions from the pressure pump vibrations which, particularly at this higher pressure, may not have been completely eliminated. Vibrations lead to energy loss in the fluid, which, as suggested above will minimise the impact of overpressure.

The mean t_c values are provided in Table 5.1 alongside the collapse amplitudes (A_c) which were rendered dimensionless from the signal processing. Conversion to pressure units, signified the pressure radiated by the main bubble collapse (p_c), and has been previously derived by calibration of the PCDs in water [183]. However, the complex nature

Table 5.1: Results summary of cavitation measurements based on n=3

Treatment	t_c (μs)	A_c (unitless)
Opt SWs	318.9 ± 12.0	3.2 ± 0.9
Opt SWs + flow	306.3 ± 7.3	2.9 ± 2.5
Opt SWs + 350 kPa	284.2 ± 1.1	3.2 ± 0.6
Opt SWs + 700 kPa	259.5 ± 8.0	0.3 ± 0.2
Opt SWs + 700 kPa + flow	287.7 ± 0.1	2.6 ± 0.5

of the test environment made calibration challenging and the *relative* changes were deemed sufficient to contrast conditions. Thus the amplitudes (A_c) sufficed. The minimum t_c and A_c were generated by the 700 kPa overpressure, and were lower than SWs alone by circa 19% and 91% respectively. This weakening of the bubble collapse but more importantly the significantly low count of cavitation events, suggested that inertial cavitation was suppressed at this condition. A comparison could be made by considering the difference in time between any two t_c measured at different lithotripter charging potentials (or energy levels), reported in the literature; because the cavitation characteristics (t_c and p_c) of a PCD signal will increase with increasing SW energy. Bailey et al.[185] noted at least a 30 μs difference in t_c between two charging potentials (i.e. between 15 and 18 kV,

as well as between 18 and 21 kV). In our overpressure experiments, 350 and 700 kPa yielded a difference of 35 μs and 59 μs respectively, relative to optimal SWs alone.

Next, the cavitation detection system was tested by assessing degassed TMMs. Figure 5.6 shows that the number of cavitation events decreased when SWs alone (a) were delivered to the TMM which was consistent with the expectation that pre-existing nucleation would be removed by the degassing procedure. When flow was applied (b), cavitation occurred for most SWs, suggesting that nuclei were introduced by flow; and the t_c was reduced, which was in accordance with observations made from Figure 5.5. In addition, despite respective decreases in the mean t_c relative to their non-degassed (Figure 5.5(a & b)) counterparts, degassing did not dramatically reduce the collapse times, for reasons likely to be those mentioned in Section 5.2.4.

In the subsequent studies, treatments were reduced to all those that did not include flow, because as shown in Table 5.1 the effect of flow was small – reducing t_c by only 4%

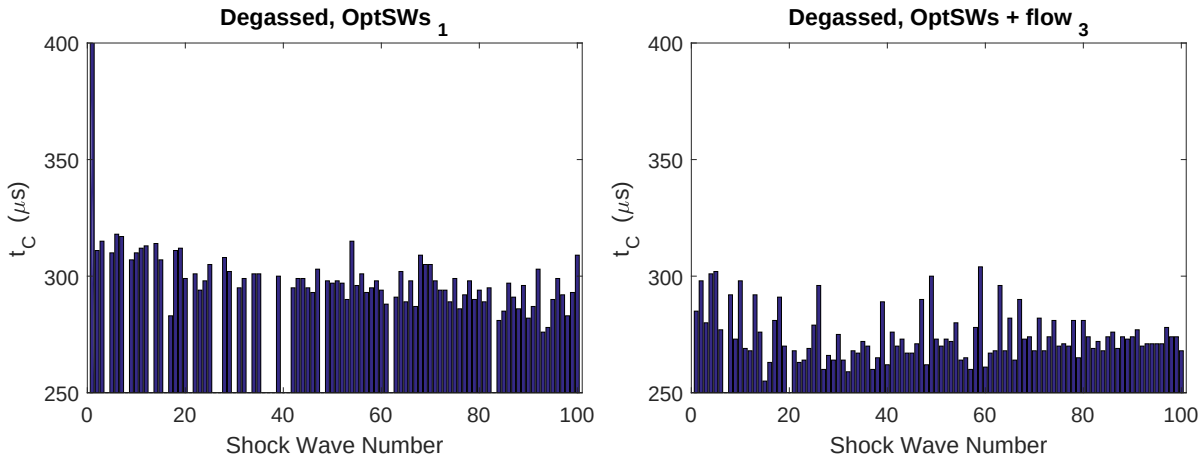


Figure 5.6: Representative cavitation bubble collapse times for the first 100 shocks within the **degassed** TMMs (note that the subscript numbers merely indicate the triplicate sample number).

relative to SWs alone; whereas in the presence of overpressure, flow reinstated cavitation.

5.3.2 mRNA delivery: single cells versus spheroids

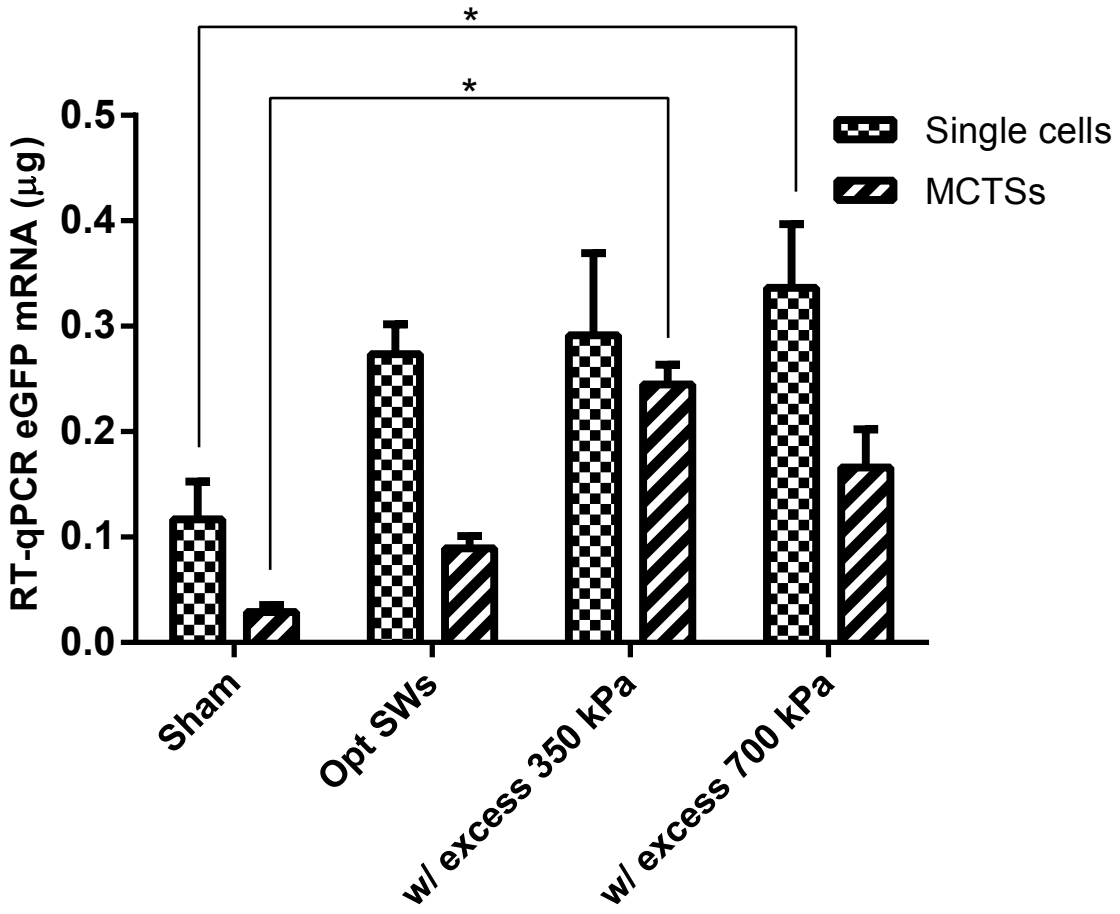
Equivalence in cell number between cell formats was sought by administering an approximately similar number of total live cells within the spheroids, to that of the

single cells. However, in comparison, many live cells in the spheroids were limited by their buried location as not all would have been surface-exposed.

Figure 5.7(a) presents results of internalised eGFP mRNA by RT-qPCR quantification, for both cell formats. Group-wise statistical significance was analysed using the two-way ANOVA test as shown in Figure 5.7(b) revealing high statistical power between treatment groups as well as between cell formats. Moreover, the relationship between cell formats and mRNA uptake did not depend on the treatment as indicated by the interaction p-value of 0.129, suggesting that the uptake variance between single cells and MCTSs was not specific to a given treatment.

Optimal shock waves alone, mediated the net uptake of $\sim$0.14 μg in the single cells but only 0.06 μg in the spheroids. It is noted that the optimal SWs were optimised in single cell conditions (*recall the SW optimisation in Chapter 3*) and therefore may not necessarily generate optimal uptake in the spheroids. Additionally, no statistical significance was found in the single cells with SWs alone, as inferred by the post-hoc Bonferroni analysis, which agreed with the quantitatively poor transfections determined in Chapter 4. The Bonferroni test was applied because it is the most conservative post-hoc statistical method, in order to eliminate the likelihood of false negatives from relatively small sample sets.

The application of the overpressures, led to a progressive increase in the uptake of single cells with increasing overpressure; whereas in the spheroids, while uptake increased with both overpressures, the most was attained at 300 kPa. The highest net (sham corrected) uptakes for single and MCTSs were 0.22 μg at 700 kPa and 0.23 μg at 350 kPa respectively. Thus, our initial hypothesis appeared to have failed through the single cell data because it was speculated that the relatively lower cell-to-cell interaction would have inhibited shear stress induced RNA internalisation. However, there were valid causes for shear stresses to have still been activated in the single cells. Firstly, 500,000 cells were contained in the 2 mm channel, hence at a density of 5,000 cells/μL which was considered to be high enough for shock wave induced cell-to-cell interactions to occur as suggested in Chapter 3, Figure 3.2, whereby higher cytotoxicity was observed when the cell concentration was increased to 500,000/mL (that is, 500 cells/μL), presumably due to more cell collisions. Secondly, a free (permeabilised) cell is



(a)

Source of Variation	Statistical significance	p-value
Treatments	$p < 0.001$	0.0006
Cell format	$p < 0.001$	0.0006
Interaction	n.s.	0.1290

(b)

Figure 5.7: (a) internalised mass of eGFP mRNA as quantified by RT-qPCR, after the various treatments at n = 3, in both cell formats (single cells and MCTSs); * represent $p < 0.05$ determined by Bonferroni multiple comparison tests. (b) Two-way ANOVA statistical analysis; n.s. represents no statistical significance at the $p < 0.05$ level.

able to internalise exogenous material at any point on its circumference. Consequently, there was opportunity for enhanced uptake in this cell-packed environment, mediated by increasing SW induced shear stresses with increasing overpressure. The reader is reminded of the impact of overpressure on minimising the SW negative pressure, therefore inhibiting the development of cavitation bubbles. Dissolution (or crushing) of cavitation nuclei by overpressure has been previously indicated [205]. Besides these effects on cavitation, direct mechanical stresses are increased as a result of the increased ambient pressure.

On the other hand, the response of the spheroids to the overpressures brought forward two different inferences, as next described:-

1) The overpressures suggested that inertial cavitation was not responsible for mRNA uptake by the spheroids, because at the higher overpressure (700 kPa) whereby cavitation was significantly reduced (*recall Table 5.1*), uptake did not fall below that which was attained with shock waves alone. However, shear stress, which was likely to be driving uptake, would have led to the increase in delivery at 350 kPa. Indeed, too much shear stress may have no longer been beneficial, and instigated a damage mechanism for the nucleotides; explaining the relative decline in intracellular eGFP mRNA at 700 kPa. Levy et al.[275], measured shear degradation of pDNA in solution, at conditions that reflected the shear forces exerted during plasmid bio-processing. Therefore, the occurrence of critical shear induced by shock waves could be strongly assumed.

2) The susceptibility of cell damage in spheroids compared to single cells in suspension is thought to be greater. It was suggested that the optimal transfectability of spheroids would have probably entailed a lighter SW dose due to the density of the individual spheroids, and the concentration of circumferential cells (being the first to have made contact with the shock waves). In support, Williams et al.[202] exposed spun down and suspended cells in vials to 75 shocks, and found lysed cells to be over three times higher in the spun down cells. Thus, given that the optimal SWs were not specifically optimised using spheroids, the increased uptake at 350 kPa may have been a result of decreased cavitational damage from the impact of the shock waves alone, through which a refinement of the SW parameters may have occurred. With further cavitation reduction, as produced by the 700 kPa overpressure, the SW tensile pressure may not

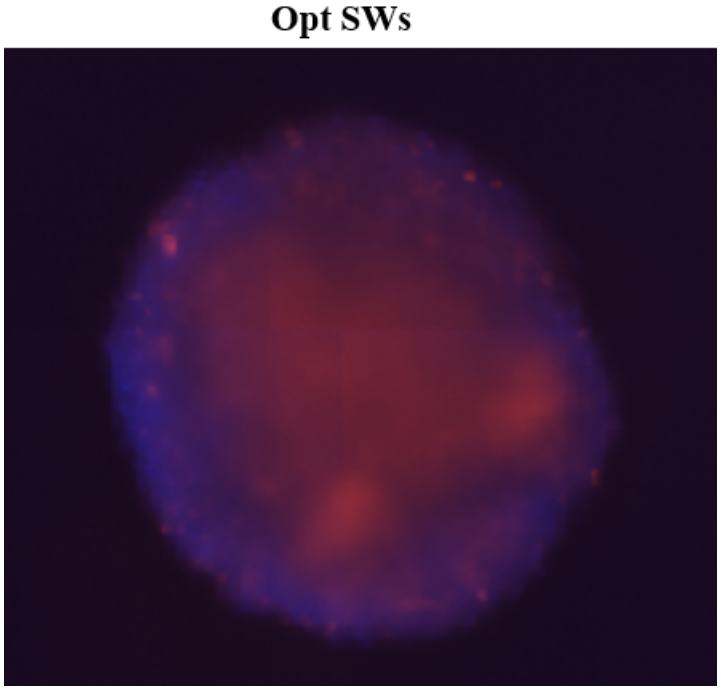
have been high enough to instate meaningful cell permeabilisation, as indicated by the lower mRNA delivery observed at 700 kPa compared to 350 kPa.

5.3.3 siRNA delivery: the effect of overpressure on MCTSs

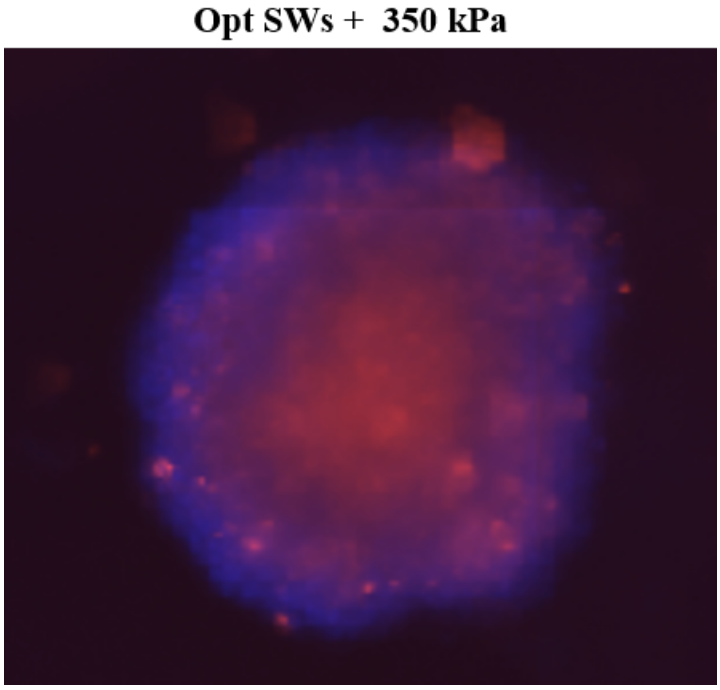
Having determined the efficiency of mRNA delivery in the CT26 spheroids with or without overpressure, this work was extended to the delivery of non-coding siRNA whose average molecular weight is between 13 and 14 kDa [276], that is, at least 22 times smaller than the mRNA transcripts (1,000 nucleotides) so far employed. The siGLO Red siRNA fluoresced upon nuclear localisation thereby indicating the intracellular presence of the siRNA. The Celigo cytometer was utilised due to high throughput imaging as well as to simplify the workflow, enabling an entire spheroid-containing well-plate to be analysed in one go. Figure 5.8 displays examples after each treatment, and represents the horizontal centre of the spheroids, as the image-based autofocus worked by focussing on the brightest signal which typically corresponded with the middle of the spheroids (assuming they were uniformly stained). In all the treatments that included the siGLO Red, the siGLO had penetrated into the inner part of the spheroid, and was passively taken up by the cells' leaky membranes as inner core cells are typically dead. The latter was confirmed by the negative controls (Figure 5.8(e)) whereby the Calcein Blue AM cell viability marker stained only the peripheral cells. On the other hand, the grainy appearance of bright red fluorescence co-localised with the blue fluorescence was indicative of specific intracellular delivery of the siRNA. On the contrary, bright fluorescent signals emanating from fairly large speckles within the non-viable core, as shown most clearly in the Sham spheroid example (Figure 5.8(d)), were artefacts that arose from non-uniform deposition of the siGLO into dead cells. It was safe to say that such artefacts were more likely to occur in the sham control samples, due to the lack of physical motion that they were subjected to.

The effect of overpressure on siRNA uptake was readily perceived, as demonstrated in Figure 5.8(b & c). Relative to the shock waves alone (a), both the 350 and 700 kPa revealed higher siRNA delivery, that surpassed the spheroid outer surface. Moreover, the brightness of the siRNA positive cells was visibly higher with overpressure, which provided favourable evidence for the contribution of local forces in enhancing the plasma membrane permeability.

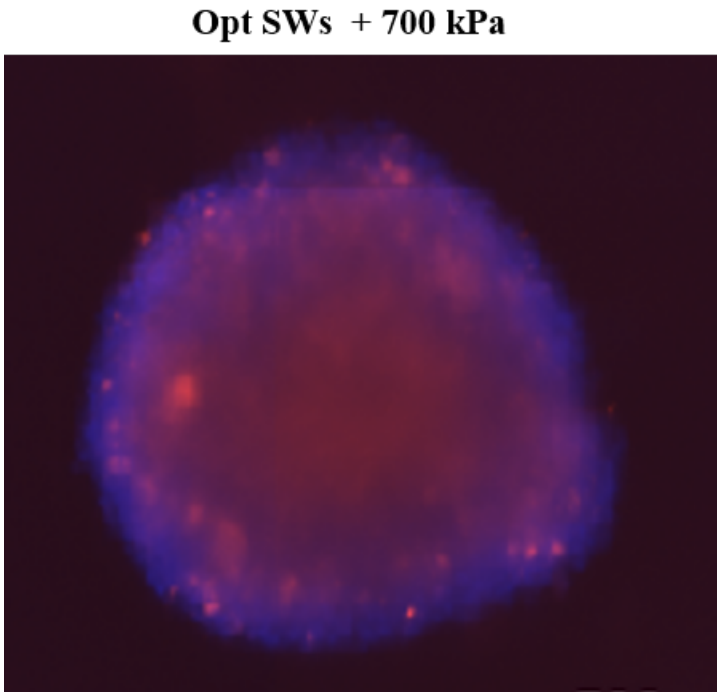
The intensity measurements of the fluorescent markers are presented in Figure 5.9; the cell viability (as quantified by the average Calcein pixel intensity) increased in the presence of overpressure compared to SWs alone, which was consistent with the significant mitigation of cell damage in cavitation-suppressed environments such as that reported by Delius et al.[203]. To assess the siRNA uptake intensities, the average siGLO pixel intensities were multiplied by the spheroid area over which the siGLO signal was present. It was found that the maximum siGLO integrated intensity was produced by the 350 kPa overpressure, but that the intensity was maintained elevated by the 700 kPa overpressure. The minimal siGLO intensity determined in the negative controls was the background signal produced by the Celigo's red filter. Statistical analysis (as performed using the one-way ANOVA and post-hoc Bonferroni tests) revealed a statistically significant difference at the $p<0.05$ level for both overpressures, relative to shams. Further, significant difference was also found between the Calcein signal of the negative control and that of the optimal SWs, indicating the impact of cavitation on cell damage. Altogether, these results confirmed the scope for non-cavitational mechanisms in gene delivery, particularly, for the uptake of small molecules such as siRNA.



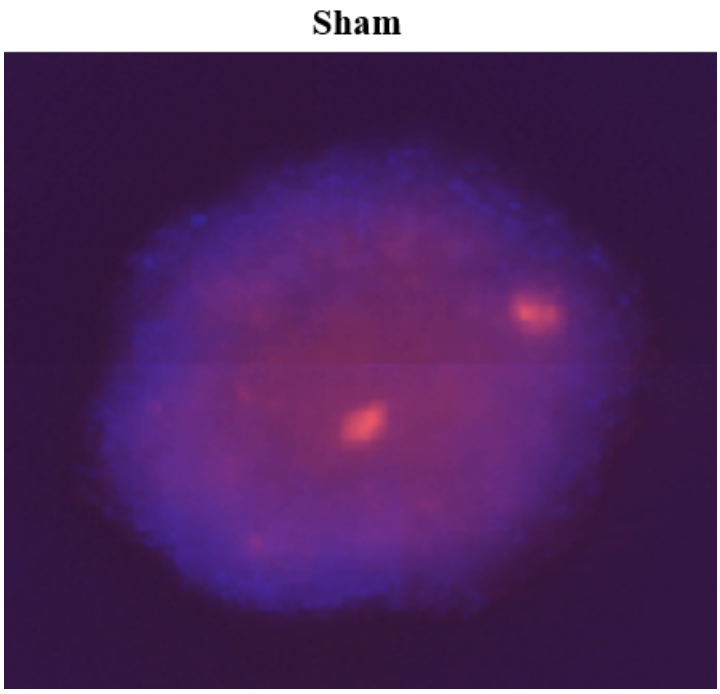
(a)



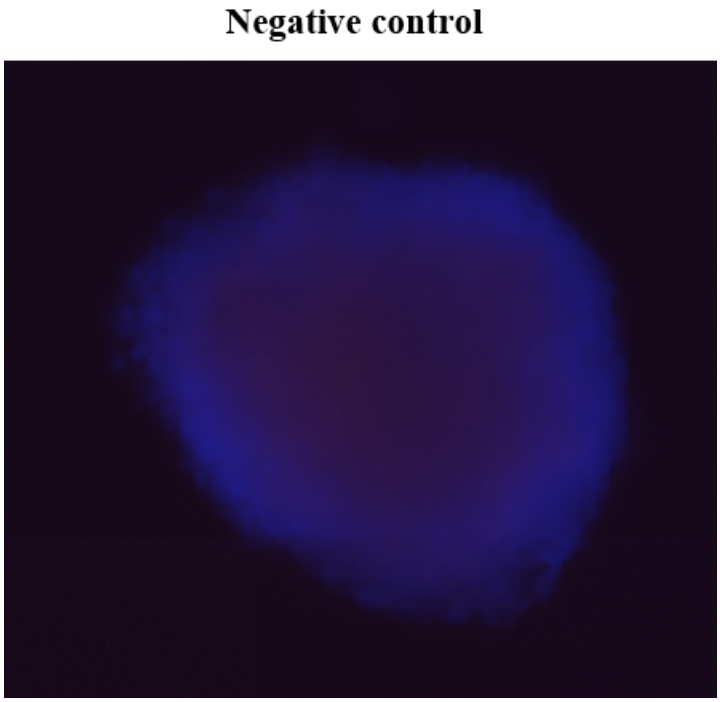
(b)



(c)

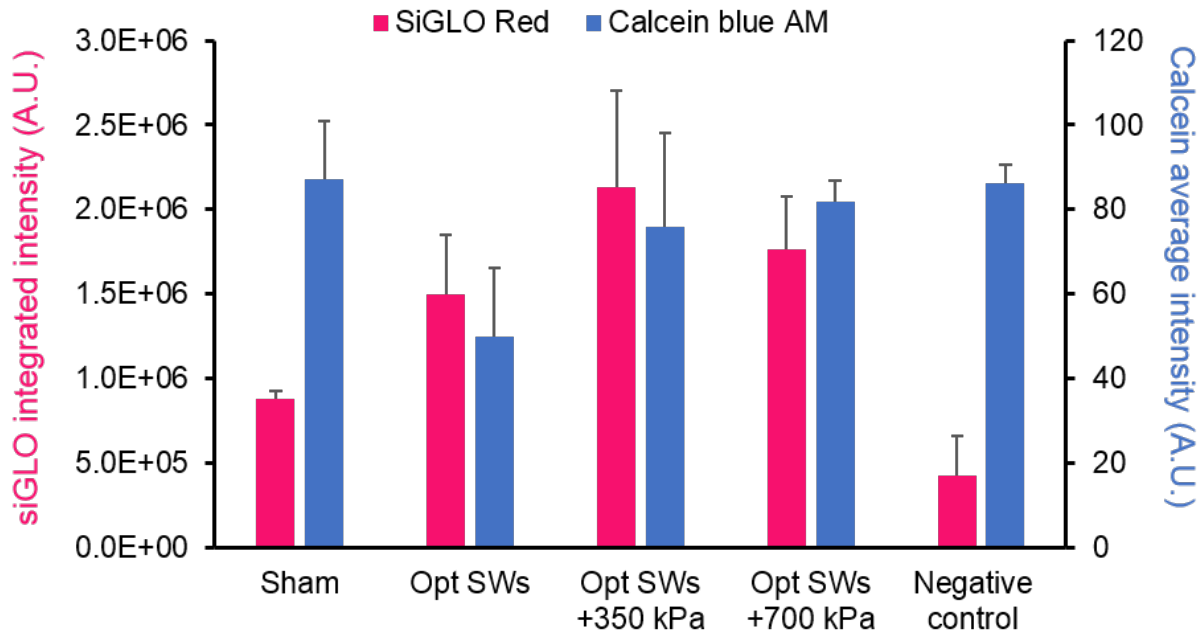


(d)



(e)

Figure 5.8: Examples of SiGLO Red uptake and cell viability (through Calcein Blue AM) in the spheroids, after treatment to (a) optimal shock waves (denoted by 'Opt SWs'), in addition to (b) 350 kPa overpressure or (c) 700 kPa overpressure; (d) sham treatment and (e) no treatment to SiGLO Red nor shock waves.



(a)

SiGLO comparisons	Bonferroni test
Sham & Opt SWs	n.s.
Sham & Opt SWs + 350 kPa	$p<0.01$ ($p = 0.0013$)
Sham & Opt SWs + 700 kPa	$p<0.05$ ($p = 0.0356$)
Opt SWs & Opt SWs + 350 kPa	n.s.
Opt SWs & Opt SWs + 700 kPa	n.s.
Opt SWs +350 kPa & Opt SWs + 700 kPa	n.s.

(b)

Calcein comparisons (wrt negative control)	Bonferroni test
Sham	n.s.
Opt SWs	$p<0.05$ ($p = 0.04$)
Opt SWs + 350 kPa	n.s.
Opt SWs + 700 kPa	n.s.

(c)

Figure 5.9: (a) Results of fluorescence intensities in the spheroids after the various treatments. Data consists of three replicate samples for one independently conducted experiment. Note that each sample consists of a set of spheroids and therefore each sample was an average itself. Error bars are the standard deviations. (b & c) statistical significance analyses for siGLO and Calcein fluorescence, using the one-way ANOVA with Bonferroni multiple comparisons tests; n.s. denotes no significance at the $p < 0.05$ (95% confidence interval) level.

5.4 Discussion

Previous work has shown that shock wave induced cavitation can be reduced by: increasing the ambient pressure ([201, 202]), modifying lithotripter waveforms ([206]) or using an acoustic diode ([208]). These studies have focused on understanding the role of cavitation in cell, tissue or vessel damage. While the goal has been to exclusively weaken the undesirable effects of cavitation (like tissue damage and vascular injury), there would have likely been a collateral decrease in the efficiency of desirable biological effects, as conveyed by Delius et al.[203] whereby they reported minimisation of cell permeabilisation with increasing overpressure. Furthermore, the impact of overpressure on the delivery of drugs or genes has not been previously addressed.

The present study was designed to suppress cavitation in order to determine the influence of shear stresses generated by the passage of shock waves through multi-cellular CT26 spheroids, on RNA delivery. As such, static overpressures were employed to remove cavitation nuclei from the sample. The compression of air was expected to be large at overpressures around 1 MPa, but the resulting compression of agarose which has a bulk modulus of $\sim$2 GPa, was estimated to be less than 0.1%.

Lithotripter-based cavitation activity was herein characterised by determination of the bubble cloud collapse times and amplitudes. The 700 kPa overpressure, substantially decreased the number of cavitation events and reduced t_c and A_c by 19% and 91% respectively, signifying the minimisation of the shock wave negative pressure. Reports by Stonehill et al.[201] and Delius et al.[203] demonstrated that considerably low overpressure was required to minimise cavitation in cells compared to solids such as aluminium foil and gallstones. The effect of fluid flow on the cavitation activity was also informed as shown in Figure 5.5(b & e). Flowing liquids tend to increase the occurrence of cavitation as at high enough flow speeds the pressure may fall (assuming negligible friction) below the vapour pressure of the liquid, causing nucleation [277]. In the present case, flow consistently increased the number of cavitation events, suggesting the introduction of nuclei.

Spheroids with a mean diameter of $\sim$533 μm were employed as they represented the largest size that could be adopted for the establishment of catabolite gradients (thus, mimicking real tumours), that did not impede handling during sample preparation and

well-plating because at this size they were visible to the naked eye. This was important, as it not only prevented physical tampering of the spheroids, but also promoted exact spheroid counts which were crucial for reliable comparison to single cells.

Spheroid imaging was realised in 2-D, as opposed to 3-D which would have entailed confocal microscopy, because for spheroid sizes around the region of 600 μm and above, these larger objects suffer from substantial light scattering from cells and high background due to out-of-plane fluorescence [278]. Therefore, the imaging cytometer was ideal as it processed high-content spheroid plates, and precluded sources of error such as time differences between staining and imaging amongst samples (and consequently variations in stain penetration). In addition, the red (siGLO) and blue (Calcein AM) fluorophores were selected as they did not spectrally overlap, such that the intensity measurements obtained from each filter were exclusive to the individual fluorophores.

The net (sham corrected) maximum mRNA uptake observed from both cell format groups was alike, indicating a 'capacity' of uptake that was independent of the experimental cell format, and likely to be a property mostly associated to the cell type, as evidenced by the various cell types tested in Chapter 3. In the spheroids, the RNA uptake trend across treatments was also similar between mRNA and siRNA. However, in the presence of siRNA, there was statistical significance at both overpressures (Figure 5.9(b)), as opposed to only at 350 kPa, as seen in the delivery of mRNA. Interestingly, Levy et al.[275] found shear sensitivity to largely increase with nucleotide molecular weight. Thus, shear damage was less susceptible to siRNA than to mRNA, giving reason to the sustained siRNA uptake at both overpressures.

Further, the acoustic mediation of cell uptake by underlying shear stresses is consistent with remarks made in a review by Miller et al.[279] who stated that a decrease in cell size increased the critical shear stress required to disrupt the membrane. In this work it was hypothesised that compared to the spheroids, the single cells would require a higher level of shear force to cause cell permeabilisation, whereas the large stresses within the spheroids would have lowered the critical shear stress. In fact, Figure 5.7 suggested that single cells required greater overpressure to significantly increase mRNA uptake compared to spheroids whereby half of the overpressure was sufficient.

Finally, there was a high likelihood of SW induced shearing effects due to the fact that the spheroids or single cells were suspended in fluid (as opposed to being embedded into the agarose) at high intra-cluster density or cell density respectively, as well as the anticipated interactions with the solid agarose boundaries that confined the thin channel; therefore promoting collisions and fluid streaming within the small channel volume. Moreover, an additional effect (which has been weakly proposed for kidney stones) is spallation [20], whereby reflections of the compressive wave at an interface may lead to a wave inversion and thereby an increase in the damaging tensile stress. However, in the present experiments the speed of sound could not have significantly changed across the interface between cells and medium, because the speed of sound in water is similar to that of tissue; suggesting that spallation should not considerably contribute to the observed bio-effects.

5.5 Closing Remarks

The influence of overpressure on lithotripter shock wave cavitation and shock wave-mediated mRNA and siRNA delivery in tumour models has been demonstrated at static pressures of 350 and 700 kPa. The overpressure resulted in reduced cell damage and enhanced delivery compared to treatment to shock waves alone. Induced shear stress was attributed to these effects, which were more pronounced in the delivery of small RNA molecules. Thus, in the clinic appropriately implemented cavitation suppression methods could be applied to protect tissue, without decreasing gene uptake.

6

Exploitation of a Lipid Nanoparticle and Cavitation Nuclei for Enhanced Transfection

Contents

6.1 Opening Remarks 129
6.2 Materials & Methods 130
6.2.1 Cell lines & culture 130
6.2.2 Gel-based cell viability assay 130
6.2.3 Lipoplexes 131
6.2.4 Configuration and preparation of samples for transfection . . 132
6.2.5 Ultrasound set-up & beam profile 134
6.2.6 Shock wave & Ultrasound exposure parameters 136
6.2.7 Lipid nanoparticle and cavitation agent stability 136
6.2.8 Control tests with Lipofectamine 137
6.2.9 GFP expression quantification 137
6.3 Results 138
6.3.1 Shock wave parameter optimisation & selection of Ultrasound exposure parameters 138
6.3.2 Post exposure stabilities 144
6.3.3 Evaluation of the LNP compared to Lipofectamine positive control 148
6.3.4 Shock wave & Ultrasound mediated LNP delivery in suspended cells 149
6.3.5 Shock wave & Ultrasound mediated LNP delivery in embedded cells 153
6.4 Discussion 156
6.5 Closing Remarks 159

6.1 Opening Remarks

The use of nanoparticles to improve the delivery of systemically administered drugs and nucleotides has been proposed for many years. Nanoparticles can protect nucleotides from rapid degradation and clearance thereby extending their bloodstream circulation. In theory, such enhanced pharmacokinetics can increase the chances of passive uptake into tissue through the Enhanced Permeability and Retention (EPR) effect, thereby improving on efficacy in the treatment of solid tumours [280]. However, to date there are only two FDA and EMA[1] market approved nano-sized drug carriers in current clinical practice that are commonly being used, i.e. Doxil and Abraxane. Further, the true utility of the EPR effect *in vivo* has recently been questioned [281] and it seems that in many cases, the nanoparticles are so stable that they do not effectively release their cargo when they do reach their target site.

In response to these challenges, strategies that combine nano-scale carrier systems with externally applied stimuli have been investigated in a plethora of the available literature, in order to both enhance tumour penetration and trigger cargo release. To achieve this, the use of ultrasound mediated cavitation has been previously reported [248]. The application of therapeutic shock waves is therefore also worthy of investigation. In addition, the choice of nanoparticle bears significance on the outcome of delivery. Lipid nanoparticles (LNPs) are generally better than polymeric nanoparticles whereby notable toxicity and acidity have been observed, and have been shown to have less storage and leakage problems compared to liposomes [113]. Additionally, some of the work on LNPs has focused on establishing formulations that can modify the release profiles [282].

In this study [2], a novel lipid nanoparticle under development by AstraZeneca (AZ), UK, was employed with the goal of exploring the mRNA transfection efficiencies that could be achieved with therapeutic shock waves or ultrasound, in two different *in vitro* configurations. The tissue mimicking environment developed in the previous chapters was maintained here, in order to attain *in vivo* relevance.

[1] European Medicines Agency

[2] forming stage 1 of 2 of a collaborative investigation with AstraZeneca, UK.

The impact of administering pre-formed cavitation nuclei in biological tissue is an important one. Firstly, it permits lowering of the ultrasound intensity by reducing the energy required to induce transient changes in tissue. Secondly, these agents could promote improved bio-effect distribution due to their infiltrating micro/nano size. Thirdly, the dearth of nuclei *in vivo* by which cavitation would not be catalysed, is in theory resolved by the external supply of biocompatible ones. In this work, re-optimisation of the shock wave parameters in light of cavitation nuclei inclusion and lipid nanoparticle stability, was performed; and suitable focused ultrasound parameters were also generated. Finally, eGFP mRNA delivery was quantified by flow cytometry and confocal microscopy.

6.2 Materials & Methods

6.2.1 Cell lines & culture

The selected lines for this study were CT26 (ATCC, CRL-2638) and a syngeneic subclone (AP3) of mouse melanoma skin cells B16-F10 (supplied by AstraZeneca, UK). CT26 cells were cultured as described in Chapter 3. B16-F10(AP3) cells were cultured in high glucose DMEM with L-glutamine, and supplemented with 10% fetal bovine serum, 1% pyruvate, 1% MEM vitamins and 1% MEM non-essential amino acids (all by Thermo Fisher Scientific). A large frozen cell bank was created in order to keep the passage number employed for experiments under twenty. With the exclusion of CT26 cells, B16-F10(AP3) cells were grown to a maximum confluence of 80-85% because at higher confluences the cells began to secrete melanin which is toxic at high concentrations in the culture medium. Both cell lines were harvested and counted as previously detailed in Chapter 3.

6.2.2 Gel-based cell viability assay

The viability of gel-embedded cells post US or SW exposure was quantified by the release of a soluble cytoplasmic enzyme, lactate dehydrogenase (LDH), into the surrounding medium. Such release was made possible by the leaky nature of necrotic cells, marked by SW or US induced injury. The degree of cell damage was proportional to the amount of LDH detected through a colorimetric assay, which, due to its linearity enabled the determination of the non-viable cell population [283].

Samples were contained within the TMM-MINI phantoms (*recall Figure 4.4*). However, the 1% agarose compartment contained 1 million embedded cells, and the channel was filled with either PBS alone, or included the SonoVue cavitation agent. Homogeneous cell distribution across the TMM was achieved by mixing equal volumes of cells in 2X medium with 2% agarose at 37 °C prior to phantom injection. Note that depending on the number of phantoms required, a stock TMM was prepared, wherein the number of cells added was double the total number of phantoms (in order to expect 1 million cells in each).

After the respective cell treatments, the phantoms' exterior were sprayed with 70% ethanol and allowed to dry. The cylindrically shaped agarose/cell constructs were then released from the phantoms and transferred into 12-well plates. 2.5 mL of supplemented DMEM (for B16-F10(AP3)) or RPMI 1640 (for CT26) medium was added to each well, and the plates were incubated for 18 hours. On the same plates, nominal positive and negative controls were included. An appropriate positive control that signified maximum LDH release (or 100% cytotoxicity) was determined, either by lysing the cells before gel setting (referred to as 'endo-lysis' in this text), or by lysing through lysis buffer administration into the medium used to incubate the constructs (referred to as 'exo-lysis'). The negative control consisted of 2.5 mL complete medium alone. Subsequently, 50 μL samples of the media were collected from each well and plated into a 96-well plate for quantification of LDH release, using the Pierce^{TM} LDH cytotoxicity assay kit (ThermoFisher Scientific) and the FLUOstar Omega micro-plate reader. The assay was performed by adding 50 μL of the reconstituted LDH assay buffer to the test wells, incubating the plate at room temperature for 30 minutes protected from light, followed by the addition of 50 μL Stop solution. Cytotoxicity was calculated as follows:

$$\%Cytotoxicity = 100 \times \frac{A_{sample} - A_{sham}}{A_{maxrelease} - A_{sham}} \tag{6.1}$$

where A indicates the absorbance readings at 490 nm subtracted from readings taken at 680 nm.

6.2.3 Lipoplexes

The lipoplexes were developed by AstraZeneca (UK) and consisted of lipid nanoparticles (LNPs) complexed with eGFP mRNA (Trilink Biotechnologies). The LNP was composed

of ionisable and neutral lipids, producing positively charged (zeta potential: +13 mV) particles with a mean diameter of 85.98 nm (polydispersity index (PDI): 0.078).

6.2.4 Configuration and preparation of samples for transfection

Aspects of the cell's native three-dimensional environment were mimicked *in vitro* by two different cell systems set up in the TMM-MINI, as depicted in Figure 6.1. Analogous to blood cells residing in vessels which are surrounded by tissue, Figure 6.1(a) consisted of 1 million cells in serum-free suspension inside the phantom's channel, and all-round 1% w/v agarose as the tissue mimicking material. In contrast, the second cell system (Figure 6.1(b)) reflected cells within the tissue architecture in close proximity to a vessel, into which the therapeutic and agent were administered. Using a custom-built die that mounted directly onto the phantom (via its drilled holes), a 70 mm^3 space was created in the middle of the phantom to contain the embedded cells, for two reasons. Firstly, unlike cells in suspension which are stirred by the shock pulse, embedded cells are fixed and thus cells outside of the focal zone remain unaffected after shock wave treatment. Secondly, in view of the narrow focal volumes of the SW (Storz Minilith SL1, *recall Chapter 4, section 4.2.1*) and US (*see section 6.2.5*) sources, the inner 4 × 5.5 mm (D × L) cylindrical cell volume was better suited to the exposure fields. The filling technique consisted of first filling the surrounding 1% agarose through the top (indicated by the dashed line in the figure) with both the die and the channel-forming rod inserted. The agarose was then left to solidify, the die was dismounted and the created void was filled with 1 million cells in 1% agarose. This section was left to solidify before removing the channel rod and filling its space with the lipoplexes and cavitation nuclei in RNAse-free water.

Two cavitation agents were tested in this study: SonoVue (SV) microbubbles, which were developed as UCAs but can act as cavitation nuclei, and the Nanocup (NC) particles (both described in Chapter 2, section 2.2.4). SonoVue (Bracco, Italy) was reconstituted in accordance to the manufacturer's instructions which involved re-suspending the 25 mg lyophilised sulphur hexafluoride powder in 5 mL sodium chloride and vigorously shaking for 20 seconds. SonoVue was administered into the channel at a 1:100 dilution. On consideration of bubble longevity prior to SW/US treatment, the exposures were

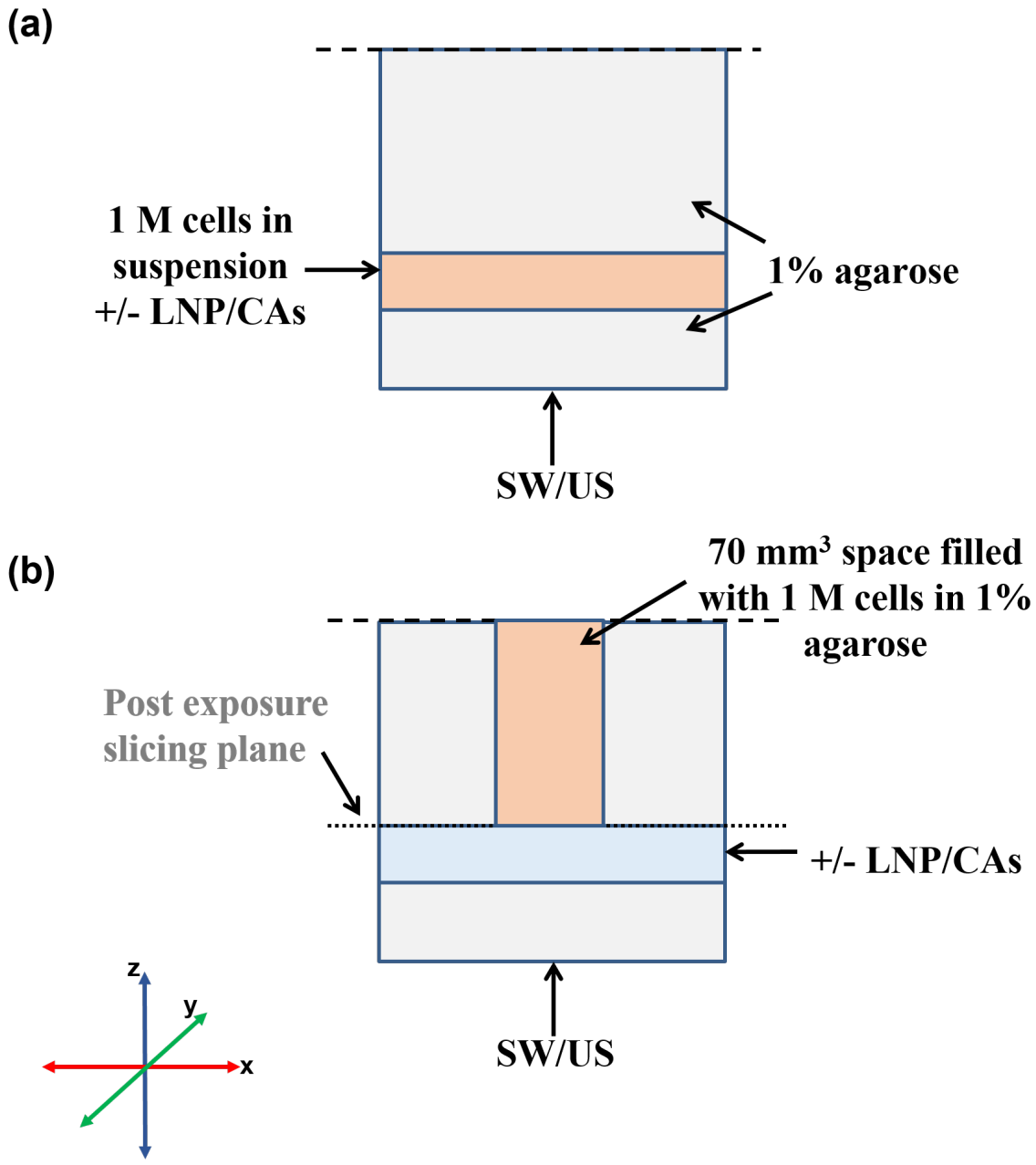


Figure 6.1: Schematic of the cell configurations within the TMM-MINI phantom, devised for the transfections; with (a) cells in suspension and (b) cells embedded in agarose; where the lipoplexed mRNA is denoted by *LNP*, and *CA* is the cavitation agent.

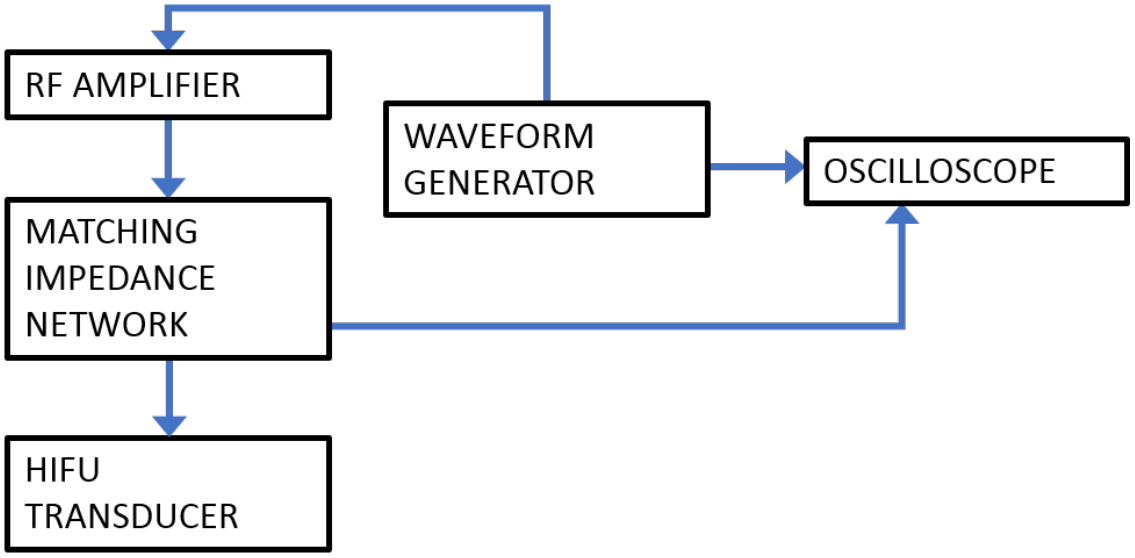
performed within ∼6 hours of SV reconstitution for each independently conducted experiment. The Nanocups (Oxsonics Ltd, Oxford, UK) were directly administered at a concentration of 1 mg/mL. Both cavitation nuclei concentrations were selected from a preliminary assessment that derived the lowest concentrations (between a selected few) that produced an apparent bio-effect enhancement compared to without nuclei.

Finally, 5 μg of the lipoplexed mRNA was supplied to each phantom channel and once added maintained cold until exposure, in order to prevent local temperature fluctuations.

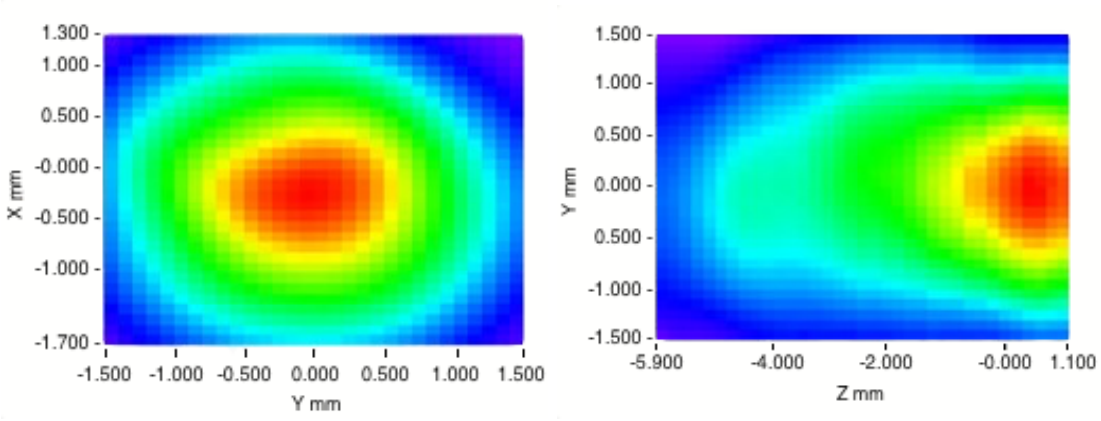
6.2.5 Ultrasound set-up & beam profile

The ultrasound source was a 0.5 MHz centre frequency focused ultrasound transducer (model H-107F-18; Sonic Concepts, Bothell, WA, USA) with a focal length of 64 mm and focus size of 3 × 20 mm (D × L) at 0.5 MHz. This working frequency was selected because frequencies below 1 MHz have been shown to decrease the inertial cavitation threshold [284], thus attaining cavitation associated with potentially less tissue damage. The transducer was attached to a previously designed coupling cone with an opening at its vertex, enabling localisation and fixation of the focus. The TMM-MINI was mounted to sit above the cone which was completely filled with water, by submerging the entire unit (i.e. transducer with cone, and phantom) underwater. Briefly, as outlined in Figure 6.2(a), a function waveform (Agilent 33250A, Agilent Technologies, CA, USA) was amplified (model 1140LA; Electronics & Innovation Ltd, NY, USA) to become a high power signal, and the impedance was matched (at the working 0.5 MHz frequency) to enable proper power transfer to the US transducer.

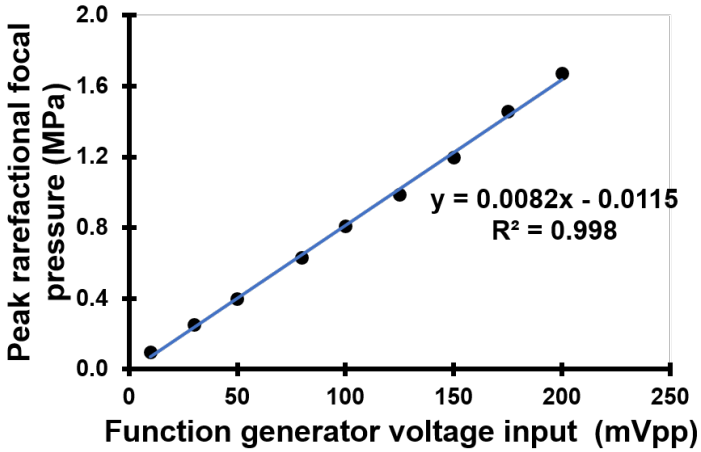
For beam profile characterisation, the TMM-MINI was built without its distal (with respect to transducer) Mylar sheet. The unit was then supported sideways inside a large tank of degassed water, in line with a needle hydrophone (Onda 1228, connected to a pre-amplifier (AH2010); Onda Corporation, CA, USA). The hydrophone was fixed to a 3-D translational rig, and transverse (X-Y plane) and axial (Y-Z plane) scans about the US focus, were performed using an automated control system (UMS, Precision Acoustics, Dorchester, UK). Transverse and axial scans of the ultrasound beam profile are shown in Figure 6.2(b) & (c) respectively. The middle of the phantom in the x-y plane corresponded to coordinates (x,y) = (0,0); while z=0 corresponded to mid-channel



(a)



(b) (c)



(d)

Figure 6.2: (a) The ultrasound set-up for the delivery experiments. (b) & (c) Characterisation of the ultrasound beam profiles inside a water-filled TMM-MINI. To enable hydrophone entry the TMM-MINI was assembled without the distal Mylar sheet. (d) Pressure calibration curve.

which was the arrangement used for experiments in the suspension format (Figure 6.1(a)). Thus, the focus fully encompassed the channel thickness (2 mm) where the cells were present. In view of the longer depth of the embedded cells format (Figure 6.1(b)), in those experiments the phantom was brought very close to the coupling cone such that the cylindrical cell volume was entirely inside the focus (20 mm long - *not fully shown*) in the axial direction. Additionally, calibration measurements relating the input voltage to the peak rarefactional pressure output (Figure 6.2(d)) were carried out. For the experiments, the unit was positioned with the base of the transducer sitting at the bottom of a 5 L tank which was continuously degassed and heated.

6.2.6 Shock wave & Ultrasound exposure parameters

The parameter search strategy employed in this study, utilised optimal exposure conditions to guide the establishment of conditions suitable for cavitation agent (CA)-assisted exposures. Optimal SW conditions for the other cell line (B16-F10(AP3)) were derived by the cell transfectability data acquisition and 2-D optimisation techniques detailed in Chapter 3 (section 3.3.3). A baseline set of SW conditions was performed consisting of energy levels 1, 4 and 8, and number of SWs: 125, 250, 500 and 1000, at 2 Hz. Subsequently, these optimal SWs were lowered for SonoVue inclusion, which was selected for the purpose of the CA-assisted parameter search, because of its extensive use in clinical practice compared to Nanocups.

A start point for the inquiry of US exposure conditions was determined through a preceding study [285] employing peak rarefactional pressures (PRFP) and exposure durations conducive to high-energy broadband emissions which lead to cavitation bio-effects. For minimal cell damage the selected low US frequency was accompanied by a low duty cycle (1.5%) to eliminate thermal effects. For consistency, the optimal PRF for SW exposures per cell line, were applied to the US exposures as well.

6.2.7 Lipid nanoparticle and cavitation agent stability

Similarly to the TMM configuration illustrated in Figure 6.1(a), the lipid nanoparticle (+/- CA) was suspended in double distilled RNAse-free water in the channel; however, in the absence of cells. Stability of the LNPs with or without the Nanocups post SW or

US exposure, was determined by dynamic light scattering (DLS) measurements using the Zetasizer Nano Range (model MAL1049741; Malvern Instruments Ltd, Malvern, UK). Immediately after respective treatment, the samples were transferred from the phantom channels to Zetasizer capillary cells and diluted 1:10 with RNAse-free water. The AccuSizer (model 780; Particle Sizing Systems Inc., Santa Barbara, CA, USA) was employed exclusively for sizing of the SonoVue particles, due to its dynamic range of 0.5-400 μm in order to capture the expected median of the SV microbubbles. Samples that included SV, were also diluted as stated above, which provided enough particles to be counted, yet below the concentration limit of 9,000 particles/mL.

6.2.8 Control tests with Lipofectamine

The cationic lipid-instigated cytotoxicity and transfection efficiency of the LNP were characterised and compared to that seen with the widely applied *in vitro* lipid-based transfection reagent Lipofectamine 2000® (Thermo Fisher Scientific). Using a 24-well plate, 200,000 CT26 cells were seeded per well in 1 mL supplemented RPMI medium. eGFP mRNA (Trilink Biotechnologies) was then complexed with varying amounts of Lipofectamine in OptiMEM medium and added to the wells at a final concentration of 500 ng mRNA/well and final Lipofectamine amounts 1, 1.5, 2 and 2.5 μL per well. For the LNP (which was already complexed with the mRNA), 0.82 μL was added to each well to obtain the same mRNA concentration. Upon a 48-hours incubation, GFP cell positivity was assessed by flow cytometry, while cell viability was determined using the MTS assay.

6.2.9 GFP expression quantification

After exposure, cell samples in the suspension format (Figure 6.1(a)) were extracted from the phantoms, plated in a 48-well plate, replenished with FCS-supplemented medium and incubated for 48 hours, at which point flow cytometry was conducted.

In contrast, cell samples in the embedded format (Figure 6.1(b)) were transferred into 12-well plates, and each well was supplemented with 2.5 mL OptiMEM medium and incubated for two days. Samples were then sliced at the interface between the channel and the cell-containing agarose compartment as shown in Figure 6.1(b), on a smooth petri-dish lid surface, using a wide blade scalpel. A Zeiss 710 laser scanning confocal

microscope (Zeiss LSM 710 NLO Axio Observer Z1; Carl Zeiss, Oberkochen, Germany) was employed for high resolution imaging of the samples. Briefly, a 10X plan-apochromat objective, was utilised for all acquisitions. A 488 nm laser line, set at a laser power of 5 – 24% provided the excitation light. To detect green fluorescence the appropriate filter was selected (505-630 nm) with a digital gain of 1.10. The default pinhole diameter of 33 μm was maintained as it provided a satisfactory compromise between high z-axis resolution and high signal intensity. Consecutive z-sections of the cell samples at the centre of the x-y plane, were obtained through z-stack scan mode with a step size of 5 μm. After image collection, the Zen imaging software (Carl Zeiss) in the image analysis module (thus far in scan mode) was used to universally apply an intensity threshold, to reduce the background fluorescence to a level that would not remove the distinguishable weaker fluorescent cells. The Z-stacks were saved in their native format (.czi) and fluorescence intensity quantification was performed using Fiji ImageJ.

6.3 Results

6.3.1 Shock wave parameter optimisation & selection of Ultrasound exposure parameters

Changing the exposure system necessitated a re-optimisation of the exposure parameters. Moreover, in view of delivery methods that can be very destructive, cell viability may be regarded as the most fundamental variable to quantify, after treatment. Building on from the cell viability protocols established in Chapter 3, it was desired to quantify cell viability in the same format in which cells were exposed. Despite utilising 'low melting point' agarose, its 65.5 °C melting point still meant that embedded cells could not be released for analysis without incurring total heat-mediated damage. Another tissue mimicking gel, 6% gelatine, was tested due to its low melting point of 35 °C but suffered from unpredictable liquefaction even in the absence of continuous water heating during the SW/US experiments.

Thus, the agarose gels, with *in situ* cell viability quantification were used with LDH release in the surrounding medium as the output. Figure 6.3 displays the colorimetric range from maximum (positive controls) to no (complete media) LDH release. The two

forms of positive control demonstrated that maximal release was obtained when cells were lysed *prior* to setting into the gel (denoted as 'endo-lysis'). Samples treated with optimal

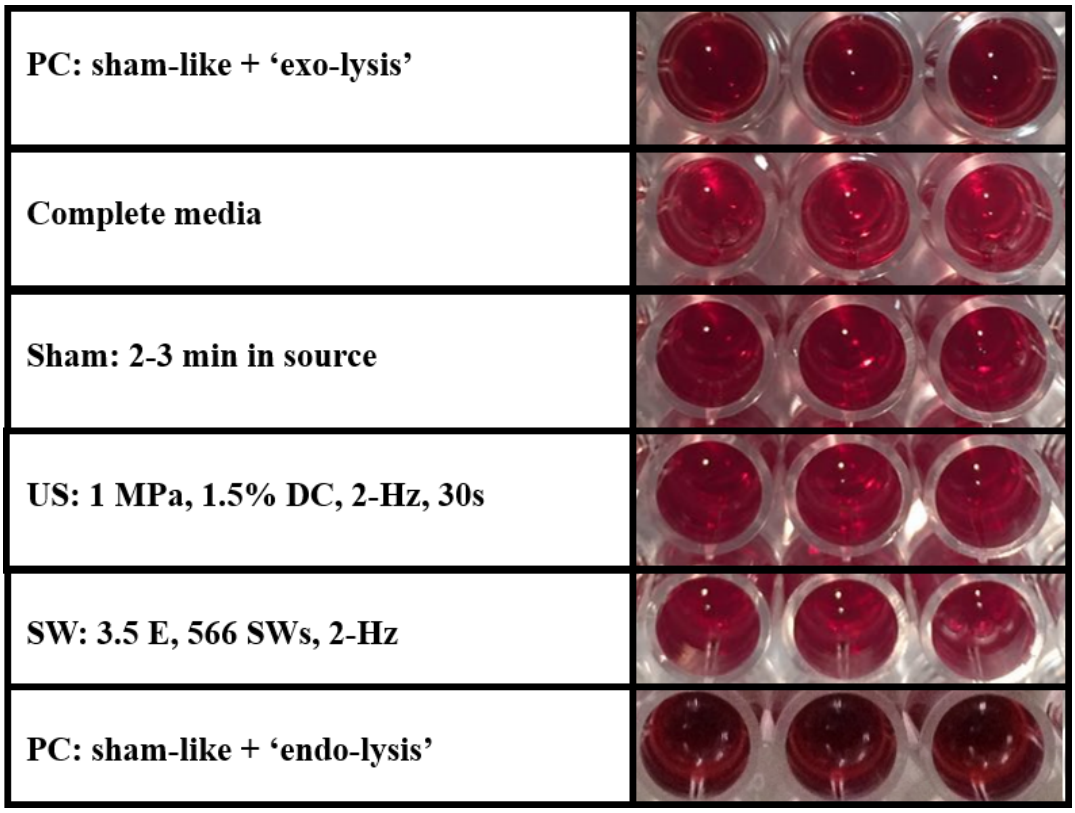
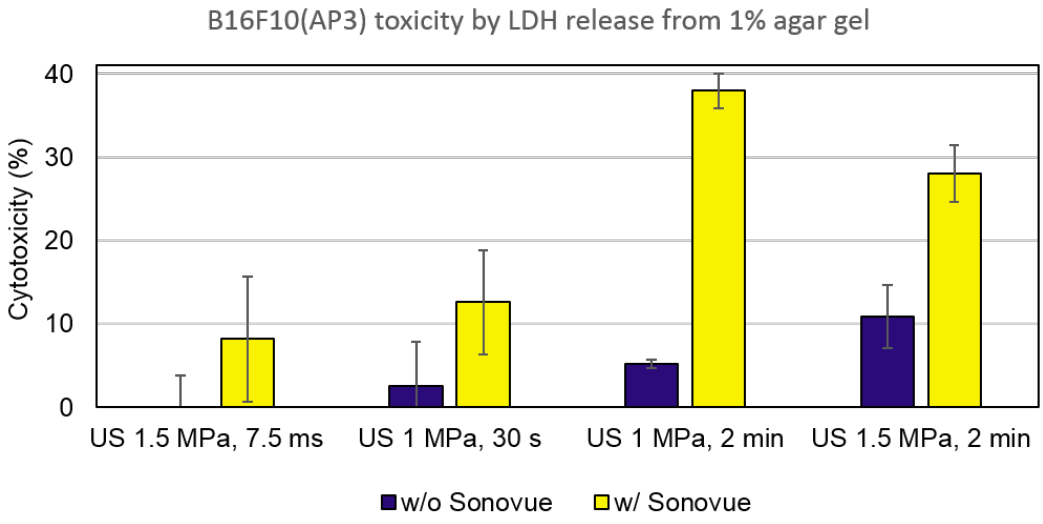


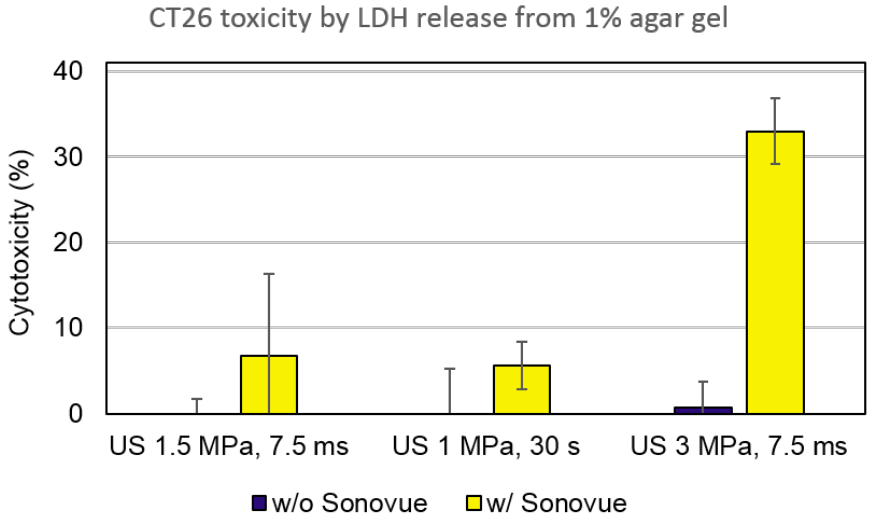
Figure 6.3: A representative plate read-out image of lactate dehydrogenase (LDH) release, from CT26 cells exposed to selected US and SW conditions, 18 hours after exposure. PC = positive control. The colour intensity increased with LDH release increase.

shock waves were confirmed to have minimal cell death relative to the sham samples, as evidenced by optical inspection. The same was apparent with the preselected US conditions, potentially revealing an approximately apt parameter spot for efficient gene delivery. Other conditions of lesser or greater intensity were tested, revealing differential cytotoxicities marked by longer exposures or the presence of a cavitation agent, as shown in Figure 6.4. In agreement with the results presented in Chapter 3, different cell lines demonstrated different responses to the same acoustic stimuli. However, while the magnitude of cytotoxicity varied between cell lines, the relative effect between treatments was maintained. A single US pulse (i.e. 7.5 milliseconds long) was sufficient to cause cell death in the presence of SonoVue, in both cell lines; whereas without SonoVue, a 30 second exposure was required for the B16-F10(AP3) cells to instigate cytotoxicity, but

not in the CT26 cells, which was thought to be the result of relatively low mechanical rigidity of the B16-F10(AP3) compared to CT26.



(a)



(b)

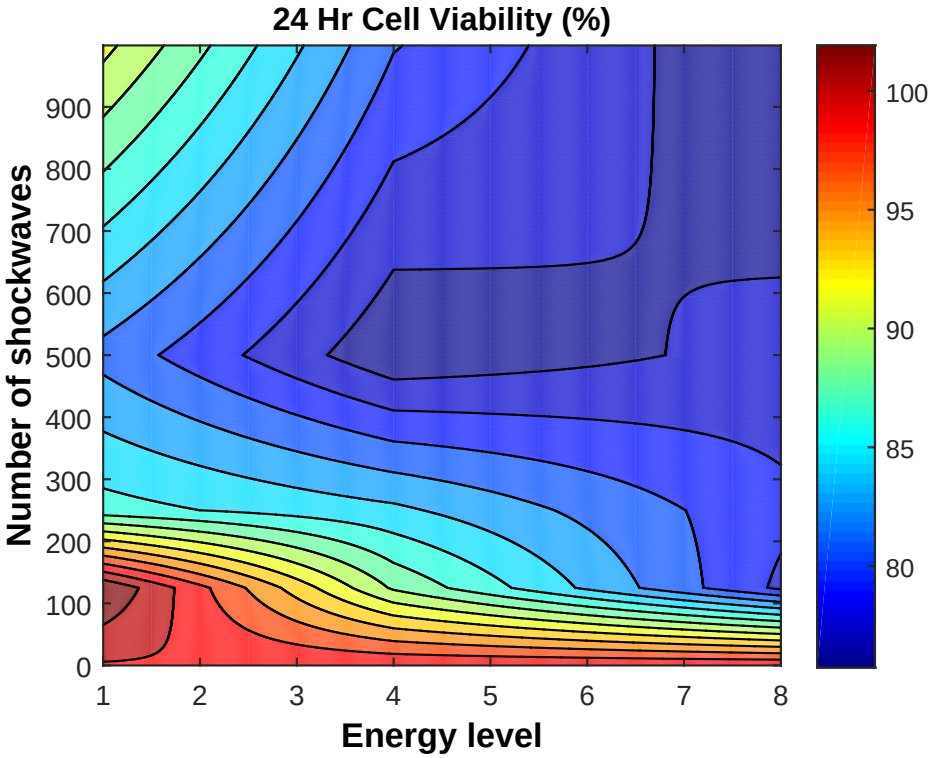
Figure 6.4: US induced cell cytotoxicity measured by LDH release from the agarose-based tissue mimicking material for (a) B16-F10(AP3) & (b) CT26, at nominated conditions, in the absence or presence of SonoVue. Peak rarefactional pressures of 1.0, 1.5 and 3.0 MPa were applied, while the exposure durations were: 7.5 ms, 30 seconds and 2 minutes. Results are based on n=3 and the error bars are the standard deviations.

In the B16-F10 cells (Figure 6.4(a)), the cell destruction caused at the longest exposure period, in the presence of SonoVue, appeared to have a greater impact at the lower

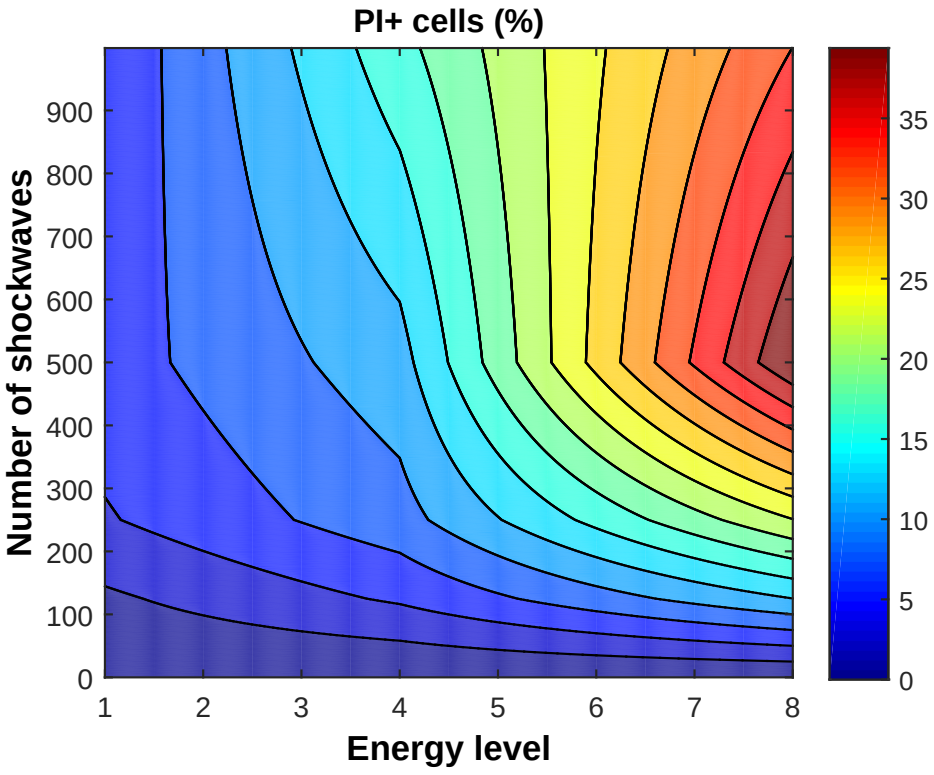
pressure amplitude (PRFP = 1 MPa). This may be indicative of some experimental error, variability in the exact SonoVue concentrations between samples (leading to the generally larger error bars observed with SonoVue), but more likely, was a result of the high polydispersity of SonoVue. Moreover, while the 1.5 MPa, 7.5 ms US treatment produced the least cytotoxicity, a longer exposure (30 seconds) was generally preferred for driving molecules deep into tissue, as opposed to a single US pulse. Indeed, the impact on efficiency of delivery was greater than the impact on the cell viability which was only effected by a ∼4% and ∼2.5% decrease for with and without SV respectively. On the other hand, in the CT26 cells (Figure 6.4(b)), high cell viability was maintained post US exposure in the absence of SV, and a mean cell death of 5.63% with SV at 1 MPa PRFP, 30 seconds treatment, was deemed satisfactory against the potential for therapeutic gain.

For optimal shock wave exposure, it was found that similarly to CT26 cells (Chapter 3), the transfectability of B16-F10 cells did not significantly change when the PRF was varied from 2-4 Hz (*see Appendix, A.5*). Figure 6.5 demonstrates maps of cell viability and permeabilisation as a function of SW energy level and number. It can be seen that the SW parameter with the greatest influence on the B16-F10 viability was the number of shock waves, while for permeabilisation it was the energy level. These observations have been previously observed in CT26 cells as well, and are in agreement with the tissue failure reported as a result of the cyclic loading through increasing shock waves [197]; and the higher transgene expression rates acquired at higher lithotripter capacitor voltages [23]. In both the cell viability and permeabilisation, there was increased dependence on the energy level with increasing number of shock waves. Figure 6.6 revealed that the energy level threshold for reversible B16-F10(AP3) permeabilisation was 5.5 which corresponds to peak positive and negative pressures of 17.66 and 5.52 MPa respectively, as measured in a water-filled TMM-MINI phantom. It should be noted that the stimulative effect of SWs on cell proliferation evidenced in the CT26 cells at low energy levels (*recall Figure 3.7, Chapter 3*), was not as marked in the B16-F10 cells.

Finally, for B16-F10(AP3) we report an expected transfection peak of 20.07% at energy level 8, 500 SWs, 2 Hz (where 8 is the highest attainable energy level of the employed Storz Minilith SW generator). However, at this optimal SW dose, which produced



(a)



(b)

Figure 6.5: Maps of B16F10(AP3) cell viability and permeabilisation in medium, after shock wave treatment at 2 Hz PRF. Data consists of three independently conducted experiments (n=9).

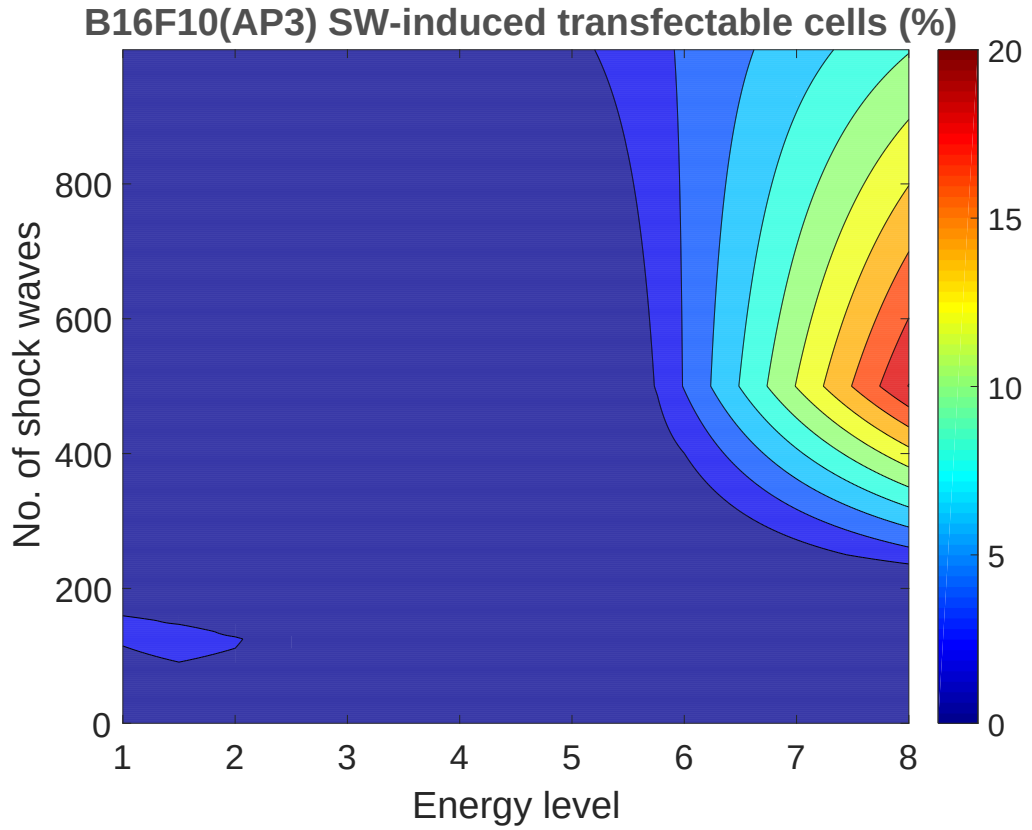


Figure 6.6: Shock wave induced transfectability of B16-F10 cells, as a function of shock wave energy and number.

the highest proportion of propidium iodide internalisation (42%) as shown in Figure 6.5(b), approximately only half of the cells were viable and thus capable of transfection. Moreover, while cancer cells are malignant such that unintended cell death may not necessarily be a bad thing, the success of transgene expression is set back by its occurrence. Furthermore, at the corresponding pulse-intensity integral (PII_{TP}, *defined in Chapter 4*) of 27.9 mJ/cm^2 significant damage to the mRNA-lipid assembly was guaranteed by the end of the shock wave treatment. Alternatively, lowering the SW dose, toward the outskirts of the transfectable zone (Figure 6.6) yielded poor transfection levels of ∼5%.

Shock wave exposure, assisted by cavitation agents, was tested using SW conditions that related to areas of low or no transfectability in the absence of CAs (*see* Figures 6.6 and 3.8 (Chapter 3) for B16-F10 and CT26 cells, respectively) because the additive effect that CAs instigate on cell damage at high areas of transfectability would cause too much loss of cell viability. In both cell lines the parameter region of 300 shocks, and 1 – 2 E, produced the lowest cytotoxicity in the presence of CA, within the TMMs. Figure

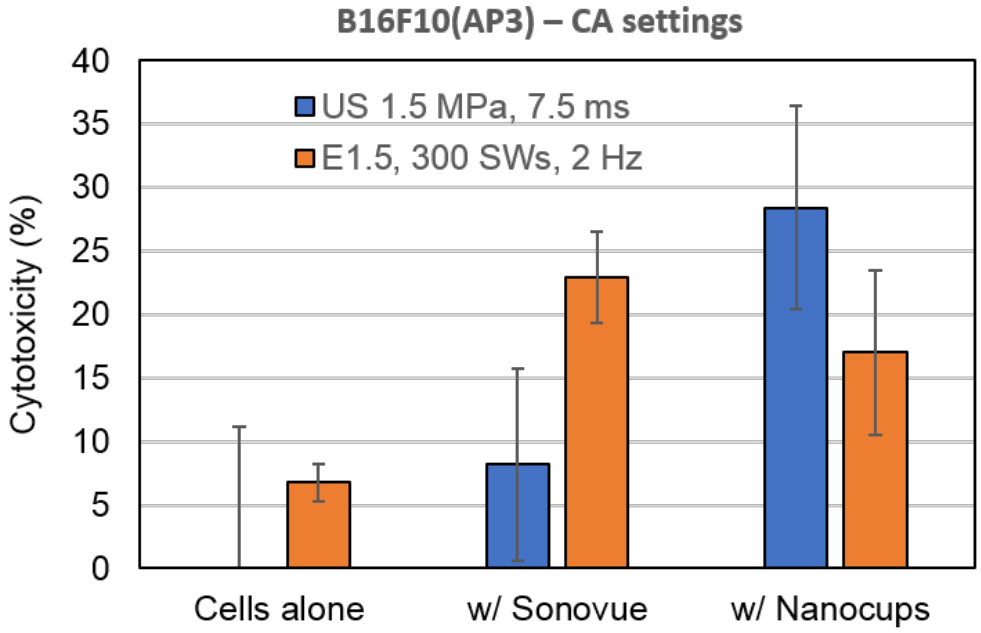
6.7 displays the SW or US induced cytotoxicities at the final settings defined for CAs.

There were key differences in the way the two different cavitation agents interacted with cells in acoustic fields. The Nanocups appeared to be more destructive in the US fields compared to shock waves, whereas SonoVue had a broader impact, encompassing dissimilar cell types. In the evidently more malleable cell line (Figure 6.7(a)), despite the minimisations of the US exposure duration and SW energy, cytotoxicities of up to 28% in the presence of CA, were found. However, in the CT26 cells, tolerable cytotoxicities in the presence of CAs (where the maximum was ∼6%) were identified. Nanocups did not have a detrimental influence on the mean viability of CT26 cells compared to cells alone, indicating the potential for efficacious therapeutic application of these cavitation nuclei.

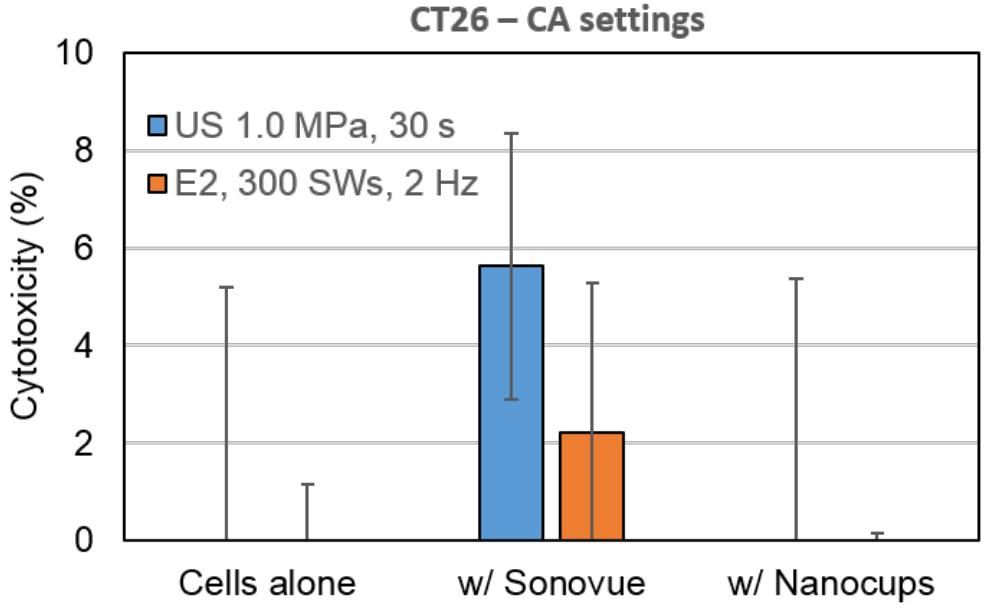
6.3.2 Post exposure stabilities

While biochemical stability is a property that is highly dependent on the lipid particle itself, acoustic fields have been shown to alter the physicochemical status or structure of lipid shells [286]. Dynamic light scattering size measurements of the lipoplexes were carried out before and after US or SW exposure, in the presence and absence of Nanocups, in order to provide information on structural changes and insight into the likelihood of cavitation.

Fresh (or in other words, newly drawn from stock) LNP (lipoplexes) and NC (Nanocups) were characterised separately and together in co-suspension as shown in Figure 6.8(a). Individually, the mean diameters of the LNP and NC were 85 (PDI: 0.1) and 545.6 (PDI: 0.05) nm respectively. However, when NCs and LNP were co-suspended, the mixture was found to increase the mean particle size and polydispersity of the major-peak population, while the intensity of free LNP (or in other words, LNP-only) significantly decreased. This was thought to be due to the larger NCs disproportionately scattering more light such that the LNP peak in the Fresh LNP + NC profile reduced in intensity compared to when measured on its own. However, the increase in size of the major-peak population suggested the formation of LNP and NC complexes due to the electrostatic attraction between positively (+13 mV) and negatively (>-20 mV [193]) charged nanoparticles. Such natural complexing, could be either beneficial or deleterious to the delivery of mRNA into cells. Non-excessively complexed NCs may hasten the LNP



(a)



(b)

Figure 6.7: Percent cytotoxicity through LDH release from the TMMs comprising (a) B16-F10(AP3) or (b) CT26 cells; at exposure conditions suitable for cavitation agent-assisted US and SW treatment. N=3; error bars are the standard deviations.

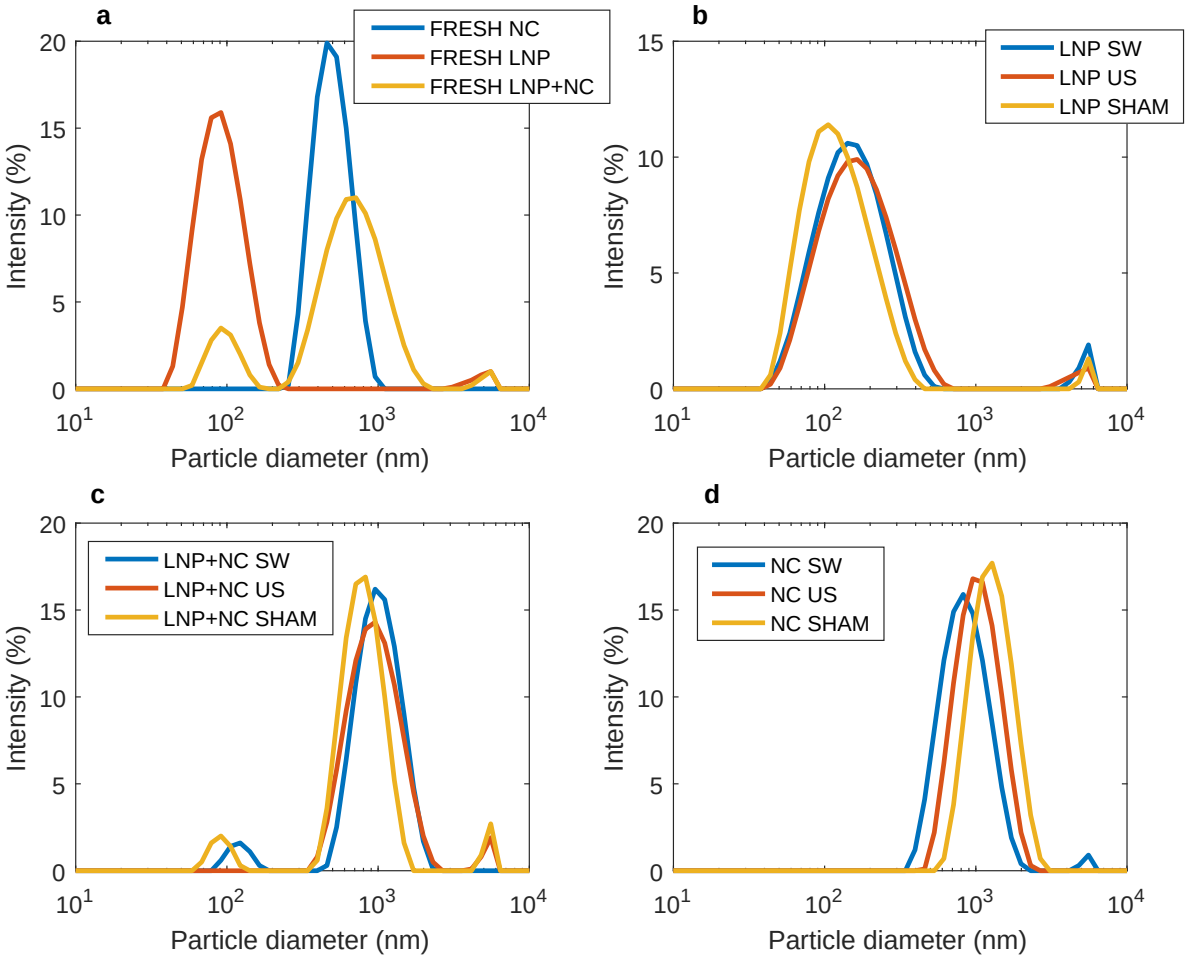


Figure 6.8: Representative dynamic light scattering measurements of LNP/NC size distributions based on n=3, after sham, shock wave or ultrasound treatment at respective optimised conditions for CT26, (a) fresh samples, (b) LNP samples, (c) LNP and NC samples, and (d) NC samples. The small peaks at 5560 nm are disregarded as micro-sized contaminants from the non-sterile Zetasizer cells.

release rates by promoting cavitation enhanced lipid shedding. Alternatively, significant impairment could be rendered to the functionality of the mRNA, if more NCs than what is required to affect only the lipid layer are complexed to the LNP (and therefore at a very short distance spatially to the mRNA). The damaging effect of microbubble proximity has been previously reported [219].

In Figure 6.8(b) the LNP alone was administered into the TMM channel. With the application of SW or US, the LNP particle mean diameter increased to 130 and 143 nm respectively. Many cationic lipids including distearol-glycero-phoshocholine (DSPC) are fusogenic [287], a property through which plasma membrane destabilisation has been reported in liposomal gene delivery [106]. Moreover, the cohesiveness of

lipid shells has been linked to the build-up of excess lipid as a result of acoustically induced lipid shedding [286].

The following case, is the interaction of sound waves with the NCs and LNP (Figure 6.8(c)). As previously noted, the co-suspension produced two distinct peaks. SW exposure in the presence of NCs demonstrated a similar right-shift of the LNP peak to that in Figure 6.8(b), thus, probably linked to a build-up of excess LNP. However, with US, the expected LNP-only population at 143 nm appeared to have been completely removed by NC activity. The same observation made earlier on the increased interaction of US fields with NCs (Figure 6.7), is relevant to the present finding. The ensuing effect, was not likely to be lipid fragmentation due to a lack of indication (indeed the resulting fragments must be accounted for somewhere in the particle size spectrum). Thus the most likely explanation for the absence of the LNP-only peak is that the LNPs had been propelled into the TMM as a result of Nanocup enhanced ultrasound induced penetration, and thus were not available in the channel post exposure.

Finally, we determined the destructive effect of US and SW on NCs as shown in Figure 6.8(d). The overall size deviation from the stock NC, was found to be a result of confounding interactions between the NCs and the phosphate buffered saline composed agarose gel, because when the gel was prepared in water instead, there were no apparent size differences between sham NC and stock NC (*refer to Appendix A.6*). Regardless, the mean particle diameters decreased by 35.6% in SWs and 25.4% in US, relative to the sham Nanocups, suggesting a relatively sustained NC stability, especially in the US field.

The attempt to characterise the stability of SonoVue post SW or US (Figure 6.9) revealed that the process of loading, exposing and sampling the SonoVue destroyed the vast majority of the formulation. SonoVue should record a mean diameter of 2–3 μm (*recall* Chapter 2, Figure 2.3). In these experiments the remaining SonoVue microbubbles recovered, even from the sham treatment, measured less than 0.80 μm. Addition of US or SW did not alter this population size or distribution. However the cytotoxicity results in Figure 6.7, where there was up to a 23% loss in the cell viability of the samples that included SonoVue, strongly implied that the set-up and technique employed here

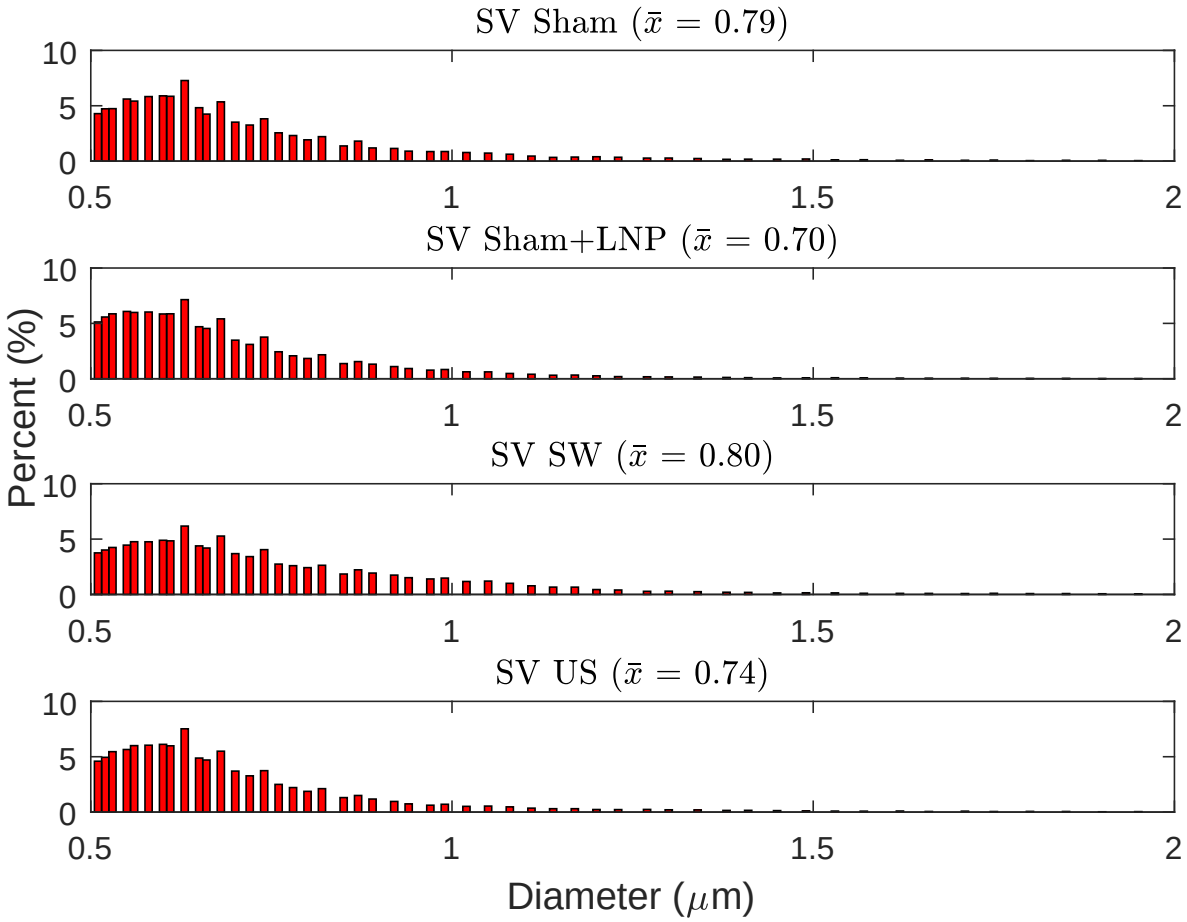


Figure 6.9: Stability results of SonoVue (SV) by optical particle size measurements (using the AccuSizer) post sham, US and SW treatments at their respective optimal conditions for CT26. Data is representative of n=3.

to sample the microbubbles after the treatments, did not permit their characterisation as only a sub-population could be recovered.

6.3.3 Evaluation of the LNP compared to Lipofectamine positive control

The level of lipid-based transfection efficiency is usually described by comparison to a standard such as Lipofectamine – a commercially available agent with a reliable success rate. The level of GFP expression achieved using the LNP did not exceed that of Lipofectamine at the higher liposome amounts (2 – 2.5 μL), as presented in Figure 6.10, which corresponded to the higher liposomal concentration range recommended by the manufacturer. However, across the various transfections, the percentage of GFP positive cells varied only by approximately 2.5%, where the LNP roughly constituted

the median value (3.2%). Such assessment shed light on the relatively poor performance of lipid vectors when administered alone; and thus the potential utility of such carriers with delivery technologies.

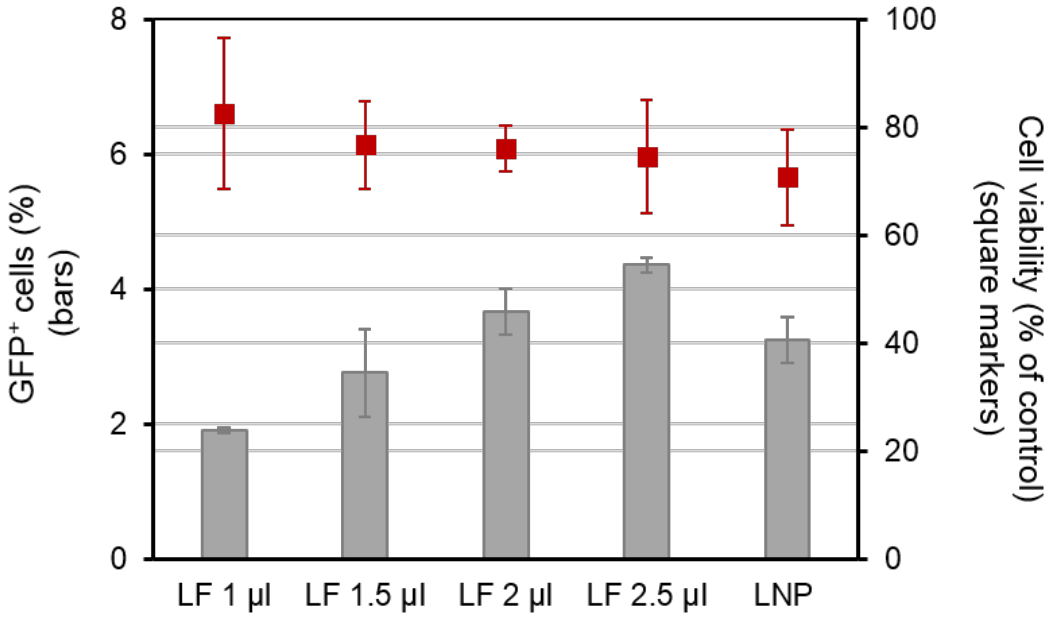


Figure 6.10: Comparison of *in vitro* lipid-based transfections on CT26 cells, between the LNP by AZ and various amounts of LF (Lipofectamine 2000). In all cases 500 ng of eGFP mRNA (Trilink Biotechnologies) was lipoplexed. Data represents n=3 for one independently conducted experiment. The error bars are the standard deviations.

The cell viabilities were found to be lower as a result of LNP transfection (70.7%) compared to all the Lipofectamine preparations (74.7 – 82.5%) as evidenced by the MTS cell viability assay, relative to non-treated controls (Figure 6.10). However, all cytotoxicities were satisfactory (>60%) and demonstrated that changes in the lipid content (of the lipoplexes) were accompanied by only small decreases in the cell viability.

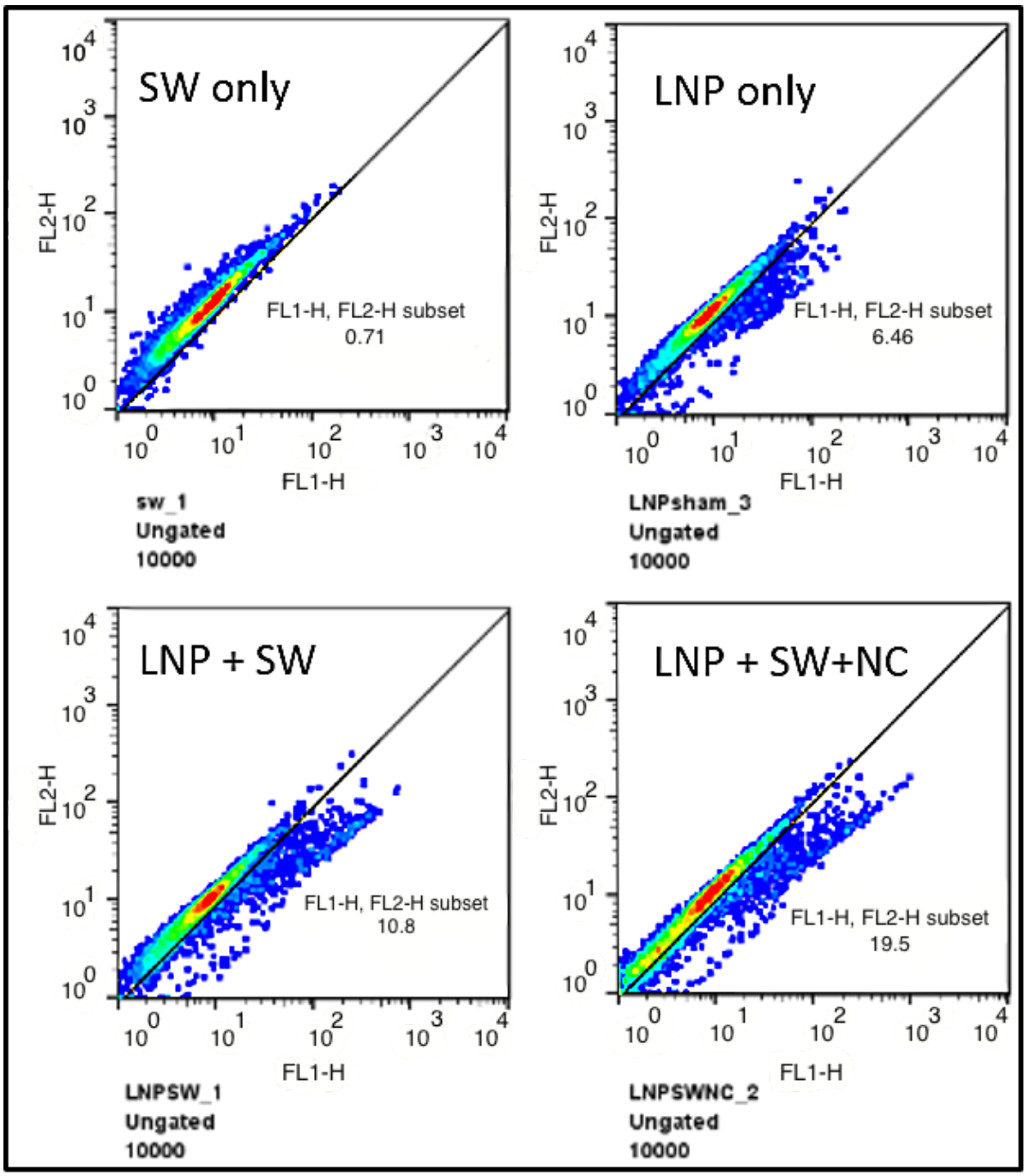
6.3.4 Shock wave & Ultrasound mediated LNP delivery in suspended cells

Experiments were streamlined in relation to the conditions that promoted enhanced transfection with the use of both focused ultrasound and lithotripter shock waves. As such, only the CT26 cells were tested for transfection, while the only employed cavitation nuclei were the Nanocups because they demonstrated the least compromise on the cell viability, and most reliable provision of extended cavitation as deduced in Figure 6.8(d).

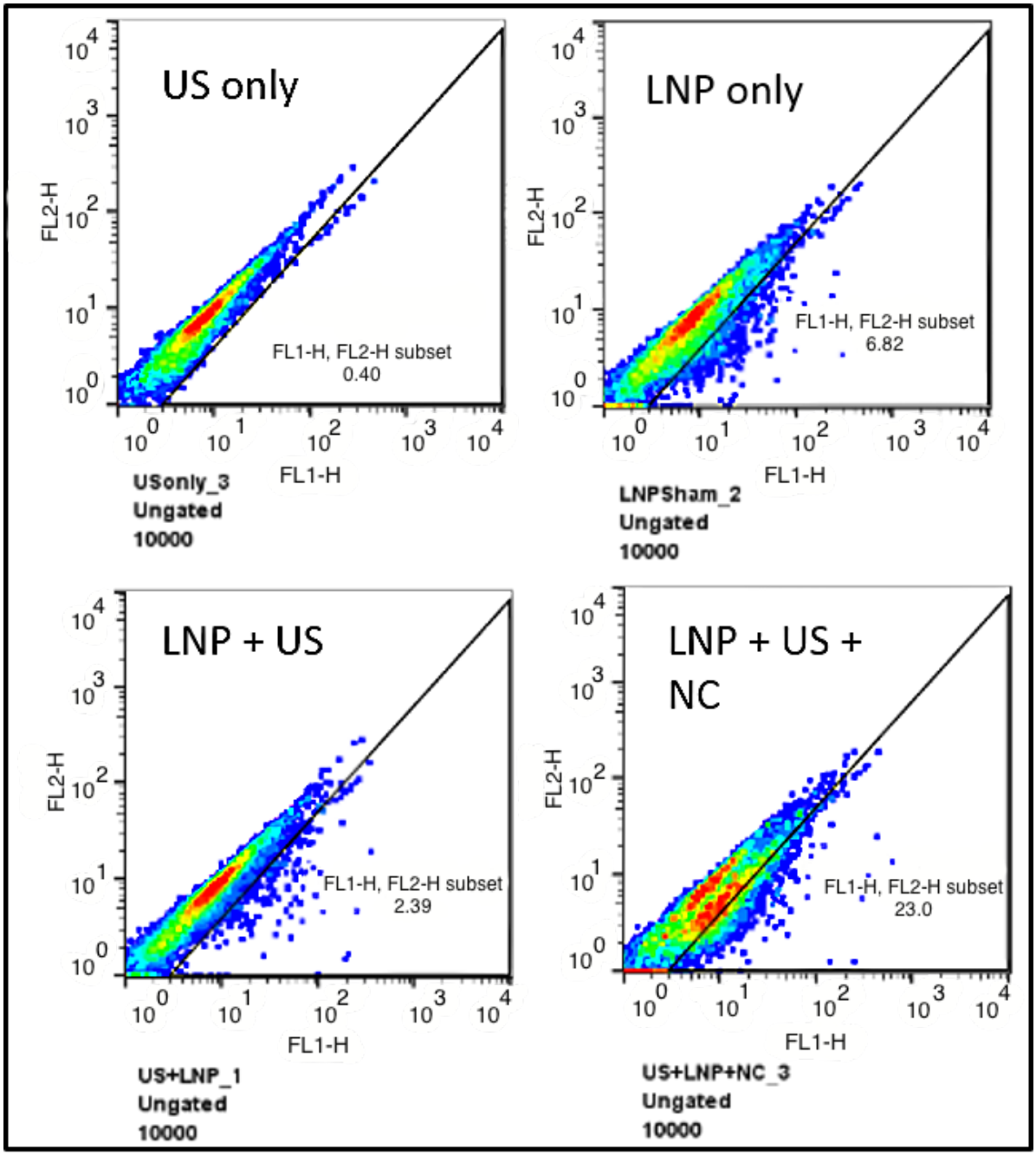
The expectations of the aqueous environment in which the CT26 cells were suspended in, were an increased probability of nucleation due to the gas content in the medium as well as shear forces at the fluid-gel boundary; ultimately leading to enhanced bio-effects.

Baseline green fluorescence was determined through SW/US treated negative controls (i.e. lacking in LNP) in order to report true GFP events in the LNP samples. It was noted that untreated negative controls produced identical background fluorescence to that of the treated negative controls. Representative GFP positivity in response to shock waves and the LNP vector, are demonstrated in Figure 6.11(a). For SW samples, the largest enhancement of GFP expression was found to be in the presence of NCs, whereby up to 3 times greater GFP positivity ($p < 0.001$) was noted relative to the sham LNP. Similarly to SWs, the addition of NCs to US exposure (Figure 6.11(b)) significantly ($p < 0.001$) enhanced mRNA delivery by approximately 3.4 times. In the absence of NCs, the parallel pattern of improved nucleic acid internalisation was minimised as follows: in SWs there was little improvement above the sham level (LNP only) whereas with US, GFP expression was significantly ($p < 0.05$) lower than the sham. This decrease of GFP expression in the US samples, may be due to the US-induced cell death (*recall* Figure 6.7(b)), where, even though the mean cytotoxicity was found to be zero, the spread in the data was $\sim$5%. It follows that even though the same level of variance was observed in the US + NC samples, the advantage of NC activity on LNP delivery, far exceeded the negative impact of US alone.

Additionally, both SW and US exposure produced distinct features. With SW application, there was a noticeable increase in the mean cellular fluorescence intensity of the 'LNP + SW' & 'LNP + SW + NC' samples by 3.55% and 6.45% respectively. Instead, US application saw the evolution of a bi-population in the presence of NCs, of which the population with increased FL1 fluorescence signified a pronounced enhancement in GFP expression; indeed, separating this positive population proved challenging even by diagonal gating and so the value of 23% GFP positive cells may be an under-estimate of the level of successful US + NC mediated LNP delivery. These results suggested some key advantages of both modalities including the ability of shock waves


SW only
FL1-H, FL2-H subset
0.71
FL2-H
FL1-H
sw_1
Ungated
10000
LNP only
FL1-H, FL2-H subset
6.46
FL2-H
FL1-H
LNPsham_3
Ungated
10000
LNP + SW
FL1-H, FL2-H subset
10.8
FL2-H
FL1-H
LNPSW_1
Ungated
10000
LNP + SW+NC
FL1-H, FL2-H subset
19.5
FL2-H
FL1-H
LNPSWNC_2
Ungated
10000

(a)


US only
FL1-H, FL2-H subset
0.40
USonly_3
Ungated
10000
LNP only
FL1-H, FL2-H subset
6.82
LNPSham_2
Ungated
10000
LNP + US
FL1-H, FL2-H subset
2.39
US+LNP_1
Ungated
10000
LNP + US +
NC
FL1-H, FL2-H subset
23.0
US+LNP+NC_3
Ungated
10000
FL1-H
FL2-H

(b)

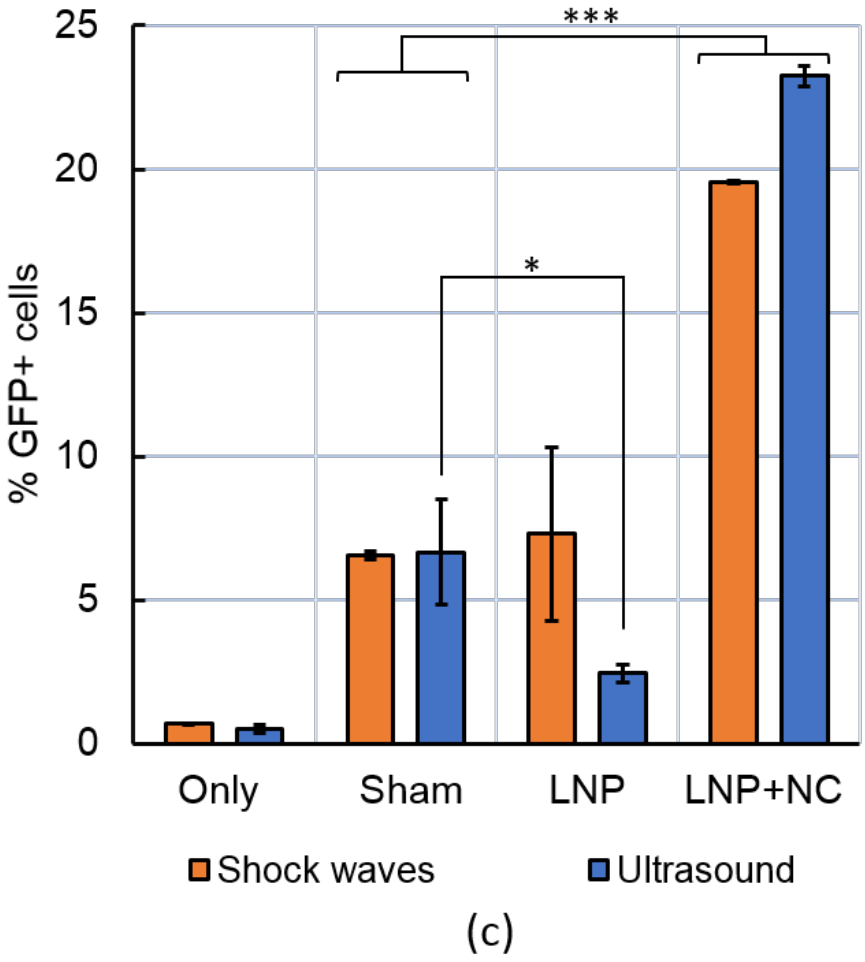


Figure 6.11: Quantification of GFP positivity in the cells in suspension exposure configuration; (a) representative flow cytometric measurements of GFP positive cells by FL1-FL2 diagonal gating, for SW conditions and (b) for US conditions. (c) results based on n=3 for one independently conducted experiment. The two-way ANOVA with Bonferroni multiple comparisons tests, revealed statistical significance at $p < 0.05$ (*) and $p < 0.001$ (***) relative to the corresponding sham controls.

to load macromolecules into cells, and the synergistic effect of focused ultrasound with nano-sized cavitation nuclei.

6.3.5 Shock wave & Ultrasound mediated LNP delivery in embedded cells

Many of the gene therapy limitations observed *in vivo*, centre around the conveyance of the delivery vector into and throughout the target site. It is for this reason that the local injection treatment option has been supported at least in situations such as non-metastasised solid tumours or in the treatment of cells left behind from an excised

tumour cavity [113]. In any case, the delivery vector must traverse either the interstitial space (in intratumoral injection) or in addition the vessel wall (in intravenous delivery) before getting to a cell. In these experiments, the utility of ultrasound and shock waves in conjunction with cavitation nuclei, was pronounced due to the inability of the LNP alone to penetrate the tissue mimicking material as shown by the confocal z-stack sections in Figure 6.12. Not surprisingly, an insignificant proportion of cells had taken up and expressed the mRNA in the LNP only samples (Figure 6.12(a)). With the addition of ultrasound (LNP + US, *not shown*), GFP fluorescence was not detected. The application of shock waves (LNP + SW), produced an apparent increase in expression but it was found to be mostly due to an increase in autofluorescence which could be distinguished from GFP by uneven intracellular fluorescence distribution, resulting in bright non-circular and irregular shapes rather than the bright round spots that characterised GFP cells. Such discrimination was possible by high-resolution probing of individual cells, using the confocal microscope.

The application of cavitation nuclei alongside either modality, induced densely localised GFP expression as shown by the imaged regions in Figure 6.12(c) & (d), but they were not homogeneously spread across the entire TMM face (radius = 2 mm) facing the channel top edge (X-Y plane). GFP expression generally increased up to a certain distance from the channel edge (i.e. along the Z-thickness of the TMM), as quantified in Figure 6.13. Comparison between samples by mean fluorescence intensity (MFI) was appropriate since the background intensity was equal across all the z-stacks (because acquisition and thresholding settings were kept the same throughout), and it could be assumed that the TMMs were identical across treatment groups [3], such that the scattered light from the agarose was a constant. As such, the MFI in the LNP + SW + NC samples peaked at 155 μm above the channel edge, signifying an increased number of GFP+ cells. A secondary peak appeared at 225 μm and declined thereafter, further indicating the inhomogeneity of SW induced transfection. Interestingly, in the LNP + US + NC samples, the peak MFI – which was circa half of that observed with

[3] while slight differences in composition may have arisen from pipetting error, all samples were always prepared from the same cells and agarose stock.

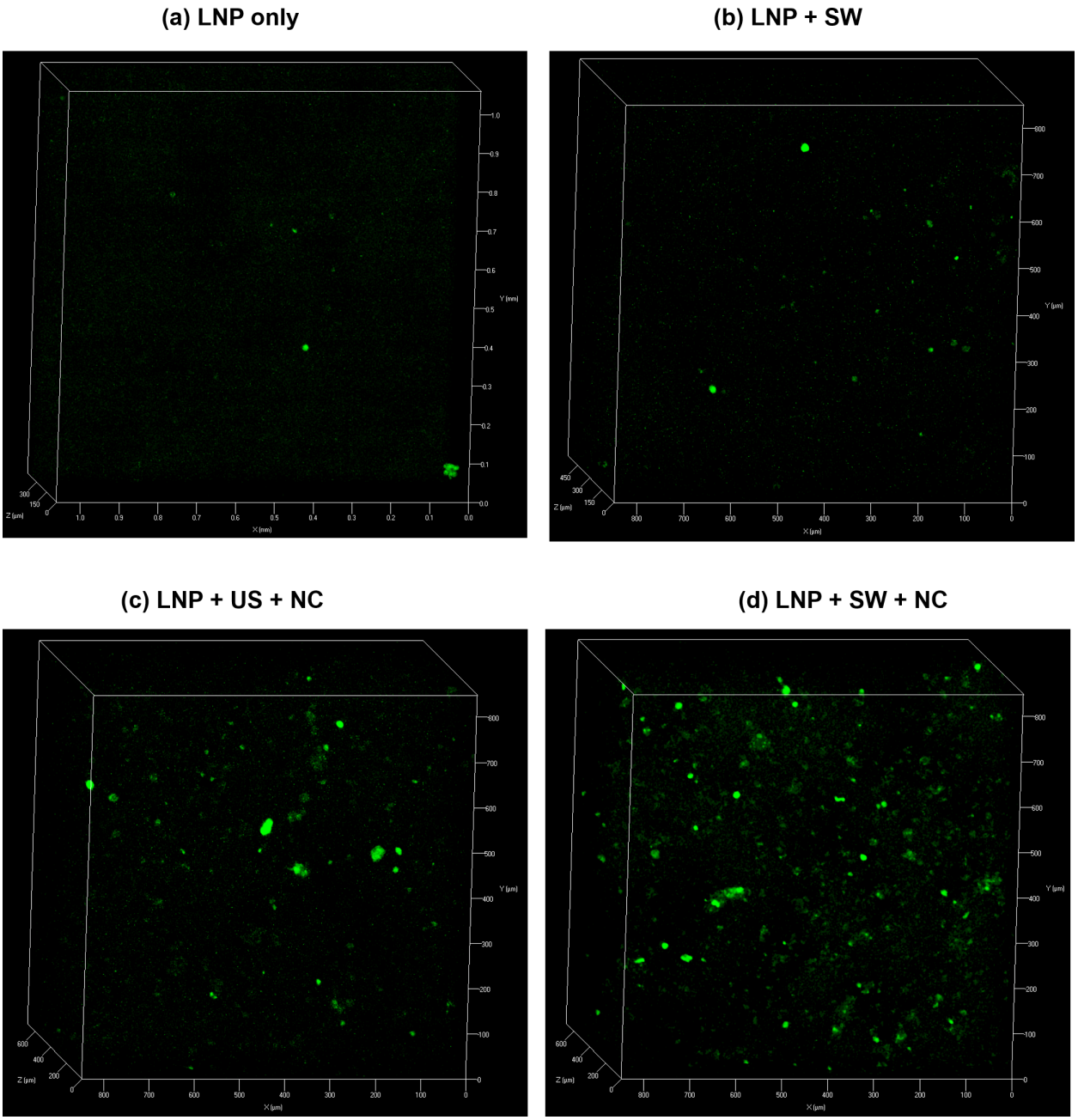


Figure 6.12: Selected confocal z-stack micrographs of the highest observed GFP expressions in the displayed treatment groups: (a) LNP only (or sham), (b) LNP with shock wave exposure, (c) LNP with ultrasound exposure in the presence of Nanocups, and (d) LNP with shock wave exposure in the presence of Nanocups.

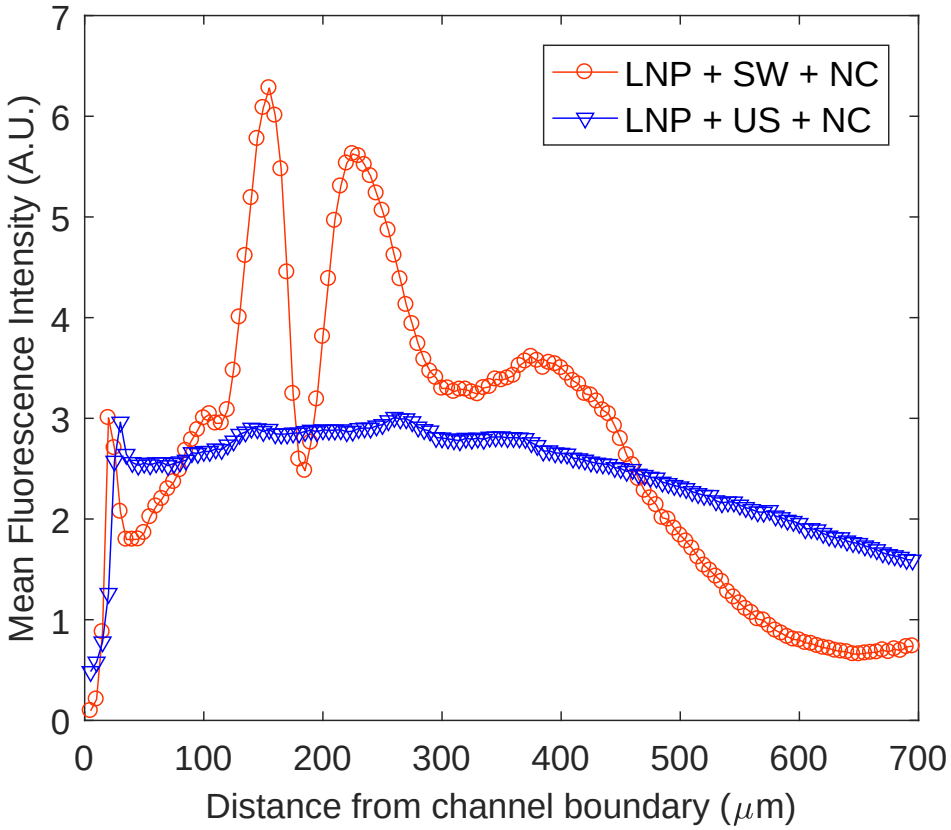


Figure 6.13: Corresponding profiles for the NC-containing samples, of fluorescence intensity along the thickness of the TMM, up to 0.695 mm above the upper edge of the channel.

SWs – was held approximately constant from 30 to 370 μm. Thus, although visibly less cells were transfected with US + NC, it was characterised by increased uniformity.

6.4 Discussion

Unprotected RNA is liable to premature degradation particularly in biological tissue, through which its cells are defended from the unwanted uptake of foreign genetic material, by a range of enzymes and mechanisms. Such resistance against exogenous material, can be overcome by lipid-based carriers of the nucleic acid. In this study, eGFP mRNA was packaged within a novel cationic lipid nanoparticle (LNP) developed by AstraZeneca. Focused ultrasound or shock waves with or without cavitation nuclei, were used to enhance the delivery of these LNP, having first established minimal induced cytotoxicity.

Here it was demonstrated that exclusive administration of the LNP, was an ineffective method of depositing its genetic cargo into tissue mimicking material, shedding light

on the failure of non-viral mechanisms to show efficacy in systems more complex than 1-D monolayer cell cultures. In cell suspensions, the LNP used alone yielded a similar transfection result to that of the average Lipofectamine control, alongside no apparent alleviation of the lipid-induced cytotoxicity (Figure 6.10). This motivated the use of enhancer methods such as ultrasound and shock waves which relied on the phenomenon of cavitation mediated delivery as inferred by the successful use of cavitation nucleation agents. However, we found that good delivery efficacy from such strategies may not be attained in all of the cell line targets as demonstrated by the significant toxicity to B16-F10(AP3) cells, induced by US or SW in the presence of SonoVue or Nanocups, thus making further consideration of this cell line unlikely to produce meaningful transfection.

Beside the several advantages of employing cavitation nuclei (as stated in section 6.1), we additionally report that only in the presence of the selected Nanocups nucleation agent, was substantially enhanced transgene delivery achieved in CT26 cells. In its absence, the lack of SW/US mediated enhancement observed even when cells were held in suspension and thereby closely interacting with the LNP; in addition to our previous non-encapsulated RNA delivery studies (*recall Chapter 3*), strongly implied that the inefficiency of the LNP + SW/US strategy was not necessarily related to inaccessibility or the mediated efficiency of transfection. Firstly, because comparably higher naked mRNA transfection using optimal shock waves was achieved than with LNP-complexed mRNA, it could be argued that the supplied sound energy for the permeation of the plasma membrane was sufficient for internalisation, but probably not enough to facilitate the opening of the lipid vector. Hence, considerable LNP delivery was noted only with the Nanocups, which served as foci for the local deposition of the SW/US energy through their implosion. In accordance, Lentacker et al. [288] reported that only in the presence of microbubbles (bound to the lipoplexes) did they observe statistically significant expression from luciferase pDNA. Secondly, the extent to which a transient pore is formed by means of SW or US exposure, may not have been adequate for LNP entry compared to naked RNA whose diameter is only a few nanometers [289]. However, although condensed nucleic acids are more favourable for transmembrane transport, Park et al.[290] performed atomic force microscopy on the

conformation of DNA post US treatment, and reported that low intensity ultrasound for at least 30 seconds sonication, instigated DNA folding that was reversible over time, thus indicating one potential benefit of delivering naked nucleic acid compared to its complexed state, when in the absence of cavitation agents.

Increased transgene expression per cell, after shock wave exposure (Figure 6.11(a)) has been previously reported by Millan-Chiu et al. [21], albeit as the prevailing effect over the magnitude of transfection (or number of expressing cells) relative to controls. On the other hand, the increased compliance of NCs under refined focused ultrasound conditions, resulted in the highest level of GFP expression observed in suspended cells. This powerful synergy has also been recognised in the delivery of oncolytic viruses [291].

The two types of cavitation nuclei employed, behaved differently under the influence of sound waves. One factor is the fact that SonoVue are soft-shelled microbubbles as they are phospholipid-based whereas the Nanocups are hard-shelled due to their polymer composition. Another factor is their size difference. The mean particle diameters of SonoVue and Nanocups are known to be $\sim$3 μm [190] and $\sim$0.5 μm [193] respectively. Small bubbles are more likely to easily penetrate into the TMM during SW/US exposure, contributing to locally induced bioeffects. Although in this study, better suited characterisation techniques for the SonoVue microbubbles within the phantom could not be performed, Kwan et al.[193] employed cavitation detection methods to investigate the impact of HIFU on SonoVue. At similar ultrasound conditions (0.5 MHz centre frequency, PRFP = 1.5 MPa) they found that the SonoVue microbubbles were destroyed and cleared in less than a 30 seconds long exposure. On the other hand, in the present experiments, the behaviour of Nanocups was found to be relatively stable as implied by the size characterisation (Figure 6.8), and was also more predictable as suggested by the consistency in the relative cytotoxicity between US and SW as shown in Figure 6.7 (i.e. in both cell lines greater US + NC induced cytotoxicity was observed relative to SW + NC induced cytotoxicity, unlike in the presence SonoVue).

Delivery of the lipoplexes into cells embedded in agarose gel, was achieved up to a depth of approximately 0.5 mm from a blood vessel-mimicking channel. It was not possible to quantify the number of transgene expressing cells microscopically because

of the inhomogeneous spread of transfection requiring the entire volumes to be imaged, and the variable intensities of cellular GFP expression making their segmentation biased. Moreover, as previously mentioned live cell release from the agarose to enable flow cytometry, was impossible. In any case, the attained penetration well exceeded the range of capillary to tumour cell distance of 33 – 63 μm reported in the literature [292].

Finally, we found the LNP to be generally stable in the presence of acoustic fields, more patently at the optimal non-CA conditions than otherwise (with NCs). Further investigation that is of interest, is on the SW/US mediated behaviour of the LNP in terms of its mRNA release profile, as well as the localisation of cavitation as a result of microbubble proximity to the LNP and to a cell.

The mediation of gene delivery between focused ultrasound and lithotripter shock waves, was difficult to categorise, despite having fixed all experimental variables and conditions, because both technologies demonstrated characteristics that would be valuable *in vivo*. However, shock waves were consistently able to achieve some degree of delivery in most of the conditions (with and without NCs) and in both cell configurations studied.

6.5 Closing Remarks

It was found that both US and SWs could improve delivery of AstraZeneca's LNP into cells. The investigation of US and SW parameters demonstrated a finite window whereby the viability of cells was maintained, and the lipid nanoparticle was found to be sufficiently stable after exposure to the selected US or SW conditions. This study demonstrated that appropriate cavitation promoting agents can be used in optimised shock wave fields to improve the delivery of nucleotides encapsulated in a lipid vector formulation. Focused ultrasound, as an alternative to shock waves, was shown to also enhance delivery, although with much greater reliance on cavitation nucleation. In the case of cell suspensions these equated to 3 – 4 fold enhancements in delivery. In 3-D culture, only the presence of cavitation nuclei achieved appreciable LNP delivery. It is therefore reasonable to conclude that there is marked utility in nano-sized cavitation nuclei with acoustic stimuli for gene delivery, irrespective of the cell environment.

7
Summary & Future Work

Contents

7.1 Summary 161
7.2 Future work 164

7.1 Summary

The application of shock waves for gene delivery is highly appealing due to their non-invasive nature, and ability to localise acoustic energy on a small target tissue area with minimal temperature change. In addition, the clinical relevance of lithotripter shock waves provides an already established pathway for the development of nucleic acid based therapies. However, this approach has thus far lacked a thorough understanding of its workings and suffers from insufficient demonstrations of a significant increase in transgene expression by shock wave mediation.

The overarching goal of this thesis was to exploit shock waves in the burgeoning area of RNA based therapies. We reported for the first time, mRNA as the genetic agent of choice for intracellular delivery using a clinical lithotripter, and developed a suitable tissue phantom that would enable good representation of the intended biological space. The shock waves were properly optimised before genetically treating cells, striking a balance between maximal cell permeabilisation and minimal cytotoxicity. Previous work has not been overly concerned with shock wave parameter optimisation, even though the sensitivity of cell treatment to the energy, number and delivery rate of shock waves has been well documented.

Prior to the delivery study, various important aspects of this strategy were characterised, as next described. Cell response was found to be highly SW dose dependent, and variable across different cell types. At the optimal SW settings which imparted maximum cell transfectability, the biological and structural stabilities of mRNA and siRNA were not found to be significantly altered. It was also of interest to determine the transport of RNA through tissue mimicking gel. By employing RNA analogs at different concentrations, penetration into the gel was readily observed with exposure to optimal SWs, to greater depths with increasing concentration. It was therefore noted that the full impact of SW induced macromolecular dissemination was supported by appropriate concentrations of it. Such potential may also be beneficial in enhancing the extravasation of drugs from tumour vasculature.

The subsequent deliveries of eGFP mRNA and eGFP siRNA were assessed by the production (through mRNA) or knock-down (through siRNA) of green fluorescent protein

(GFP) and measured by fluorescence intensity (Chapter 3). Statistically significant changes in GFP expression relative to controls were attained in both RNA deliveries, with exposure to optimal shock waves, whereby a 52 fold increase and a 2 fold decrease in mRNA and siRNA based expressions respectively, was reported. However, folds increase of GFP expression in terms of its fluorescence intensity, is an indeterminate measurement of the transfection efficiency because to put it simply, even between two low values, a fold increase can be numerically quite high (e.g. consider the fluorescence intensity values 0.1 and 1 in arbitrary units (A.U.), giving a fold increase of 10!). Still, this analysis was fitting for identifying the feasibility of gene delivery mediated by a given technology. In Chapter 3 a strong feasibility was revealed by lithotripter shock waves.

More fundamental quantitative forms of describing the delivery efficiency that are more useful from a broad therapy approach, are the proportion of transfected cells both by *actual* delivery (RNA) and outcome (transgene) as well as the effective RNA dose, as opposed to target protein-specific measurements. It was found that shock waves beneficially affected circa 25% of cells for therapy, but that only ∼1% of cells ultimately expressed the target protein, in parts due to: the degradation of the delivered naked mRNA, and the potential for increased mRNA decay during intracellular trafficking. In theory this may also have been a result of the stochasticity in mRNA translation (which was evidenced by the presence of gene expression in not *all* of the conducted experiments). It was also found that 4.2% of the administered RNA dose was internalised into the cells.

Regarding the kinetics of shock wave induced mRNA delivery, it was accepted that for a shock wave dose associated to no cytotoxicity and good cell transfectability (denoted as the optimum SWs in this thesis), mRNA transfer into the cells during SW treatment was not a linear process, and that it was the number of cells rather than the state of cellular permeability that increased with increasing number of shock waves. There was also qualitative evidence on mRNA exportation during treatment because of the negative mRNA transfer rates that exceeded the mRNA degradation rate, although further work would be required here. The kinetics of the therapeutic gain were predictable and consistent between the number of transgenic cells and the mass of transgenic protein.

Lastly, a recommendation on re-dosing (alongside its proper timing) was discussed for a significant therapeutic improvement in SW-mediated naked RNA based gene therapy.

The above described bioeffects could be mainly associated with inertial cavitation, which was later confirmed in Chapter 6, as the inclusion of cavitation nuclei led to significantly increased gene delivery. However, the impact of non-cavitational mechanisms involved in RNA uptake was investigated by using multicellular tumour spheroids (MCTSs). The MCTSs result in an *in vitro* cancer cell environment that is more realistic, and in addition result in the amplification of shear stresses. The suppression of cavitation was effected by exposing the cell samples to shock waves, in the presence of 350 and 700 kPa overpressure. Notably, it was found that at 700 kPa overpressure, the number of cavitation events and the mean bubble collapse time were substantially reduced, which meant that the tensile pressure of the shock wave (which is conducive to cavitation) was minimised. Comparison between SW exposure in the absence or presence of overpressure, revealed that the highest siRNA and mRNA uptakes in the spheroids occurred with the 350 kPa overpressure, and the lowest uptakes were recorded in the absence of overpressure. At the higher overpressure of 700 kPa, the level of increase in RNA uptake depended on the type of RNA nucleotide being delivered. The induced shear stresses were attributed to the changes in cell membrane permeability and subsequent intracellular transport of nucleotides. These findings developed further understanding of how shock waves impart access into cells, in more relevant diseased cell models.

As presented in Chapter 4, through several quantitative ways of determining shock wave mediated naked mRNA delivery, its efficiency was not found to be high enough to potentially translate *in vivo*. Therefore, a lipid nanoparticle (LNP) or protective vector that preserved the mRNA, as well as cavitation promoting agents (Nanocups or SonoVue) were employed, to leverage the capability of shock wave therapy both in the delivery and tissue penetration of the nucleotide. In these studies, focused ultrasound was also employed as an alternative to shock waves. The SW and US exposure parameters were optimised with the aim to minimise cytotoxicity with and without the cavitation agent and maintain LNP stability. It was found that in the presence of SonoVue, cytotoxicity was unavoidable in both SW and US exposures. However, with the Nanocups minimal

cytotoxicity was achieved. By escape from a vessel-mimicking channel, the lipoplexed mRNA penetrated into tissue mimicking material up to circa 500 μm with exposure to the acoustic stimuli and Nanocups cavitation agent. In a different configuration that enabled the quantification of this delivery, cells were suspended in the channel but maintained in the phantom, through which the highest gene expression achieved was in almost a quarter of the cells, in the presence of Nanocups. Comparison between shock waves and ultrasound revealed different strengths in both technologies; with shock waves there was evidence in favour of enhanced cellular gene expression, whereas with ultrasound, the distribution of gene expression was found to be more homogeneous across the TMM.

Finally, it is important to raise the relevant issue of *in vitro* effects as a result of specific experimental material, as reviewed by Miller et al.[279]. In this thesis, such effects were characterised through a preliminary study in Chapter 3 to determine the best choice of cell containment. In the case of the vial based cell experiments, the wall thickness was found to attenuate the SW positive pressure, which could be related to the attenuation of sound waves *in vivo* by body fat, characterised in the literature. Moreover, in the case of the tissue mimicking phantoms (employed in Chapters 3 through to 6), it was ensured that no reflecting surfaces due to the material interfering with the entry of shock waves were present, as they were designed to be large enough to exceed the aperture angle of the shock waves.

In conclusion, this thesis laid the foundation work in the development of shock wave mediated RNA based gene therapy, by establishing the efficiency of RNA delivery, the induced delivery profiles, the entailed mechanisms of delivery mediation, and the potential for significantly boosted gene expression in combination therapy.

7.2 Future work

This work has initiated and extensively progressed a shock wave strategy of delivery for RNA nucleotides. Future work that would considerably advance the research should look to *1.* study and identify medical indications in which such therapy can be suitably applied, and *2.* extend this work *in vivo* by delivering RNA-based therapeutics or vaccines, through animal studies. A clinical perspective was presented in Chapter 1,

whereby the genetic treatment of renal cells involved in the formation of renal stones, could be achieved by implementation of this strategy. Testing this application, could consider in the first instance the use of animal models of Dent's disease or Bartter syndrome type V, and appropriate coding RNAs. These *in vivo* studies should aim to determine to what extent a gene needs to be augmented or knocked down before the intended therapeutic effect is realised. It is noted that to enable the identification of suitable targets, it is necessary to gain a better understanding of why different cell types respond differently to SWs, by perhaps establishing the SW-induced transfectability as a function of the mechanical and elastic properties for an array of cell types.

Furthermore, an important area for future research would be based on comparative studies for other genetic agents such as DNA and ASO, to establish the performance of these agents relative to RNA, in shock wave induced gene delivery and kinetics. Another potential endeavour is the determination of the amount of cavitation nuclei that can be supplied for a given density of cells or target tissue size for maximal therapeutic outcome, beside optimisation of the shock wave parameters (which was carried out in this thesis).

Finally, a forward-looking recommendation is in the development of a mathematical model that can accurately predict levels of SW induced gene expression for different doses of administered RNA, as well as predict the pharmacokinetics of this delivery strategy. At an *in vitro* level, the presented kinetics data in Chapter 4 may serve as the model inputs. The model should ultimately help to expedite translation into the clinic.

These future developments may produce additional insight, and support the advancement of nucleic acid based cell therapies mediated by lithotripter shock waves, for the enhanced treatment of suited genetic disorders in humans.

Appendices

A
Appendix

Contents

A.1 siRNA delivery controls 168
A.2 Stock mRNA quantitation 168
A.3 The RT-qPCR reaction cycling programme 169
A.4 PCDs bracket design and assembly 169
A.5 Shock wave PRF effect on B16-F10(AP3) cells 170
A.6 Dynamic light scattering measurements of NCs, for phantom gels prepared in purified (Milli-Q) water 171

A.1 siRNA delivery controls

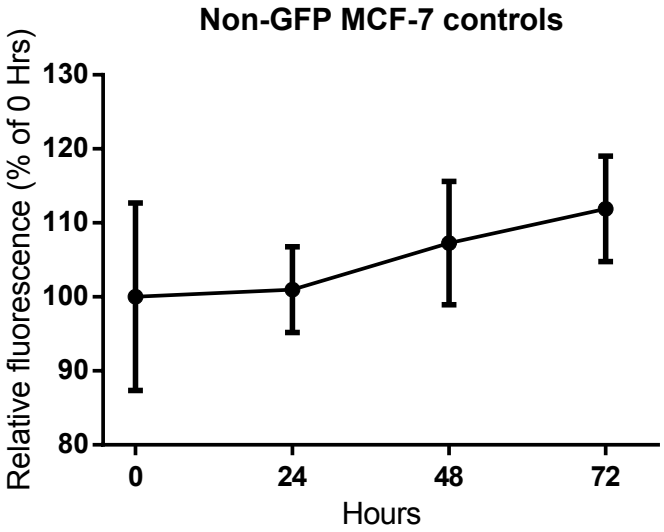


Figure A.1: Supplementary controls using non-GFP MCF-7 cells to determine background fluorescence, based on n = 3. Error bars are the standard deviations.

A.2 Stock mRNA quantitation

The A_{260} = 2.335 and A_{280} = 1.198. Thus the concentration was 93.4 μg/ml instead of the assumed 100 μg/ml, and purity was high ($A_{260/280}$ = 1.95). Subsequently, to administer 5 μg mRNA to the kinetic samples, 53.5 μL of the stock was added.

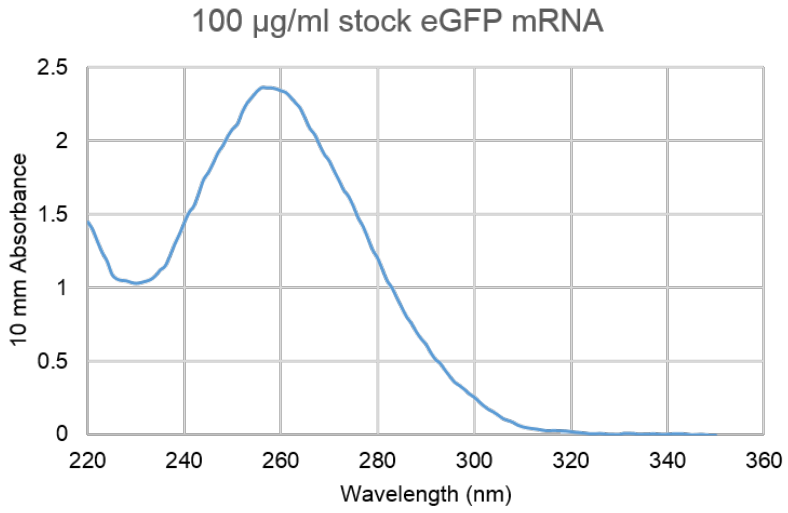


Figure A.2: A representative absorption spectrum of a 100 μg/ml mRNA stock for a kinetics independently conducted experiment.

A.3 The RT-qPCR reaction cycling programme

Activation:

50 °C for 3 minutes hold

95 °C for 5 minutes hold

40 PCR cycles of:

95 °C for 15 seconds

60 °C for 30 seconds

40 °C, 1 minute

Melting curve:

95 °C for 15 seconds

60 °C for 1 minutes

95 °C for 15 seconds

A.4 PCDs bracket design and assembly

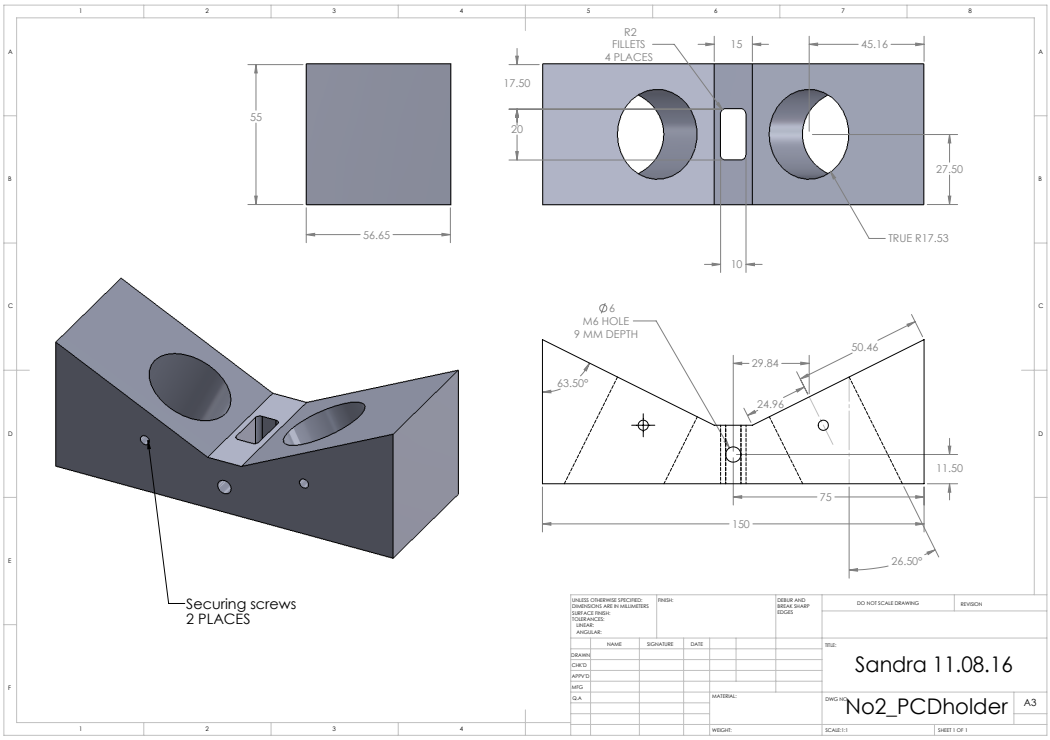


Figure A.3: PCD bracket (or holder) CAD design.

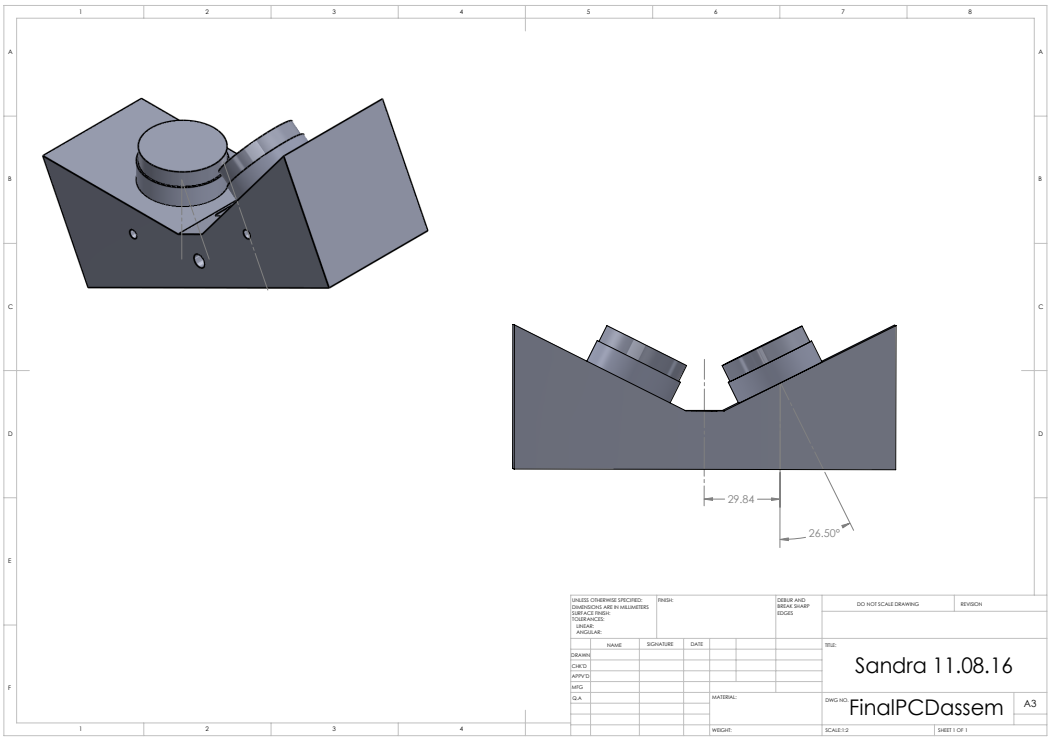
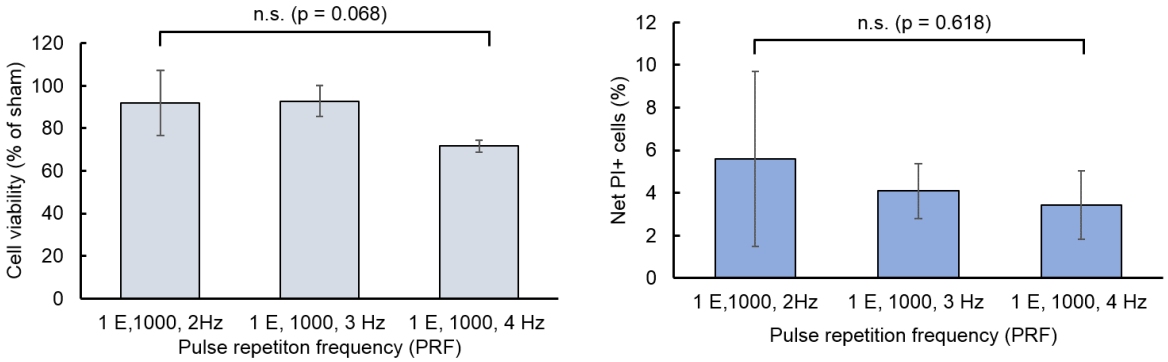


Figure A.4: PCDs and bracket assembly.

A.5 Shock wave PRF effect on B16-F10(AP3) cells



(a) (b)

Figure A.5: No statistical significance (n.s.) across PRF groups was found in both the viability and permeabilisation of B16-F10(AP3) cells, using the one-way Analysis of Variance (ANOVA) test at the $p<0.05$ level. Data represents $n = 3$, and the error bars are the standard deviations.

A.6 Dynamic light scattering measurements of NCs, for phantom gels prepared in purified (Milli-Q) water

Table A.1 provides a comparison between sham NC (in the usual TMM composition of this thesis i.e. PBS based agarose – presented in Chapter 6), water-based gel sham NC (Figure A.6), and fresh NC (from stock – presented in Chapter 6).

Table A.1: Collected DLS data of NC controls based on n=3

Sample NC	Mean particle diameter (nm)	PDI
Fresh NC	477.85 ± 4.45	0.12 ± 0.02
Sham NC	1049.70 ± 290.34	0.24 ± 0.05
Water based gel sham NC	476.57 ± 3.76	0.05 ± 0.02

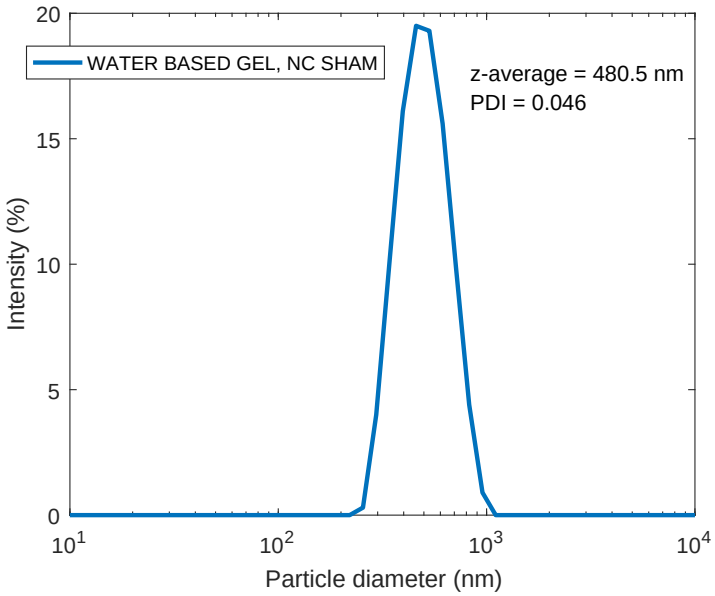


Figure A.6: Representative DLS size measurement of the water-based gel Nanocups sham.

Bibliography

[1] Vincent T Devita, Robert C Young, and George P Canellos. "Combination versus single agent chemotherapy: a review of the basis for selection of drug treatment of cancer". In: *Cancer* 35.1 (1975), pp. 98–110.

[2] Sijumon Kunjachan et al. "Multidrug resistance: Physiological principles and nanomedical solutions". In: *Advanced drug delivery reviews* 65.13 (2013), pp. 1852–1865.

[3] Pei Yun Teo et al. "Co-delivery of drugs and plasmid DNA for cancer therapy". In: *Advanced drug delivery reviews* 98 (2016), pp. 41–63.

[4] Cristina Núñez et al. "An overview of the effective combination therapies for the treatment of breast cancer". In: *Biomaterials* 97 (2016), pp. 34–50.

[5] Andrew B Hill et al. "Overcoming gene-delivery hurdles: Physiological considerations for nonviral vectors". In: *Trends in biotechnology* 34.2 (2016), pp. 91–105.

[6] Kelley A Parato et al. "Recent progress in the battle between oncolytic viruses and tumours". In: *Nature Reviews Cancer* 5.12 (2005), pp. 965–976.

[7] Hao Yin et al. "Non-viral vectors for gene-based therapy". In: *Nature Reviews Genetics* 15.8 (2014), pp. 541–555.

[8] Min Suk Shim and Young Jik Kwon. "Stimuli-responsive polymers and nanomaterials for gene delivery and imaging applications". In: *Advanced drug delivery reviews* 64.11 (2012), pp. 1046–1059.

[9] Sophie Mehier-Humbert et al. "Ultrasound-mediated gene delivery: kinetics of plasmid internalization and gene expression". In: *Journal of Controlled Release* 104.1 (2005), pp. 203–211.

[10] Marc Derieppe et al. "Real-time assessment of ultrasound-mediated drug delivery using fibered confocal fluorescence microscopy". In: *Molecular Imaging and Biology* 15.1 (2013), pp. 3–11.

[11] M Duvshani-Eshet et al. "Therapeutic ultrasound-mediated DNA to cell and nucleus: bioeffects revealed by confocal and atomic force microscopy". In: *Gene therapy* 13.2 (2006), pp. 163–172.

[12] Victor Frenkel. "Ultrasound mediated delivery of drugs and genes to solid tumors". In: *Advanced drug delivery reviews* 60.10 (2008), pp. 1193–1208.

[13] Diane Dalecki. "Mechanical bioeffects of ultrasound". In: *Annu. Rev. Biomed. Eng.* 6 (2004), pp. 229–248.

[14] TG Leighton. "The acoustic bubble. 1994". In: *ISBN: 0-12-44190-8* (1994).

[15] Mingxi Wan, Yi Feng, and Gail ter Haar. *Cavitation in Biomedicine: Principles and Techniques*. Springer, 2015.

[16] Annemieke Van Wamel et al. "Vibrating microbubbles poking individual cells: drug transfer into cells via sonoporation". In: *Journal of controlled release* 112.2 (2006), pp. 149–155.

[17] Paul Prentice et al. "Membrane disruption by optically controlled microbubble cavitation". In: *Nature Physics* 1.2 (2005), pp. 107–110.

[18] Douglas L Miller and Jianming Song. "Tumor growth reduction and DNA transfer by cavitation-enhanced high-intensity focused ultrasound in vivo". In: *Ultrasound in medicine & biology* 29.6 (2003), pp. 887–893.

[19] Victor Frenkel et al. "Pulsed high-intensity focused ultrasound enhances thrombolysis in an in vitro model 1". In: *Radiology* 239.1 (2006), pp. 86–93.

[20] Robin O Cleveland and James A McAteer. "The physics of shock wave lithotripsy". In: *Smith's Textbook on Endourology* 1 (2007), pp. 529–558.

[21] Blanca Millán-Chiu et al. "Shock Waves and DNA-Cationic Lipid Assemblies: A Synergistic Approach to Express Exogenous Genes in Human Cells". In: *Ultrasound in medicine & biology* 40.7 (2014), pp. 1599–1608.

[22] K Anwer et al. "Ultrasound enhancement of cationic lipid-mediated gene transfer to primary tumors following systemic administration." In: *Gene therapy* 7.21 (2000).

[23] Peter E Huber et al. "A comparison of shock wave and sinusoidal-focused ultrasound-induced localized transfection of HeLa cells". In: *Ultrasound in medicine & biology* 25.9 (1999), pp. 1451–1457.

[24] Michael J Stechman, Nellie Y Loh, and Rajesh V Thakker. "Genetic causes of hypercalciuric nephrolithiasis". In: *Pediatric nephrology* 24.12 (2009), pp. 2321–2332.

[25] Joel D Hernandez, Jonathan S Ellison, and Thomas S Lendvay. "Current trends, evaluation, and management of pediatric nephrolithiasis". In: *JAMA pediatrics* 169.10 (2015), pp. 964–970.

[26] Jaime Uribarri, Man S Oh, and Hugh J Carroll. "The first kidney stone". In: *Annals of internal medicine* 111.12 (1989), pp. 1006–1009.

[27] Joshua K Fine et al. "Effect of medical management and residual fragments on recurrent stone formation following shock wave lithotripsy". In: *The Journal of urology* 153.1 (1995), pp. 27–33.

[28] Maria Julia Calonge et al. "Genetic heterogeneity in cystinuria: the SLC3A1 gene is linked to type I but not to type III cystinuria". In: *Proceedings of the National Academy of Sciences* 92.21 (1995), pp. 9667–9671.

[29] Hiromi Koike et al. "An efficient gene transfer method mediated by ultrasound and microbubbles into the kidney". In: *The journal of gene medicine* 7.1 (2005), pp. 108–116.

[30] Oswald T Avery, Colin M MacLeod, and Maclyn McCarty. "Studies on the chemical nature of the substance inducing transformation of pneumococcal types induction of transformation by a desoxyribonucleic acid fraction isolated from pneumococcus type III". In: *The Journal of experimental medicine* 79.2 (1944), pp. 137–158.

[31] Ellen Borenfreund and Aaron Bendich. "A study of the penetration of mammalian cells by deoxyribonucleic acids". In: *The Journal of biophysical and biochemical cytology* 9.1 (1961), pp. 81–91.

[32] Basil S Pawlyk et al. "Gene replacement therapy rescues photoreceptor degeneration in a murine model of Leber congenital amaurosis lacking RPGRIP". In: *Investigative ophthalmology & visual science* 46.9 (2005), pp. 3039–3045.

[33] Frederick F Lang et al. "Phase I trial of adenovirus-mediated p53 gene therapy for recurrent glioma: biological and clinical results". In: *Journal of Clinical Oncology* 21.13 (2003), pp. 2508–2518.

[34] Julianna Lisziewicz et al. "Combination gene therapy: synergistic inhibition of human immunodeficiency virus Tat and Rev functions by a single RNA molecule". In: *Human gene therapy* 11.6 (2000), pp. 807–815.

[35] Sandy B Primrose and Richard Twyman. *Genomics: applications in human biology*. John Wiley & Sons, 2008.

[36] Pietro Genovese et al. "Targeted genome editing in human repopulating haematopoietic stem cells". In: *Nature* 510.7504 (2014), pp. 235–240.

[37] H Parekh-Olmedo et al. "Gene therapy progress and prospects: targeted gene repair". In: *Gene therapy* 12.8 (2005), pp. 639–646.

[38] Salima Hacein-Bey-Abina et al. "Sustained correction of X-linked severe combined immunodeficiency by ex vivo gene therapy". In: *New England Journal of Medicine* 346.16 (2002), pp. 1185–1193.

[39] Theodore Friedmann. "A brief history of gene therapy." In: *Nature genetics* 2.2 (1992), pp. 93–98.

[40] Jane D Mount et al. "Sustained phenotypic correction of hemophilia B dogs with a factor IX null mutation by liver-directed gene therapy". In: *Blood* 99.8 (2002), pp. 2670–2676.

[41] Artur V Cideciyan et al. "Human RPE65 gene therapy for Leber congenital amaurosis: persistence of early visual improvements and safety at 1 year". In: *Human gene therapy* 20.9 (2009), pp. 999–1004.

[42] Wolfgang Walther and Peter M Schlag. "Current status of gene therapy for cancer". In: *Current opinion in oncology* 25.6 (2013), pp. 659–664.

[43] Mario R Mautino, Nicholas Keiser, and Richard A Morgan. "Inhibition of human immunodeficiency virus type 1 (HIV-1) replication by HIV-1-based lentivirus vectors expressing transdominant Rev". In: *Journal of virology* 75.8 (2001), pp. 3590–3599.

[44] Serge Braun. "Gene-based therapies of neuromuscular disorders: an update and the pivotal role of patient organizations in their discovery and implementation". In: *The journal of gene medicine* 15.11-12 (2013), pp. 397–413.

[45] Desmond ST Nicholl. *An introduction to genetic engineering*. Cambridge University Press, 2008.

[46] W French Anderson. "Human gene therapy: scientific and ethical considerations". In: *Journal of Medicine and Philosophy* 10.3 (1985), pp. 275–292.

[47] Shawn Doonan. *Nucleic acids*. Vol. 20. Royal Society of Chemistry, 2004.

[48] P Saraswat et al. "DNA as therapeutics; an update". In: *Indian journal of pharmaceutical sciences* 71.5 (2009), p. 488.

[49] Siddhesh D Patil, David G Rhodes, and Diane J Burgess. "DNA-based therapeutics and DNA delivery systems: a comprehensive review". In: *The AAPS journal* 7.1 (2005), E61–E77.

[50] Ravinay Bhindi et al. “Brothers in arms: DNA enzymes, short interfering RNA, and the emerging wave of small-molecule nucleic acid-based gene-silencing strategies”. In: *The American journal of pathology* 171.4 (2007), pp. 1079–1088.

[51] Julian Davies and Antonio Jimenez. “A new selective agent for eukaryotic cloning vectors.” In: *The American journal of tropical medicine and hygiene* 29.5 Suppl (1980), pp. 1089–1092.

[52] Nirpendra Singh et al. “Inhibition of HIV-1 Integrase gene expression by 10-23 DNAzyme”. In: *Journal of biosciences* 37.3 (2012), pp. 493–502.

[53] Maria Konarska, Witold Filipowicz, and Hans J Gross. “RNA ligation via 2’-phosphomonoester, 3’5’-phosphodiester linkage: requirement of 2’, 3’-cyclic phosphate termini and involvement of a 5’-hydroxyl polynucleotide kinase”. In: *Proceedings of the National Academy of Sciences* 79.5 (1982), pp. 1474–1478.

[54] Maya Kahan-Hanum et al. “A library of programmable DNAzymes that operate in a cellular environment”. In: *Scientific reports* 3 (2013), p. 1535.

[55] Astrid Sigel, Helmut Sigel, and Roland KO Sigel. *Interplay between metal ions and nucleic acids*. Vol. 10. Springer Science & Business Media, 2012.

[56] J. Thomas August. *Gene Therapy*. Advances in pharmacology. Academic Press, 1997. URL: `https://books.google.co.uk/books?id=onvulAEACAAJ`.

[57] Phillip P Chan and Peter M Glazer. “Triplex DNA: fundamentals, advances, and potential applications for gene therapy”. In: *Journal of Molecular Medicine* 75.4 (1997), pp. 267–282.

[58] Changxian Shen et al. “Triplex-forming oligodeoxynucleotides targeting survivin inhibit proliferation and induce apoptosis of human lung carcinoma cells”. In: *Cancer gene therapy* 10.5 (2003), pp. 403–410.

[59] Samantha L Ginn et al. “Gene therapy clinical trials worldwide to 2012–an update”. In: *The journal of gene medicine* 15.2 (2013), pp. 65–77.

[60] T. Strachan and A.P. Read. *Human molecular genetics two*. Wiley-Liss, 1999. URL: `https://books.google.co.uk/books?id=6Y9qAAAAMAAJ`.

[61] K Pinel et al. “Long-term in vivo imaging of translated RNAs for gene therapy.” In: *Gene therapy* 21.4 (2014).

[62] Penn Medicine. *New Role for Transfer RNA*. 2010. URL: `http://news.pennmedicine.org/news-bites/2010/06/new-role-for-transfer-rna.html` (visited on 02/09/2016).

[63] P Ponsaerts, VFI Van Tendeloo, and ZN Berneman. “Cancer immunotherapy using RNA-loaded dendritic cells”. In: *Clinical & Experimental Immunology* 134.3 (2003), pp. 378–384.

[64] Thierry Bettinger et al. “Peptide-mediated RNA delivery: a novel approach for enhanced transfection of primary and post-mitotic cells”. In: *Nucleic acids research* 29.18 (2001), pp. 3882–3891.

[65] Chad V Pecot et al. “RNA interference in the clinic: challenges and future directions”. In: *Nature Reviews Cancer* 11.1 (2011), pp. 59–67.

[66] Sayda M Elbashir et al. “Duplexes of 21-nucleotide RNAs mediate RNA interference in cultured mammalian cells”. In: *nature* 411.6836 (2001), pp. 494–498.

[67] Sayda M Elbashir et al. "Functional anatomy of siRNAs for mediating efficient RNAi in Drosophila melanogaster embryo lysate". In: *The EMBO journal* 20.23 (2001), pp. 6877–6888.

[68] Mahmoud Elsabahy, Adil Nazarali, and Marianna Foldvari. "Non-viral nucleic acid delivery: key challenges and future directions". In: *Current drug delivery* 8.3 (2011), pp. 235–244.

[69] Yoshihito Ueno et al. "Synthesis of nuclease-resistant siRNAs possessing universal overhangs". In: *Bioorganic & medicinal chemistry* 17.5 (2009), pp. 1974–1981.

[70] Jonathan Hall. "Unravelling the general properties of siRNAs: strength in numbers and lessons from the past". In: *Nature Reviews Genetics* 5.7 (2004), pp. 552–557.

[71] Yuki Naito and Kumiko Ui-Tei. "siRNA design software for a target gene-specific RNA interference". In: *Frontiers in genetics* 3 (2012), p. 102.

[72] Martin Jinek and Jennifer A Doudna. "A three-dimensional view of the molecular machinery of RNA interference". In: *Nature* 457.7228 (2009), pp. 405–412.

[73] J.A. Roth. *Gene-Based Therapies for Cancer*. Current Cancer Research. Springer New York, 2010. URL: `https://books.google.co.uk/books?id=mKmZtKp4YjgC`.

[74] Meihong Chen et al. "Vector-based siRNA delivery strategies for high-throughput screening of novel target genes". In: *J RNAi Gene Silencing* 1 (2005), pp. 5–11.

[75] Donald D Rao et al. "siRNA vs. shRNA: similarities and differences". In: *Advanced drug delivery reviews* 61.9 (2009), pp. 746–759.

[76] Phong Trang et al. "Systemic delivery of tumor suppressor microRNA mimics using a neutral lipid emulsion inhibits lung tumors in mice". In: *Molecular Therapy* 19.6 (2011), pp. 1116–1122.

[77] Ramesh A Shivdasani. "MicroRNAs: regulators of gene expression and cell differentiation". In: *Blood* 108.12 (2006), pp. 3646–3653.

[78] Prasun J Mishra and Glenn Merlino. "MicroRNA reexpression as differentiation therapy in cancer". In: *The Journal of clinical investigation* 119.8 (2009), pp. 2119–2123.

[79] Asad U Khan. "Ribozyme: a clinical tool". In: *Clinica chimica acta* 367.1 (2006), pp. 20–27.

[80] Jérôme Mulhbacher, Patrick St-Pierre, and Daniel A Lafontaine. "Therapeutic applications of ribozymes and riboswitches". In: *Current opinion in pharmacology* 10.5 (2010), pp. 551–556.

[81] Alessio Peracchi. "Prospects for antiviral ribozymes and deoxyribozymes". In: *Reviews in medical virology* 14.1 (2004), pp. 47–64.

[82] D. Siderovski. *Regulators of G Protein Signalling*. Methods in Enzymology pt. 1. Elsevier Science, 2004. URL: `https://books.google.co.uk/books?id=1Vb86gbTzfUC`.

[83] Ronald T Mitsuyasu et al. "Phase 2 gene therapy trial of an anti-HIV ribozyme in autologous CD34+ cells". In: *Nature medicine* 15.3 (2009), pp. 285–292.

[84] Janet L Macpherson et al. "Long-term survival and concomitant gene expression of ribozyme-transduced CD4+ T-lymphocytes in HIV-infected patients". In: *The journal of gene medicine* 7.5 (2005), pp. 552–564.

[85] Li Wang, Wayne L Gerlach, Geoff Symonds, et al. "Target sequence-specific inhibition of Hiv-replication by ribozymes directed to tatRNA". In: *Nucleic acids research* 23.15 (1995), pp. 2909–2913.

[86] A Gatignol et al. "Towards gene therapy against HIV-1: new therapeutic target in gag RNA accessible to ribozymes and RNA interference molecules". In: *BMC Infect Dis* 14.Suppl 2 (2014), p. 019.

[87] Christopher G Janson and Matthew J During. *Peptide nucleic acids, morpholinos and related antisense biomolecules*. Springer, 2006.

[88] Peter Järver et al. "Peptide-mediated cell and in vivo delivery of antisense oligonucleotides and siRNA". In: *Molecular therapy. Nucleic acids* 1.6 (2012), e27.

[89] Sakari Kauppinen, Birte Vester, and Jesper Wengel. "Locked nucleic acid (LNA): High affinity targeting of RNA for diagnostics and therapeutics". In: *Drug Discovery Today: Technologies* 2.3 (2005), pp. 287–290.

[90] Carl Laxton et al. "Selection, optimization, and pharmacokinetic properties of a novel, potent antiviral locked nucleic acid-based antisense oligomer targeting hepatitis C virus internal ribosome entry site". In: *Antimicrobial agents and chemotherapy* 55.7 (2011), pp. 3105–3114.

[91] Melissa P Knauert and Peter M Glazer. "Triplex forming oligonucleotides: sequence-specific tools for gene targeting". In: *Human molecular genetics* 10.20 (2001), pp. 2243–2251.

[92] John C Burnett and John J Rossi. "RNA-based therapeutics: current progress and future prospects". In: *Chemistry & biology* 19.1 (2012), pp. 60–71.

[93] Jean-Remi Bertrand et al. "Comparison of antisense oligonucleotides and siRNAs in cell culture and in vivo". In: *Biochemical and biophysical research communications* 296.4 (2002), pp. 1000–1004.

[94] Saurabh Singh, Ajit S Narang, and Ram I Mahato. "Subcellular fate and off-target effects of siRNA, shRNA, and miRNA". In: *Pharmaceutical research* 28.12 (2011), pp. 2996–3015.

[95] P Shannon Pendergrast et al. "Nucleic acid aptamers for target validation and therapeutic applications". In: *Journal of biomolecular techniques: JBT* 16.3 (2005), p. 224.

[96] T Welzel et al. "Transfection of cells with custom-made calcium phosphate nanoparticles coated with DNA". In: *Journal of Materials Chemistry* 14.14 (2004), pp. 2213–2217.

[97] Viktoriya V Sokolova et al. "Effective transfection of cells with multi-shell calcium phosphate-DNA nanoparticles". In: *Biomaterials* 27.16 (2006), pp. 3147–3153.

[98] Martin Jordan, Annette Schallhorn, and Florian M Wurm. "Transfecting mammalian cells: optimization of critical parameters affecting calcium-phosphate precipitate formation". In: *Nucleic acids research* 24.4 (1996), pp. 596–601.

[99] Martin Jordan and Florian Wurm. "Transfection of adherent and suspended cells by calcium phosphate". In: *Methods* 33.2 (2004), pp. 136–143.

[100] Xingguo Cheng and Liisa Kuhn. "Chemotherapy drug delivery from calcium phosphate nanoparticles". In: *International journal of nanomedicine* 2.4 (2007), p. 667.

[101] Mónica Munoz-Úbeda et al. "Why is less cationic lipid required to prepare lipoplexes from plasmid DNA than linear DNA in gene therapy?" In: *Journal of the American Chemical Society* 133.45 (2011), pp. 18014–18017.

[102] Marie Morille et al. "Progress in developing cationic vectors for non-viral systemic gene therapy against cancer". In: *Biomaterials* 29.24 (2008), pp. 3477–3496.

[103] Hongtao Lv et al. "Toxicity of cationic lipids and cationic polymers in gene delivery". In: *Journal of Controlled Release* 114.1 (2006), pp. 100–109.

[104] Rebecca L Matz et al. "Polyplex exposure inhibits cell cycle, increases inflammatory response, and can cause protein expression without cell division". In: *Molecular pharmaceutics* 10.4 (2013), pp. 1306–1317.

[105] Shinichi Mochizuki et al. "The role of the helper lipid dioleoylphosphatidylethanolamine (DOPE) for DNA transfection cooperating with a cationic lipid bearing ethylenediamine". In: *Biochimica et Biophysica Acta (BBA)-Biomembranes* 1828.2 (2013), pp. 412–418.

[106] Maria C Pedroso de Lima et al. "Cationic lipid–DNA complexes in gene delivery: from biophysics to biological applications". In: *Advanced drug delivery reviews* 47.2 (2001), pp. 277–294.

[107] Darya A Medvedeva et al. "Novel cholesterol-based cationic lipids for gene delivery". In: *Journal of medicinal chemistry* 52.21 (2009), pp. 6558–6568.

[108] IM Hafez, N Maurer, and PR Cullis. "On the mechanism whereby cationic lipids promote intracellular delivery of polynucleic acids". In: *Gene therapy* 8.15 (2001), pp. 1188–1196.

[109] Virginie Escriou et al. "Cationic lipid-mediated gene transfer: effect of serum on cellular uptake and intracellular fate of lipopolyamine/DNA complexes". In: *Biochimica et Biophysica Acta (BBA)-Biomembranes* 1368.2 (1998), pp. 276–288.

[110] Shubiao Zhang et al. "Cationic compounds used in lipoplexes and polyplexes for gene delivery". In: *Journal of Controlled Release* 100.2 (2004), pp. 165–180.

[111] Uta Lungwitz et al. "Polyethylenimine-based non-viral gene delivery systems". In: *European Journal of Pharmaceutics and Biopharmaceutics* 60.2 (2005), pp. 247–266.

[112] RI Zhdanov, OV Podobed, and VV Vlassov. "Cationic lipid–DNA complexes—lipoplexes—for gene transfer and therapy". In: *Bioelectrochemistry* 58.1 (2002), pp. 53–64.

[113] Lene Jorgensen and Hanne Morck Nielson. *Delivery technologies for biopharmaceuticals: peptides, proteins, nucleic acids and vaccines*. John Wiley & Sons, 2009.

[114] Amit C Nathwani et al. "Adenovirus-associated virus vector–mediated gene transfer in hemophilia B". In: *New England Journal of Medicine* 365.25 (2011), pp. 2357–2365.

[115] Robert Coffin et al. "OncoVEX: A family of oncolytic herpes simplex viruses optimised for therapeutic use". In: *Journal of Immunotherapy* 27.6 (2004), S21.

[116] D Bouard, N Alazard-Dany, and F-L Cosset. "Viral vectors: from virology to transgene expression". In: *British journal of pharmacology* 157.2 (2009), pp. 153–165.

[117] Eliot Marshall. "Gene therapy death prompts review of adenovirus vector". In: *Science* 286.5448 (1999), pp. 2244–2245.

[118] Liliane Tenenbaum, Enni Lehtonen, and Paul E Monahan. "Evaluation of risks related to the use of adeno-associated virus-based vectors". In: *Current gene therapy* 3.6 (2003), pp. 545–565.

[119] J Gehl. "Electroporation: theory and methods, perspectives for drug delivery, gene therapy and research". In: *Acta Physiologica Scandinavica* 177.4 (2003), pp. 437–447.

[120] DJ Wells. "Gene therapy progress and prospects: electroporation and other physical methods". In: *Gene therapy* 11.18 (2004), pp. 1363–1369.

[121] Thomas L Ellis et al. "Nonthermal irreversible electroporation for intracranial surgical applications: laboratory investigation". In: *Journal of neurosurgery* 114.3 (2011), pp. 681–688.

[122] Sophie Mehier-Humbert and Richard H Guy. "Physical methods for gene transfer: improving the kinetics of gene delivery into cells". In: *Advanced drug delivery reviews* 57.5 (2005), pp. 733–753.

[123] Iben Spanggaard et al. "Gene electrotransfer of plasmid antiangiogenic metargidin peptide (AMEP) in disseminated melanoma: safety and efficacy results of a phase I first-in-man study". In: *Human Gene Therapy Clinical Development* 24.3 (2013), pp. 99–107.

[124] Adil I Daud et al. "Phase I trial of interleukin-12 plasmid electroporation in patients with metastatic melanoma". In: *Journal of Clinical Oncology* 26.36 (2008), pp. 5896–5903.

[125] Lluis M Mir. "Application of electroporation gene therapy: past, current, and future". In: *Electroporation Protocols: Preclinical and Clinical Gene Medicine* (2008), pp. 3–17.

[126] Georg Widera et al. "Increased DNA vaccine delivery and immunogenicity by electroporation in vivo". In: *The Journal of Immunology* 164.9 (2000), pp. 4635–4640.

[127] Sandhya Vasan et al. "In vivo electroporation enhances the immunogenicity of an HIV-1 DNA vaccine candidate in healthy volunteers". In: *PloS one* 6.5 (2011), e19252.

[128] Christian Plank, Olivier Zelphati, and Olga Mykhaylyk. "Magnetically enhanced nucleic acid delivery. Ten years of magnetofection—Progress and prospects". In: *Advanced drug delivery reviews* 63.14 (2011), pp. 1300–1331.

[129] Christian Plank et al. "The magnetofection method: using magnetic force to enhance gene delivery". In: *Biological chemistry* 384.5 (2003), pp. 737–747.

[130] Jun Sung Kim et al. "Toxicity and tissue distribution of magnetic nanoparticles in mice". In: *Toxicological Sciences* 89.1 (2006), pp. 338–347.

[131] F Scherer et al. "Magnetofection: enhancing and targeting gene delivery by magnetic force in vitro and in vivo". In: *Gene therapy* 9.2 (2002), pp. 102–109.

[132] Mi Kyung Yu et al. "Drug-loaded superparamagnetic iron oxide nanoparticles for combined cancer imaging and therapy in vivo". In: *Angewandte Chemie International Edition* 47.29 (2008), pp. 5362–5365.

[133] Arash Noori, P Ravi Selvaganapathy, and Joanna Wilson. "Microinjection in a microfluidic format using flexible and compliant channels and electroosmotic dosage control". In: *Lab on a Chip* 9.22 (2009), pp. 3202–3211.

[134] Robert F Marchington et al. "Optical injection of mammalian cells using a microfluidic platform". In: *Biomedical optics express* 1.2 (2010), pp. 527–536.

[135] Anthony Delalande et al. "Sonoporation: mechanistic insights and ongoing challenges for gene transfer". In: *Gene* 525.2 (2013), pp. 191–199.

[136] Sophie Mehier-Humbert et al. "Plasma membrane poration induced by ultrasound exposure: implication for drug delivery". In: *Journal of controlled release* 104.1 (2005), pp. 213–222.

[137] F Ronald Young. *Cavitation*. World Scientific, 1999.

[138] CMH Newman and T Bettinger. "Gene therapy progress and prospects: ultrasound for gene transfer". In: *Gene therapy* 14.6 (2007), pp. 465–475.

[139] Katharina Tschoep et al. "Shock waves: a novel method for cytoplasmic delivery of antisense oligonucleotides". In: *Journal of molecular medicine* 79.5-6 (2001), pp. 306–313.

[140] Kimberly R Byrnes et al. "Low power laser irradiation alters gene expression of olfactory ensheathing cells in vitro". In: *Lasers in surgery and medicine* 37.2 (2005), pp. 161–171.

[141] Makoto Ogura et al. "In vivo targeted gene transfer in skin by the use of laser-induced stress waves". In: *Lasers in surgery and medicine* 34.3 (2004), pp. 242–248.

[142] Giuseppe Palumbo et al. "Targeted gene transfer in eucaryotic cells by dye-assisted laser optoporation". In: *Journal of Photochemistry and Photobiology B: Biology* 36.1 (1996), pp. 41–46.

[143] Woan-Ruoh Lee et al. "Erbium: YAG laser-mediated oligonucleotide and DNA delivery via the skin: an animal study". In: *Journal of controlled release* 115.3 (2006), pp. 344–353.

[144] SHR Hosseini et al. "Development of shock wave assisted therapeutic devices and establishment of shock wave therapy". In: *Minimally Invasive Therapy & Allied Technologies* 15.4 (2006), pp. 230–240.

[145] Gopinathan K Menon, Nikiforos Kollias, and Apostolos G Doukas. "Ultrastructural evidence of stratum corneum permeabilization induced by photomechanical waves". In: *Journal of investigative dermatology* 121.1 (2003), pp. 104–109.

[146] Aoune Barhoumi et al. "Light-induced release of DNA from plasmon-resonant nanoparticles: towards light-controlled gene therapy". In: *Chemical Physics Letters* 482.4 (2009), pp. 171–179.

[147] Ellen F Fynan et al. "DNA vaccines: protective immunizations by parenteral, mucosal, and gene-gun inoculations". In: *Proceedings of the National Academy of Sciences* 90.24 (1993), pp. 11478–11482.

[148] Tamera M Pertmer et al. "Gene gun-based nucleic acid immunization: elicitation of humoral and cytotoxic T lymphocyte responses following epidermal delivery of nanogram quantities of DNA". In: *Vaccine* 13.15 (1995), pp. 1427–1430.

[149] Mark F Hamilton, David T Blackstock, et al. *Nonlinear acoustics*. Vol. 427. Academic press San Diego, 1998.

[150] Richard Courant and Kurt Otto Friedrichs. *Supersonic flow and shock waves*. Vol. 21. Springer Science & Business Media, 1999.

[151] M Thiel, M Nieswand, and M Dörffel. "Review: The use of shock waves in medicine—a tool of the modern OR: An overview of basic physical principles, history and research". In: *Minimally Invasive Therapy & Allied Technologies* 9.3-4 (2000), pp. 247–253.

[152] Ching-Jen Wang et al. “Shock wave therapy induces neovascularization at the tendon–bone junction. A study in rabbits”. In: *Journal of Orthopaedic Research* 21.6 (2003), pp. 984–989.

[153] TG Muir and EL Carstensen. “Prediction of nonlinear acoustic effects at biomedical frequencies and intensities”. In: *Ultrasound in medicine & biology* 6.4 (1980), pp. 345–357.

[154] John A Ogden, Anna Tóth-Kischkat, and Reiner Schultheiss. “Principles of shock wave therapy.” In: *Clinical orthopaedics and related research* 387 (2001), pp. 8–17.

[155] Andrew J Coleman and John E Saunders. “A survey of the acoustic output of commercial extracorporeal shock wave lithotripters”. In: *Ultrasound in medicine & biology* 15.3 (1989), pp. 213–227.

[156] Douglas L Miller, Chunyan Dou, and Jianming Song. “Lithotripter shockwave-induced enhancement of mouse melanoma lung metastasis: dependence on cavitation nucleation”. In: *Journal of endourology* 18.9 (2004), pp. 925–929.

[157] GON Oosterhof et al. “The influence of high-energy shock waves on the development of metastases”. In: *Ultrasound in medicine & biology* 22.3 (1996), pp. 339–344.

[158] Charles Marnick and Phil Gunby. “FDA approves lithotripter for kidney stone shattering”. In: *JAMA* 253.5 (1985), pp. 620–623.

[159] D Dalecki et al. “Thresholds for intestinal hemorrhage in mice exposed to a piezoelectric lithotripter”. In: *Ultrasound in medicine & biology* 21.9 (1995), pp. 1239–1246.

[160] Michael Delius et al. “Biological effects of shock waves: lung hemorrhage by shock waves in dogs—pressure dependence”. In: *Ultrasound in medicine & biology* 13.2 (1987), pp. 61–67.

[161] James A McAteer and Andrew P Evan. “The acute and long-term adverse effects of shock wave lithotripsy”. In: *Seminars in nephrology*. Vol. 28. 2. Elsevier. 2008, pp. 200–213.

[162] T Kishimoto et al. “Side effects of extracorporeal shock-wave exposure in patients treated by extracorporeal shock-wave lithotripsy for upper urinary tract stone.” In: *European urology* 12.5 (1985), pp. 308–313.

[163] L Filipczyński and J Wojcik. “Estimation of transient temperature elevation in lithotripsy and in ultrasonography”. In: *Ultrasound in medicine & biology* 17.7 (1991), pp. 715–721.

[164] Victor F Humphrey. “Ultrasound and matter—Physical interactions”. In: *Progress in biophysics and molecular biology* 93.1 (2007), pp. 195–211.

[165] Food, Drug Administration, et al. “Guidance for Industry and FDA Staff Information for Manufacturers Seeking Marketing Clearance of Diagnostic Ultrasound Systems and Transducers”. In: *Silver Spring: US FDA* (2008).

[166] Jürgen Eggers et al. “Sonothrombolysis with transcranial color-coded sonography and recombinant tissue-type plasminogen activator in acute middle cerebral artery main stem occlusion results from a randomized study”. In: *Stroke* 39.5 (2008), pp. 1470–1475.

[167] SP Meshram et al. “Ultrasonic cavitation induced degradation of Congo red in aqueous solutions”. In: *Chemical Engineering Research Bulletin* 14.2 (2010), pp. 119–123.

[168] D Felipe Gaitan et al. “Sonoluminescence and bubble dynamics for a single, stable, cavitation bubble”. In: *The Journal of the Acoustical Society of America* 91.6 (1992), pp. 3166–3183.

[169] Rocio Alvarez-Román et al. “Skin permeability enhancement by low frequency sonophoresis: lipid extraction and transport pathways”. In: *Journal of pharmaceutical sciences* 92.6 (2003), pp. 1138–1146.

[170] Constantin C Coussios and Ronald A Roy. “Applications of acoustics and cavitation to noninvasive therapy and drug delivery”. In: *Annu. Rev. Fluid Mech.* 40 (2008), pp. 395–420.

[171] AJ Coleman et al. “Acoustic emission and sonoluminescence due to cavitation at the beam focus of an electrohydraulic shock wave lithotripter”. In: *Ultrasound in medicine & biology* 18.3 (1992), pp. 267–281.

[172] Charles C Church. “A theoretical study of cavitation generated by an extracorporeal shock wave lithotripter”. In: *The Journal of the Acoustical Society of America* 86.1 (1989), pp. 215–227.

[173] AJ Coleman et al. “The spatial distribution of cavitation induced acoustic emission, sonoluminescence and cell lysis in the field of a shock wave lithotripter”. In: *Physics in medicine and biology* 38.11 (1993), p. 1545.

[174] MJ Choi, AJ Coleman, and JE Saunders. “The influence of fluid properties and pulse amplitude on bubble dynamics in the field of a shock wave lithotripter”. In: *Physics in medicine and biology* 38.11 (1993), p. 1561.

[175] Peter Huber, Knut Jöchle, and Jürgen Debus. “Influence of shock wave pressure amplitude and pulse repetition frequency on the lifespan, size and number of transient cavities in the field of an electromagnetic lithotripter”. In: *Physics in medicine and biology* 43.10 (1998), p. 3113.

[176] AR Williams et al. “Investigation of cavitation in flowing media by lithotripter shock waves both in vitro and in vivo”. In: *Ultrasound in medicine & biology* 15.1 (1989), pp. 53–60.

[177] AJ Coleman, MJ Choi, and JE Saunders. “Detection of acoustic emission from cavitation in tissue during clinical extracorporeal lithotripsy”. In: *Ultrasound in medicine & biology* 22.8 (1996), pp. 1079–1087.

[178] Andrew J Coleman et al. “Acoustic cavitation generated by an extracorporeal shockwave lithotripter”. In: *Ultrasound in medicine & biology* 13.2 (1987), pp. 69–76.

[179] Lawrence A Crum. “Acoustic cavitation”. In: *1982 Ultrasonics Symposium*. IEEE. 1982, pp. 1–11.

[180] Diane Dalecki et al. “The influence of contrast agents on hemorrhage produced by lithotripter fields”. In: *Ultrasound in medicine & biology* 23.9 (1997), pp. 1435–1439.

[181] Pei Zhong, Yufeng Zhou, and Songlin Zhu. “Dynamics of bubble oscillation in constrained media and mechanisms of vessel rupture in SWL”. In: *Ultrasound in medicine & biology* 27.1 (2001), pp. 119–134.

[182] Pei Zhong et al. “Inertial cavitation and associated acoustic emission produced during electrohydraulic shock wave lithotripsy”. In: *The Journal of the Acoustical Society of America* 101.5 (1997), pp. 2940–2950.

[183] Robin O Cleveland et al. “A dual passive cavitation detector for localized detection of lithotripsy-induced cavitation in vitro”. In: *The Journal of the Acoustical Society of America* 107.3 (2000), pp. 1745–1758.

[184] Miklós Gyöngy and Constantin-C Coussios. “Passive spatial mapping of inertial cavitation during HIFU exposure”. In: *IEEE Transactions on Biomedical Engineering* 57.1 (2010), pp. 48–56.

[185] Michael R Bailey et al. “Cavitation detection during shock-wave lithotripsy”. In: *Ultrasound in medicine & biology* 31.9 (2005), pp. 1245–1256.

[186] Tetsuya Kodama and Kazuyoshi Takayama. “Dynamic behavior of bubbles during extracorporeal shock-wave lithotripsy”. In: *Ultrasound in medicine & biology* 24.5 (1998), pp. 723–738.

[187] J Debus, WJ Lorenz, P Huber, et al. “A new method of quantitative cavitation assessment in the field of a lithotripter”. In: *Ultrasound in medicine & biology* 22.3 (1996), pp. 329–338.

[188] Thomas J Polascik. *Imaging and focal therapy of early prostate cancer*. Springer, 2013.

[189] Emil Brujan. *Cavitation in Non-Newtonian Fluids: With Biomedical and Bioengineering Applications*. Springer Science & Business Media, 2010.

[190] Jerry S Cheung et al. “Microbubbles as a novel contrast agent for brain MRI”. In: *Neuroimage* 46.3 (2009), pp. 658–664.

[191] Emilio Quaia. *Contrast media in ultrasonography*. Springer, 2005.

[192] Wen-Shiang Chen et al. “A comparison of the fragmentation thresholds and inertial cavitation doses of different ultrasound contrast agents”. In: *The Journal of the Acoustical Society of America* 113.1 (2003), pp. 643–651.

[193] James J Kwan et al. “Ultrasound-Propelled Nanocups for Drug Delivery”. In: *small* 11.39 (2015), pp. 5305–5314.

[194] Wolfgang Sass et al. “The mechanisms of stone disintegration by shock waves”. In: *Ultrasound in medicine & biology* 17.3 (1991), pp. 239–243.

[195] Xufeng Xi and Pei Zhong. “Dynamic photoelastic study of the transient stress field in solids during shock wave lithotripsy”. In: *The Journal of the Acoustical Society of America* 109.3 (2001), pp. 1226–1239.

[196] Thomas Bräuner, Franz Brümmer, and Dieter F Hülser. “Histopathology of shock wave treated tumor cell suspensions and multicell tumor spheroids”. In: *Ultrasound in medicine & biology* 15.5 (1989), pp. 451–460.

[197] Danny Howard and Bradford Sturtevant. “In vitro study of the mechanical effects of shock-wave lithotripsy”. In: *Ultrasound in medicine & biology* 23.7 (1997), pp. 1107–1122.

[198] Murtuza Lokhandwalla and Bradford Sturtevant. “Mechanical haemolysis in shock wave lithotripsy (SWL): I. Analysis of cell deformation due to SWL flow-fields”. In: *Physics in Medicine and Biology* 46.2 (2001), p. 413.

[199] Jonathan B Freund, Tim Colonius, and Andrew P Evan. “A cumulative shear mechanism for tissue damage initiation in shock-wave lithotripsy”. In: *Ultrasound in medicine & biology* 33.9 (2007), pp. 1495–1503.

[200] James A Rooney. "Shear as a mechanism for sonically induced biological effects". In: *The Journal of the Acoustical Society of America* 52.6B (1972), pp. 1718–1724.

[201] Mark A Stonehill et al. "An acoustically matched high pressure chamber for control of cavitation in shock wave lithotripsy: Mechanisms of shock wave damage in vitro". In: *Methods in cell science* 19.4 (1998), pp. 303–310.

[202] James C Williams et al. "Cell damage by lithotripter shock waves at high pressure to preclude cavitation". In: *Ultrasound in medicine & biology* 25.9 (1999), pp. 1445–1449.

[203] Michael Delius. "Minimal static excess pressure minimises the effect of extracorporeal shock waves on cells and reduces it on gallstones". In: *Ultrasound in medicine & biology* 23.4 (1997), pp. 611–617.

[204] Oleg A Sapozhnikov et al. "Effect of overpressure and pulse repetition frequency on cavitation in shock wave lithotripsy". In: *The Journal of the Acoustical Society of America* 112.3 (2002), pp. 1183–1195.

[205] Robin O Cleveland et al. "Effect of overpressure on dissolution and cavitation of bubbles stabilized on a metal surface". In: *The Journal of the Acoustical Society of America* 103.5 (1998), pp. 3038–3038.

[206] Andrew P Evan et al. "Kidney damage and renal functional changes are minimized by waveform control that suppresses cavitation in shock wave lithotripsy". In: *The Journal of urology* 168.4 (2002), pp. 1556–1562.

[207] Yufeng Zhou and Pei Zhong. "Suppression of large intraluminal bubble expansion in shock wave lithotripsy without compromising stone comminution: Refinement of reflector geometry". In: *The Journal of the Acoustical Society of America* 113.1 (2003), pp. 586–597.

[208] Songlin Zhu et al. "Reduction of tissue injury in shock-wave lithotripsy by using an acoustic diode". In: *Ultrasound in medicine & biology* 30.5 (2004), pp. 675–682.

[209] Shiping Bao et al. "In vivo transfection of melanoma cells by lithotripter shock waves". In: *Cancer research* 58.2 (1998), pp. 219–221.

[210] Darrell B Tata, Floyd Dunn, and Donald J Tindall. "Selective clinical ultrasound signals mediate differential gene transfer and expression in two human prostate cancer cell lines: LnCap and PC-3". In: *Biochemical and biophysical research communications* 234.1 (1997), pp. 64–67.

[211] Sorin V Pislaru et al. "Optimization of ultrasound-mediated gene transfer: comparison of contrast agents and ultrasound modalities". In: *European heart journal* 24.18 (2003), pp. 1690–1698.

[212] Allan Lawrie et al. "Ultrasound enhances reporter gene expression after transfection of vascular cells in vitro". In: *Circulation* 99.20 (1999), pp. 2617–2620.

[213] Ling Yong et al. "Microbubble-mediated sonoporation for highly efficient transfection of recalcitrant human B-cell lines". In: *Biotechnology journal* 9.8 (2014), pp. 1081–1087.

[214] Jose L Tlaxca et al. "Analysis of in vitro transfection by sonoporation using cationic and neutral microbubbles". In: *Ultrasound in medicine & biology* 36.11 (2010), pp. 1907–1918.

[215] IRINA V LARINA, B MARK EVERS, and RINAT O ESENALIEV. "Optimal drug and gene delivery in cancer cells by ultrasound-induced cavitation". In: *Anticancer research* 25.1A (2005), pp. 149–156.

[216] Achim M Loske et al. “Tandem shock waves to enhance genetic transformation of Aspergillus niger”. In: *Ultrasonics* 54.6 (2014), pp. 1656–1662.

[217] Eleanor Stride et al. “Enhancement of microbubble mediated gene delivery by simultaneous exposure to ultrasonic and magnetic fields”. In: *Ultrasound in medicine & biology* 35.5 (2009), pp. 861–868.

[218] Yoichi Negishi et al. “Delivery of siRNA into the cytoplasm by liposomal bubbles and ultrasound”. In: *Journal of Controlled Release* 132.2 (2008), pp. 124–130.

[219] Héctor R Guzmán et al. “Bioeffects caused by changes in acoustic cavitation bubble density and cell concentration: a unified explanation based on cell-to-bubble ratio and blast radius”. In: *Ultrasound in medicine & biology* 29.8 (2003), pp. 1211–1222.

[220] P Lukes et al. “Tandem shock waves in medicine and biology: a review of potential applications and successes”. In: *Shock Waves* 26.1 (2016), pp. 1–23.

[221] U Lauer et al. “Shock wave permeabilization as a new gene transfer method.” In: *Gene therapy* 4.7 (1997), pp. 710–715.

[222] Douglas L Miller et al. “Ultrasonic enhancement of gene transfection in murine melanoma tumors”. In: *Ultrasound in medicine & biology* 25.9 (1999), pp. 1425–1430.

[223] Jianming Song et al. “Combined shock-wave and immunogene therapy of mouse melanoma and renal carcinoma tumors”. In: *Ultrasound in medicine & biology* 28.7 (2002), pp. 957–964.

[224] MAURICE STEPHAN MICHEL et al. “Acoustic energy: a new transfection method for cancer of the prostate, cancer of the bladder and benign kidney cells”. In: *Anticancer research* 24.4 (2004), pp. 2303–2308.

[225] R Murata et al. “The effects of radial shock waves on gene transfer in rabbit chondrocytes in vitro”. In: *Osteoarthritis and Cartilage* 15.11 (2007), pp. 1275–1282.

[226] Raffi Bekeredjian et al. “Impact of microbubbles on shock wave-mediated DNA uptake in cells in vitro”. In: *Ultrasound in medicine & biology* 33.5 (2007), pp. 743–750.

[227] Chang Hoon Ha et al. “Novel mechanism of gene transfection by low-energy shock wave”. In: *Scientific reports* 5 (2015).

[228] Luz M Lopez-Marin et al. “Shock wave-induced damage and poration in eukaryotic cell membranes”. In: *The Journal of membrane biology* (2016), pp. 1–12.

[229] Steven Mo et al. “Ultrasound-enhanced drug delivery for cancer”. In: *Expert opinion on drug delivery* 9.12 (2012), pp. 1525–1538.

[230] Franz Brümmer, Th Bräuner, and Dieter F Hülser. “Biological effects of shock waves”. In: *World Journal of Urology* 8.4 (1990), pp. 224–232.

[231] Franz Brümmer et al. “Effect of shock waves on suspended and immobilized L1210 cells”. In: *Ultrasound in medicine & biology* 15.3 (1989), pp. 229–239.

[232] S Gambihler, M Delhis, and JW Ellwart. “Permeabilization of the plasma membrane of L1210 mouse leukemia cells using lithotripter shock waves”. In: *The Journal of membrane biology* 141.3 (1994), pp. 267–275.

[233] Michael Delius and Gerhard Adams. “Shock wave permeabilization with ribosome inactivating proteins: a new approach to tumor therapy”. In: *Cancer research* 59.20 (1999), pp. 5227–5232.

[234] GON Oosterhof et al. "The in vitro effect of electromagnetically generated shock waves (Lithostar) on the Dunning R3327 PAT-2 rat prostatic cancer cell-line". In: *Urological research* 17.1 (1989), pp. 13–19.

[235] Ikramy A Khalil et al. "Uptake pathways and subsequent intracellular trafficking in nonviral gene delivery". In: *Pharmacological reviews* 58.1 (2006), pp. 32–45.

[236] Simon P Langdon. *Cancer Cell Culture: Methods and Protocols*. Vol. 88. Springer Science & Business Media, 2004.

[237] Xianqiang Li et al. "Generation of destabilized green fluorescent protein as a transcription reporter". In: *Journal of Biological Chemistry* 273.52 (1998), pp. 34970–34975.

[238] Anna M Weihs et al. "Shock wave treatment enhances cell proliferation and improves wound healing by ATP release-coupled extracellular signal-regulated kinase (ERK) activation". In: *Journal of Biological Chemistry* 289.39 (2014), pp. 27090–27104.

[239] Stefan Gambihler, Michael Delius, and Walter Brendel. "Biological effects of shock waves: cell disruption, viability, and proliferation of L1210 cells exposed to shock waves in vitro". In: *Ultrasound in medicine & biology* 16.6 (1990), pp. 587–594.

[240] Raffi Karshafian et al. "Sonoporation by ultrasound-activated microbubble contrast agents: effect of acoustic exposure parameters on cell membrane permeability and cell viability". In: *Ultrasound in medicine & biology* 35.5 (2009), pp. 847–860.

[241] IEC IEC61846. "61846 Ultrasonics-Pressure pulse lithotriptors-Characteristics of fields". In: *International Electrotechnical Commission, Geneva, Switzerland* (1998).

[242] N Smith et al. "A comparison of light spot hydrophone and fiber optic probe hydrophone for lithotripter field characterization". In: *Review of Scientific Instruments* 83.1 (2012), p. 014301.

[243] Andrew Fire, Marshall Nirenberg, and Krishnarao Appasani. *RNA interference technology: from basic science to drug development*. Cambridge University Press, 2005.

[244] Alex Forbrich et al. "Microbubble-enhanced ultrasound liberation of mRNA biomarkers in vitro". In: *Ultrasound in medicine & biology* 39.6 (2013), pp. 1087–1093.

[245] Marie-Luce De Temmerman et al. "mRNA-Lipoplex loaded microbubble contrast agents for ultrasound-assisted transfection of dendritic cells". In: *Biomaterials* 32.34 (2011), pp. 9128–9135.

[246] Gerlinde Schwake et al. "Predictive modeling of non-viral gene transfer". In: *Biotechnology and bioengineering* 105.4 (2010), pp. 805–813.

[247] Derek W Bartlett and Mark E Davis. "Insights into the kinetics of siRNA-mediated gene silencing from live-cell and live-animal bioluminescent imaging". In: *Nucleic acids research* 34.1 (2006), pp. 322–333.

[248] Robert Carlisle et al. "Enhanced tumor uptake and penetration of virotherapy using polymer stealthing and focused ultrasound". In: *Journal of the National Cancer Institute* (2013), djt305.

[249] Ahad Rahim et al. "Physical parameters affecting ultrasound/microbubble-mediated gene delivery efficiency in vitro". In: *Ultrasound in medicine & biology* 32.8 (2006), pp. 1269–1279.

[250] Jochen Guck et al. “Optical deformability as an inherent cell marker for testing malignant transformation and metastatic competence”. In: *Biophysical journal* 88.5 (2005), pp. 3689–3698.

[251] M Duvshani-Eshet et al. “Therapeutic ultrasound-mediated DNA to cell and nucleus: bioeffects revealed by confocal and atomic force microscopy”. In: *Gene therapy* 13.2 (2005), pp. 163–172.

[252] DL Miller and RM Thomas. “The role of cavitation in the induction of cellular DNA damage by ultrasound and lithotripter shock waves in vitro”. In: *Ultrasound in medicine & biology* 22.5 (1996), pp. 681–687.

[253] Ernest L Madsen et al. “Tissue-mimicking agar/gelatin materials for use in heterogeneous elastography phantoms”. In: *Physics in medicine and biology* 50.23 (2005), p. 5597.

[254] Lynda JM Juffermans et al. “Ultrasound and microbubble-targeted delivery of small interfering RNA into primary endothelial cells is more effective than delivery of plasmid DNA”. In: *Ultrasound in medicine & biology* 40.3 (2014), pp. 532–540.

[255] Keller Rinaudo et al. “A universal RNAi-based logic evaluator that operates in mammalian cells”. In: *Nature biotechnology* 25.7 (2007), pp. 795–801.

[256] International Electrotechnical Committee et al. “Ultrasonics–pressure pulse lithotripters–characteristics of fields”. In: *IEC standard* 61846 (1998).

[257] Electro Medical Systems. *Swiss PiezoClast Operation Instructions*. URL: `http://www.paroco.co.rs/ems/PiezoClast1.pdf` (visited on 12/15/2016).

[258] Tetsuya Kodama, Michael R Hamblin, and Apostolos G Doukas. “Cytoplasmic molecular delivery with shock waves: importance of impulse”. In: *Biophysical journal* 79.4 (2000), pp. 1821–1832.

[259] MR Bailey et al. “Bioeffects of positive and negative acoustic pressures invivo”. In: *The Journal of the Acoustical Society of America* 100.6 (1996), pp. 3941–3946.

[260] Jian Ye et al. “Primer-BLAST: a tool to design target-specific primers for polymerase chain reaction”. In: *BMC bioinformatics* 13.1 (2012), p. 1.

[261] Brett E Houk, Gunther Hochhaus, and Jeffrey A Hughes. “Kinetic modeling of plasmid DNA degradation in rat plasma”. In: *AAPS PharmSci* 1.3 (1999), pp. 15–20.

[262] Lioudmila V Sharova et al. “Database for mRNA half-life of 19 977 genes obtained by DNA microarray analysis of pluripotent and differentiating mouse embryonic stem cells”. In: *DNA research* 16.1 (2009), pp. 45–58.

[263] Mads Kærn et al. “Stochasticity in gene expression: from theories to phenotypes”. In: *Nature Reviews Genetics* 6.6 (2005), pp. 451–464.

[264] Pete Corish and Chris Tyler-Smith. “Attenuation of green fluorescent protein half-life in mammalian cells”. In: *Protein engineering* 12.12 (1999), pp. 1035–1040.

[265] Stefan Stangl et al. “In vivo imaging of CT26 mouse tumours by using cmHsp70. 1 monoclonal antibody”. In: *Journal of cellular and molecular medicine* 15.4 (2011), pp. 874–887.

[266] Helen M Beere. “The stress of dying’: the role of heat shock proteins in the regulation of apoptosis”. In: *Journal of Cell Science* 117.13 (2004), pp. 2641–2651.

[267] Bart Lammertink et al. “Duration of ultrasound-mediated enhanced plasma membrane permeability”. In: *International journal of pharmaceutics* 482.1 (2015), pp. 92–98.

[268] Robyn K Schlicher et al. “Mechanism of intracellular delivery by acoustic cavitation”. In: *Ultrasound in medicine & biology* 32.6 (2006), pp. 915–924.

[269] Carolin Leonhardt et al. “Single-cell mRNA transfection studies: delivery, kinetics and statistics by numbers”. In: *Nanomedicine: Nanotechnology, Biology and Medicine* 10.4 (2014), pp. 679–688.

[270] Katherine W Ferrara, Mark A Borden, and Hua Zhang. “Lipid-shelled vehicles: engineering for ultrasound molecular imaging and drug delivery”. In: *Accounts of chemical research* 42.7 (2009), pp. 881–892.

[271] Franziska Hirschhaeuser et al. “Multicellular tumor spheroids: an underestimated tool is catching up again”. In: *Journal of biotechnology* 148.1 (2010), pp. 3–15.

[272] Wolfgang Mueller-Klieser. “Three-dimensional cell cultures: from molecular mechanisms to clinical applications”. In: *American Journal of Physiology-Cell Physiology* 273.4 (1997), pp. C1109–C1123.

[273] Mark A Haidekker, Nicolas L’Heureux, and John A Frangos. “Fluid shear stress increases membrane fluidity in endothelial cells: a study with DCVJ fluorescence”. In: *American Journal of Physiology-Heart and Circulatory Physiology* 278.4 (2000), H1401–H1406.

[274] Indu Khurana. *Medical Physiology for undergraduate students*. Elsevier Health Sciences, 2014.

[275] MS Levy et al. “Effect of shear on plasmid DNA in solution”. In: *Bioprocess and Biosystems Engineering* 20.1 (1999), pp. 7–13.

[276] Sundaram Ramakrishnan. “Hydrogel-siRNA for cancer therapy”. In: *Cancer biology & therapy* 11.9 (2011), pp. 849–851.

[277] Christopher E Brennen. *Cavitation and bubble dynamics*. Cambridge University Press, 2013.

[278] Oksana Sirenko et al. “High-content assays for characterizing the viability and morphology of 3D cancer spheroid cultures”. In: *Assay and drug development technologies* 13.7 (2015), pp. 402–414.

[279] Morton W Miller, Douglas L Miller, and Andrew A Brayman. “A review of in vitro bioeffects of inertial ultrasonic cavitation from a mechanistic perspective”. In: *Ultrasound in medicine & biology* 22.9 (1996), pp. 1131–1154.

[280] Aaron C Anselmo and Samir Mitragotri. “Nanoparticles in the clinic”. In: *Bioengineering & Translational Medicine* 1.1 (2016), pp. 10–29.

[281] F Danhier. “To exploit the tumor microenvironment: Since the EPR effect fails in the clinic, what is the future of nanomedicine?” In: *Journal of Controlled Release* 244 (2016), pp. 108–121.

[282] Rainer H Mueller, Karsten Maeder, and Sven Gohla. “Solid lipid nanoparticles (SLN) for controlled drug delivery–a review of the state of the art”. In: *European journal of pharmaceutics and biopharmaceutics* 50.1 (2000), pp. 161–177.

[283] Francis Ka-Ming Chan, Kenta Moriwaki, and Maria Jose De Rosa. “Detection of necrosis by release of lactate dehydrogenase activity”. In: *Immune Homeostasis: Methods and Protocols* (2013), pp. 65–70.

[284] Christy K Holland and Robert E Apfel. "Thresholds for transient cavitation produced by pulsed ultrasound in a controlled nuclei environment". In: *The Journal of the Acoustical Society of America* 88.5 (1990), pp. 2059–2069.

[285] Susan M Graham et al. "Inertial cavitation to non-invasively trigger and monitor intratumoral release of drug from intravenously delivered liposomes". In: *Journal of Controlled Release* 178 (2014), pp. 101–107.

[286] Mark A Borden et al. "Influence of lipid shell physicochemical properties on ultrasound-induced microbubble destruction". In: *IEEE transactions on ultrasonics, ferroelectrics, and frequency control* 52.11 (2005), pp. 1992–2002.

[287] K Dane Wittrup and Gregory L Verdine. *Protein engineering for therapeutics*. Vol. 503. Academic Press, 2012.

[288] Ine Lentacker et al. "Ultrasound exposure of lipoplex loaded microbubbles facilitates direct cytoplasmic entry of the lipoplexes". In: *Molecular pharmaceutics* 6.2 (2009), pp. 457–467.

[289] John J Kasianowicz et al. "Characterization of individual polynucleotide molecules using a membrane channel". In: *Proceedings of the National Academy of Sciences* 93.24 (1996), pp. 13770–13773.

[290] DongHee Park et al. "Sound Packing DNA: packing open circular DNA with low-intensity ultrasound". In: *Scientific reports* 5 (2015).

[291] Rachel Myers et al. "Polymeric Cups for Cavitation-mediated Delivery of Oncolytic Vaccinia Virus". In: *Molecular Therapy* (2016).

[292] Joanne R Less et al. "Microvascular architecture in a mammary carcinoma: branching patterns and vessel dimensions". In: *Cancer research* 51.1 (1991), pp. 265–273.